NANOOBJECTS & NANOSTRUCTURING

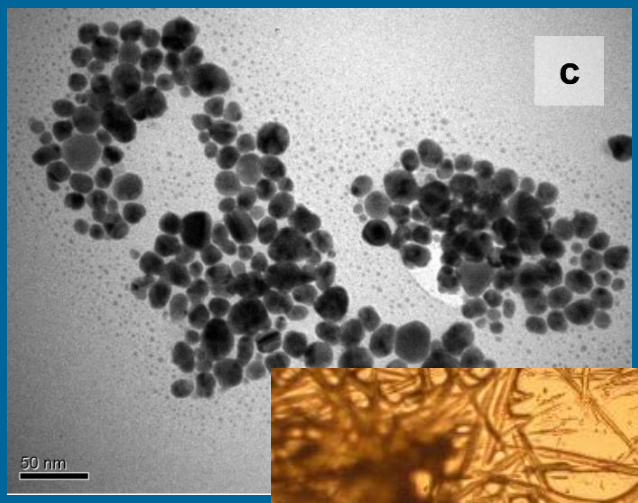

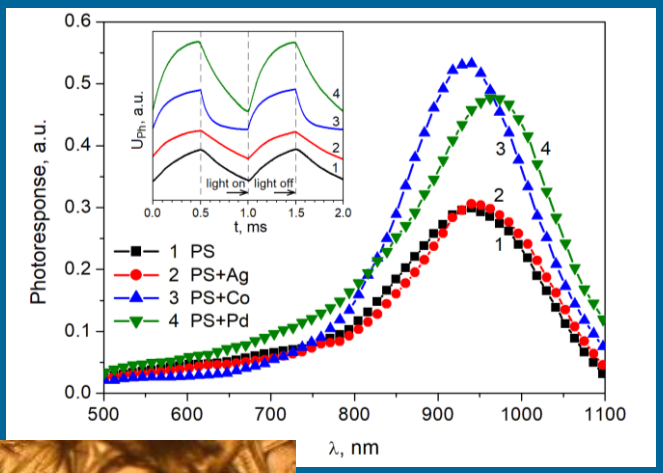

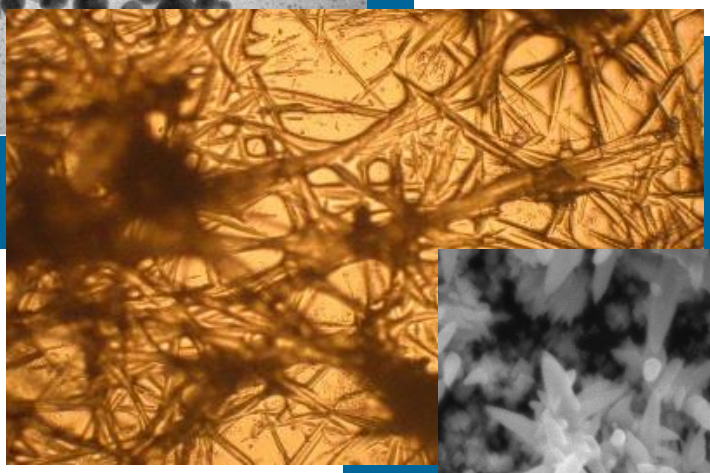

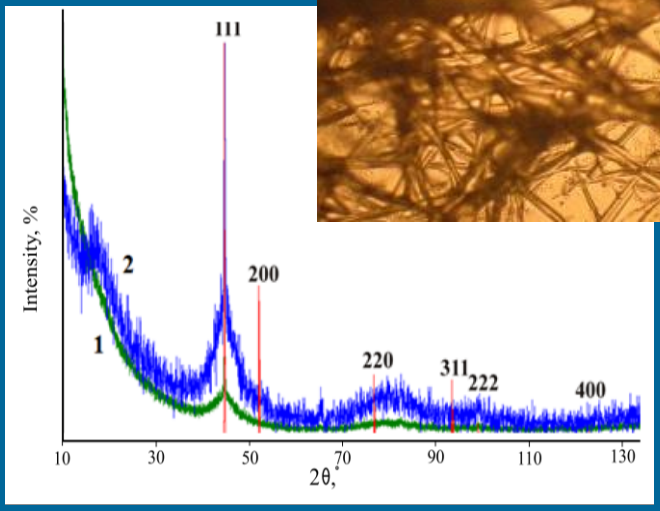

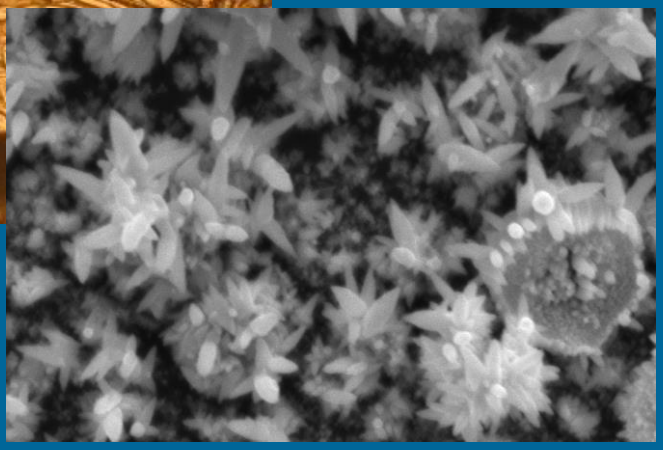

VOLUME I

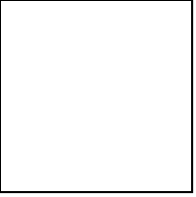

NANOOBJECTS & NANOSTRUCTURING

COLLECTIVE MONOGRAPH

VOLUME I

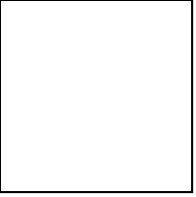

NANOOBJECTS & NANOSTRUCTURING

COLLECTIVE MONOGRAPH

VOLUME I

Edited by
Lidiya M. Boichyshyn, CSc
Oleksandr V. Reshetnyak. DSc

Nova Printing Inc.
Mississauga, Ontario, Canada
2022

Nova Printing Inc.
2550 Goldenridge Road
Mississauga, ON, L4X 3S3
Tel: 905-281-3231

Nanoobjects & Nanostructuring. Volume I / Edited by Lidiya M. Boichyshyn and Oleksandr. V. Reshetnyak. – Mississauga, Ontario: Nova Printing Inc., 2022. – 160 + *xviii* p.

This Book is Dedicated
to the 150th Anniversary of
Shevchenko Scientific Society

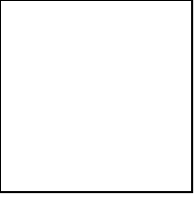

ABOUT THE EDITORS

Lidiya M. Boichyshyn

Lidiya Boichyshyn, CSc, Docent, Associated Professor of the Department of Physical and Colloid Chemistry of Ivan Franko National University of Lviv (Lviv, Ukraine), Chairwoman of Organizing Committee of International Research and Practice Conference «Nanoobjects & Nanostructuring» (N&N). She is the author of three monographs, 22 patents and more than 300 publications in various journals and conference proceedings. His scientific activity is in the fields of physical chemistry of nanosystems, amorphous metallic alloys, power sources and chemical ecology. She is Deputy Editor-in-Chief of the scientific journal "*Proceedings of Shevchenko Scientific Society. Chemical Sciences*" (Lviv, Ukraine), Valid Member and Deputy Head of the Shevchenko Scientific Society (Lviv, Ukraine).

Contact address:
6 Kyryla & Mefodiya Str., Lviv, 79005, Ukraine
Tel: (+38) (032) 2600–397
E-mail: lidiya.boichyshyn@lnu.edu.ua

Oleksandr V. Reshetnyak

Oleksandr Reshetnyak, DSc, Professor, Laureate of the Borys Paton National Prize of Ukraine (2021), Head of the Department of Physical and Colloid Chemistry of Ivan Franko National University of Lviv (Lviv, Ukraine), Vice-chairman of Program Committee of International Research and Practice Conference «Nanoobjects & Nanostructuring» (N&N). He is the author of three monographs and more than 400 publications in various journals and conference proceedings. His scientific activity is in the fields of physical chemistry of nanosystems, conductive polymers and its composites, electrochemistry of organic compounds. He is a Editor-in-Chief of the scientific journal "*Proceedings of Shevchenko Scientific Society. Chemical Sciences*" (Lviv, Ukraine) and Member of editorial boards of a collection of scientific works *«Visnyk Lvivskogo Universytetu, Seria Khimia»* (Lviv, Ukraine). He is also Valid Member of the Shevchenko Scientific Society (Lviv, Ukraine), member of the Bureau of the Scientific Council of the National Academy of Sciences of Ukraine on the problem of "Electrochemistry» (Kyiv, Ukraine).

Contact address:
6 Kyryla & Mefodiya Str., Lviv, 79005, Ukraine
Tel: (+38) (032) 2600–397
E-mail: oleksandr.reshetnyak@lnu.edu.ua

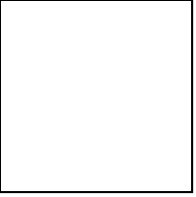

CONTENTS

LIST OF CONTRIBUTORS

O. I. Aksimentyeva
Ivan Franko National University of Lviv, 79005 Lviv, Ukraine

L. Ardanova
Minnesota State University, Mankato, 56001 Minnesota, USA

L. I. Bazylyak
Department of Physical Chemistry of Fossil Fuels of the Institute of Physical-Organic Chemistry and Coal Chemistry NAS of Ukraine, 79060 Lviv, Ukraine

L. M. Boichyshyn
Ivan Franko National University of Lviv, 79005 Lviv, Ukraine

E. Get'man
Vasyl' Stus Donetsk National University, 21027 Vinnytsia, Ukraine

P. V. Gorskyi
Institute of Thermoelectricity of the NAS and MES of Ukraine, 58029 Chernivtsi, Ukraine; Yu. Fedkovych Chernivtsi National University, 58012 Chernivtsi, Ukraine

O. M. Hertsyk
Ivan Franko National University of Lviv, 79005 Lviv, Ukraine

Yu. Yu. Horbenko
Ivan Franko National University of Lviv, 79005 Lviv, Ukraine

T. G. Hula
Ivan Franko National University of Lviv, 79005 Lviv, Ukraine

D. S. Kamenskyh
V. P. Kukhar Institute of Bioorganic Chemistry and Petrochemistry, National Academy of Sciences of Ukraine, Kyiv-94 02094, Ukraine

Kh. I. Khrushchyk
Ivan Franko National University of Lviv, 79005 Lviv, Ukraine

M. O. Kovbuz
Ivan Franko National University of Lviv, 79005 Lviv, Ukraine

O. I. Kuntyi
Lviv Polytechnic National University, 79013, Lviv Ukraine

A. R. Kytsya
Department of Physical Chemistry of Fossil Fuels of the Institute of Physical-Organic Chemistry and Coal Chemistry NAS of Ukraine, 79060 Lviv, Ukraine

M. M. Lopachak

Ivan Franko National University of Lviv, 79005 Lviv, Ukraine

O. Mariichak
Vasyl' Stus Donetsk National University, 21027 Vinnytsia, Ukraine

G. V. Martynyuk
Rivne State Humanitarian University, Rivne, Ukraine

A. S. Mazur
Lviv Polytechnic National University, 79013, Lviv Ukraine

L. S. Monastyrskii
Ivan Franko National University of Lviv, 79005 Lviv, Ukraine

Yu. Oleksii
Vasyl' Stus Donetsk National University, 21027 Vinnytsia, Ukraine

I. B. Olenych
Ivan Franko National University of Lviv, 79005 Lviv, Ukraine

N. L. Pandiak
Ukrainian National Forestry University, 79057 Lviv, Ukraine

S. Radio
Vasyl' Stus Donetsk National University, 21027 Vinnytsia, Ukraine

O. V. Reshetnyak
Ivan Franko National University of Lviv, 79005 Lviv, Ukraine

Y. V. Sheludko
V. P. Kukhar Institute of Bioorganic Chemistry and Petrochemistry, National Academy of Sciences of Ukraine, Kyiv-94 02094, Ukraine

M. V. Shepida
Lviv Polytechnic National University, 79013, Lviv Ukraine

T. V. Tkachenko
V. P. Kukhar Institute of Bioorganic Chemistry and Petrochemistry, National Academy of Sciences of Ukraine, Kyiv-94 02094, Ukraine

V. O. Yevdokymenko
V. P. Kukhar Institute of Bioorganic Chemistry and Petrochemistry, National Academy of Sciences of Ukraine, Kyiv-94 02094, Ukraine

O. A. Yezerska
Fraunhofer Institute for Manufacturing Technology and Advanced Materials, 28359 Bremen, Germany

G. I. Zozulya
Lviv Polytechnic National University, 79013, Lviv Ukraine

Institutions of Authors

1. Department of Physical Chemistry of Fossil Fuels of the Institute of Physical-Organic Chemistry and Coal Chemistry NAS of Ukraine, 79060 Lviv, Ukraine
2. Fraunhofer Institute for Manufacturing Technology and Advanced Materials, 28359 Bremen, Germany
3. Institute of Thermoelectricity of the NAS and MES of Ukraine, 58029 Chernivtsi, Ukraine; Yu. Fedkovych Chernivtsi National University, 58012 Chernivtsi, Ukraine
4. Lviv Polytechnic National University, 79013, Lviv Ukraine
5. Ivan Franko National University of Lviv, 79005 Lviv, Ukraine
6. Minnesota State University, Mankato, 56001 Minnesota, USA
7. Rivne State Humanitarian University, Rivne, Ukraine
8. Ukrainian National Forestry University, 79057 Lviv, Ukraine
9. Vasyl' Stus Donetsk National University, 21027 Vinnytsia, Ukraine
10. V. P. Kukhar Institute of Bioorganic Chemistry and Petrochemistry, National Academy of Sciences of Ukraine, Kyiv-94 02094, Ukraine

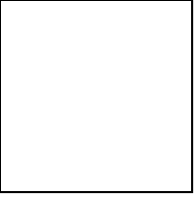

LIST OF ABBREVIATIONS

AgNCs	silver nanoclusters
AgNPs	silver nanoparticles
AFM	atomic force microscopy / microscope
AMA	amorphous metallic alloy
CI	crystallinity index
CP	conducting polymer
CVA	cyclic voltammetry / voltammogram
CVC	current-voltage characteristic
DBSA	dodecylbenzene sulfonic acid
DSC	differential scanning calorimetry
DP	degree of polymerization
DTG	differential thermogravimetry
E_A	energy of activation
EDXMA	X-ray microanalysis
EIS	electrochemical impedance spectroscopy
EN	electronegativity
GO	graphene oxide
HER	hydrogen evolution reaction
MCC	microcrystalline cellulose
ML	monolayer
MNPs	metal nanoparticles
NaPA	polyacrylate (sodium salt)
NC	nanocellulose
PAA	polyacrylic acids
PAn	polyaniline
PL	photoluminescence
PMAA	polymethacrylic acids
PMMA	polymethyl methacrylate
PoA	poly-ortho-anisidine
PoT	poly-ortho-toluidine
PS	polystyrene
pSi	porous silicon
PVA	polyvinyl alcohol
PVP	polyvinylpyrrolidone

REE	rare-earth elements
rGO	reduced graphene oxide
RL	rhamnolipid
SCE	saturated calomel electrode
St-MA	copolymer of styrene with malein anhydride (styromal)
TEM	transmission electron microscopy / microscope
TES	thermoelectric superlattice
TESMC	thermoelectric superlattice – metal couple
T_C	Curie temperature
TG	thermogravimetry
thermoEMF	thermoelectromotive force ()
TM	thermomagnetogram
TSA	toluene sulfonic acid
TSD	thermally stimulated depolarization
VA	voltammetry / voltammogram
XRD	X-ray diffraction

PREFACE

International Research and Practice Conference «Nanoobjects & Nanostructuring» (N&N) is dedicated to problems of nanomaterials, nanochemistry and nanotechnologies, namely physical chemistry of nanosized and nanostructured materials; nanostructuring in 0D–3D systems: thermodynamic and kinetics aspects; synthesis and characterisation of nanoobjects; organic and inorganic nanomaterials, supramolecular chemistry; application of nanostructurized systems etc.

The 2nd Conference was held at Ivan Franko National University of Lviv, Ukraine on September 26–28, 2022. Both famous and young scientists has been presented the results of studies which were carried out above all in the Ukrainian universities and research Institutes of the National Academy of Sciences of Ukraine, and also in the scientific centers of Finland, Germany, Hungary, Poland, Slovak Republic, and USA.

Presented Collective Monograph contains the papers which were selected between oral presentation on 2nd International Research and Practice Conference «Nanoobjects & Nanostructuring» (N&N-2022) and were recommended by Program and Organizing Committees to publishing in the expanded form.

The *Chapter 1* is dedicated by processes of nanofabrication, structure, and properties of hybrid nanocomposites based on dielectric polymer or semiconductor matrices with conducting polymers. It is determined that the concentration dependence of the specific conductivity of composites has a percolation character, when a dielectric polymer matrix causes significant delocalization of the charge along the macrochains. It is shown that semiconductor nanocrystals embedded in the polymer matrix and conducting polymers integrated with porous semiconductor mediums significantly affect the electrical, electrooptical, and luminescent properties of composites, what expands the functionality of conducting polymer composites for their application in organic electronic devices.

The results of the calculations of mixing energies (interaction parameters) in isostructural β-YF_3 components of the Gd_1–xLn_xF_3, Ln = Sm–Lu, Y systems are presented in *Chapter 2*. It is shown that the magnitude of the mixing energy is determined mainly by the difference in the sizes of the substituting structural units and, to a lesser extent, by the differrence in the degrees of ionicity of the chemical bond in the components. A diagram of thermodynamic stability is presented, which makes it possible to predict the temperature ranges of the existence of continuous series of solid solutions, as well as the limits of substitution depending on their decomposition temperature. The regions of thermodynamic stability, instability, and supposed metastability of solid solutions are determined and dependences of decomposition temperatures on composition for the studied systems are plotted.

It is proposed that the results of the work can be useful in choosing the ratio of components in "mixed" matrices, as well as the amount of activator in practically important medical nanomaterials.

A diffusion theory of the electrical contact resistance of a thermoelectric superlattice (TES) – metal couple is proposed in *Chapter 3*. On its basis, the thickness of the transient contact layer and the value of the electrical contact resistance of TES – metal are determined. Moreover, the law of growth of the transient contact layer is found. It is concluded that the electrical contact resistance of the thermoelectric material-metal for the bismuth-nickel telluride couple is due to the deviation surface of the semiconductor from the ideal plane and the presence of an oxide film on the surface of the TES.

The effect of nanocrystallization during thermal treatment of Fe-, Al-, and Co-based amorphous alloys (AMA) and nature of doping agents (rare-earth and transition metals) on their physico-chemical properties is analyzed in the *Chapters 4*, *5* and *7*. The nature of the nanocrystalline phases has been identified by X-ray diffraction method. The corrosion resistance of AMAs has been studied in NaCl and KOH aqueous solutions by voltammetry method in potentiodynamic mode.

The *Chapter 6* presents an influence of the surfactant nature on the main parameters of silver nanoparticles (AgNPs) synthesized by different electrochemical methods. It has been established that via electrochemical methods it is possible to synthesize the AgNPs with small sizes under the conditions of effective stabilization of nanoclusters and nanoparticles by surfactants. The type of surfactants determines the complexes' stability as well as the cathodic polarization which are influential factors in the controlled synthesis of AgNPs.

The results of the studies of inorganic nanosystems created by depositing ZnO, reduced graphene oxide (rGO) or metal nanoclusters on the porous silicon (PSi) are presented in *Chapter 8*. The possibility of controlling the spectrum of multicolor photoemission of the PSi–ZnO nanosystems by adjusting the excitation energy has been demonstrated. The incorporation of the rGO or metal nanoclusters into the porous layer leads to an increase in the efficiency of the photoelectric structures due to better surface passivation and the formation of additional conductive channels. It was proposed that found sensitivity of the PSi-based nanosystems to γ- and β-radiation can be used in dosimetric devices.

The *Chapter 9* is dedicated of the problem of nanocellulose (NC) production from the microcrystalline cellulose (MCC) obtained from air-dry soybean straw by the method of organ-solvent cooking obtained. It is shown, that due to the destruction of amorphous binders in the original MCC observe ordering of the structure of the obtainned NC, which is expressed in reducing the degree of polymerization more than twice compared to the initial MCC. It is determined that NC forms an anisotropic relief which consists of many parallel bands (ridges) and striped reliefs with almost parallel-oriented linear stripes.

Editors

Chapter 1

NANOFABRICATION OF HYBRID COMPOSITES WITH DIELECTRIC AND SEMICONDUCTOR MATRICES

O. I. Aksimentyeva[1], Yu. Yu. Horbenko[1], I. B. Olenych[1], and G. V. Martynyuk[2]

[1]*Ivan Franko National University of Lviv, 79005 Lviv, Ukraine*

[2]*Rivne State Humanitarian University, Rivne, Ukraine*

Corresponding author: olena.aksimentyeva@lnu.edu.ua

Contents

Abstract

The processes of nanofabrication, structure, and properties of hybrid nanocomposites based on dielectric polymer (polymethylmethacrylate, polyvinyl alcohol, polystyrene, etc.) or semiconductor matrices (porous silicon, gallium, or indium selenide, titanium dioxide) with conducting polymers of different nature were studied. The conducting polymer forms its own polymer network inside the host dielectric polymer or semiconductor matrix. It is shown that the concentration dependence of the specific conductivity of composites has a percolation character with a low "percolation threshold" in the range of 1,7–2,5 vol.%. According to EPR-spectroscopy, a dielectric polymer matrix causes significant delocalization of the charge along the macrochains. Semiconductor nanocrystals embedded in the polymer matrix and conducting polymers integrated with porous semiconductor mediums significantly affect the electrical, electrooptical, and luminescent properties of composites causing the shift of spectrum and change of its intensity. The connection between the conditions of synthesis, structure, and properties of materials can cause the expanding functionality of conducting polymer composites for their application in organic electronic devices – gas sensors, organic displays, solar cells, etc.

1.1 Introduction

The rapid development of science and technology led to the emergence of "intellectual" or "smart" polymer nanomaterials, which thanks to multifunctional properties, ease of processing, and environmental stability are extremely promising for modern science-intensive technologies [1–10]. The use of conducting polymer fillers in the structure of "intelligent" material allows the creation of highly efficient devices of a new generation: flexible sensors [3, 6], biosensors [4, 8], supercapacitors [9], antistatic and anti-radar coatings [10], solar cells [5, 7], and organic displays [11]. The principle of operation of these devices is based on the change of electronic properties of conjugated polymers [1, 5, 12–14].

Conjugated polyaminoarenes, in particular polyaniline and its derivatives, have their own electronic conductivity and act as conductive fillers in composites with polymer matrices [6]. Such compounds are characterized by high conductivity and stability [5, 12, 15], simplicity of synthesis, and relatively low cost. These polymers can be considered "synthetic nanometals" with a particle diameter of 10–20 nm and unique electronic, optical, electrochemical, and catalytic properties, including the ability to absorb radioactive rays.

It is known that in polymer-polymer systems, formed by dielectric polymer matrices of different types, conductivity can appear even at low content of conductive filler [6, 14].

The study of percolation phenomena in filled polymer systems is an important fundamental task, as the description of the properties of systems in the vicinity of the critical point opens up prospects for the creation of nanomaterials with predicted functional characteristics.

1.2 Nanofabrication of Conducting Polymers in Dielectric Polymer Matrices

Conducting polymer composites based on conjugated polyaminoarenes – polyaniline and its derivatives are of great interest due to their low relative density, corrosion resistance, good manufacturability (recyclability), and the possibility to control the conductivity. The creation of conducting polymer composites with highly elastic polymer matrices allows for improving the mechanical properties, in particular their flexibility, microhardness, tensile strength, thermoplasticity, etc. [3, 6]. Therefore, macromolecular matrices are intensively searched not only to improve the mechanical properties but also to preserve the features of charge transfer and optical absorption of conducting polymers (CP) in polymer matrices.

The improvement of electrical and optical properties of conducting polymer-polymer composites is achieved at a very low concentration of conducting polymer filler ($\leq$ 5% by volume) and depends on its dispersion degree and filler-matrix interfacial adhesion [6]. At a certain critical concentration value of conductive filler, depending on systems, a jump-like change in properties is observed [6, 9]. That is, the dependence of electrical conductivity (σ) on the volume content of the filler (φ, %) is nonlinear. This is usually an example of a typical percolation transition of a composite from a non-conductive to a conductive state. Herewith, the molecules of the conductive filler or their aggregates form a polymer mesh penetrating the entire volume of the material.

1.2.1 Percolation Phenomena in Polymer-Polymer Nanocomposites

For a scientifical explanation of the complex dependence of conductivity on the content of conductive filler in composite materials (two-phase systems), a "percolation theory" for a continuous medium was formulated. This theory determines the value of the critical volume concentration of the conductive phase φ_C, i.e. the percolation threshold that allows the insulator-conductor transition in stochastic systems [6, 16–19]. The theory of percolation (flow, impregnation) is a mathematical theory used in different fields of science to describe the emergence of infinite connected structures (clusters) in random (stochastic) mediums consisting of individual elements [20].

This theory allows describing processes of diverse nature in conditions when the properties of the system change abruptly with a gradual change in one of the parameters (for example, concentration) [16, 17]. It is used in chemistry to describe the processes of polymerization and analysis of the mutual distribution of phases in different media.

Percolation processes can also lead to self-organization and the formation of nanostructures, including fractals. Many publications [16, 17, 20−22] present various models that characterize the dependence of the percolation threshold on the content of the loading filler.

To describe the concentration dependence of the conductivity of filled heterogeneous composite systems, we can use the basic approaches of the theory of effective environment and the symmetric Bruggeman formula [22]:

$$(1-p)\frac{(\sigma_{DC}-\sigma_m)}{2\sigma_{DC}+\sigma_m}+p\frac{(\sigma_{DC}-\sigma_f)}{2\sigma_{DC}+\sigma_f}=0, \quad (1.1)$$

where σ_f, σ_m, σ_{DC} − electrical conductivity of the filler, polymer matrix, and composite, respectively; p − the effective volume content of the filler.

The main equation of percolation theory (Kirkpatrick's model or scaling law) in filled polymer systems, which reflects the dependence of electrical conductivity (σ) on the bulk content of the filler (φ) after the percolation threshold is the dependence:

$$\sigma \infty (\varphi-\varphi_c)^t, \quad (1.2)$$

where φ − the volume fraction of filler; φ_c − the percolation threshold, i.e. the lowest content of filler at which a continuous cluster of conductivity is formed from particles under the condition $\varphi > \varphi_c$; t − the critical conductivity index.

To determine the critical parameters, a logarithmic dependence $\lg\sigma - \lg(\varphi - \varphi_c)$ is constructed. The slope of the obtained line gives the value of "t". For a three-dimensional system, the universal constant t acquires values of 1.6 −2.06, which is mainly dependent on the topological dimension of the system and not dependent on the structure of the particles forming the clusters and their interaction [20–23].

The study of percolation phenomena in filled polymer systems is an important task because the description of the properties of the systems near the critical point opens the perspectives for the creation of nanomaterials with predicted functional characteristics. In this work, the electrical properties of polymer-polymer composites based on dielectric polymer matrices, namely polymethyl methacrylate (PMMA), a copolymer of styrene with malein anhydride − styromal (St-MA), polyvinyl alcohol (PVA), polyacrylic (PAA) and polymethacrylic (PMAA) acids, ED-20 epoxy matrices, and conducting polymer fillers – poly-ortho-toluidine (PoT), poly-ortho-anisidine (PoA) and polyaniline (PAn) were studied [3, 6, 10, 13, 14, 24–26].

It is shown that the concentration dependence of the specific conductivity on the content of fillers has a percolation character (Fig. 1.1) with a low "percolation threshold", which depends on the nature of the polymer matrix and conducting polymer (Table 1.1). Increasing the filler content leads to a sharp transition from the non-conductive to the conductive state (there is a phase transition insulator-conductor). In this case, all the filler particles are completely delocalized throughout the polymer matrix and become conductive, and the formed composite has the maximum conductivity. It was found that composites

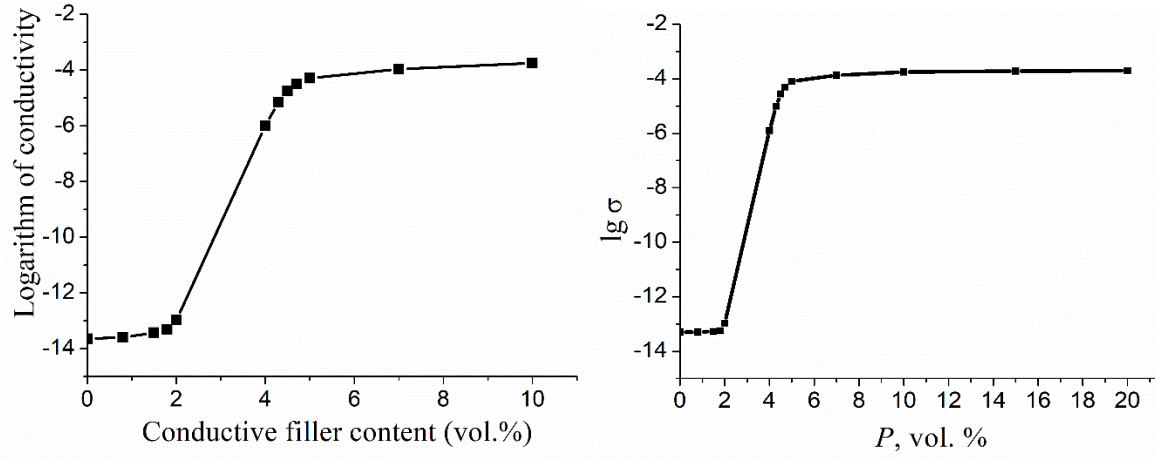

Figure 1.1 Dependence of logarithm of specific conductivity on the content of conductive filler for: (*a*) PVA-polyaniline composites, φ_c = 2.3 vol. %; (*b*) PMMA-PAn, φ_c = 2.0 vol. %

Table 1.1 Percolation parameters of polymer composites with conducting polymer fillers

Polymer matrix	Conducting polymer filler	Percolation threshold φ, vol. %	Critical index of conductivity, t
PVA	PAn	2.1	1.75
	PoT	2.8	1.58
	PoA	1.7	1.88
PMMA	PAn	2.0	1.43
	PoT	3–4	1.48
PAA	PoT	2.3	1.38
St-MA	PoT	10	2.53
	PAn	8.4	2.67
	PoA	8.0	2.56
ED-20	PAn	2.5–5	–

based on the investigated polymer matrices are characterized by low values of the percolation threshold, which are typical for composites with a conductive polymer phase. The calculated values of the critical index of conductivity are in the range of 1.4–2.6, which is characteristic of a three-dimensional system [27]. This constant is mainly dependent on the topological dimension of the system and not dependent on the structure of the particles forming clusters and their interaction.

At the same time, the value of $t \approx 2$ is observed for many two-phase materials. Significant deviations of this value for composites based on the StMA matrix ($t \approx 2.58$–2.9) can be caused by several reasons: contact phenomena, in particular, if tunnel contacts are

realized between the conductive elements of the material, instead of ohmic [28], different morphology, and different specific surface of the material [29]. The deviation of the critical index "*t*" from universal values can be explained by the peculiarities of composites formation in "*in situ*" polymerization conditions, when the conductive filler is formed directly in the dielectric polymer matrix, and by the presence of anisotropic forms of conductive filler [30].

1.2.2 Features of Charge Transfer in Conductive Polymer Composites

The study of the influence of the polymeric matrix on the regularities of charge transport in nanosystems with conductive polymers is an interesting scientific task due to the possibility of their practical application. We chose the PMMA-PAn polymer nanocomposites obtained from polymer "blends" in a common organic solvent [6, 13, 14]. It was found if the content of PAn becomes higher than 2 vol. %, the conductivity value of the PMMA-PAn composite exceeds the conductivity of the PMMA matrix by 8–9 orders of magnitude, and remains almost constant. It is interesting that the conductivity of the PMMA-PAn composite with a filler content of 2–15 vol. % slightly exceeds the conductivity of pure PAn (Table 1.2). We assume that high values of the specific conductivity (σ) exceeding the percolation threshold for PMMA-PAn composites are caused by the formation of their own conductive network inside the host polymer. Thus formed continuous conductive phase is uniformly distributed over the entire volume of the polymer composite – a continuous conductivity cluster is formed [16–18].

As shown by B. Wessing and co-authors [31], the conductivity in thermally compressed PAn composites doped with d,l-camphorosulfonic acid with PMMA, containing 40 % PAn, may be higher than that of pure PAn. A probable cause of this phenomenon may be the additional doping of the polyaniline by PMMA functional groups near the melting point. On the other hand, the dielectric polymeric matrix can affect the degree of coupling of the conductive polymer structure by orienting the macrochains in one direction forming 1D structures [32]. The presence of structures of this type ensures the preservation of the physicomechanical properties of high-polymer matrices without disrupting the semiconductor nature of the conductivity of the conjugated polymer. Moreover, it sometimes even enhances charge transport, affecting its electronic structure, which leads to changes in the concentration of polaron charge carriers. Perhaps, in this case, a structural matrix effect is appeared, which consists of the ability of the polymer matrix to influence the length and chemical structure of polyaminoarene chains, including their spatial structure. Using ESR

Table 1.2 The dependence of the specific conductivity on the content of the polymeric filler for PMMA-PAn composites

ω, vol. % of PAn	0	1	2	4	10	20	100
$\sigma_{298}\cdot 10^6$, S·m^{-1}	10^{-8}	7.03	81.2	52.8	27.6	2,16	3,60

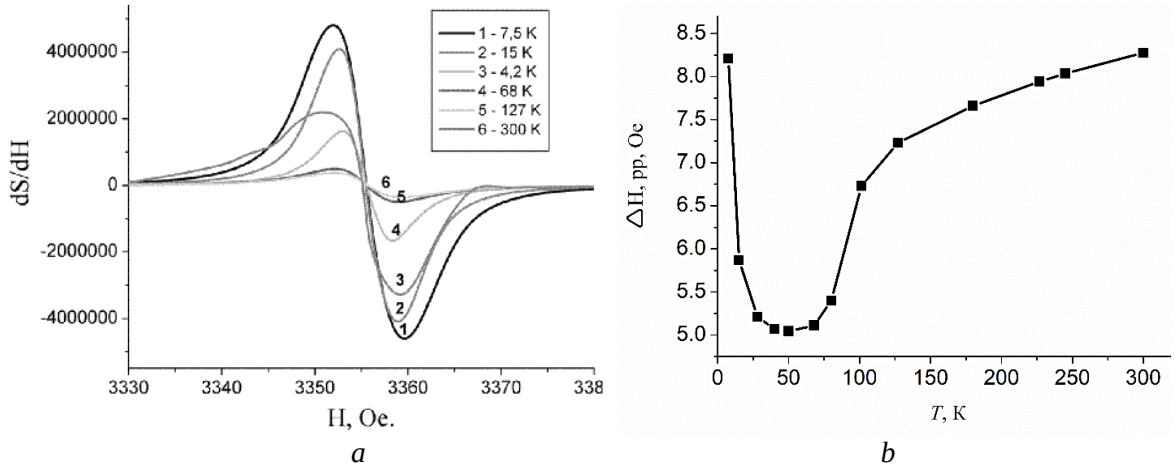

Figure 1.2 (*a*) ESR spectra for PMMA-PAn (10 vol. %) at different temperatures; (*b*) Dependence of signal width ΔH_{pp} (distance between peaks) on temperature for PMMA-PAn (10 vol. %)

spectroscopy in the range T = 4.2−300 K it was established that PMMA-PAn composites give a clear EPR signal at room temperature with a g-factor value of 2.0025 ± 0.0002 (Fig. 1.2, *a*). According to the analysis of the ESR temperature dependence, it can be assumed a significant delocalization of charge carriers along the PMMA dielectric polymeric matrix causes increased values of the specific conductivity (Table 1.2). This is also evidenced by the change in the shape of the ESR signal, namely its significant extension − the distance between the peaks ΔHpp increases to 5.05−8.29 Oe for the PMMA-PAn composite (Fig. 1.2, *b*) compared to the unfilled PAn (3.1−3.4 Oe) [31, 33, 34].

Therefore, it was established a strong interaction between the PMMA polymer matrix and the PAn filler, which is manifested in the low percolation threshold values for these composites explained by the formation of a spatial conductive network. On the other hand, the dielectric polymeric matrix can affect the structure of the conjugated polymer, and, therefore, the number of unpaired spins corresponding to the charge carrier concentration. The results of ESR spectroscopy confirmed this assumption. The electronic structure of the material significantly changed because of PMMA-PAn formation may indicate the formation of a composite with a molecular degree of dispersion, in other words, a nanocomposite.

Among industrial polymer matrices, polystyrene (PS) attracts special attention due to its excellent mechanical properties, transparency in visible spectral range, easy processing, and availability [36–44]. PS-CP composites are used in various industries for the production of antistatic screens, conductive coatings on the surface of various natures, thin-film chips, as well as sensors for the detection of ammonia, and hydrogen sulfide [38, 39]. The growing interest in protection against electromagnetic interference using of polymer-polymer composites based on CP is due to the increased variety of commercial, military, and scientific electronic devices. It is shown [40] that the polymer complex PAn doped with dodecylbenzene sulfonic acid (DBSA) and polystyrene-polybutadiene-b-styrene copolymer can be used as a coating for protection against electromagnetic interference in the 50–60 Hz and 1–100 GHz bands.

Currently, there are many methods of synthesis of conductive composites based on PS and polyaminoarenes [39–44]. Despite the variety of ways to obtain such polymer composites, they nevertheless have some drawbacks − complex, long, multi-stage process technology. Synthesized composites are in the form of a dispersed powder, which makes it impossible to form films and conductive coatings by irrigation or inkjet printing on work surfaces. Besides, it causes an uneven distribution of polyaminoarene in the matrix of PS, heterogeneous structure and low sedimentation stability of the system, and low conductivity of composites. The use of polyaniline as a conductive polyaminoarene reduces the choice of conductive polymeric fillers and narrows the scope of such composites in modern industry. A new nanotechnological approach in the formation of polystyrene composites with polyaminoarenes is *in situ* polymerization when conjugated conducting polymer is synthesized directly in the polymer matrix solution, i.e. aniline polymerizes to polyaniline [40, 43]. This leads to higher dispersion and uniform miscibility of PAn nanoparticles in the polymer matrix. *In situ* polymerization of aniline in the presence of $(NH_4)_2S_2O_8$ is descrybed in a lot of research. The use of PoT as a filler in the PS matrix is little known, in particular, copolymers poly(aniline-co-o-toluidine) nanocolloidal particles in aqueous poly(styrene sulfonic acid) matrix (PPS) [37]. We used aminoarenes – *o*-toluidine and aniline, which differ in the presence of a substituent on the benzene ring, as monomers for the formation of a conductive polymer filler in the PS dielectric polymer matrix. In the *o*-toluidine molecule, the presence of methyl substituent in the *ortho* position to the amino group determines the hydrophobic properties of aminoarene and in traditional solvents in contrast to unsubstituted aniline.

In the process of nanofabrication polymer-polymer composites by the *in situ* polymerization method, various mechanisms of formation and self-organization of the conductive phase of conjugated polyaminoarenes are possible. Depending on the nature and initial concentration of the monomer in the reaction mixture, different morphological features of the formed film can be observed (Fig. 1.3). The polystyrene matrix (Fig. 3, *a*) is characterized by excellent homogeneity, smooth morphology, and absence of agglomerates or crystalline formations. In the process of oxidative polymerization of aniline in the PS matrix, a formation of PAn nanofibrils which formed a continuous polymer network takes place

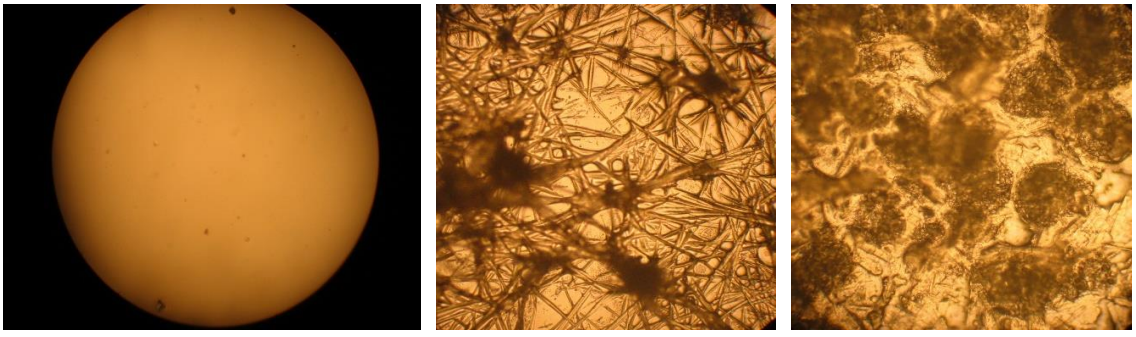

a *b* *c*

Figure 1.3 Microphotos of films: (*a*) PS and composites (*b*) PS-PAn-TSA, *(c)* PS-PoT-TSA. Filler content 10 wt. %, magnification ×150, film thickness 0.2 ± 0.02 mm

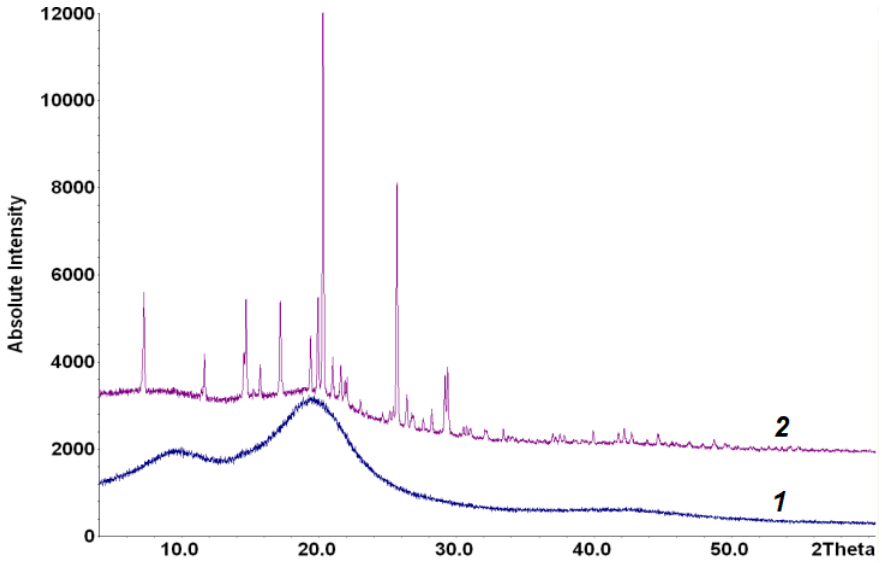

Figure 1.4 X-ray diffraction patterns of PS (*1*) and PS-PoT-TSA (*2*) composite (10 wt. %)

(Fig. 3, *b*). The formation of PoT network in PS matrix is observed at the low concentration of *o*-toluidine in the reaction mixture (3–5 wt. %). The highly ordered conductive regions of the PoT filler embedded in the matrix of polystyrene are observed at higher monomer concentrations (Fig. 3, *c*).

Investigation of the structure of composites by X-ray powder diffraction method showed that the original PS is practically amorphous, and the diffraction pattern of the PS has a wide peak at $2\theta = 19^{\circ}$ (Fig. 1.4). A calculated average apparent crystallite size is D = 9.3±1.3 Å. In PS-PAn composites, additional polyaniline peaks are observed at $2\theta = 14.5°$, 19.7°, 25.3°, and 27.1°, which are almost completely leveled at 7 wt. % polyaminoarene content [43]. The composite PS-PoT-TSA is characterized by a predominantly ordered structure and, accordingly, a high degree of crystallinity, while the content of the amorphous component is low. A high level of structure ordering in PS-PoT-TSA composites is connected with the crystalline structure of the filler PoT-TSA confirmed in [46, 47]. The spatial and geometric similarity of fragments of PoT and TSA leads to the formation of an ordered and more compact structure of the doped polymer.

Polystyrene has poor conductivity, the resistivity is at the level of 10^{14}–10^{15} Ohm·cm [46]. At a low concentration of polymer filler (near 2 wt. % PAn-TSA or PoT-TSA) nanofabricated in PS matrix the specific volume resistance falls in 10–12 order and demonstrates percolation behavior inherent in nanostructured systems [18, 46]. After reaching the percolation threshold (0,75 % for PS-PAn composites [43]) the resistance of PS composites with conducting polyamenoarenes is significantly reduced (Table 1.3). The reduction of the resistivity of the composite is proportional to the concentration of conducting polymer filler. At the content of conducting polymer filler in PS-PoT-TSA composite near 20 wt. %, a value of specific volume resistance at room temperature ρ_{293} = 6,8 Ohm·cm, specific conductivity $\sigma_{293} = (1.5\pm0,2)10^{-1}$ S/cm. For PS-PAn-TSA composite, the values of conductivi-

Table 1.3 The parameters of conductivity of polystyrene-polyaminoarene composites

Sample	Monomer concentration, M	Filler content, wt. %	σ_{293}, S/cm	ρ_{293}, Ohm·cm	E_a, eV
PS-PAn-TSA	0.01	2	0.023	44.1	0.93 ± 0.01
	0.03	6	0.027	37.3	0.63 ± 0.01
	0.05	10	0.029	33.9	0.71 ± 0.02
	0.075	15	0.033	30.5	0.81 ± 0.02
	0.10	20	0.037	27.1	0.37 ± 0.01
PAn-TSA		100	0.043	23.7	0.08 ± 0.01
PS-PoT-TSA	0.01	2	0.049	20.4	0.73 ± 0.02
	0.03	6	0.059	16.9	0.62 ± 0.04
	0.05	10	0.073	13.6	0.57 ± 0.01
	0.075	15	0.098	10.2	0.44 ± 0.01
	0.10	20	0.150	6.8	0.40 ± 0.03
PoT-TSA		100	0.294	3.4	0.047 ± 0.003

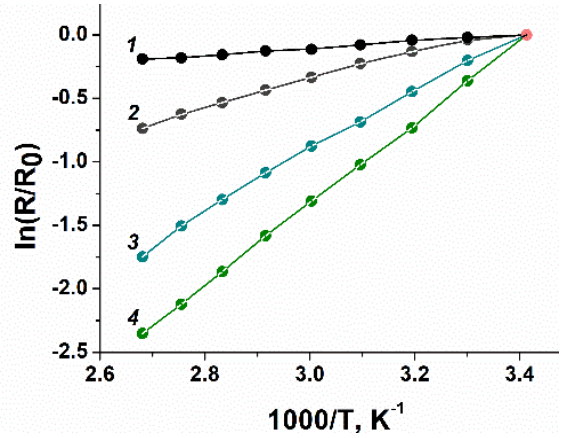

Figure 1.5 Temperature dependence of normalized resistance: PoT-TSA (*1*), PAn-TSA (*2*), PS-PoT-TSA (*3*), PS-PAn-TSA (*4*) at 10 wt. % content of polymer filler

ty are less (4,3±0,2) 10^{-2} S/cm at the same content of polymer filler (Table 1.3). Structural and morphological features of the composites may explain it.

The temperature dependence of the normalized resistance of the polymer fillers and composites as $(R/R_0) = f(1/T)$ is linear in the temperature range 303–373 K (Fig. 1.5). The activation energy of conductivity E_a was calculated by the equation:

$$\rho = \rho_0 \cdot \exp\left(E_a / 2kT\right), \tag{1.3}$$

where ρ – specific electrical resistance, k – Boltzmann constant, T – temperature. E_a was found 0.047 ± 0.003 eV for PoT-TSA and 0.08 ± 0.01 eV for PAn-TSA fillers. The calculated activation energy of charge transport for PS-PoT-TSA composites decreases with content of filler from 0.73 ± 0.02 eV (2 wt. %) to 0.57 ± 0.02 eV (5 wt. %), and 0.40 ± 0.03 eV (20 wt. %). It is similar to PS-PAn-TSA composites (Table 3). To conclude, the dielectric polymer matrix causes a significant increase in activation energy for both fillers – PAn-TSA and PoT-TSA.

TSA-doped poly-*ortho*-toluidine as a conductive filler significantly increases the electrical conductivity of polystyrene-polyaminoarene composites due to the formation of a highly ordered structure. The spatial and geometric similarity of fragments of PoT and TSA leads to the formation of an ordered and compact structure of the polymer filler in a polystyrene matrix.

Synthesized polymer-polymer composites can be used for various purposes, in particular, the production of antistatic screens, conductive coatings on the surface of various natures, thin-film chips by the inkjet printing, or the watering of the composite material on the substrate (work surface). This method allows you to apply the composite on a plastic or other substrate in the form of paint, which dries quickly. One of the most interesting applications of conducting polymer nanocomposites is the creation of chemical sensors sensitive elements [47–50], especially, gas sensors for monitoring the toxic gases in the environment and industry.

1.2.3 Formation of Flexible Elements of Gas Sensors

Nowadays, gas-sensitive films based on conducting polymers (PAn and its derivatives, polyoxythiophenes, etc.) are one of the most promising sensor media. The properties of these polymers are based on chemical redox reactions and provide various mechanisms for the generation and transformation of electrochemical, electrical, or optical signals [47–58]. The creation of composite sensor media based on conducting polymers and dielectric polymer matrices allows to combine of the advantages of each of the components – the sensitivity of conjugated polymers to the action of gases with the flexibility, lightness, and recyclability of polymer matrices. Moreover, such sensor elements can operate at normal temperatures. Nanocomposites based on conjugated polyarenes are quite sensitive to gases, released because of food freshness losses (NH_3, H_2S [49, 57-59]), vapors of organic compounds [60], chemical components of military explosives, and gases released in their storage (NO_2, SO_2, etc.) [61].

Composites of conducting polymers with dielectric polymer matrices are usually obtained by mixing a conducting polymer filler with non-conductive highly plastic polymers (PMMA, PVA, PS, cellulose derivatives) followed by thermal pressing [61, 62]. The most promising method of providing elasticity and thermal-plasticity of polyaminoarenes is the creation of polymer composites in which components mix at the molecular level. This method is used to obtain polymer-polymer composites with an ordered structure, as well as nanosized composites from polymers insoluble in water and in most organic solvents. We

used such approaches to polymerize aminoarenes in a polymer gel (PVA, PAA, PMAA) whose macromolecules act as "soft" templates [6]. It was shown that the interaction of the functional groups of the polymer matrix with the amino groups of the polymeric filler is possible [14]. The interaction affects the kinetics of polymerization and all the physical, chemical, and mechanical properties of composites [6, 14, 63]. It was found that the mass fraction of 0.35-1.05 % of the monomer in the initial composition is optimal [64].

Obtaining the free flexible films of a composite of conjugated polyaminoarene and a highly elastic polymer matrix was carried out by oxidative polymerization of 0.01–0.025 M aminoarenes solution at the equimolar content of oxidizer (ammonium persulfate) in an aqueous gel of PVA (PAA or PMAA) with concentration 0.125–5 w. % during 24 h. The films were formed by pouring the composition on the surface of Teflon or glass with subsequent monolithization of the film at room temperature over 6–8 h and finally at 331–333 K for 1 hour. After separation from the substrate homogeneous flexible sensitive films were obtained [65].

In the process of oxidative polymerization of aminoarenes within 24 hours at a monomer : oxidizer ratio of 1:1 almost complete (95–98 %) conversion of the monomer is achieved. It corresponds to the 4.5–15 w. % content of the conductive polymer in the final composite. The obtained polymer-polymer composites form flexible, highly elastic "free" films (Fig. 1.6, *a*, *d*) easy for preparing indicator tapes. The structure of the film composites based on PVA and polyaminoarenes is sufficiently homogeneous and compact and at the same time, its globular nature is preserved (Fig. 1.6, *b*, *c*, *e*). Composites with matrices based on polymer electrolytes (PAA, PMAA) form not only flexible but also transparent "glass-like" films (Fig. 1.6, *f*).

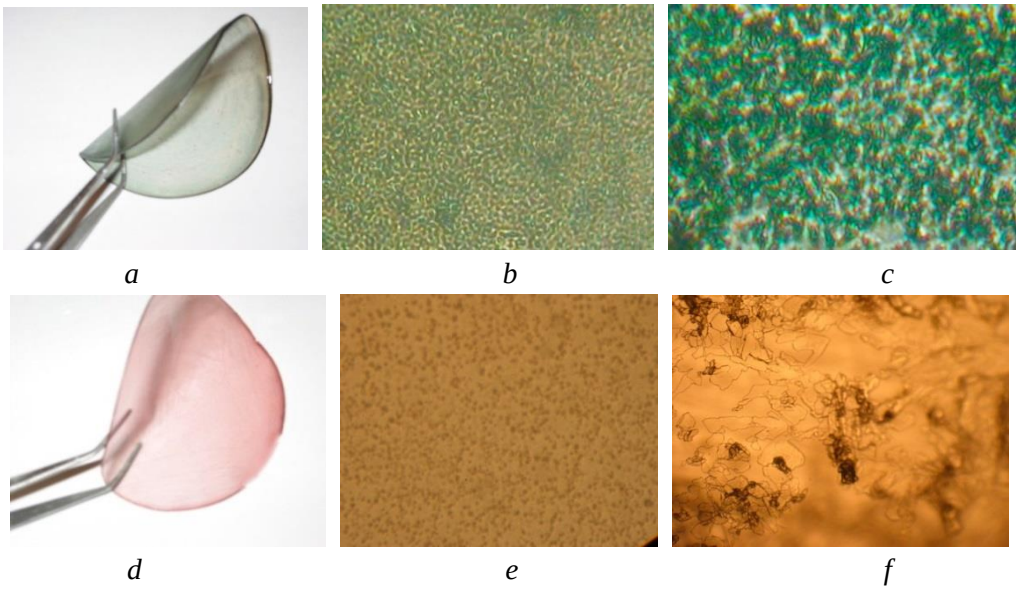

Figures 1.6 Microphotographs of composite polymer films: PVA-PoT (*a*, *b*), PVA-PAn (*c*), PMAA-PoA (*d*, *e*), PAA-PoT (*f*). Zoom 600 (*b*, *c*, *e*, *f*).

Film composites of polyaminoarenes in highly elastic polymer matrices under the influence of polar gases (ammonia) exhibit a gas-chromic effect with general laws similar to those observed for films of individual polyaminoarenes [49]. There is a significant change in the optical absorption spectra of composites under the action of ammonia. The general increase of intensity (Fig. 1.7, *a*, *b*) and shift of the position of the maxima of absorption bands (Fig. 1.7, *b*) are observed. The most significant changes were found for the band at 750–830 nm (absorption in the polaron zone) for PVA-PAn films. The action of ammonia caused almost complete neglect of this band due to the deprotonation processes with the formation of ammonium cations and the decrease of the carrier's concentration. Instead, a band appears at 580–620 nm, attributed to the imino-quinone fragments in the structure of polyaminoarenes [66, 67].

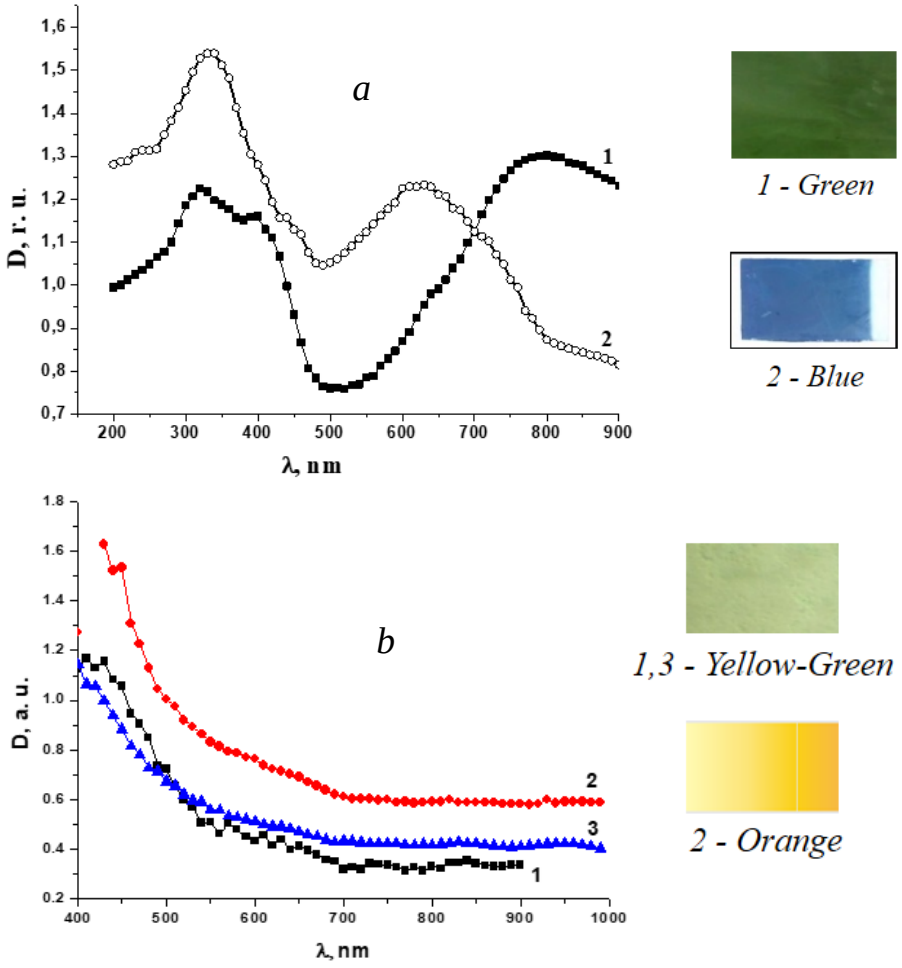

Figure 1.7 (*a*) Absorption spectra of composite films PVA-PAn (7.2 w. %) on air (*1*) and in ammonia environment, P = 1.4 kPa (*2*). The thickness of the film is 0.15 mm. (*b*) Absorption spectra of PVA-PoA (8,0 w. %) films on air (*1*), in ammonia environment (*2*), and after resorption in the air for 2 h (*3*). The thickness of the film is 0.12 mm.

Importantly visual changes in the color of the film are observed simultaneously. At the initial moment, the PVA-PAn film has an intense green color and retains it in the absence of ammonia in the media, indicating the freshness of the food product. The color of the indicator changes from green to blue in the presence of small amounts of ammonia (partial pressure P = 10–30 Pa). Production of films based on PAn derivatives, for example, PoT or PoA allows for a significant expansion in the color set. Because of food freshness losses, the color of the indicator changes dramatically - from bright green to blue for PAn and PoT or from yellow-green to orange for PoA. The allocation of ammonia is intensified if the food product is spoiled. Accordingly, the sensory film becomes pale blue for PAn and PoT or burgundy for PoA

The response speed of the sensor based on polymer composites depends on the temperature, gas pressure, and type of indicator substance embedded in the polymer matrix, but generally ranges from a few seconds to several minutes.

For practical realization, we offer available flexible indicator films based on the composites of elastic polymer matrices (PVA, PAA, PMAA) with conjugated polyaminoarenes, changing their color under the action of gases. The polymer matrices do not affect the regularities of optical absorption, ensuring the use of synthesized composites for gas sensor production.

1.3 Nanofabrication of Hybrid Structures Semiconductor – Conjugated Polymer

Improving the efficiency of organic electronic devices is possible due to the development of hybrid nanocomposites based on conducting polymers with dielectric matrices or inorganic semiconductors. These composites ccan be fabricated by simple, safe, and energy-saved methods without vacuum technologies. Semiconductor materials with spatially inhomogeneous structures, layered, porous, or dispersive, attract special attention due to the possibility of a new type of hybrid materials formation [68–72].

The methods of obtaining nanostructures based on polymers and semiconductors have attracted great attention due to the prospect of solar cells, light-emitting diodes, sensors, lasers, and memory device production [72–75]. Especially, the heterogeneous systems based on nano-crystal porous silicon (pSi) have a wide application in optoelectronics and sensor devices. The luminescence in the visible and near IR regions of the spectrum is one of the most important properties of such structures. The excitation of luminescence is possible due to the quantum-size effects as a result of the porous structure nanometer size [76]. Heterostructures based on pSi and surface organic layers, namely, conjugated conducting polymers, have been studied intensively [75, 77].

Heterogeneous systems based on nanostructured organic and inorganic semiconductors can be considered a new class of hybrid materials with enhanced functionality. A polymer film on the surface of a semiconductor can serve as a protective layer or create an electrical contact, thereby influencing the spectra of photosensitivity, absorption or emissi-

on, and electro-optical and sensory characteristics of nanostructures. We studied the physiccal and chemical processes occurring under the conditions of formation of conjugated polymers in nanostructured semiconductor media: porous silicon (pSi) [73–75], layered crystals of GaSe, InSe [78, 79], nanostructured TiO_2 [80], etc., structure and properties of the obtained nanomaterials. To identify the regularities of the interaction of components in polymer-semiconductor hybrid nanosystems, a complex approach was applied, namely, the study of the structure, chemical composition, and surface morphology of nanostructured semiconductors and organic-inorganic composites by electron and atomic force microscopy, X-ray diffraction, and IR spectroscopy. The effect of surface modification of nanostructured semiconductors on the radiation spectra characteristics, changes in electrical and optical characteristics, and sensor sensitivity were evaluated.

1.3.1 Formation of Hybrid Nanostructures Based on Porous Silicon

The electronic properties of silicon can be changed due to the formation of nanostructures – spatially separated silicon areas with minimum dimensions of several nanometers. In this case, the charge carriers acquire additional energy due to the quantum effect [72].

Among the techniques for obtaining silicon-based nanostructures, the most accessible is the creation of nanocrystals by etching voids with dimensions of several nanometers in single-crystal silicon. This material, called porous silicon, has the light-emitting ability and other unique properties that make it a valuable material for the production of sensors. The photoelectrochemical etching was used to obtain pSi, covered in works [74, 75].

To clarify the nature of the surface formations, the topology of the obtained pSi was investigated by atomic force microscopy (AFM). It was established that with fairly high homogeneity of the polished surface of the single crystal, there are certain surface defects. These protrusions, up to 2 nm high, can be centers for the structural inhomogeneities formation during the anodization of the sample (Fig. 1.8).

A comparison of AFM images of the surface of monocrystalline silicon before and after etching indicates the periodic structural modifications that can be attributed to the pSi layer. The pSi surface after anodization has vertical cylindrical protrusions, formed because of electrochemical etching of separate areas on the monocrystalline silicon surface (Fig. 1.8, *b*). By profile analysis of AFM images, it was determined that the depth of protrusions in the pSi reaches 45–50 nm with a total thickness of the etched layer of about 5 μm.

The chemical composition of the surface was identified by FTIR spectroscopy (Fig. 1.9, *a, b*). For monocrystalline silicon, an absorption band at 1100 cm^{-1}, corresponding to Si-O-Si valence vibrations [81], and at 620 cm^{-1}, corresponding to the deformation mode of $Si-H_2$ [82], were found. The absorption band at 1100 cm^{-1} is caused by silicon oxidation, and at 620 cm^{-1} – by water molecules adsorbed from the air.

The IR spectrum of pSi revealed an absorption band at 1100 cm^{-1}, observed in mono-Si (Si-O-Si oscillations), as well as oscillations of the C-O bond, corresponding to an absorption band at 1111 cm^{-1}, C-C oscillations at 1188 cm^{-1}, CH_2-OH, CH-OH and C-OH

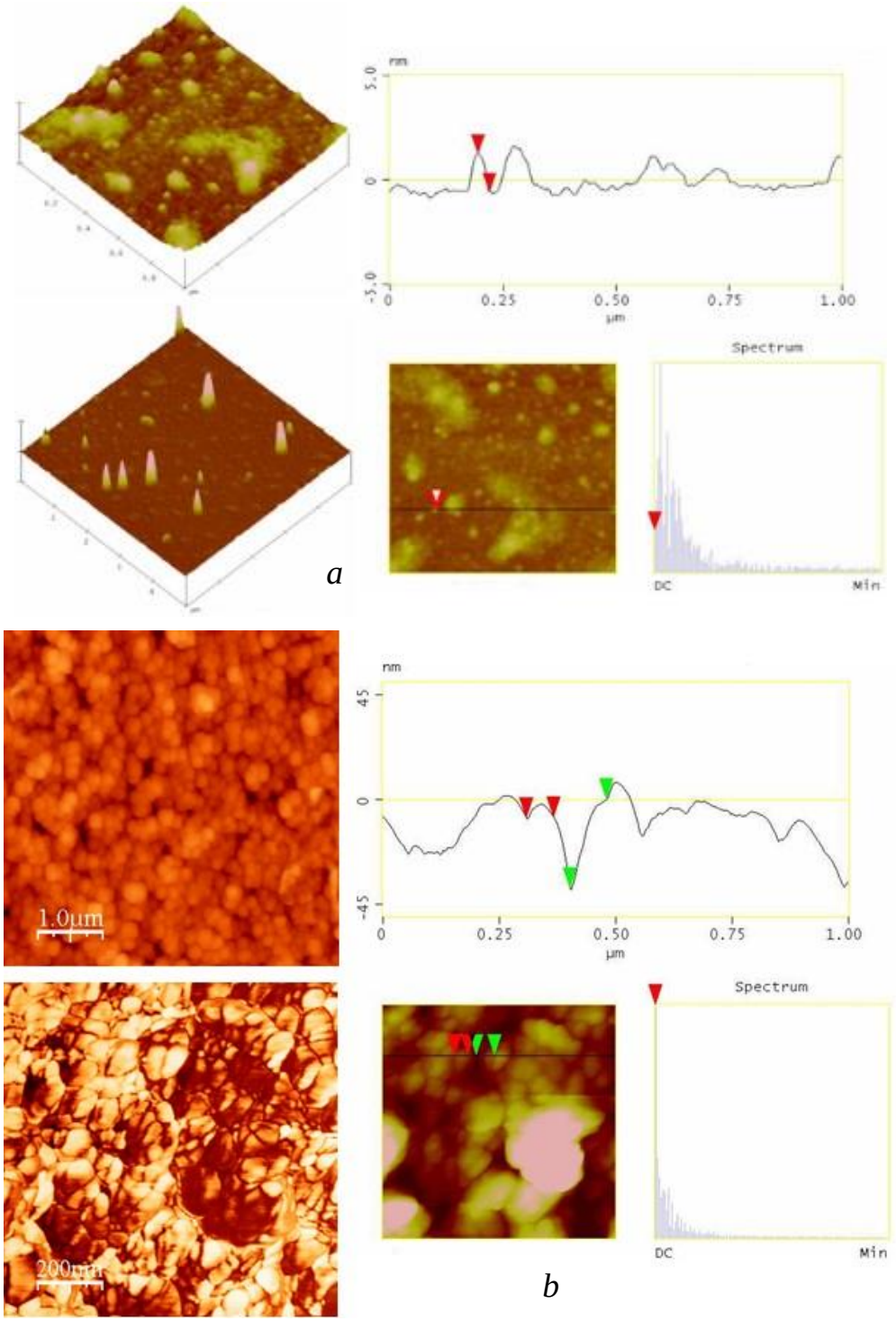

Figure 1.8 AFM image and surface profile of porous silicon before (*a*) and after (*b*) photoelectrochemical etching

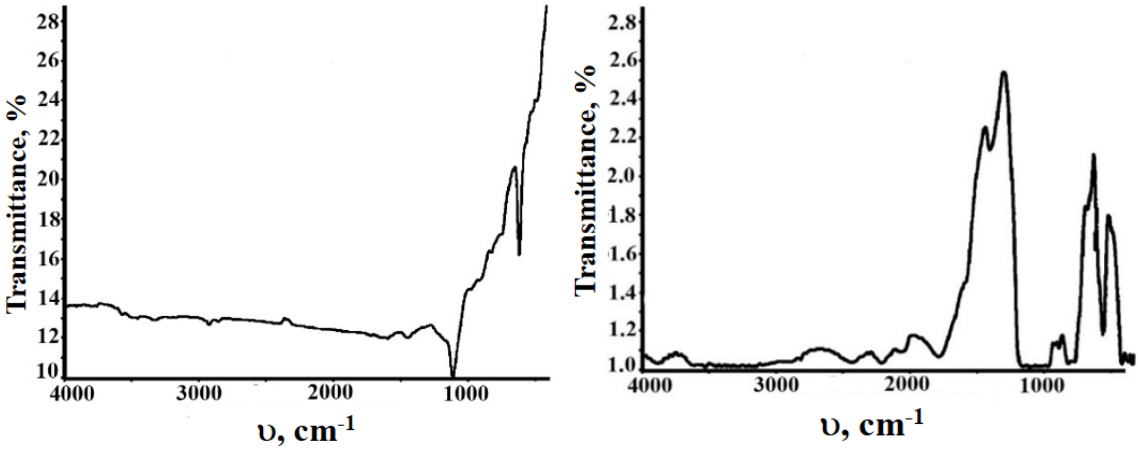

a *b*

Figure 1.9 FTIR transmission spectra of single crystal silicon (*a*) and porous silicon (*b*)

vibrations at 1050, 1072, and 1097 cm^{-1}, respectively, and Si-O-Si vibrations at 1240 cm^{-1}. The broad absorption band at 2900–3620 cm^{-1} corresponds to the absorption of O-H bond vibrations in water molecules adsorbed on the pSi surface [45, 46]. The absorption band at 835–890 cm^{-1} is associated with the adsorption of water molecules and fluorine because of the etching of pSi in HF. Absorption bands at 940 and 980 cm^{-1} are associated with the vibration of hydrogen and hydroxyl groups.

Therefore, the newly formed developed surface of nanocrystalline silicon has a complex chemical structure. The presence of functional groups makes it very sensitive to external factors. Conjugated polymers, integrated into the pores of nanocrystalline silicon, can act as a passivating layer and cause new functional properties appearance.

Porous silicon-polymer nanostructures are obtained by electropolymerization in two ways – galvanostatic electrolysis of pSi in a monomer solution [77] or electrochemical etching of monocrystalline silicon in the presence of monomer in the etching solution. In the second case, electrochemical polymerization processes take place simultaneously with etching [78], and the thickness of the polymer layer is uncontrolled. At the same time, the anodic current densities used for silicon anodization (20–60 mA/cm^2) correspond to high positive potentials and lead to significant electrochemical degradation of the polymer. Therefore, an important condition is the control of electrochemical polymerization potentials. This possibility can be provided by electrochemical polymerization in the cyclic potential sweep mode [84].

For example, the polymerization of *o*-anisidine is evidenced by the gradual increase of the response currents on the cyclic voltammograms (CVA) (Fig. 1.10, *a*). The appearance of redox maxima, characteristic of an electroactive polymer, on the CVAs is evidence of the formation of a pSi-polymer heterostructure. The linear dependence of the current of the anode peak I_p at E = 0.4–0.6 V on the number of cycles of the potential sweep at N = 4–16 allows for controlling the thickness of the electroactive polymer films. It was established, the amount of charge (Q) and, accordingly, the mass of the polyarene, integrated into

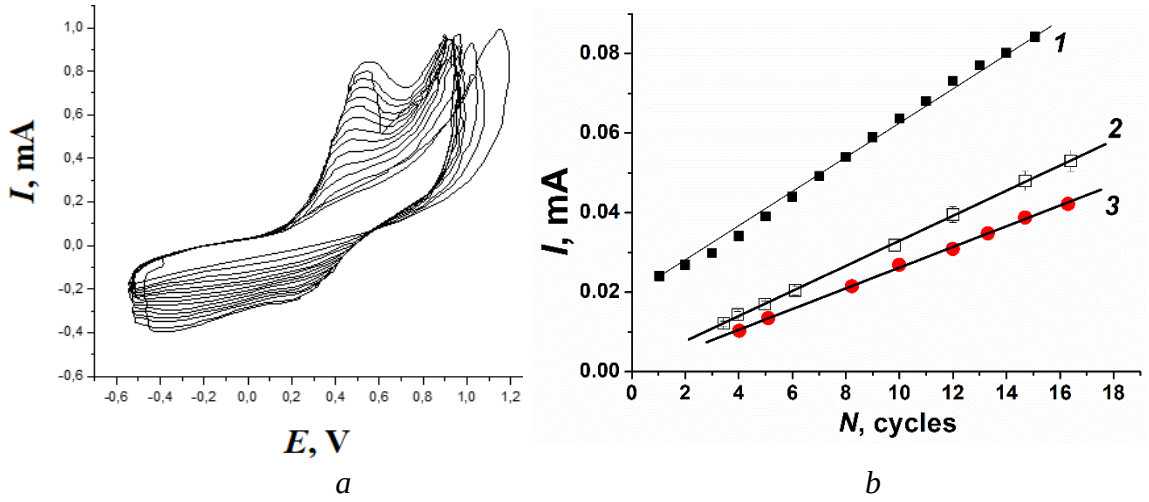

Figure 1.10 (*a*) CVA obtained during electrochemical polymerization of PoA on the pSi surface from 0.1 M solution of *ortho*-anisidine in 0.5 M H_2SO_4 at a potential scan rate of 40 mV/s; (*b*) Dependence of the current of the CVA anodic maximum on the number of cycles for obtaining pSi-PAn (*1*, *2*) and pSi-PoA (*3*) heterostructures. Potential scan rate: 80 (*1*) and 40 (*2*, *3*) mV/s.

the pSi, depends on the speed (ν) and the number of scanning cycles (*N*) of the potential during electrochemical polymerization. At a constant ν the maximum currents change proportionally to *N* in the process of formation of conducting polymer on the pSi surface (Fig. 1.10, *b*). According to the statistical analysis of AFM images of the pSi surface and obtained nanostructures (Fig. 1.11) the thickness of the pSi-polymer hybrid layer reaches 40–45 nm with a pSi pore depth of more than 200 nm. While the globular structure of the polymer is preserved.

The value of the cubic cell parameter "*a*" found from the X-ray diffraction data for pSi samples is 5.42467 Å, and for the pSi-PAn is 5.42984 Å. The error of the experiment did not exceed 10^{-3}Å, so it can be assumed some growth of the parameter *a* and, accordingly, the volume of the unit cell due to the formation of PAn chains in the pores of silicon.

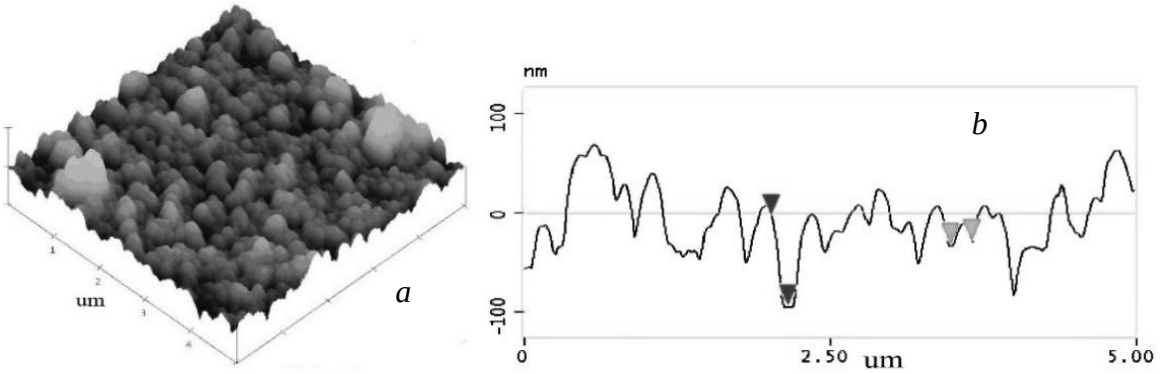

Figure 1.11 AFM image (*a*) and profile analysis (*b*) of the porous silicon surface with PAn film

Obtained pSi-polymer samples were studied for photo- (cathode) luminescence and sensor sensitivity [73–75, 85]. The newest approach to the formation of polymer-semiconductor hybrid nanostructures is the creation of electrochromic systems with optical properties controlled by applying voltage or current.

1.3.2 Electrochromic Structures Based on Porous Silicon and Polymer

Porous silicon nanostructures have a wide band of visible PL [74] allowing to change the intensity and spectral position of the emission maximum within wide limits with optical filters, in particular electrochromic polymer films. The transmission spectra of such films can be changed by applying an electric current. In addition, a silicon plate with a porous layer is not only a substrate for the electrochemical polymerization of PAn but also an electrode of an electrochromic cell [86, 87].

The PAn thin-film coating is transparent to both excitation and pSi-generated radiation. An important property of conjugated polymers is the ability to change electrical and optical characteristics depending on the degrees of oxidation [88]. The electrochromic effect of PAn films can be used in organic displays, shutter and filter optical devices, and optical sensors [88, 89]. It is possible to control the PL spectrum of nanoporous silicon by the color change and color intensity of PAn films under the applied voltage. We proposed a hybrid nanostructure for the production of fluorescent devices with an electrically controlled emission band [87].

The external voltage applied to the electrochromic structure causes a change in the optical transmittance of PAn film at 600–750 nm and, respectively, a change in the radiation intensity in the long-wavelength part of the PL spectrum of pSi. The change of voltage from –10 to +10 V causes the change of spectral maximum from 635 to 600 nm and a decrease in PL intensity (Fig. 1.12, 1.13).

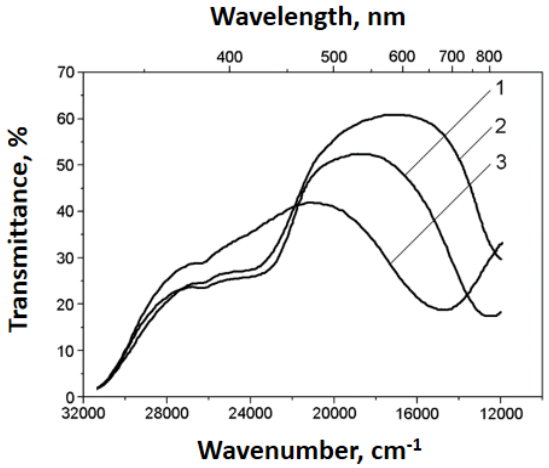

Figure 1.12 PL spectra of an electrochromic structure based on pSi (*1*) with an applied voltage of 10 V (*2*) and +10 V (*3*)

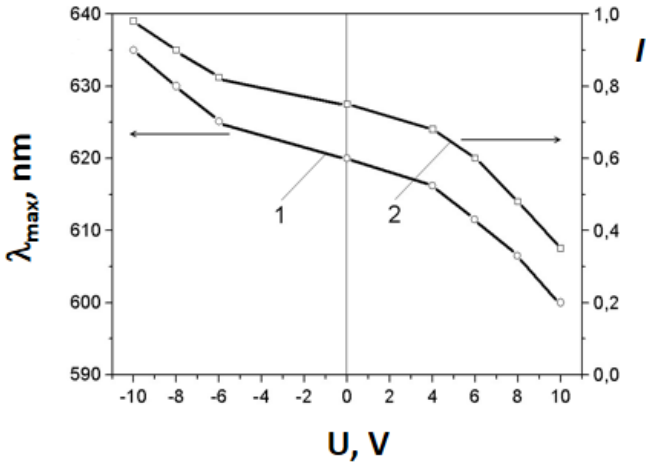

Figure 1.13 Dependence of the spectral position of the PL maximum (*1*) and its integral intensity (*2*) on the voltage applied to the electrochromic structure

The optical transmittance spectra of the PAn film depend on the magnitude and polarity of the applied voltage, due to the processes of electron and proton transport with the transformation of various forms of the polymer [88]. PAn changes from the colorless reduced state (leucoemeraldine), which transmits light in the entire visible part of the spectrum, to the green semi-oxidized form (emeraldine salt), which absorbs light in the wavelength range of 500–650 nm. Completely oxidized polyaniline (pernigraniline) is dark blue, almost black, and absorbs light in almost the entire visible range of the spectrum. Therefore, because of the electrochromic effect, the PAn film can reversibly change its color from almost transparent to yellow, green, and blue and transitional shades with a corresponding change in optical spectra.

The change in the optical properties of polyaniline in the SnO_2-PAn-pSi-Si hybrid structure has a similar nature to electrochromic effects in proton electrolytes. It is caused by changes in the oxidation degree of the CP under an external potential. The use of PAn as an active electrochromic layer opens up the possibility of creating optical elements operating according to the two-electrode scheme. Thus, PAn films deposited on the surface of porous silicon can act as an optical filter of pSi photoluminescence radiation with an electrically controlled transmission band.

1.3.3 "In situ" Fabrication of Hybrid Nanostructure with Layered Semiconductors

Two-dimensional (2D) semiconductor nanocrystals fabricated in the platelike form have been intensely investigated since the invention of single-layer graphene. GaSe with chemically passive selenium terminated surfaces is among the desirable materials for the production of single-layers 2D plates, even extracted and isolated from bulk. Several

groups succeeded in mechanical [90, 91], thermal, and laser-induced [92] GaSe exfoliation. Recent perspective [93] indicates that 2D platelike nanoparticles (including GaSe) are excellent PL emitters due to suppression of the absorption strengths into one electronic state contrary to the band for bulk material. Not far ago we found that the mutual interaction of components in the hybrid composites containing GaSe and conducting PAn leads to an essential conductivity increase, UV shifting in GaSe luminescence spectra, responsible for plate-like particle formation, etc [4].

Preparation of composite was carried out by oxidative polymerization of aniline under ammonium persulfate $(NH_4)_2S_2O_8$ in an aqueous medium in the presence of toluene sulfonic acid (TSA) as a doping and stabilizing agent. Method of obtaining composite consists of several stages. Originally performed dispersing a sample (45–150 mg of GaSe plates or nanopowder GaSe with particle size 60-80 nm) in a solution of surfactant – 0.12 M TSA using ultrasound for 30 min. Then 0.205 g of monomer droplets were injected in GaSe dispersion with continuous stirring, and after 10 min 0.005 ml of 0.47 M solution of oxidant $(NH_4)_2S_2O_8$ was added. The process was carried out at T = 293 K for 24 hours. Finally, a dark dispersion of composite was isolated in the form of the precipitate by centrifuging. For investigations, we took samples with the content of inorganic component 10–12 wt. % [94].

TEM images of PAn-powdered GaSe samples are presented in Fig. 1.14. Expanded images (Fig. 1.14, *a*, *b*) demonstrate the presence of two types of nanoobjects: thin stripes (up to few nanometres in height and up to 100 nm in length) and discs with rather broad diameters distribution (5–20 nm). As shown by HRTEM (Fig. 1.14, *c*, *d*) the heights of such stripes consist of GaSe elementary sandwiches, packed along *c* crystallographic axis. It should be noted; that there is an essential broadening of lattice plane spacing in this direction yielding 0.833 nm. Compared with the same value for bulk GaSe materials (0.796 nm for (0002) plane spacing), the *c* lattice parameter increased by about 4,4 %. The elementary tetralayers of GaSe structure along direction are somehow bent by mechanical stresses, applied normally to that direction on the whole particles (Fig. 1.14 *c*, *d*), but we did not observe any extended defects or elementary tetralayers fractures. The number of such monolayers (ML) per particle could vary in the 1020 range (5–10 lattice parameters). The smaller particles (1–2 ML) during interaction with electron beam collinear to edges in plate-like particle geometry simply do not effectively scatter electrons to make them visible by TEM, by were detected by optical measurements earlier [95] and as discs on Fig. 1.14, *a*, *e*. They are the same particles but the top/bottom of them are oriented normally to the electron beam. We can also observe lattice fringed on one well oriented with respect to electron beam particle: this time the spacing yields 0.969 nm coinciding exactly with a triple value of (10–10) lattice plane [96]. From TEM and HRTEM images we suggest that particles are a few ML thick to observe lattice spacing similar to mechanically exfoliated GaSe flakes [91].

Gallium monoselenide crystal lattice consists of tetralayers –Se–Ga–Ga–Se–, bounded by the week van der Waals forces. The distance between layers of Se-Se is approximately 3.25 Å. It is possible to include polymeric chains of PAn between layers of Se-Se (the width of an aniline molecule is about 2.5 Å at the thickest point of the benzene ring).

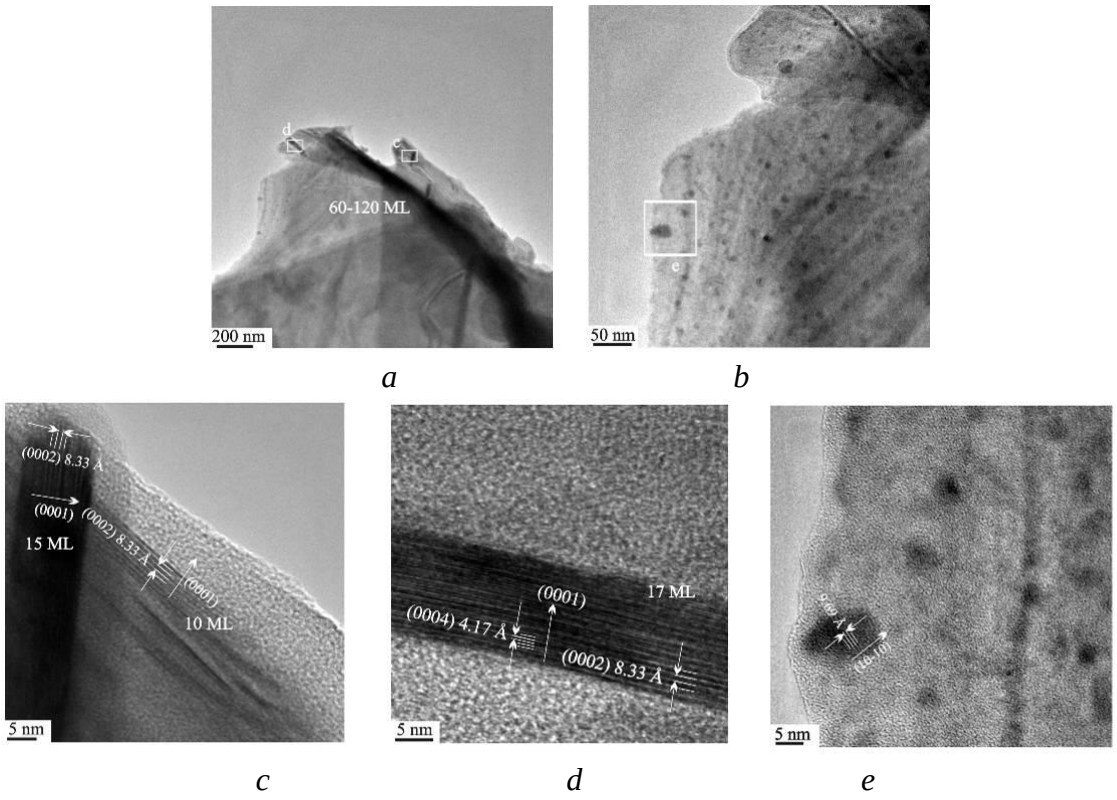

Figure 1.14 Representative (*a*, *b*) TEM and HRTEM (*c*, *d*, *e*) of boxed areas (in *a*, *b*) images of exfoliated by PANI GaSe nanoparticles. In the (*c*, *d*) images the lattice planes could be attributed to the (0001) direction along the crystallographic *c* axis, while in the (*e*) image – to the (10–10) direction along the crystallographic axis of hexagonal GaSe.

But polymerization obviously results in a much larger spatial hindrance of long PAn molecules when forming crystalline composite structures based on hexagonal GaSe. This changes the diffraction pattern [96], which now does not accurately describe the prevailing model of orientation, creating the additional diffraction reflections and clearly elucidated by HRTEM. When powdering the single crystal plates this composite phase is apparently saved, but there is simply hexagonal GaSe, in contrary to the sample PAn-GaSe. As was mentioned earlier [95], powdered fractured GaSe samples exhibit numerous extended defects-cleavage stairs on the surface. The aniline molecules diffuse into them during filling the van der Waals gap of particles with the further formation of a few ML composites based on PAn-GaSe. The model of such interaction is presented in Fig. 1.15.

The edges of GaSe tetralayer sandwiches have high adsorption activity. The terminal gallium atoms on the surface of the nanoparticles act as a strong Lewis acid. Amino groups, on the other hand, are Lewis bases, leading to the adsorption of aniline on defects. Adsorbed aniline molecules diffuse into the van der Waals gap (vdW9) with linear dimensions commensurate with the dimensions of the benzene ring. The polymerization of aniline leads to the formation of free tetralayer GaSe plates wrapped by polyaniline chains, ensuring

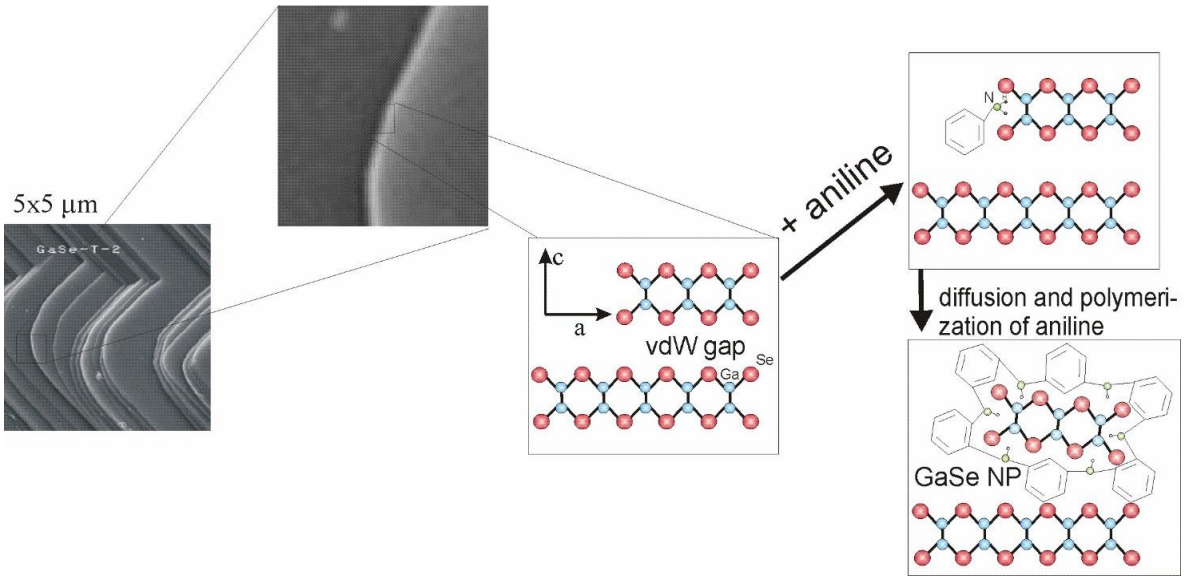

Figure 1.15 Schematic representation of the interaction of GaSe nanoparticles with polyaniline [94]

good gallium passivation at the ends of the plates. In this way, graphene-like particles stabilized by a polymer nanolayer are formed.

1.4 Conclusion

The methods of electrochemical and "in situ" polymerization are extremely promising for the synthesis of hybrid nanostructures based on conductive polymers and dielectric polymer matrices, as well as porous or layered semiconductor structures. Such materials are characterized by increased optical, sensory, and electrochromic activity. The improvement of the properties of the obtained nanomaterials is caused by the formation of conductive polymer chains directly in the dielectric polymer matrix or in the pores of the semiconductor. As a result, the characteristic nanometer dimensions of the hybrid structure and the electronic properties of the conjugated polymer are preserved.

Keywords

- polymerization
- conducting polymer
- dielectric matrix
- structure
- percolation
- porous silicon
- luminescence
- gas sensors

References

1. *Aguilar M. R., Román J. S.* Smart polymers and their applications. Second edition. Woodhead Publishing: Sawston, Cambridge, 2019. 687 p. DOI: https://doi.org/10.1016/C2017-0-00049-6
2. *Shahinpoor M., Schneider H.-J.* Intelligent Materials. RSC Publishing: London, 2007. 532 p. DOI: https://doi.org/10.1039/9781847558008
3. *Aksimentyeva O. I., Tsizh B. R., Horbenko Yu. Yu., Konopelnyk O. I., Martynyuk G. V., Chokhan' M. I.* Flexible elements of gas sensors based on conjugated polyaminoarenes // Mol. Cryst. Liq. Cryst. 2018. Vol. 670 (1). P. 3–10. DOI: https://doi.org/10.1080/15421406. 2018.1542057.
4. *Feron K., Lim R., Sherwood C., Keynes A., Brichta A., Dastoor P. C.* Organic bioelectronics: Materials and biocompatibility // J. Mol. Sci. 2018. Vol. 19 (8). DOI: https://doi.org/10.3390/ ijms19082382
5. *Heeger A. J.* Semiconducting and metallic polymers: the fourth generation of polymeric materials // Synth. Met. 2002. Vol. 123. P.23−42. DOI: https://doi.org/10.1021/jp011611w
6. *Aksimentyeva O. I., Konopelnyk O. I., Martyniuk G. V.* Synthesis and physical–chemical properties of composites of conjugated polyaminearenes with dielectric polymeric matrixes // Computational and Experimental Analysis of Functional Materials. Apple Academic Press: New York, 2017. P. 331−370. DOI: https://doi.org/10.1201/9781315366357
7. *Ziadan K. M., Hussein H. F., Ajeel K. I.* Study of the electrical characteristics of poly(o-toluidine) and application in solar cell / Energy Procedia. 2012. Vol. 18. P. 157–164. DOI: https://doi.org/ 10.1016/j.egypro.2012.05.027
8. *Khan A., Jawaid M., Khan A. A. P., Asiri A. M.* Electrically conductive polymers and polymer composites: from synthesis to biomedical applications. Wiley: Hoboken, New Jersey, 2018. 264 p.
9. *Bakhmatyuk B. P., Aksimentyeva O. I., Dupliak I. Ya., Horbenko Yu. Yu.* Electrochemical properties of polyaniline in aqueous environments of iodide and bromide in the system of electrochemical energy source // Phys. Chem. Solid State. 2016. Vol. 17 (2). P. 234–240. DOI: https://doi.org/ 10.15330/pcss.17.2.234-240. (in Ukrainian).
10. *Aksimentyeva O. I., Chepkov I. B., Filipsonov R. V., Malynych S. Z., Gamernyk R. V., Martyniuk G. V., Horbenko Yu. Yu.* Hybrid composites with the low reflection of IR radiation // Phys. Chem. Solid State. 2020. Vol. 21 (4). P. 764–770. DOI: https://doi.org/10.15330/ pcss.21.4.764-770
11. *Aksimentyeva O., Konopelnyk O., Olenych I., Poliovyi D., Horbenko Yu., Myhalets A.* Physical-chemistry of electro-optical phenomena in conjugated polymer systems Proceedings of the VI Ukrainian Congress of Electrochemistry, Lviv, Ukraine, 4-7 June 2018. P. 112–114. (in Ukrainian).
12. *Mac Diarmid A. G.* "Synthetic metals": a novel role for organic polymers (Nobel lecture) // Angew. Chem. Int. Ed. 2001. Vol. 125. P. 11–22. DOI: https://doi.org/10.1016/S0379-6779(01)00508-2
13. *Martynyuk G. V., Aksimentyeva O. I.* Features of charge transport in polymer composites polymer-thylmethacrylate – polyaniline // Phys. Chem. Solid State. 2020. Vol. 21 (2). P. 319–324. DOI: https://doi.org/10.15330/pcss.21.2.319-324.
14. *Aksimentyeva O., Konopelnyk O., Opaynych I., Tsizh B., Ukrainets A., Ulansky Y., Martyniuk G.* Interaction of components and conductivity in polyaniline-poly(methylmethacrylate) nanocomposites // Rev. Adv. Mater. Sci. 2010. Vol. 23 (2). P. 185–188.
15. *Aksimentyeva O. I.* Electrochemical methods of synthesis and conductivity of conjugated polymers. Svit: Lviv, 1998. 123 p. (in Ukrainian).
16. *Tarasevich Yu. Yu.* Percolation. Theory. Application. Algorithms. Chemistry: Moskow, 2002. – 110 p. (in Russian).
17. *Christensen K.* Percolation theory. MIT Press: London, 2002, 40 p.

18. *Mamunya E. P., Yurzhenko M. V., Lebedev E. V., Levchenko V. V., Chervakov O. V., Matkovska O. K., Sverdlikovska O. S.* Electroactive polymeric materials. Alpha Reklama: Kyiv, 2013. 402 p. (in Ukrainian).
19. *Herega A.* Some applications of the percolation theory: review of the century beginning // J. Mater. Sci. Eng. 2015. Vol. 5. P. 409–414 DOI: https://doi.org/10.17265/2161-6213/2015.11-12.004
20. *Lysenkov E. A., Klepko V. V.* Analysis of the percolation behavior of electrical conductivity of systems based on polymer and carbon nanotubes // Journal of *Nano*- and Electronic Physics. 2016. Vol. 8 (1).
21. *Zabrodsky A. G., Nemov S. A., Ravych Yu. I.* Electronic properties of disordered systems. Nauka: St. Petersburg, 2000. 72 p.
22. *Efros A. L., Shklovskii B. I.* Critical behaviour of conductivity and dielectric constant near the metal-non-metal transition threshold // Phys. Status Solidi. 1976. Vol. 76 (2). P. 475–485. DOI: https://doi.org/10.1002/pssb.2220760205
23. *Berezkin V. I., Popov V. V.* Percolation transition in carbon composites based on fullerenes and thermally expanded graphite // Phys. Solid State. 2018. Vol. 60 (1). P. 202–206. DOI: https:// doi.org/10.1134/S1063783418010043
24. *Yevchuk O., Aksimentyeva O., Horbenko Yu.* Optical and electrical properties of the conjugated polyaminoarenes composites with polymer electrolytes // Visnyk Lviv Univ., Ser. Chem. 2012. Vol. 53. P. 352–356. (in Ukrainian).
25. *Aksimentyeva O., Dutka V., Horbenko Yu., Martynyuk H., Riy U., Halechko H*. Composites of the conductive polyaminoarenes in the matrix of styromal // Proc. Shevchenko Sci. Soc. Chem. Sci. 2017. Vol. XLVIII. P. 7–16.
26. *Martyniuk G., Aksimentyeva O.* Influence of conductive polymer filler on electrical conductivity and microhardness of composites with dielectric polymeric matrices // Proc. Shevchenko Sci. Soc. Chem. Sci. 2020. Vol. LX. P. 14–21. DOI: https://doi.org/10.37827/ntsh.chem. 2020.60.014
27. *Berëzkyn V. Y., Popov V. V.* Percolation transition in carbon composite on the basis of fullerenes and exfoliated graphite // Phys. Solid State. 2018. Vol. 60 (1). P. 207–211. DOI: https://doi.org/ 10.1134/S1063783418010043
28. *Eletskyi A. V., Knyzhnyk A. A., Potapkyn B. V., Kenny Kh. M.* Influence of methods of formation of polymer composite materials with carbon nanotubes on mechanisms of electrical conductivity // UFN. 2015. Vol. 185, 225. DOI: https://doi.org/10.3367/UFNr.0185.201503a.0225 (in Russian).
29. *Afanasov Y. M., Morozov V. A., Seleznev A. N., Avdeev V. V.* Conductive composites on the basis of thermally expanded graphite // Inorg. Mater. 2008. Vol. 44 (6).
30. *Aksimentyeva O. I., Martyniuk G. V.* Percolation phenomena in the polymer composites with conducting polymer fillers // Phys. Chem. Solid State. 2021. Vol. 22 (4). P. 811–816. DOI: https:// doi.org/10.15330/pcss.22.4.811-816
31. *Kahol P. K., Ho J. C., Chen Y. Y., Wang C. R., Neeleshwar S., Tsai B., Wessling C.* On metallic characteristics in some conducting polymers // Synth. Metals. 2005. Vol. 151 (1). P. 65–72. DOI: https://doi.org/10.1016/j.synthmet.2005.03.017
32. *Shaari H. A. H., Ramli M. M., Mohtar M. N., Rahman N. A., Ahmad A.* Synthesis and conductivity studies of poly(methyl methacrylate) (PMMA) by co-polymerization and blending with polyaniline (PANi) // Polymer. 2021. Vol. 13 (12). DOI: https://doi.org/10.3390/ polym13121939
33. *Adhikary S., Banerji P.* Polyaniline composite by in situ polymerization on a swollen PVA gel // Synth. Met. 2009. Vol. 159. P. 2519–2524. DOI: https://doi.org/10.1016/j.synthmet. 2009.08.050
34. *Lapkowski M., Geniès E. M.* Evidence of two kinds of spin in polyaniline from in situ EPR and electrochemistry: Influence of the electrolyte composition // J. Electroanal. Chem. Interfacial Electrochem. 1990. Vol. 279 (1-2). P. 157–168. DOI: https://doi.org/10.1016/0022-0728(90)85173-3.

35. *Srinivasan D., Natarajan T. S., Bhat S. V., Wessling B.* Electron spin resonance absorption in organic metal polyaniline and its blend with PMMA // Solid State Commun. 1999. Vol. 2 (5). P. 503–508. DOI: https://doi.org/10.1016/S0038-1098(99)00109-X
36. *Al-Thani, N., Hassan, M. K., Bhadra, J.* Polyaniline/polystyrene blends: in-depth analysis of the effect of sulfonic acid dopant concentration on ac conductivity using broadband dielectric spectroscopy // Int. J. Polym. Sci. 2018. Vol. 2018. DOI: https://doi.org/10.1155/2018/ 1416531
37. *Manoharan D., Chandrasekaran J., Maruthamuthu S., Kathirvel P., Jayamurugan P.* Synthesis of poly(aniline-co-*o*-toluidine) nanocolloidal particles in aqueous poly(styrene sulfonic acid) by dispersion polymerization method // J. Nanostructure Chem. 2015 Vol. *5* (1). P. 115–122. DOI: https://doi.org/10.1007/s40097-014-0142-x
38. *Bhadra J., Al-Thani N. J., Madi N. K., Al-Maadeed M. A.* Preparation and characterization of chemically synthesized polyaniline - polystyrene blends as a carbon dioxide gas sensor // Synth. Met. 2013. Vol. 181. P. 27–36. DOI: https://doi.org/10.1016/j.synthmet.2013.07.026
39. *Bhadra J., Al-Thani N. J., Madi N. K., Al-Maadeed M. A.* High performance sulfonic acid doped polyaniline–polystyrene blend ammonia gas sensors // J. Mater. Sci. Mater. Electron. 2016. Vol. 27. P. 8206–8216. DOI: https://doi.org/10.1007/s10854-016-4825-6
40. *Schettini A. R. A., Soares B. G.* Study of microwave absorbing properties of polyaniline/STF conducting composite prepared by in situ polymerization // Macromol. Symp. 2011. Vol. 299–300. P. 164–174. DOI: https://doi.org/10.1002/masy.200900106
41. *Roichman Y., Titelman G. I., Silverstein M. S.* Polyaniline synthesis: influence of powder morphology on conductivity of solution cast blends with polystyrene // Synth. Met. 1999. Vol. 98. P. 201–209. DOI: https://doi.org/10.1016/S0379-6779(98)00190-8
42. *Kim Y. H., Park B. J., Choi H. J., Choi S. B.* Preparation of polystyrene/polyaniline composite particles and their electrorheology // J. Phys. Conf. Ser. 2009. Vol. 149. DOI: https://doi.org/ 10.1088/1742-6596/149/1/012017
43. *Ghasemi H., Sundarara U.* Electrical properties of in situ polymerized polystyrene/polyaniline composites: The effect of feeding ratio // Synth. Met. 2012. Vol. 162 (13–14). P. 1177–1183. DOI: https://doi.org/10.1016/j.synthmet.2012.04.037
44. *Sudha J. D., Sivakala S.* Conducting polystyrene/polyaniline blend through template-assisted emulsion polymerization // Colloid Polym. Sci. 2009. Vol. 287 (11). P. 1347–1354. DOI: https://doi.org/ 10.1007/s00396-009-2101-5
45. *Aksimentyeva O. I., Konopelnyk O. I., Horbenko Yu. Yu., Martyniuk G. V.* Nanofabrication of conducting polymerfillers in polymer matrix: Polystyrene-poly-o-toluidine composites // Mol. Cryst. Liq. Cryst. 2022. https://doi.org/10.1080/15421406.2022.2073531
46. *Stepura A. L., Aksimentyeva O. I., Demchenko P. Yu.* Features of the structure and physical-chemical properties of poly-ortho-toluidine doped with toluenesulfonic acid // Phys. Chem. Solid St. 2019. Vol. 20 (1). P. 77–82. DOI: https://doi.org/10.15330/pcss.20.1.82
47. *Khan A. A., Shaheen S.* Electrical conductivity, isothermal stability and amine sensing studies of a synthetic poly-o-toluidine/multiwalled carbon nanotube/Sn(IV) tungstate composite ion exchanger doped with p-toluenesulfonic acid // Anal. Methods. 2015. Vol. 7. P. 2077–2086. DOI: https:// doi.org/10.1039/C4AY02911A
48. *Qi X-Y., Yan D., Jiang Z., Cao Y-K., Yu Z-Z., Yavari F., Koratkar N.* Enhanced electrical conductivity in polystyrene nanocomposites at ultra-low graphene content // ACS Appl. Mater. Interfaces. 2011. Vol. 3 (8). P. 3130–3133. DOI: https://doi.org/10.1021/am200628c
49. *Aksimentieva O. I., Tsizh B. R., Chokhan M. I.* Sensors for control of gaseous media in the food industry and the environment: a monograph. Pyramida: Lviv, 2017. 284 p. (in Ukrainian).
50. *Kuswandi B.* Freshness sensors for food packaging. Reference module in food science. Elsevier, 2017. DOI: https://doi.org/10.1016/B978-0-08-100596-5.21876-3

51. *Dong X., Zhang X., Wu X., Cui H., Chen D.* Investigation of gas-sensing property of acid-deposited polyaniline thin-film sensors for detecting H_2S and SO_2 // Sensors. 2016. Vol. 16. P. 1888–2003. DOI: https://doi.org/10.3390/s16111889
52. *Horbenko Yu., Tsizh B., Dzeryn M., Olenych I., Aksimentyeva O., Bogatyrev V.* Sensitive elements of gas sensors based on poly-o-toluidine/silica nanoparticles composite // Acta Phys. Pol. 2022. Vol. 141 (4). P. 386–389. Doi: http://doi.org/10.12693/APhysPolA.141.386
53. *Shahzad N., Khalid U., Iqbal A., Rahman M. Ur.* eFresh – a device to detect food freshness // Int. J. Soft Comput. Eng. 2018. Vol. 8 (3). P. 1–4.
54. *Aksimentyeva O. I., Tsizh B. R., Horbenko Yu. Yu., Martyniuk G. V., Konopelnyk O. I., Chokhan' M. I.* Flexible elements of gas sensors based on conjugated polyaminoarenes // Mol. Cryst. Liq. Cryst. 2018. Vol. 670 (1). P. 3–10. DOI: https://doi.org/10.1080/15421406.2018. 1542057
55. *Park S. J. Park C. S., Yoon H.* Chemo-electrical gas sensors based on conducting polymer hybrids. Polymers. 2017. Vol. 9 (5). DOI: https://doi.org/10.3390/polym9050155
56. *Pandey S.* Highly sensitive and selective chemiresistor gas/vapor sensors based on polyaniline nanocomposite: A comprehensive review // J. Sci. Adv. Mater. Dev. 2016. Vol. 1. P. 431–453. DOI: https://doi.org/10.1016/j.jsamd.2016.10.005
57. *Mustafa F., Andreescu S.* Chemical and biological sensors for food-quality monitoring and smart packaging // Foods. 2018. Vol. 7. DOI: https://doi.org/10.3390/foods7100168
58. *Tsizh B. R., Chokhan M. I., Aksimentyeva O. I., Konopelnyk O. I., Poliovyi D. O*. Sensors based on conducting polyaminoarenes to control the animal food freshness // Mol. Cryst. Liq. Cryst. 2008. Vol. 497. P. 586–592. DOI: https://doi.org/10.1080/15421400802463043
59. *Tsizh B., Aksimentyeva O., Goliaka P., Chokhan M.* Gas sensors for analysis of food products. SPOLOM: Lviv, 2021. 236 p.
60. *Aksimentyeva O. I., Tsizh B. R., Horbenko Yu. Yu., Stepura A. L.* Detection of the organic solvent vapors by the optical gas sensors based on polyaminoarenes // Scientific Messenger of LNU VMB. Series: Food Technologies. 2021. Vol. 23 (95). P. 20–24. DOI: https://doi.org/ 10.32718/nvlvet-f9504
61. *Nynaru V., Jayamani E., Srinivasulu M., Han E. C. W., Bakri M. K. B* Short review on conductive polymer composites as functional materials // Key Eng. Mater. 2019. Vol. 796. P. 17–21. DOI: https://doi.org/10.4028/www.scientific.net/KEM.796.17
62. *Grosh M., Arman A., De S. K., Chatterjee S.* Low temperature electrical conductivity of polyaniline-polyvinyl alcohol blends // Solid State Commun. 1997. Vol. 103 (11). P.629–633. DOI: https://doi.org/10.1016/S0038-1098(97)00236-6
63. *Aksimentyeva O. I., Konopelnyk O. I., Tsizh B. R., Yevchuk O. M., Chokhan M. I.* Flexible elements of optical sensors based on conjugate polymer systems // SEMST. 2011. Vol. 2 (8). P. 34–39. (in Ukrainian).
64. *Aksimentyeva O. I., Ukrainets A. M., Konopelnyk O. I., Yevchuk O. M.* Method of obtaining conductive polymer composites. Patent № 53159 (UA). Publ.15.01.2003, Bull. №1. (in Ukrainian).
65. *Akimentyeva O. I., Tsizh B. R., Chokhan M. I., Yevchuk O. M.* Sensor for visual control of ammonia content. Patent № 65401 (UA). Publ. 12.12.2011, Bull. №23 (in Ukrainian).
66. *Sverdlova O.V.* Electronic spectra in organic chemistry. Khimiya: Leningrad, 1985. 248 p. (in Russian)
67. *Murrell I. N.* The theory of the electronic spectra of organic molecules // J. Chem. Educ. 1965. Vol. 42 (1). P. A58. DOI: https://doi.org/10.1021/ed042pA58
68. *Jung J., Chang M., Yoon H.* Interface engineering strategies for fabricating nanocrystal-based organic-inorganic nanocomposites // Appl. Sci. 2018. Vol. 8 (8). DOI: https://doi.org/10.3390/ app8081376
69. *Reddy K. R., Hemavathi B., Balakrishna G. R., Raghu A. V., Naveen S., Shankar M. V.* Organic conjugated polymer-based functional nanohybrids: Synthesis methods, mechanisms and its appli-

cations in electrochemical energy storage supercapacitors and solar cells // Polymer composites with functionalized nanoparticles. 2018. P. 357–379. DOI: https://doi.org/10.1016/B978-0-12-814064-2.00011-1

70. *Liu P.* Preparation and characterization of conducting polyaniline/silica nanosheet composites // Curr. Opin. Solid State Mater. Sci. 2008. Vol. 12. P. 9–13. DOI: https://doi.org/10.1016/j.cossms.2009.01.001
71. *Olenych I. B., Aksimentyeva O. I., Monastyrskii L. S., Dzendzeliuk O. S.* Effect of radiation on the electrical and luminescent properties of conjugated polymer–porous silicon composite // Mol. Cryst. Liq. Cryst. 2016. Vol. 640 (1). P. 165–172. DOI: http://doi.org/10.1080/15421406.2016.1257328
72. *Bisi O., Ossicini S., Pavesi L.* Porous silicon: a quantum sponge structure for silicon-based optoelectronics. Surface science reports // Surf. Sci. Rep. 2000. Vol. 38. P. 1–126. DOI: https://doi.org/10.1016/S0167-5729(99)00012-6
73. *Olenych I. B., Aksimentyeva O. I.* Photosensitive organic-inorganic hybrid structures based on porous silicon // Mol. Cryst. Liq. Cryst. 2018. – Vol. 671 (1). P. 90–96. DOI: https://doi.org/10.1080/15421406.2018.1542091
74. *Olenych I. B., Monastyrskii L. S., Aksimentyeva O. I., ed. Sattler K. D.* Chapter 22. Photovoltaic structures based on porous silicon // Silicon Nanomaterials Sourcebook: Arrays, Functional Materials, Industrial Nanosilicon. Volume two. CRC Press: USA, University of Hawaii at Manoa, 2017. P. 495**–**518. DOI: https://doi.org/10.4324/9781315153551
75. *Aksimentyeva O. I., Monastyrsky L. S., Savchyn V. P., Stakhira P. Y., Yarytska L. I., Pavlyk M. R.* Structure and luminescence properties of the hybrid composites: Porous silicon – polyphenylacetylene // Physics and Chemistry of Solis State. 2010. Vol. 11 (3). P. 690–695.
76. *Koyama H., Koshida N.* Electrical properties of luminescent porous silicon // J. Lumin. 1993. Vol. 57. P. 293**–**299. DOI: https://doi.org/10.1016/0022-2313(93)90147-F
77. *Halliday D. P., Eggleston J. M., Adams P. N., Pentland I. A., Monkman A. P.* Visible electroluminescence from polyaniline – porouse silicon junction // Synth. Met. 1997. Vol. 85. P. 1245–1246. DOI: https://doi.org/10.1016/S0379-6779(97)80223-8
78. *Voitovych S. A., Grygorchak I. I., Aksimentyeva O. I.* Lateral semiconductive and polymer conductive nano layered structures: preparing, properties and applying // Mol. Cryst. Liq. Cryst. 2008. Vol. 497. P. 55–54. DOI: https://doi.org/10.1080/15421400802458498
79. *Stakhira P. Y., Aksimentyeva O. I., Dorosh O. B., Savchyn V. P., Cherpak V. V., Konopelnyk O. I.* Properties of heterojunctions based on inorganic and organic semiconductors: Polyphenylacetylene-InSe(:Ag) heterostructure // Ukr. J. Phys. 2004. Vol. 49 (11). P. 1193–1198.
80. *Aksimentyeva O. I., Poliovyi D. O., Fechan A. V., Yevchuk O. M.* Nanostructured electrochromic layers // Mol. Cryst. Liq. Cryst. 2008. Vol. 497. P. 362–369. DOI: https://doi.org/10.1080/15421400802458225
81. *Tarutina L. I., Pozdniakova F. Yu.* Spectral analysis of polymers. Khimia: Leningrad, 1986. 248 p.
82. *Kopylov A. A., Holodilov A. N.* Infrared absorption in porous silicon obtained in electrolytes containing ethanol // Physics and Technics of Semiconductors. 1997. Vol. 31 (5). P. 470–472.
83. *Canham L. T.* Silicon quantum wire array fabrication by electrochemical and chemical dissolution of wafers // Appl. Phys. Lett. 1990. Vol. 57. P. 1046–1048. DOI: https://doi.org/10.1063/1.103561
84. *Aksimentyeva O. I., Monastyrsky L. S., Yevchuk O. M., Olenych I. B., Pavlyk M. R.* The method of obtaining polymer-semiconductor hybrid composites. Patent № 55629 (UA). Publ. 27.12.2010. Bull. №24. (in Ukrainian).
85. *Olenych I., Aksimentyeva O., Horbenko Y., Tsizh B.* Organic-inorganic nanocomposites for gas sensing // International Conference Radio Electronics & Info Communications (UkrMiCo), 2016. P. 1–3. DOI: https://doi.org/10.1109/UkrMiCo.2016.7739609

86. *Olenych I. B., Aksimentyeva O. I., Monastyrskii L. S., Pavlyk M. R.* Electrochromic effect in photoluminescent porous silicon – polyaniline hybrid structures // J. Appl. Spectrosc. 2012. Vol. 79 (3). P. 495–498. DOI: https://doi.org/10.1007/s10812-012-9629-8
87. *Olenych I. B., Aksimentyeva O. I., Monastyrskii L. S.* A method of obtaining an electrochromic structure based on porous silicon. Patent № 127257 (UA). Publ. 25.07.2018. Bull. № 14. (in Ukrainian).
88. *Aksimentyeva O. I., Konopelnyk O. I., Poliovyi D. O.* Electrooptic phenomena in conjugated polymeric systems based on polyaniline and its derivatives // Computational and Experimental Analysis of Functional Materials. Apple Academic Press: New York, 2017. P. 91−150. DOI: https://doi.org/10.1201/9781315366357
89. *Mu L., Zhou L., Pang J., Xu M., Chen Z., Zhou Y., Wang J., Peng J.* Color reproduction of reflective display based on conjugated electrochromic polymer // Org. Electronics. 2020. Vol. 85. DOI: https://doi.org/10.1016/j.orgel.2020.105850
90. *Late D. J., Liu B., Matte R. H. S. S., Rao C. N. R., Dravid V. P.* Rapid characterization of ultrathin layers of chalcogenides on SiO_2/Si substrates // Adv. Funct. Mater. 2012. Vol. 22. P. 1894−1905. DOI: https://doi.org/10.1002/adfm.201102913
91. *Hu P. A., Wen Z., Wang L., Tan P., Xiao K.* Synthesis of few-layer GaSe nanosheets for high performance photodetectors // ACS Nano. 2012. Vol. 6. P. 5988−5994. DOI: https://doi.org/10.1021/nn300889c
92. *Gautam U. K., Vivekchand S. R. C., Govindaraj A., Kulkarni G. U., Selvi N. R., Rao C. N. R.* Generation of onions and nanotubes of GaS and GaSe through laser and thermally induced exfoliation // J. Amer. Chem Soc. 2005. Vol. 127. P. 3658−3659. DOI: https://doi.org/10.1021/ja042294k
93. *Chikan V., Kelley D. F.* Synthesis of highly luminescent GaSe nanoparticles // NanoLett. 2002. Vol. 2. P. 141−145. DOI: https://doi.org/10.1021/nl015641m
94. *Aksimentyeva O. I., Demchenko P. Yu., Savchyn V. P., Balitskii O. A.* Structure, electrical and luminescent properties of the polyaniline–GaSe hybrid nanocomposites // Mol. Cryst. Liq. Cryst. 2011. Vol. 536. P. 297−303. DOI: https://doi.org/10.1080/15421406.2011.538345
95. *Balyts'kyi O. O.* Fracture of layered gallium and indium chalcogenides // Mater. Sci. 2005. Vol. 41. P. 839−842. DOI: https://doi.org/10.1007/s11003-006-0050-4
96. *Aksimentyeva O. I., Demchenko P. Yu., Savchyn V. P., Balitskii O. A.* To the chemical exfoliation phenomena during layered GaSe-polyaniline interaction // Nanoscale Res. Lett. 2013. Vol. 8. DOI: https://doi.org/10.1186/1556-276X-8-29

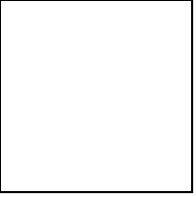

Chapter 2

PREDICTING OF THERMODYNAMIC STABILITY OF NANOMATERIALS BASED ON $Gd_{1-x}Ln_xF_3$, Ln = Sm–Lu, Y SOLID SOLUTIONS

E. Get'man[1], O. Mariichak[1], Yu. Oleksii[1], L. Ardanova[2], and S. Radio[1]

[1]*Vasyl' Stus Donetsk National University, 21027 Vinnytsia, Ukraine*

[2]*Minnesota State University, Mankato, 56001 Minnesota, USA*

Corresponding author: radio@donnu.edu.ua

Contents

Abstract

The mixing energies (interaction parameters) are calculated, within the framework of the crystal energy approach, taking into account differences in the sizes of substituting structural units and degrees of chemical bond ionicity in isostructural β-YF_3 components of the $Gd_{1-x}Ln_xF_3$, Ln = Sm–Lu, Y systems. It is shown that the magnitude of the mixing energy is determined mainly by the difference in the sizes of the substituting structural units and, to a lesser extent, by the difference in the degrees of ionicity of the chemical bond in the components. The critical decomposition (stability) temperatures of continuous series of solid solutions and the decomposition temperatures of limited solid solutions of trifluorides of rare-earth elements (REE) with a β-YF_3 type of structure for compositions with x = 0.01, 0.03, 0.05, 0.10 and 0.50 are determined. A diagram of thermodynamic stability is presented, which makes it possible to predict the temperature ranges of the existence of continuous series of solid solutions, as well as the limits of substitution (x) depending on the decomposition temperature (T_d) or the decomposition temperature according to the given limits of substitution of limited series of solid solutions. The regions of thermodynamic stability, instability, and supposed metastability of solid solutions are determined. The decomposition temperatures of unlimited series of solid solutions are calculated in GdF_3–SmF_3, GdF_3–EuF_3, GdF_3–TbF_3, GdF_3–DyF_3, GdF_3–HoF_3, GdF_3–ErF_3, GdF_3–TmF_3, GdF_3–YbF_3, GdF_3–LuF_3 systems in the composition range $1.0 > x > 0$ with step x = 0.05, and dependences of decomposition temperatures on composition (domes of decomposition) for the above systems are plotted. Domes of decomposition can be used to supplement the melting diagrams previously studied by the methods of physicochemical analysis in the low-temperature region of the above systems. Within the error of the method, the calculation results do not contradict the experimental data described earlier in the literature. The results of the work can be useful in choosing the ratio of components in "mixed" matrices, as well as the amount of activator in practically important medical nanomaterials.

2.1 Introduction

Trifluorides of rare-earth elements (REE) previously have attracted the attention of researchers in various fields of science and technology, such as optoelectronic devices, phosphors, lasers, and others [1]. In recent years, studies on their application in the form of nanomaterials in medicine as optical 3D devices, probes for visualization of biological objects [2, 3], for intracellular labels or measurements [4], and in immunoassays [5] have become relevant. The interest in $Gd_{1-x}Ln_xF_3$ solid solutions is due to the fact that Gd is located in the middle of the REE series and its ionic radius is close to the ionic radii of most REEs [6], so it is easily substituted by them. In addition, a group of REE trifluorides from SmF_3 to LuF_3 (β-YF_3 structural type) can crystallize in the same structural type with GdF_3, which also favours the isomorphous substitution of gadolinium for other REE up to the formation of continuous series of solid solutions. These crystals are considered suitable

matrix materials for use in lasers or scintillators due to their high transparency over a wide range of wavelengths from ultraviolet to infrared [7]. Their band gap is more than 10 eV. REE trifluoride crystals also have low refractive indices (about 1.5), which limits the nonlinear effects obtained by pumping a high-power laser source, as well as low phonon energies [7]. The use of solid solutions, rather than individual compounds, is due to the fact that their properties can be purposefully controlled depending on the composition.

However, the physical and chemical foundations for the synthesis of solid solutions (state diagrams and, in particular, the solubility regions based on the components of these systems) are given much less attention than the "composition – physical properties" dependencies. Although the melting diagrams of $Gd_{1-x}Ln_xF_3$ systems with both components with the β-YF_3 type of structure have been studied quite a lot by the methods of physicochemical analysis (GdF_3–TbF_3, GdF_3–DyF_3, GdF_3–HoF_3, GdF_3–ErF_3, GdF_3–TmF_3, GdF_3–YbF_3, GdF_3–LuF_3, YF_3–GdF_3), the main attention was paid to the construction of liquidus and solidus lines, as well as to the study of polymorphic transitions at high temperatures [8–11]. In the above systems, near temperatures slightly below subsolidus temperatures, the components do not form continuous series of solid solutions, since they crystallize in different types of structures. With decreasing temperature, they become isostructural and form continuous series of solid solutions [8–11]. However, the phase compositions at these temperatures are practically not characterized; in particular, there are no data on substitution limits and stability regions of solid solutions. This, apparently, is due, on the one hand, to the interest of researchers, mainly, in the growth of single crystals of REE trifluorides, and, on the other hand, to the insufficient sensitivity of the thermal analysis used to very small thermal effects of the formation and decomposition of solid solutions compared to the thermal effects of melting.

At the same time, it is known [12–14] that solid solutions synthesized at high temperatures tend to decompose upon cooling, which can lead to degradation of materials based on them, changes and irreproducibility of their properties during storage and operating. In this regard, before the synthesis of solid solutions and the study of properties depending on the composition, it is desirable to evaluate the limits of isomorphous substitutions depending on temperature and the stability of solid solutions in the corresponding regions of the systems.

At the same time, as far as we know, in most cases, the solid-phase synthesis of solid solutions of REE trifluorides is carried out at lower temperatures in the range of ~473–1273 K [15–23], and by the low-temperature hydrothermal method, at temperatures up to 573 K [24–32], both methods are used in a number of works [29–33]. Solid solutions of nanocrystals attracting the attention of researchers are synthesized at even lower temperatures. Thus, $Gd_{0.985}Tb_{0.015}F_3$ nanocrystals were obtained using the sol-gel and low-temperature hydrothermal method at a final temperature of 483 K [34].

Insufficient information about substitution limits at temperatures lower than subsolidus temperatures in the above systems forces researchers to choose the composition of matrices and modifying additives either by analogy with related systems or by the "trial and error" method, which can lead to excessive consumption of expensive reagents and an increase in the duration of studies.

Taking into account the above, we have carried out studies on predicting the substitution limits and thermodynamic stability of $Gd_{1-x}Ln_xF_3$, Ln = Sm–Lu, Y solid solutions, with the orthorhombic structure of β-YF_3 [35] in a wide range of compositions and temperatures.

2.2 Method for Calculating Substitution Limits and Thermodynamic Stability of $Gd_{1-x}Ln_xF_3$, Ln = Sm–Lu, Y Solid Solutions and Initial Data

In the general case, the mixing energy (interaction parameter) Q consists, according to V.S. Urusov [12–14], of three contributions due to the difference in the sizes of the substituting structural units (Q_δ), the degrees of ionicity of the chemical bond in the components (Q_ε), and the crystal structures of the components ($\Delta H_{II–I}/x_1$), where $\Delta H_{II–I}$ is the enthalpy of the polymorphic transition from the structure of the substituting component to the structure of the substituted:

$$Q = Q_\delta + Q_\varepsilon + \Delta H_{II–I}/x_1. \quad (2.1)$$

Since the work studies the intersubstitution of REE in groups of systems, both components of which are isostructural to β-YF_3, the third term in the above equation is equal to zero. The second term of the equation, according to [12–14], must be taken into account in cases where the difference in the electronegativity (EN) of ions substituting each other is greater than 0.4, or the difference in the degrees of ionicity of the chemical bond in the components of the systems is greater than 0.05, or if the size factor is very small. In this case, the dimensional parameter is only 0.031 or less (Table 1.1), so it is desirable to take Q_ε

Table 2.1 Some initial data and results of calculation of mixing energies and critical decomposition temperatures of $Gd_{1-x}Ln_xF_3$, Ln = Sm–Lu, Y solid solutions

Ln	V, Å	δ	C, kJ	Q_δ, kJ/mol	Q_ε, kJ/mol	Q, kJ/mol	T_{cr}, K
Sm	207.371	0.0311	138.32	14.203	0.094	14.297	854
Eu	204.325	0.0149	137.40	3.260	0.476	3.736	223
Gd	201.572	–	139.28	–	–	–	–
Tb	198.414	0.0052	138.32	0.397	0.094	0.491	29
Dy	195.225	0.0107	137.68	1.681	0.376	2.057	123
Ho	192.796	0.0149	137.40	3.260	0.476	3.736	223
Er	190.583	0.0188	137.20	5.190	0.847	6.037	360
Tm	188.633	0.0223	136.52	7.302	1.506	8.808	526
Yb	187.033	0.0252	135.56	9.325	2.353	11.678	697
Lu	185.686	0.0277	137.48	11.267	0.712	11.979	715
Y	191.175	0.0176	139.28	4.608	0.0245	4.632	276

into account. Taking into account the difference in the sizes of the substituting structural units and the difference in the degrees of ionicity of the chemical bond in the components, the mixing energy will be (in kJ/mol) [12–14]:

$$Q = Q_\delta + Q_\varepsilon = C\,m\,n\,z_m\,z_x\,\delta^2 + 1390\,m\,z_m\,z_x\,\alpha\,(\Delta\varepsilon)^2 / (2R_1), \quad (2.2)$$

where: $C = 137.5$ – the average value of the empirical parameters (Table 1.1) calculated from the expression $C = 20(2\Delta\chi + 1)$ [14] for the difference in EN of cations and anions $\Delta\chi$, taken from [36]; $m = 4$ – number of structural units in components; $n = 8.9$ – effective coordination number of a substituting structural unit for a structure of the β-YF_3 type (taken from S. Batsanov [37], since in β-YF_3 the cation is surrounded by anions located at two significantly different distances); z_m, z_x – modules of charges of structural units (Ln^{3+} and F^-); $R_1 = 2.4$ Å – interatomic distance "cation–anion" in the GdF_3 structure, calculated as the sum of crystalline ionic radii according to Shannon [6]; $\alpha = 1.693$ – the reduced Madelung constant is calculated using the Templeton formula [38]; $\Delta\varepsilon$ – differences in the degrees of ionicity of the chemical bond in the components (Table 2.2), calculated from the difference in the EN of REE cations and anions taken from [36]; δ – the relative difference in the sizes of substituting structural units (size parameter), calculated from the cubic roots of the unit cell volumes (Table 1.1), taken from [35]. The accuracy of calculating the mixing energy using the formula

$$Q_\delta = C\,m\,n\,z_m\,z_x\,\delta^2 \quad (2.3)$$

is ±13 % [13].

Since the values of the dimensional parameters in all cases are significantly less than 0.1 (Table 2.1), according to the recommendation [12–14], the values of the critical decom-

Table 2.2 On the calculation of the contribution to the mixing energy due to the difference in the degrees of ionicity of the chemical bond in the components of the $Gd_{1-x}Ln_xF_3$ systems, Ln = Sm–Lu, Y

Ln	$\chi(Ln^{3+})$	$\chi(F^-) - \chi(Ln^{3+})$	ε_{Ln}	$\Delta\varepsilon$
Sm	1.410	2.958	0.844	0.004
Eu	1.433	2.935	0.839	0.009
Gd	1.386	2.982	0.848	
Tb	1.410	2.958	0.844	0.004
Dy	1.426	2.942	0.840	0.008
Ho	1.433	2.935	0.839	0.009
Er	1.438	2.930	0.836	0.012
Tm	1.455	2.913	0.832	0.016
Yb	1.479	2.889	0.828	0.020
Lu	1.431	2.937	0.837	0.011
Y	1.340	3.028	0.850	0.002

position temperatures of solid solutions were calculated in the approximation of regular solid solutions by the expression $T_{cr} = Q / 2kN$, where k is the Boltzmann constant, N is the Avogadro's number. The decomposition temperature T_d was calculated from the given substitution limit x or the substitution limit x from the decomposition temperature, according to the Becker equation [39]:

$$-(1 - 2x) / \ln[x/(1 - x)] = kN \times T_d / Q. \quad (2.4)$$

In these two cases, according to [12–13], the Q value was taken in cal/mol.

2.3 Results and Its Discussion

Some initial data and results of calculations of the mixing energy and critical decomposition temperatures T_{cr} are summarized in Tables 2.1–2.2. As can be seen from the data presented, with an increase in the REE number, the size parameter δ and, consequently, the contribution to the mixing energy Q_δ first decreases in the series of systems with Sm–Eu trifluorides, and then naturally increases in the series of systems with Tb–Lu trifluorides. This is due to the fact that in a series of systems with Sm–Eu trifluorides, the difference between the radii of REE and gadolinium ions decreases, while in a series of systems with Tb–Lu trifluorides, on the contrary, it increases [6]. The critical decomposition temperatures change symbatically with the change in the mixing energy Q_δ. The value of the mixing energy is determined to a greater extent by the contribution due to the difference in the sizes of the substituting structural units Q_δ and to a lesser extent by the difference in the degrees of ionicity of the chemical bond in the components of the systems Q_ε.

Based on the calculated values of the critical decomposition temperatures T_{cr} (for $x = 0.50$) and decomposition temperatures T_d (for $x = 0.01$; $x = 0.03$; $x = 0.05$; $x = 0.10$) (Table 2.3) their dependences on REE numbers were plotted (diagram of thermodynamic stability of solid solutions, see Figure 2.1). From the presented diagram, in the general case, it follows that the continuous series of solid solutions are thermodynamically stable in the temperature ranges above the critical ones (above the curve *e*). At lower temperatures (below curve *e*), they can decompose, forming two rows of limited solid solutions in each sys-

Table 2.3 Decomposition temperatures (K) of $Gd_{1-x}Ln_xF_3$ Ln = Sm–Lu solid solutions, for $x = 0.01$, 0.03, 0.05, and 0.10

Ln	T_d, K at x				Ln	T_d, K at x			
	0.01	0.03	0.05	0.10		0.01	0.03	0.05	0.10
Sm	364	462	522	622	Ho	95	121	136	162
Eu	95	121	136	162	Er	154	195	220	262
Gd	–	–	–	–	Tm	224	284	322	383
Tb	12	16	18	21	Yb	297	377	426	508
Dy	52	66	71	89	Lu	305	387	437	521

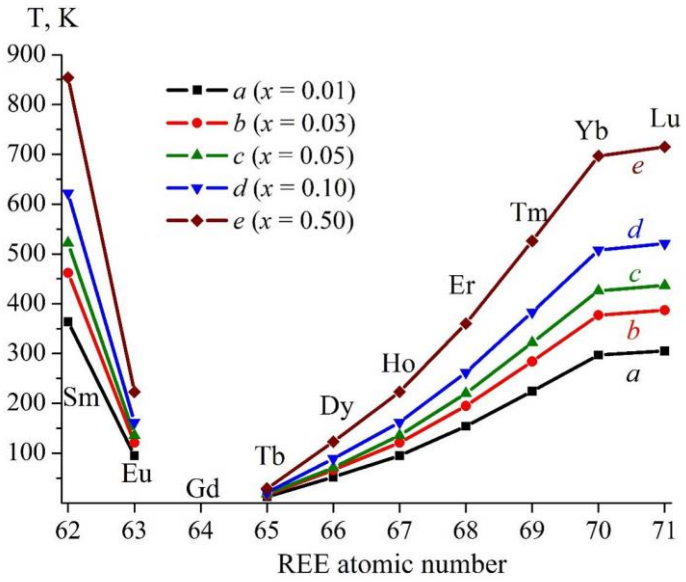

Figure 2.1 Dependences of the calculated decomposition temperatures of $Gd_{1-x}Ln_xF_3$, Ln = Sm–Lu solid solutions for $x = 0.01$ (*a*), $x = 0.03$ (*b*), $x = 0.05$ (*c*), $x = 0.10$ (*d*), and $x = 0.50$ (*e*) on the atomic number of REE (diagram of thermodynamic stability of solid solutions)

tem, if the diffusion rate is sufficient for the formation and growth of a new phase. Similarly, limited solid solutions with the compositions $x = 0.01$, $x = 0.03$, $x = 0.05$, and $x = 0.10$ at temperatures above curves *a*, *b*, *c*, and *d* are thermodynamically stable, below they can decompose.

It is known that as the temperature decreases, the mobility of the structural units of the solid solution decreases due to a decrease in the diffusion rate, and the solubility regions narrow [12–14]. This happens until the diffusion rate becomes so small that the decrease in the solubility regions practically stops, i.e. spontaneous quenching occurs and solid solutions can become metastable. If we assume that the quenching temperature is close to the temperature at which the components begin to interact upon heating, leading to the formation of a solid solution, we can estimate the spontaneous quenching temperature and the metastability region in the system, as was done in other systems [40–41]. Since $Gd_{1-x}Tb_xF_3$ was synthesized in [34] at a final temperature of 483 K, we will assume that spontaneous quenching of solid solutions of the systems under consideration occurs at temperatures below ~483 K.

In all $Gd_{1-x}Ln_xF_3$ systems, continuous series of solid solutions that are thermodynamically stable at temperatures above the critical ones (29–854 K, Table 2.1, Figure 2.1, curve *e*) become thermodynamically unstable as the temperature drops below the critical ones and can decompose into two regions of limited solid solutions. At temperatures below ~483 K, solid solutions may not decompose, spontaneous quenching will occur and they will become metastable.

Based on the foregoing, it can be assumed that, upon cooling, continuous series of solid solutions in systems with Sm, Yb, Lu trifluorides in the range from melting temperatu-

res to critical ones (854, 697, and 715 K, respectively), will be thermodynamically stable, in the temperature range from critical up to ~483 K will decompose into two solid solutions, which can become metastable at lower temperatures. Since the critical temperature of solid solutions based on thulium trifluoride (526 K) differs from the temperature of spontaneous quenching (~483 K) within the calculation error (±13 %), it is not possible to unambiguously judge their behavior at temperatures close to critical ones.

Continuous series of solid solutions in systems with Eu, Tb, Dy, Ho, Er, Y trifluorides in the range from melting temperatures to critical ones (up to 223, 29, 123, 223, 360, and 276 K, respectively) are thermodynamically stable, and below critical may not decompose, i.e. become metastable.

Using the graphic dependences (Figure 2.1), one can visually estimate the decomposition temperature of limited series of solid solutions by setting the substitution limit or determine the substitution limit of gadolinium for REE by setting the decomposition temperature. To determine the substitution limit for a given temperature, it is necessary to draw an isotherm until it intersects with a vertical line drawn from the REE number. This will allow determining the range of compositions in which the substitution limit is located, and the interpolation of the vertical segment between the two nearest curves gives the substitution limit. The substitution limit can be determined more precisely by constructing for a specific system the dependence of the decomposition temperatures calculated from the Becker equation on the composition (domes of decomposition), which, in the approximation of regular solid solutions, will be practically symmetrical.

Since the previously published melting diagrams did not show the stability regions of solid solutions below subsolidus temperatures [8–11], we used the Becker equation to calculate the decomposition temperatures in the GdF_3–SmF_3, GdF_3–EuF_3, GdF_3–TbF_3, GdF_3–DyF_3, GdF_3–HoF_3, GdF_3–ErF_3, GdF_3–TmF_3, GdF_3–YbF_3, GdF_3–LuF_3 systems in the composition range $1.0 > x > 0$ with a step $x = 0.05$ and plotted for the above systems the dependences of the decomposition temperatures on the composition (domes of decomposition, Figures 2.2–2.4). Using them, with greater accuracy, one can graphically determine the

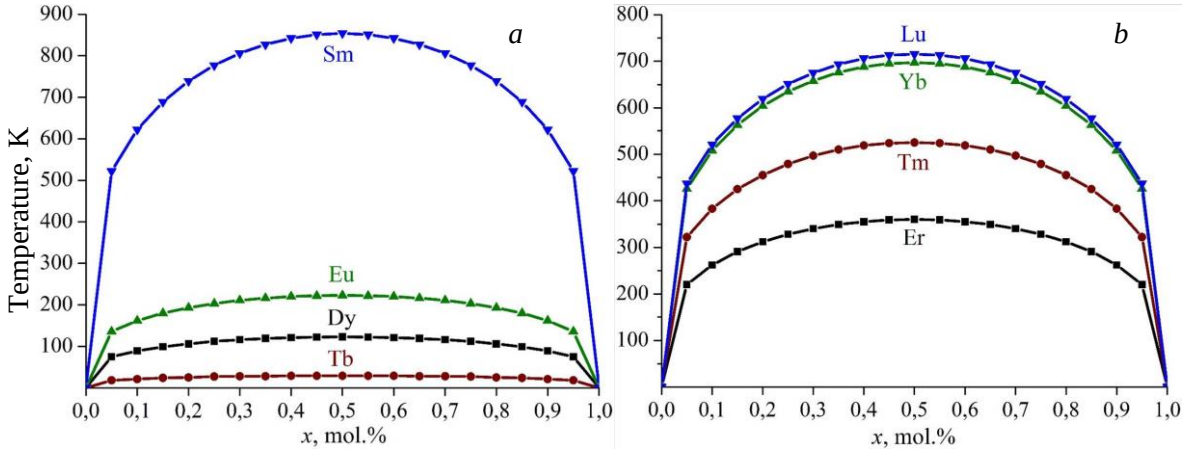

Figure 2.2 Calculated domes of decomposition of $Gd_{1-x}Ln_xF_3$, Ln = Sm, Eu, Dy, Tb (*a*) and Ln = Er, Tm, Yb, Lu (*b*) solid solutions

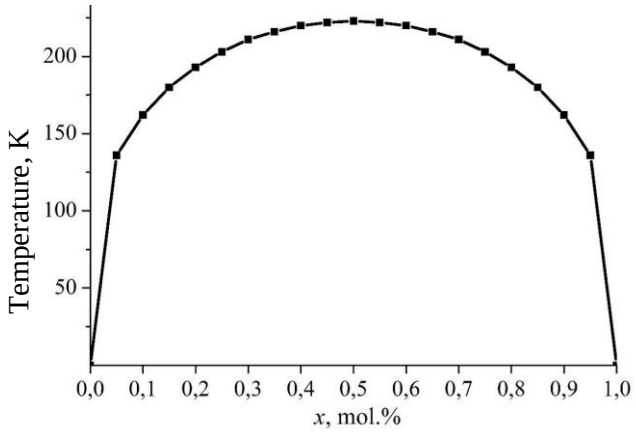

Figure 2.3 – Calculated dome of decomposition of $Gd_{1-x}Ho_xF_3$ solid solutions

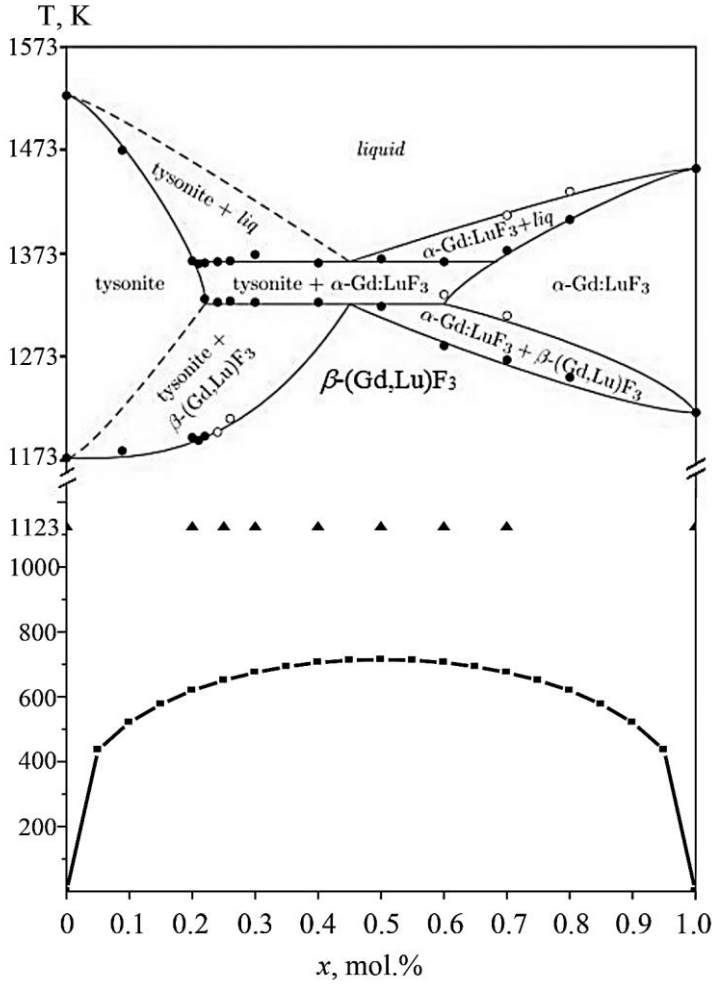

Figure 2.4 Calculated dome of decomposition of $Gd_{1-x}Lu_xF_3$ solid solutions (■); ▲ – compositions of a continuous series of $Gd_{1-x}Lu_xF_3$ solid solutions at 1123 K according to X-ray diffraction data [42]; top – melting diagram of the $Gd_{1-x}Lu_xF_3$ system (taken from [42])

equilibrium composition at a given temperature, or the decomposition temperature at a given composition, as well as the stability regions of solid solutions.

Domes of decomposition can also be used to supplement those previously studied in [8–11] by methods of physicochemical analysis of melting diagrams in the low-temperature region. As an example, in Figure 5 shows such a "hybrid" diagram of the state of the $Gd_{1-x}Lu_xF_3$ system. When constructing it, we used the melting diagram of $Gd_{1-x}Lu_xF_3$ system [42] and the dome of decomposition calculated by us for the same system. It can be used to visually determine the region of stability of continuous series of solid solutions over the entire temperature range.

2.4 Comparison of Calculation Results with Published Experimental Data for Some $Gd_{1-x}Ln_xF_3$ Systems

To the best of our knowledge, there are no data in the literature on the mixing energies and critical decomposition temperatures of solid solutions of the $Gd_{1-x}Ln_xF_3$, Ln = Sm–Lu, and Y composition, both with limited and unlimited miscibility of components.

However, it was previously established that in these systems, solid solutions crystallize from the melt with a discontinuity due to the non-isostructural nature of the components [8]. Then, upon further cooling, due to polymorphic transitions, continuous series of solid solutions from components with the β-YF_3 structure are formed in the systems. This agrees with our results, according to which a continuous series of solid solutions should exist in the region of thermodynamic stability that we have determined, i.e., between solidus temperatures (or temperatures of polymorphic transitions) and solid solution domes of decomposition. The critical decomposition (stability) temperatures of solid solutions in the $Gd_{1-x}Tb_xF_3$ and $Gd_{1-x}Lu_xF_3$ systems calculated by us are 29 and 715 K, respectively (Table 2.1). This also does not contradict the results of experimental studies [34, 42], according to which continuous series of solid solutions of $Gd_{1-x}Tb_xF_3$ and $Gd_{1-x}Lu_xF_3$ compositions were synthesized at temperatures of 483 and 1123 K, i.e., within the ranges of thermodynamic stability predicted by us for these systems (Table 2.1, Figures 2.1, 2.2, and 2.4).

2.5 Conclusions

Using the crystal-chemical approach in the approximation of regular solid solutions, the mixing energies (interaction parameters) and critical decomposition (stability) temperatures of solid solutions with the β-YF_3 structure of the $Gd_{1-x}Ln_xF_3$, Ln = Sm–Lu, and Y systems are calculated. As the REE number increases, the calculated mixing energies and critical decomposition temperatures of solid solutions of the $Gd_{1-x}Ln_xF_3$, Ln = Sm–Lu systems first decrease in the series of Sm–Eu trifluoride systems and then increase in the series of Tb–Lu trifluoride systems. This is due to the fact that in a series of systems with Sm–Eu trifluorides, the difference between the radii of REE and gadolinium ions decreases,

while in a series of systems with Tb–Lu trifluorides, on the contrary, it increases. It is shown that the total value of the mixing energy is determined mainly by the component due to the difference in the sizes of the substituting structural units and, to a lesser extent, the difference in the degrees of ionicity of the chemical bond of the system components. The presented thermodynamic stability diagram for the $Gd_{1-x}Ln_xF_3$, Ln = Sm–Lu systems makes it possible to visually evaluate not only the thermodynamic stability, instability, and presumed metastability of solid solutions in a wide range of compositions and temperatures, but also to evaluate the substitution limits for limited series of solid solutions at a given decomposition temperature or the temperature of their decomposition according to a given substitution limit. More precisely, they can be determined from dependences of the decomposition temperatures on the composition of each of the systems.

The decomposition temperatures of solid solutions with the β-YF_3 structure in the GdF_3–SmF_3, GdF_3–EuF_3, GdF_3–TbF_3, GdF_3–DyF_3, GdF_3–HoF_3, GdF_3–ErF_3, GdF_3–TmF_3, GdF_3–YbF_3, GdF_3–LuF_3 systems were calculated using the Becker equation, and the dependences of the decomposition temperatures on the composition (domes of decomposition) were plotted. They can be used to supplement the melting diagrams in the low-temperature region previously studied by the methods of physicochemical analysis.

The calculated critical decomposition (stability) temperatures of solid solutions in the $Gd_{1-x}Tb_xF_3$, and $Gd_{1-x}Lu_xF_3$ systems are 29 and 715 K, respectively. This does not contradict the results of experimental studies, according to which $Gd_{1-x}Tb_xF_3$ and $Gd_{1-x}Lu_xF_3$ solid solutions were synthesized at temperatures of 483 K [34] and 1123 K [42], i.e., within the ranges of thermodynamic stability predicted by us for these systems.

Keywords

- solid solution
- nanomaterials
- thermodynamic stability
- mixing energy
- isomorphous substitutions
- rare-earth elements
- fluorid

References

1. *He L., Xia L., Yang Y., Zheng Q., Jiang N., Xu C., Liu Y., Lin D.* Morphology-controlled synthesis, growth mechanism and fluorescence of YF_3:Eu^{3+}, Bi^{3+} // Mater. Res. Bull. 2017. Vol. 95. P. 483–490. DOI: https://doi.org/10.1016/j.materresbull.2017.08.014
2. *Chen F., Wang Zh.-Y., Zhang Y.-Y., Yu K.-H., Weng L.-X., Wei W.* Synthesis of poly(acrylic acid)-functionalized $La_{1-x}Eu_xF_3$ nanocrystals with high photoluminescence for cellular imaging. Acta Phys.-Chim. Sin. 2017. Vol. 33 (7). P. 1446–1452. DOI: 10.3866/PKU.WHXB201704102

3. *Li F., Li Ch., Liu X., Bai T., Dong W., Zhang X., Shi Zh., Feng Sh.* Microwave-assisted synthesis and up-down conversion luminescent properties of multicolor hydrophilic LaF_3:Ln^{3+} nanocrystals // Dalton Trans. 2013. Vol. 42 (6). P. 2015-2022. DOI: https://doi.org/10.1039/C2DT32295A
4. *Wang F., Zhang Y., Fan X., Wang M.* One-pot synthesis of chitosan/LaF_3:Eu^{3+} nanocrystals for bioapplications // Nanotechnology. 2006. Vol. 17 (5). P. 1527–1532. https://doi.org/10.1088/0957-4484/17/5/060
5. *Zhang W., Hua R., Shao W., Zhao J., Na L.* Bioconjugations of polyethylenimine-capped LaF_3:Ce, Tb nanoparticles with bovine serum albumin and photoluminescent properties // J. Nanosci. Nanotechnol. 2014. Vol. 14 (5). P. 3690-3695. https://doi.org/10.1166/jnn.2014.7971
6. *Shannon R. D.* Revised effective ionic radii and systematic studies of interatomic distances in halides and chalcogenides // Acta Cryst. 1976. Vol. A32. P. 751-767. DOI: https://doi.org/10.1107/S0567739476001551
7. *Yoshikawa A., Satonaga T.* Binary Fluorides: $(Gd,Y)F_3$ and $K(Y,Lu)_3F_{10}$. In: Fukuda T., Chani V.I. (Eds.) Shaped Crystals. Advances in Materials Research, Vol. 8. Springer, Berlin, Heidelberg, 2007. P. 301–321. DOI: https://doi.org/10.1007/978-3-540-71295-4_21
8. Trivalent metal fluoride systems. Phase diagrams of fluoride systems RF_3-R"F_3 // Personal site of Pavel Pavlovich Fedorov. URL: http://ppfedorov.narod.ru/index/phase_diagrams_of_fluoride_systems_rf3_r_f3/0-73. Accessed June 30, 2022
9. *Korshunov B. G., Safonov V. V.* Galogenidnyye sistemy: Spravochnik [Halide Systems: A Handbook]. Moscow: Metallurgy, 1984. 304 p. (in Russian)
10. *Sobolev B. P.* The Rare Earth Trifluorides: The high temperature chemistry of the rare earth trifluorides. Barcelona: Institut d'Estudis Catalans, 2000. 520 p.
11. *Sobolev B. P., Fedorov P. P., Galkin A. K., Sidorov V. S., Ikrami D. D.* Phase Diagrams of Binary Systems Formed by Rare Earth Trifluorides. In: Givargizov E.I. (eds) Growth of Crystals. Vol. 13. Springer, Boston, MA, 1986. P. 229–236. DOI: https://doi.org/10.1007/978-1-4615-7119-3_23
12. *Urusov V. S.* Energetic theory of miscibility gaps in mineral solid solutions // Fortschr. Mineral. 1975. Vol. 52. P. 141–150.
13. *Urusov V. S.* Teoriia izomorfnoi smesimosti [Theory of isomorphous miscibility]. Moscow: Nauka, 1977. 251 p. (in Russian)
14. *Urusov V. S.* Crystal Chemical and Energetic Characterization of Solid Solution. In: Saxena S.K. (eds) Thermodynamic Data. Advances in Physical Geochemistry, vol 10. Springer, New York, NY. 1992. P. 162-193. DOI: https://doi.org/10.1007/978-1-4612-2842-4_6
15. *Chen G., Qiu H., Fan R., Hao Sh., Tan Sh., Yang Ch., Han G.* Lanthanide-doped ultrasmall yttrium fluoride nanoparticles with enhanced multicolor upconversion photoluminescence // J. Mater. Chem. 2012. Vol. 22 (38). P. 20190–20196. DOI: https://doi.org/10.1039/C2JM32298F
16. *Wang G., Qin W., Xu Y., Wang L., Wei G., Zhu P., Kim R.* Size-dependent upconversion luminescence in YF_3:Yb^{3+}/Tm^{3+} nanobundles // J. Fluorine Chem. 2008. Vol. 129 (11). P. 1110–1113. DOI: https://doi.org/10.1016/j.jfluchem.2008.07.026
17. *Jia G., Huang C., Wang Ch., Jiang J., Li Sh., Ding Sh.* Facile synthesis and luminescence properties of uniform and well-dispersed YF_3:Eu^{3+} architectures // CrystEngComm. 2012. Vol. 14 (13). P. 4425–4430. DOI: https://doi.org/10.1039/C2CE06571A
18. *Yanes A. C., Santana-Alonso A., Méndez-Ramos J., del-Castillo J., Rodríguez V. D.* Novel sol-gel nano-glass-ceramics comprising Ln^{3+}-doped YF_3 nanocrystals: Structure and high efficient UV upconversion // Adv. Funct. Mater. 2011. Vol. 21 (16). P. 3136-3142. DOI: https://doi.org/10.1002/adfm.201100146
19. *Rahman P., Green M.* The synthesis of rare earth fluoride based nanoparticles // Nanoscale 2009. Vol. 1 (2). P. 214–224. DOI: https://doi.org/10.1039/B9NR00089E

20. *Yan L., Gao W., Han Q., Li X., Wang R., Zhang Ch., Zhang M., Wang L., Zheng H.* Investigation on YF_3:Eu^{3+} architectures and their luminescent properties // CrystEngComm. 2015. Vol. 17 (43). P. 8242–8247. DOI: https://doi.org/10.1039/C5CE01586C
21. *Razumkova I. A., Denisenko Yu. G., Boyko A. N., Ikonnikov D. A., Aleksandrovsky A. S., Azarapin N. O., Andreev O. \V.* Synthesis and upconversion luminescence in LaF_3:Yb^{3+}, Ho^{3+}, GdF_3:Yb^{3+}, Tm^{3+} and YF_3:Yb^{3+}, Er^{3+} obtained from sulfide precursors // Z. Anorg. Allg. Chem. 2019. Vol. 645 (24). P. 1393-1401. DOI: https://doi.org/10.1002/zaac.201900204
22. *Wang S., Song Sh., Deng R., Guo H., Lei Y., Cao F., Li X., Su Sh., Zhang H.* Hydrothermal synthesis and upconversion photoluminescence properties of lanthanide doped YF_3 sub-microflowers // CrystEngComm. 2010. Vol. 12 (11). P. 3537–3541. DOI: https://doi.org/10.1039/C0CE00023J
23. *Chai G., Dong G., Qiu J., Zhang Q., Yang Zh.* Phase transformation and intense 2.7 μm emission from Er^{3+} doped YF_3/YOF submicron-crystals // Sci. Rep. 2013. Vol. 3. Art. No. 1598. DOI: https://doi.org/10.1038/srep01598
24. *Li G., Lai Y., Bao W., Li L., Li M., Gan Sh., Long T., Zou L.* Facile synthesis and luminescence properties of highly uniform YF_3:Ln^{3+} (Ln = Eu, Tb, Ce, Dy) nanocrystals in ionic liquids // Powder Technol. 2011. Vol. 214 (2). P. 211–217. DOI: https://doi.org/10.1016/j.powtec.2011.08.012
25. *Yuan Zh., Shen Ch., Zhu Y., Bai A., Wang J. Liu Y., Lyu Y.* Multiple morphologies of YF_3:Eu^{3+} microcrystals: Microwave hydrothemal synthesis, growth mechanism and luminescence properties // Ceram. Int. 2016. Vol. 42 (1). Pt. 2. P. 1513–1520. DOI: https://doi.org/10.1016/j.ceramint.2015.09.099
26. *He L., Xia L., Yang Y., Zheng Q., Jiang N., Xu Ch., Liu Y., Lin D.* Morphology-controlled synthesis, growth mechanism and fluorescence of YF_3:Eu^{3+}, Bi^{3+} // Mater. Res. Bull. 2017. Vol. 95. P. 483–490. DOI: https://doi.org/10.1016/j.materresbull.2017.08.014
27. *Cui X., Hu T., Wang J., Zhang J., Zhong X., Chen Y., Li X., Yang J., Gao C.* Ionic transportation and dielectric properties of YF_3:Eu^{3+} nanocrystals // Nanomaterials. 2018. Vol. 8 (12). Art. No. 995. DOI: https://doi.org/10.3390/nano8120995
28. *Gong C., Li Q., Liu R., Hou Y., Wang J., Dong X., Liu B., Yang X., Yao Z., Tan X., Li D., Liu J., Chen Z., Zou B., Cui T., Liu B.* Structural phase transition and photoluminescence properties of YF_3 and YF_3:Eu^{3+} under high pressure // Phys. Chem. Chem. Phys. 2013. Vol. 15 (45). P. 19925–19931. DOI: https://doi.org/10.1039/C3CP53230E
29. *Luo P., Huang P., Wang J., Yao Ch., Zhao Y., Zhou B., Zheng Q., Zhang X., Jiang W., Wang L.* Controllable synthesis of glass ceramics containing YF_3:Eu^{3+} nanocrystals: Well-preserved Eu and prolonged lifetime // J. Am. Ceram. Soc. 2020. Vol. 103 (5). P. 3089–3096. DOI: https://doi.org/10.1111/jace.17021
30. *Tao F., Hu C., Wang Zh., Zhu G., Sun Y., Shu D.* Hydrothermal synthesis and luminescence properties of YF_3:Ln (Ln = Sm, Dy, Tb and Pr) nano-/microcrystals // Ceram. Int. 2013. Vol. 39 (4). P. 4089–4098. DOI: https://doi.org/10.1016/j.ceramint.2012.10.263
31. *Murali G., Kaur S., Chae Y.Ch., Ramesh M., Kim J., Suh Y.D., Lim D.-K., Lee S.H.* Monodisperse, shape-selective synthesis of YF_3:Yb^{3+}/Er^{3+} nano/microcrystals and strong upconversion luminescence of hollow microcrystals // RSC Adv. 2017. Vol. 7 (39). P. 24255-24262. DOI: https://doi.org/10.1039/C7RA02188G
32. *Cui Y., Fan X., Hong Zh., Wang M.* Synthesis and luminescence properties of lanthanide(III)-doped YF_3 nanoparticles // J. Nanosci. Nanotechnol. 2006. Vol. 6 (3). P. 830–836. DOI: https://doi.org/10.1166/jnn.2006.119
33. *Zalkin A., Templeton D. H.* The crystal structures of YF_3 and related compounds // J. Am. Chem. Soc. 1953. Vol. 75 (10). P. 2453–2458. DOI: https://doi.org/10.1021/ja01106a052
34. *Waetzig G. R., Horrocks G. A., Jude J. W., Zuin J. W., Banerjee S.* X-ray excited photoluminescence near the giant resonance in solid-solution $Gd_{1-x}Tb_xOCl$ nanocrystals and their retention upon

solvothermal topotactic transformation to $Gd_{1-x}Tb_xF_3$ // Nanoscale. 2016. Vol. 8 (2). P. 979–986. DOI: https://doi.org/10.1039/C5NR07819A

35. *Batsanova L. R.* Rare-earth fluorides // Russ. Chem. Rev. 1971. Vol. 40 (6). P. 465–484. DOI: http://dx.doi.org/10.1070/RC1971v040n06ABEH001932
36. *Li K., Xue D.* Estimation of electronegativity values of elements in different valence states // J. Phys. Chem. A. 2006. Vol. 110 (39). P. 11332–11337. DOI: https://doi.org/10.1021/jp062886k
37. *Batsanov S. S.* On effective coordination number of atoms in crystals // Zh. Neorgan. Khimii 1977. Vol. 22 (5). P. 1155–1159 (in Russian)
38. *Templeton D.H.* Madelung constants and coordination // J. Chem. Phys. 1953. Vol. 21. P. 2097–2098. DOI: https://doi.org/10.1063/1.1698788
39. *Becker R.* Über den Aufbau binarer Legierungen // Z. Metallkunde. 1937. Vol. 29. P. 245-249 (in German)
40. *Get'man E.I., Radio S.V.* Predicting the Substitution of Rare-Earth Elements with Cerium in the Solid Solutions Based on Nanoscale Ln_2SiO_5 (Ln = Tb–Lu, Y) // Nanosistemi, Nanomateriali, Nanotehnologii. 2019. Vol. 17 (4). P. 701–710. DOI: https://doi.org/10.15407/nnn.17.04.701
41. *Oleksii Yu. A., Get'man E. I., Radio S. V., Ardanova L. I., Zubov E. E.* Isomorphous substitutions and Stability of Solid Solutions in $La_{1-x}Ln_xF_3$, Ln = Ce–Ho Systems // 2021 IEEE 11th International Conference Nanomaterials: Applications & Properties (NAP). 2021. P. 1–5. DOI: 10.1109/NAP51885.2021.9568596
42. *Ranieri I. M., Baldochi S. L., Klimm D.* The phase diagram GdF_3–LuF_3 // J. Solid State Chem. 2008. Vol. 181 (5). P. 1070–1074. DOI: https://doi.org/10.1016/j.jssc.2008.02.017

Chapter 3

SOME THERMOELECTRIC CAPABILITIES OF SUPERLATTICES AND NANOPOWDERS

P. V. Gorskyi[1,2]

[1]*Institute of Thermoelectricity of the NAS and MES of Ukraine, 58029 Chernivtsi, Ukraine*
[2]*Yu. Fedkovych Chernivtsi National University, 58012 Chernivtsi, Ukraine*

Corresponding author: gena.grim@gmail.com

Contents

Abstract

The paper proposes a diffusion theory of the electrical contact resistance of a thermoelectric superlattice (TES) – metal couple (TESMC). On its basis, the thickness of the transient contact layer and the value of the electrical contact resistance of TES – metal are determined. Moreover, the law of growth of the transient contact layer is found. It is shown that the upper limit of the electrical contact resistance for bismuth telluride-nickel couple at 500 K can reach $4 \cdot 10^{-5}$Ohm·cm^2. At the same time, it was found that the non-parabolicity of the band spectrum of the superlattice, described by the Fivaz model, depending on the degree of openness of the Fermi surface of the thermoelectric superlattice, can reduce this value by at least 60–100 times. However, the obtained experimental data, on the one hand, and the predicted significant difference in contact resistance for *n*- and *p*-type materials, on the other hand, give reason to assume that the electrical contact resistance of the thermoelectric material-metal for the bismuth-nickel telluride couple is due to the deviation surface of the semiconductor from the ideal plane and the presence of an oxide film on the surface of the TES. Yet the thermoelectromotive forces (thermoEMF) of the powder based thermoelectric materials is coinsiderated.

3.1 Introduction. Diffusion theory of Electrical Contact Resistance Thermoelectric Superlattice – Metal

The metal-semiconductor contact resistance consists of two main parts: the resistance caused by the potential barrier at the metal-semiconductor interface and the resistance caused by the transient layer formed by the diffusion of the metal into the semiconductor and (or) vice versa. Regarding the “barrier” part of the resistance, it can be said that in the most general case it is caused by two mechanisms: thermoelectron emission and tunneling of charge carriers through the barrier. In [1], we gave a brief overview of these mechanisms and the conditions for their manifestation. Regarding the manifestation of these mechanisms in the real operating conditions of thermoelectric devices, it turned out that even in cooling modules on the hot side, and even more so in generator modules, there is a combined or transient mode in which both mechanisms operate. Based on such considerations, we calculated the “barrier” part of the contact resistance. As for the part of the contact resistance due to the transient layer, it should be noted that prior to our studies carried out in the above mentioned work, this part was found by simply multiplying the thickness of the transient layer by the resistivity of the semiconductor material, in particular TESMC. The thickness of the transient layer was determined experimentally based on the results of metallographic and electron microscopic studies. We, however, proposed to determine the

distribution of the metal in the transient layer as a solution to the equation of stationary diffusion from a source with constant volume intensity. In this case, the thickness of the transient layer acted as a parameter of the theory, the limits of change of which were estimated according to the experimental data given in the literature. It should be noted that although we obtained a certain agreement between the results of our theoretical calculations and the experiment, this approach is suitable in the case when the contact structure is created, for example, by sputtering a contact metal or an anti-diffusion layer on the surface of a semiconductor from a source with constant volume intensity. In the case of creating contact structures by electrochemical or purely chemical deposition of an anti-diffusion layer on the TESMC surface with subsequent soldering, the diffusion process, during which the transient layer is formed, is fundamentally nonstationary and the theory developed in [1, 2] ceases to be correct.

Experimental studies of the properties of contact structures and transient contact layers, analysis of their effect on consumer characteristics, failure and durability of thermoelectric devices, temporal evolution of transient contact layers, the effect of semiconductor surface treatment methods on electrical contact resistance, methods for reducing contact resistances and methods for their accurate measurement are discussed in a number of works, including [3–7]. But to date, a consistent theory of electrical resistance of contact structures created by soldering and their degradation has not been developed. A partial solution to this problem is the aim of this work. In the course of the work, the equation of non-stationary diffusion of metal in TESMC is solved taking into account the matter balance, and the exact law of growth of the transient contact layer and the normalized distribution of the metal in it are found. The temperature dependence of the electrical contact resistance of the transient contact layer is calculated and the process of long-term diffusion of nickel in the TESMC layer based on Bi(Sb)–Te(Se) is analyzed, which is of fundamental importance for the reliability of thermoelectric generator modules.

3.1.1 Solution of the Equation of Non-Stationary Diffusion of Metal in TESMC and Its Consequences

If the diffusion coefficient D of metal in TESMC is considered constant, then in a one-dimensional approximation this equation will be given by:

$$\frac{\partial c}{\partial t} = D\frac{\partial^2 c}{\partial x^2}, \tag{3.1}$$

where c is concentration of metal atoms, t is time, x is coordinate counted from the interface deep into TESMC. For the case of a semi-confined medium, the solution of equation (3.1) can be taken in the form:

$$c = c_0 \operatorname{erfc}\left(x/\sqrt{2Dt}\right), \tag{3.2}$$

where erfc(…) is the so-called additional error integral. Solution (3.2) satisfies the obvious initial condition $c(t=0)=0$ and the obvious boundary condition $c(x=0)=c_0$. However, the solution of Equation (3.1) in the form Equation (3.2) does not yet determine the law of growth of the transient layer with time. In order to determine it, we equate the number of metal atoms that will leave the nickel boundary layer in a certain time t_0 due to the boundary flux to the number of them that will be distributed in the transient layer of thickness x_0 in the same time:

$$c_0 \frac{2\sqrt{Dt_0}}{\sqrt{\pi}} = c_0 \int_0^{x_0} \operatorname{erfc}\left(x/2\sqrt{Dt_0}\right)dx. \tag{3.3}$$

When writing the equation, we believe that only the thickness of the boundary layer of nickel changes during the diffusion process, and the concentration of atoms in it remains unchanged until it is completely exhausted. Equation (3.3) leads to the following transcend-dental equation:

$$\frac{1}{\sqrt{\pi}} = \int_0^{\alpha_0} \operatorname{erfc}(\alpha)d\alpha, \tag{3.4}$$

the solution of which is $\alpha_0 = 6.771$, and, therefore, the growth of the transient layer occurs according to the law $x_0 = 13.552\sqrt{Dt_0}$. Thus, the thickness h of the spent part of nickel layer is matched by the thickness $6.771\sqrt{\pi}h \approx 12h$ of transient contact layer. In this case, the concentration distribution of metal atoms in the transient layer, normalized to its thickness, is determined by the formula

$$c(x) = c_0 \operatorname{erfc}\left(6.771x/x_0\right) \tag{3.5}$$

and it is shown in Fig. 3.1.

It is noteworthy that the ratio between the thickness of the transient contact layer and the thickness of the spent nickel layer is an invariant of the diffusion process that determines the formation of the transient contact layer. The value of the diffusion coefficient determines only the time dependence of the thickness of the transient contact layer and, consequently, the contact resistance of the TES-metal.

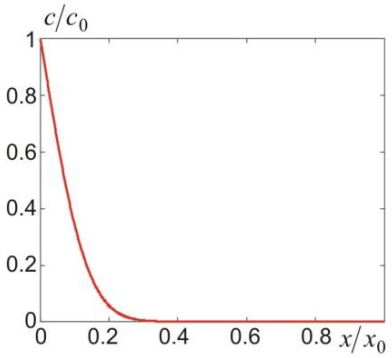

Figure 3.1 Distribution of metal atoms in a transient contact layer

3.1.2 Calculation of Electrical Contact Resistance

Using the theory of composites and taking into account the phenomenon of percolation associated with the formation of metal clusters in the thickness of the transient layer, we determine the electrical contact resistance TES – metal at an arbitrary temperature *T*. To do this, we first determine the volume fraction of metal in the transient layer:

$$\nu(x) = \frac{(A_m/\rho_m)\mathrm{erfc}(6.771x)}{(A_m/\rho_m)\mathrm{erfc}(6.771x) + (M_s/\rho_s)\mathrm{erf}(6.771x)}, \tag{3.6}$$

where A_m and ρ_m are atomic mass and metal density, respectively; M_s and ρ_s – molecular mass and TES density, respectively; erf(…) and erfc(…) – the so-called error integral and additional error integral. Then, with regard to percolation effect, the electrical contact resistance of the transient layer will be determined as:

$$r_{ce}(T) = 48h\int_0^1 \{R(x) - \sigma_m(T)(3\nu(x)-1) - \sigma_s(T)(2-3\nu(x))\}^{-1} dx, \tag{3.7}$$

where h is the thickness of spent metal layer; $\sigma_m(T)$ – specific electrical conductivity of metal; $\sigma_s(T)$ – specific electrical conductivity of TES and, besides

$$R(x) = \sqrt{[\sigma_m(T)(3\nu(x)-1) + \sigma_s(T)(2-3\nu(x))]^2 + 8\sigma_m(T)\sigma_s(T)}. \tag{3.8}$$

The temperature dependence of the specific electrical conductivity of a thermoelectric superlattice is determined as follows:

$$\sigma_s(T) = 0.08\frac{\sqrt{\pi^5 n_0}ae^2 l(T)}{ahT_{2D}(T)} \times$$
$$\times \int_0^\infty\int_0^\pi \frac{y\exp\left[\left(y + K^{-1}(1-\cos x) - \eta\right)/T_{2D}(T)\right]dxdy}{\left\{1+\exp\left[\left(y + K^{-1}(1-\cos x) - \eta\right)/T_{2D}(T)\right]\right\}^2\sqrt{2y + 4\pi K^{-1}n_0 a^3\sin^2 x}}, \tag{3.9}$$

where $T_{2D}(T) = 4\pi m^* kT/h^2 n_0 a$; $l(T) = l_0 T_0/T$; $K = h^2 n_0 a/4\pi m^*\Delta$; n_0 is volume concentration of free charge carriers; m^* – effective mass of charge carriers in the plane of layers; a – the smallest distance between translationally equivalent layers; l_0 – the length of free path of charge carriers at certain fixed temperature T_0; Δ is the half-width of a narrow miniband, which in the framework of the Fivaz model characterizes the interlayer motion of charge carriers, the rest of the designations are generally accepted; η may be determined from the equation

$$\frac{T_{2D}(T)}{\pi}\int_0^\pi \ln\left\{1+\exp\left[\left(\eta - K^{-1}(1-\cos x)\right)/T_{2D}(T)\right]\right\}dx - 1 = 0. \tag{3.10}$$

The scattering of charge carriers on the deformation potential of acoustic phonons was considered to be decisive. Specific calculations were performed in the temperature

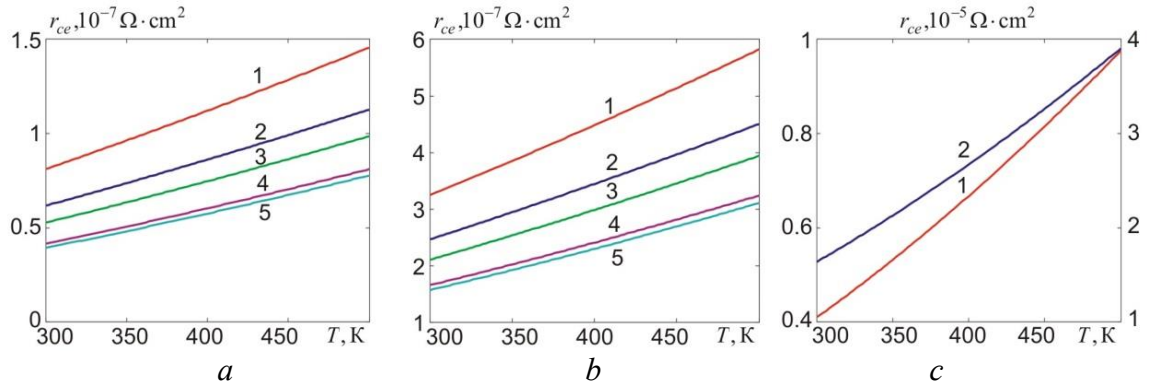

Figure 3.2 Temperature dependences of the contact resistance of TES based on bismuth telluride-nickel couple at the thicknesses of spent nickel layer: *a*) 5 μm, *b*) 20 μm at the degrees of nonparabolicity *K*: *1* – 0.1, *2* – 0.5, *3* – 1, *4* – 5, *5* – 10, as well as for the parabolic case (*c*) at the thicknesses of spent nickel layer: *1* – 5 μm (left axis), *2* – 20 μm (right axis)

range $T = 300$–500 K for different values of the parameter *K*, which characterizes the degree of openness of the Fermi surface of the TES, and, therefore, the degree of non-parabolicity of its band spectrum.

The results of calculations of the temperature dependences of electrical contact resistance for the TES based on bismuth telluride — nickel couple at the thicknesses of spent nickel layer 5 and 20 μm, respectively, are given in Fig. 3.2. For comparison, the same figure shows the results of calculations of the contact resistance of TES with a parabolic band spectrum. In the latter case, the temperature dependence of the effective mass caused by the electron-phonon interaction was taken into account. In all the cases the specific electrical conductivity of metal was considered to be inversely proportional to temperature and at $T_0 = 300$ K it was assumed that $\sigma_{m0} = 1.43 \cdot 10^5$ S/cm.

When constructing the plots in Fig. 3.2, *a*, *b*, the following values of TES parameters were taken: $m^* = m_0 = 9.1 \cdot 10^{-31}$ kg, $a = 3$ nm, $n_0 = 3 \cdot 10^{19}$ cm^{-3}, $l_0 = 20$ nm, $T_0 = 300$ K.

When constructing the plots in Fig. 3.2, *c* it was assumed that the specific electrical conductivity of bismuth telluride at $T_0 = 300$ K is $\sigma_{s0} = 1.4 \cdot 10^3$ S/cm and is inversely proportional to $T^{1.7}$. Moreover, when constructing all the plots it was assumed that $A_m = 58$, $\rho_m = 9\,100$ kg/m^3, $M_s = 802$, $\rho_s = 7\,860$ kg/m^3. It can be seen from the figures that at the thickness of spent nickel layer 5 μm the electrical contact resistance of TES in the considered range of temperatures and nonparabolicity degrees varies from $3.93 \cdot 10^{-8}$ to $1.46 \cdot 10^{-7}$ Ohm·cm^2, and at the thickness of spent nickel layer 20 μm — from $1.57 \cdot 10^{-7}$ to $5.82 \cdot 10^{-7}$ Ohm·cm^2. However, in the case of thermoelectric material with a parabolic band spectrum at the thickness of spent nickel layer 5 μm the contact resistance varies from $4.09 \cdot 10^{-6}$ to $9.75 \cdot 10^{-6}$ Ohm·cm^2, and at the thickness of spent nickel layer 20 μm – from $1.64 \cdot 10^{-5}$ to $3.9 \cdot 10^{-5}$ Ohm·cm^2. Traditionally, the anti-diffusion layer is made 20 μm thick. Therefore, a comparison of the calculated values of the electrical contact resistance with those traditionally "assigned" and used in the design of thermoelectric generators and coolers allows us to conclude that the thickness of the diffusing nickel layer does not exceed 5 μm, while the

remaining 15 μm remain on the surface. In so doing, the transition from traditional contact structures to heterostructures described by the Fivaz model, depending on the degree of openness of the Fermi surface of TES, should reduce the contact resistance by a factor of 60–100.

It should be noted that, according to [8], the diffusion coefficients of nickel in *p* and *n* type TESMCs differ even in orders of magnitude. This difference is caused primarily by the difference in activation energies of nickel diffusion in these materials. Therefore, the values of contact resistances reached during the same time of formation of the transient layer should differ significantly from each other. In practice, however, such a difference is not observed. Therefore, it should be assumed that the main role in the formation of contact resistance is played by the roughness of the contact surfaces of the thermoelectric legs and the presence of oxide films on them.

3.2 ThermoEMF of Powder Based Thermoelectric Materials

It is considered that the thermoelectric figure of merit of powder-based TESMC should increase considerably, since this is facilitated by energy barriers occurring due to vacuum or dielectric gaps between powder particles [9–11]. Tunnelling of free charge carriers through these gaps should increase the contribution of charge carriers with high energies to kinetic coefficients, including thermoEMF. If this filtering is strong enough, i.e. charge carriers that have passed through and not passed through the barriers differ significantly in energy, then it should lead to a significant increase in thermoEMF for two reasons. First, if the electron gas is degenerate, albeit weakly, then an increase in the fraction of charge carriers with an energy greater than the chemical potential should lead to a significant increase in the thermoEMF due to the fact that the contact and volume components of the thermoEMF are opposite in sign. In the nondegenerate gas, on the contrary, the signs of these components are identical, the contact component being the main one. Therefore, in the nondegenerate gas this factor plays a lesser role. Second, according to the general principles of quantum mechanics, the scattering index *r* must increase as the energy of the charge carriers increases [12]. If we are dealing with a material for which the quadratic law of charge carrier dispersion is valid, then the inequality $-0.5 \le r \le 3.5$ is true for this index. In semiconductor TESMC, in the area relevant for thermoelectric applications, the situation is most often realized, in which the value *r* is the smallest possible and corresponds to scattering of charge carriers with energy-independent cross-section, hence, the mean free path length [13]. In this case the thermo EMF of a powder-based material does not depend on the particle size of the powder, and therefore is the same as that of a single-crystal material, if we do not consider the possibility of changing the character of energy spectrum of charge carriers, for instance, due to dimensional quantization at particularly small particle sizes [13]. However, this parameter can be increased, in particular, by alloying the TESMC [14]. Therefore, the purpose of this paper section is to consider the dependence of the thermoEMF on the powder particle size arising when the scattering index increases beyond the minimum value.

3.2.1 General Formula for the ThermoEMF of Powder-Based TESMC

To derive a general formula determining the thermoEMF of a powder-based TESMC, we will use the approach we developed earlier in [15]. We will proceed from the general formula for the thermoEMF in the impurity conduction region, which in the case of an isotropic TESMC with a parabolic law of charge carrier dispersion can be represented as

$$\alpha = \frac{\int_0^\infty v^2(\varepsilon)\tau(\varepsilon)\varepsilon\left(-\partial f^0/\partial\varepsilon\right)g(\varepsilon)d\varepsilon}{eT\int_0^\infty v^2(\varepsilon)\tau(\varepsilon)\left(-\partial f^0/\partial\varepsilon\right)g(\varepsilon)d\varepsilon} - \frac{\zeta}{eT}. \tag{3.11}$$

In this formula: e – electron (hole) charge with corresponding sign; T – absolute temperature; ε – electron (hole) energy; f^0 – the Fermi-Dirac equilibrium distribution function; $v(\varepsilon)$, $\tau(\varepsilon)$, and $g(\varepsilon)$ – energy-dependent only electron velocity, their relaxation time and density of states, respectively; ζ – the chemical potential of the TESMC electronic subsystem.

The relaxation time $\tau(\varepsilon)$ in our case depends on both the scattering mechanisms characteristic of single crystals and the scattering of electrons (holes) at the boundaries of powder particles. As a consequence, it can be represented as:

$$\tau(\varepsilon) = \left\langle \frac{\tau_0 \varepsilon^r L}{\tau_0 \varepsilon^r v(\varepsilon) + L} \right\rangle. \tag{3.12}$$

In this formula: τ_0 – some constant value with respect to energy; L – possible mean free path of electron due to scattering at the boundaries of the powder particle, angular brackets denote averaging over all possible free path lengths within the particle.

In turn, the constant τ_0 can be expressed in terms of the mean free path of an electron (hole) $l_{e,h}$ in a single-crystal material, based on the ratio:

$$l_{e,h} = \frac{A\tau_{0e,h}\int_0^\infty \varepsilon^{r+1} f^0(\varepsilon)d\varepsilon}{\int_0^\infty \sqrt{\varepsilon} f^0(\varepsilon)d\varepsilon} = A\tau_{0e,h}(kT)^{r+0.5}\frac{F_{r+1}(\eta)}{F_{1/2}(\eta)}, \tag{3.13}$$

where A – the coefficient of proportionality between the velocity of electron and the square root of its energy; $F_m(\eta)$ – the Fermi index integral m; $\eta = \zeta / kT$. By determining Equation (3.13) $\tau_{0e,h}$, substituting the result in Equation (3.12), averaging over the free path lengths inside the powder particle, which, for simplicity, we assume as a sphere of radius r_0, and finally calculating the thermoEMF using Equation (3.11), we arrive at the following result:

$$\alpha = \frac{k}{e}\left\{\frac{\int_0^\infty\int_0^1\int_{-1}^1 f_1(x,\eta)x^{r+2.5}\left[\frac{x^{r+0.5}F_{1/2}(\eta)}{F_{r+1}(\eta)} + \frac{r_0}{l_{e,h}}\sqrt{y^2+1+2zy}\right]^{-1} y^2 dzdydx}{\int_0^\infty\int_0^1\int_{-1}^1 f_1(x,\eta)^{r+1.5}\left[\frac{x^{r+0.5}F_{1/2}(\eta)}{F_{r+1}(\eta)} + \frac{r_0}{l_{e,h}}\sqrt{y^2+1+2zy}\right]^{-1} y^2 dzdydx} - \eta\right\}. \tag{3.14}$$

In this formula, $f_1(x, \eta)$ – the energy derivative of the Fermi-Dirac distribution function, other notations explained above or generally accepted.

It is easy to see from this formula that, first, at $r = -0.5$ the thermoEMF is independent of the powder particle radius, second, at $r_0 / l_{e,h} \to \infty$ the thermoEMF tends to the value characteristic of single crystals.

3.2.2 Results of Calculating the ThermoEMF of Powder-Based TESMC and Their Discussion

Results of calculating the thermoEMF of powder-based TESMC by formula (3.14) are given in Fig. 3.3. The figures show that for all considered degrees of degeneracy at the minimum possible scattering index, the thermoEMF for a single crystal and powder-based TESMC is the same and has a minimum value. However, if the scattering index differs from the minimum possible, the thermoEMF becomes dependent on the size of the powder particle and decreases in magnitude as its radius decreases, the greater the scattering index. However, if we assume that the scattering index does not change in going from a single crystal to powder, then even at its maximum value a tangible decrease in thermoEMF occurs only at particle radii less than 40 electron (hole) free path lengths. Taking into account that the typical value of this length for materials based on the *Bi(Sb)-Te(Se)* system at 300 K is about 20 nm, it turns out that a significant decrease in thermoEMF can occur only in materials based on submicron or nanopowders with an average particle radius of less than 0.8 μm.

It should be noted, however, that the assumption that the scattering index is unchanged in going from a single crystal to powder is somewhat simplified. The point is that the grinding of a single-crystal material to a powdery state and its subsequent fabrication as a TESMC by hot pressing, extrusion, or electrospark plasma sintering involves a number of mechanical and thermal effects on the initial single crystal, which affect the defectiveness

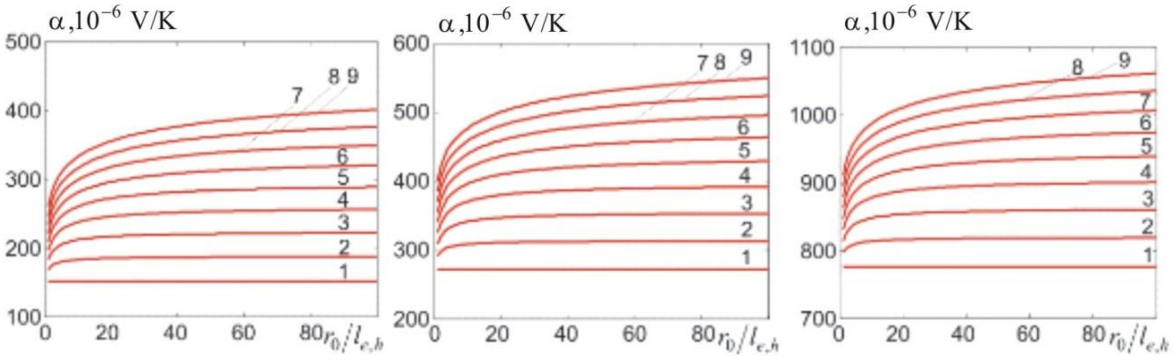

a *b* *c*

Figure 3.3 Dependences of the thermoEMF of powder-based TESMC on the radius of powder particle at: (*a*) $\eta = 1$; (*b*) $\eta = -1$; (*c*) $\eta = -7$. In each figure, curves *1–9* are plotted for scattering index r values between –0.5 and 3.5 in 0.5 increments.

of the material, and, consequently, the scattering mechanisms of charge carriers in it, and thus the value of the scattering index. If the starting material is manufactured in such a way that in the temperature range of application the scattering index is greater than the minimum value, there are factors that can both increase and decrease the value of the scattering index in going from a single crystal to powder. The formation of vacuum or dielectric barriers in the gaps between the TESMC particles, provided that their height and width are optimal for changing the scattering index with a satisfactory probability of charge carriers passing through the barriers, should be considered an enhancing factor. The formation of structural defects inside the material particles with an energy-independent or weakly energy-dependent scattering cross-section of charge carriers on them should be considered a decreasing factor. Thus, on the one hand, the possibility of a significant increase in the figure of merit of TESMC in going from a single crystal to powder is determined by the ratio between the competing processes of energy filtration of charge carriers and formation of defects with an energy-independent or weakly energy-dependent cross section of scattering of charge carriers on them. On the other hand, it follows from our earlier studies [15] that in going from a single crystal to powder, the electrical conductivity decreases at any value of the scattering index, and much more strongly than the thermoEMF. Thus, in going from a single crystal to powder with small particle size, the power factor of the material decreases, owing to which the thermoelectric figure of merit of the material can increase only with a sharp decrease in thermal conductivity, mainly due to its lattice (phonon) component. However, in a powder material, the thermoEMF can be fully or partially recovered by annealing, which reduces the number of defects with an energy-independent or weakly energy-dependent cross section of scattering of charge carriers on them. And such recovery does occur in some thermoelectric materials based, for example, on submicron powders [16]. But this mechanism alone still cannot fully explain the change in thermoEMF in going from single crystals to powders. The fact is that, for example, according to the data of [16] the ratio of electrical conductivity to thermal conductivity increased by a factor of 100 in going from a single crystal to powder with an average particle radius equal to 0.2 μm, while the figure of merit increased only 6-fold, which indicates a decrease of thermoEMF by approximately 4 times. And even when the scattering index drops from maximum to minimum, the thermoEMF decreases by a factor of only 2.7 at the degrees of degeneracy considered in this paper. Thus, either the charge carrier gas was more strongly degenerate, or there are other mechanisms that lead to thermoEMF decrease.

3.3 Conclusions

1) A strict diffusion theory of the electrical contact resistance of the transient layer is constructed.
2) The growth law of the transient contact layer is found.
3) The temperature dependence of the electrical contact resistance of the transient contact layer was calculated both for the case of TES and for the case of a thermoelectric mate-

rial with a traditional band spectrum, and it was shown that the transition to TES makes it possible to reduce the electrical contact resistance by a factor of 60–100.

4) It is shown that in powder-based materials the thermoEMF decreases with decreasing average powder particle radius the more the relaxation time depends on the energy. However, at particle radii larger than the free path of the charge carriers, it is still larger than even in a single crystal, provided that the free path of the charge carriers is energy-independent.
5) A significant decrease in the thermoEMF in going from a single crystal to a powder-based material can only occur if either the scattering index decreases due to the formation of defects that scatter charge carriers with an energy-independent cross section or if a dimensional quantization of the energy spectrum of charge carriers occurs as the size of the powder particle decreases.
6) The thermoEMF of powder-based TESMC can be restored completely or, at least partially, as a result of annealing, reducing the concentration of "harmful" defects with a small scattering index.

Key words

- diffusion
- matter balance
- boundary layer thickness
- superlattice
- contact resistance

References

1. *Vikhor L. M., Anatychuk L. I., Gorskyi P. V.* Electrical resistance of metal contacts to Bi_2Te_3 based thermoelectric legs // J. Appl. Phys. 2019. Vol. 126. P. 164503-1–164503-8. DOI: https://doi.org/10.1063/1.5117183
2. *Gorskyi P. V., Vikhor L. N.* Electrical contact resistance of “thermoelectric material-metal”couple. Proceedings of XXI International scientific and practical conference “Modern Information and Electron Technologies”, Odesa, Ukraine, 25–29 May 2020. P. 104–105.
3. *Semenyuk V.* Effect of electrical contact resistance on the performance of cascade thermoelectric coolers // J. Electron. Mater. 2019. Vol. 48. P. 1870–1876. DOI: https://doi.org/10.1007/s11664-018-6785-5.
4. *Gupta R. P.* Practical contact resistance measurement method for bulk Bi_2Te_3-based thermoelectric devices // J. Electron. Mater. 2013. Vol. 42. P. 1–5. https://doi.org/10.10007/s11664-013-2806-6.
5. *Sabo E. P.* Technology of chalcogen thermoelements. Physical backgrounds. Continued. 3.5. Electrochemical metallization // J. Thermoelectricity. 2011. Is. 1. P. 26–35.
6. *Aswal D. K., Basu R., Singh A.* Key issues in development of thermoelectric power generators: high figure-of-merit materials and their highly conducting interfaces with metallic interconnects // Energy Convers. Manag. 2016. Vol. 114. P. 50–67.

7. *He R., Shierning C., Nielsch K.* Thermoelectric devices: a review of devices, architectures and contact optimization // Adv. Mater. Technol. 2018. Vol. 3. 1700256. P. 1–17.
8. *Lan Y. C., Wang D. Z., Chen G., Ren Z. F.* Diffusion of nickel and tin in *p*-type $(Bi,Sb)_2Te_3$ and *n*-type $Bi_2(Te,Se)_3$ thermoelectric materials // Appl. Phys. Let. 2008. Vol. 92. 101910. P. 1–3. DOI: https://doi.org/10.1063/1.2896310
9. *Bulat L. P., Pshenai-Severin D. A.* Effect of tunnelling on the thermoelectric figure of merit of the bulk nanostructured materials // Physics of the Solid State. 2010. Vol. 52. P. 452–458.
10. *Bulat L. P., Drabkin I. A., Karatayev V. V., Osvenskiy V. B., Parkhomenko Yu. N., Pshenai-Severin D. A., Pivovarov G. I., Tabachkova N. Yu.* Energy filtration of current carriers in nanostructured material based on bismuth telluride // Physics of the Solid State. 2011. Vol. 53. P. 29–34.
11. *Snarskii A. A., Sarychev A. K., Bezsudnov I. V., Lagarkov A. N.* Thermoelectric figure of merit of the bulk nanostructured composites with distributed parameters. Semiconductors. 2012. Vol. 46. P. 677–683.
12. *Landau L. D., Lifshits E. M.* Quantum mechanics. Moscow: Nauka, 1974. 752 p. (in Russian)
13. *Goltsman B. M., Kudinov V. A., Smirnov I. A.* Semiconductor thermoelectric materials based on Bi_2Te_3. Moscow: Nauka, 1972. 320 p. (in Russian)
14. *Anatychuk L. I.* Thermoelements and thermoelectric devices. Handbook. Kyiv: Naukova dumka, 1979. 768 p. (in Russian)
15. *Gorskyi P. V., Mikhalchenko V. P.* Electric conductivity of contacting particles of thermoelectric material // J. Thermoelectricity. 2013. No 2. P. 12–18.
16. *Stilbance L. S., Terekhov A. D., Sher E. M.* Some issues of transport phenomena in heterogeneous system. In: Thermoelectric materials and films. Proceedings of All-Union Meeting on deformation and size effects in thermoelectric materials and films, technology and application of films, Leningrad, USSR, 1976. P. 199.

Chapter 4

THE EFFECT OF NANOSTRUCTURING ON THE CORROSION RESISTANCE OF AMORPHOUS ALLOYS

O. M. Hertsyk[1], T. G. Hula[1], M. O. Kovbuz[1], O. A. Yezerska[2], and N. L. Pandiak[3]

[1]*Ivan Franko National University of Lviv, 79005 Lviv, Ukraine*

[2]*Fraunhofer Institute for Manufacturing Technology and Advanced Materials, 28359 Bremen, Germany*

[3]*Ukrainian National Forestry University, 79057 Lviv, Ukraine*

Corresponding author: oksana.hertsyk@lnu.edu.ua

Contents

Abstract

The effect of nanostructuring on the corrosion resistance of Fe-based amorphous alloys in a 0.5 M NaCl aqueous solution has been studied using various physicochemical methods (diffractometry, potentiometry, voltammetry, electrochemical impedance spectroscopy).

It has been established that temperature modification of amorphous alloys $Fe_{80}Si_6B_{14}$, $Fe_{78.5}Ni_{1.0}Mo_{0.5}Si_{6.0}B_{14.0}$, $Fe_{73.1}Cu_{1.0}Nb_{3.0}Si_{15.5}B_{7.4}$ at 373 and 473 K does not cause any changes in the structure of amorphous alloys, and the surface of the samples is further oxidized with the temperature rise. High-temperature modification at T = 673 K causes nanocrystallization of the samples, with the development of Fe_3B crystals that are 20–30 nm in size in the amorphous phase. As a result, the surface of the alloy is activated and corrosion currents increase. More significant changes can be observed for the $Fe_{80}Si_6B_{14}$ amorphous alloy.

4.1 Introduction

Structural changes occur in Fe-based amorphous alloys (AMA) under the effect of high temperatures, leading to changes in the physical and chemical properties of such materials [1–5]. Therefore, it is important to predict the properties of alloys after their application at high temperatures [6–13]. The creation of such materials is based on two important requirements: first, the availability of raw materials and the complexity of their production, and second, the duration of use of target products without loss of operational requirements. In many cases, the limited use of new polymer or metal-based materials directly depends on their corrosion resistance.

It can be considered that corrosion is the greatest threat to structural and functional materials (sensor, biomultisensor technologies, electronic devices, analytical tools, information systems, and catalytic heterogeneous chemical processes [10–13]. Considerable attention paid recently to heat treatment of alloys with an amorphous structure is related to the possibility of acquiring special physicochemical properties in the nanocrystalline state, while the initial metastable amorphous state obtained through ultra-rapid hardening does not always yield optimal characteristics. Heating of amorphous samples causes volumetric and structural changes, differences in the composition of the near-surface layer and, therefore, affects important physicochemical properties. Understanding of the processes occurring during this process is important for predicting new characteristics and possible future application of alloys.

It is also important to study the corrosion resistance of such nanocrystallized amorphous alloys in various aggressive environments, in particular, the reference 0.5 M aqueous solution of sodium chloride.

4.2 Experimental

AMA ribbons $Fe_{800}Si_{6.0}B_{14.0}$, $Fe_{78.5}Ni_{1.0}Mo_{0.5}Si_{6.0}B_{14.0}$, $Fe_{73.1}Cu_{1.0}Nb_{3.0}Si_{15.5}B_{7.4}$, and $Fe_{51.7}Ni_{21.7}Cr_{6.2}Mo_{0.6}V_{1.5}Si_{5.2}B_{13.1}$ ($20 \cdot 10^{-6}$ m) thick, were obtained using the method of ultra-rapid cooling of the melt in a helium atmosphere (H.V. Kurdiumov Institute of Metal Physics of the National Academy of Sciences of Ukraine). Contact (*c*) and external (*e*) surfaces of AMA ribbons can be differentiated by the technology of obtaining them.

X-ray structural studies of alloy samples designed for a wide range of high-precision and rapid structural studies were carried out using the DRON-3 X-ray diffractometer.

The methods of potentiometry, voltammetry and electrochemical impedance spectroscopy (EIS) were used to assess the corrosion resistance of amorphous metal alloys. Electrochemical studies of AMA were carried out using the Jaissle Potentiostat-Galvanostat IMP 88PC-R device according to a three-electrode scheme: reference electrode – saturated silver chloride, working electrode – AMA sample (1 cm^2), auxiliary – platinum plate (2 cm^2). Corrosion potentials and currents were determined on the basis of the corresponding voltammograms. The studies were performed using the EIS method, with the Gamry Potentiostat Reference 600 device, and further processing was performed in the respective Gamry Echem Analyst computer program. To calculate the impedance components, a circuit consisting of two resistors and a capacitor ($R_1(C_{dl}R_2)$) was used, where R_1 is the electrolyte resistance, R_2 is the charge transfer resistance, and C_{dl} is the constant phase element characterizing the capacity of the electric double layer.

Amorphous metal alloys $Fe_{78.5}Ni_{1.0}Mo_{0.5}Si_{6.0}B_{14.0}$ and $Fe_{73.1}Cu_{1.0}Nb_{3.0}Si_{15.5}B_{7.4}$ in their initial state show amorphous structure (Fig. 4.1). The given diffractograms show halos in the area of the angles 2θ = (45–50)° and (85–90)°, this pointing to the amorphous state of the original studied samples.

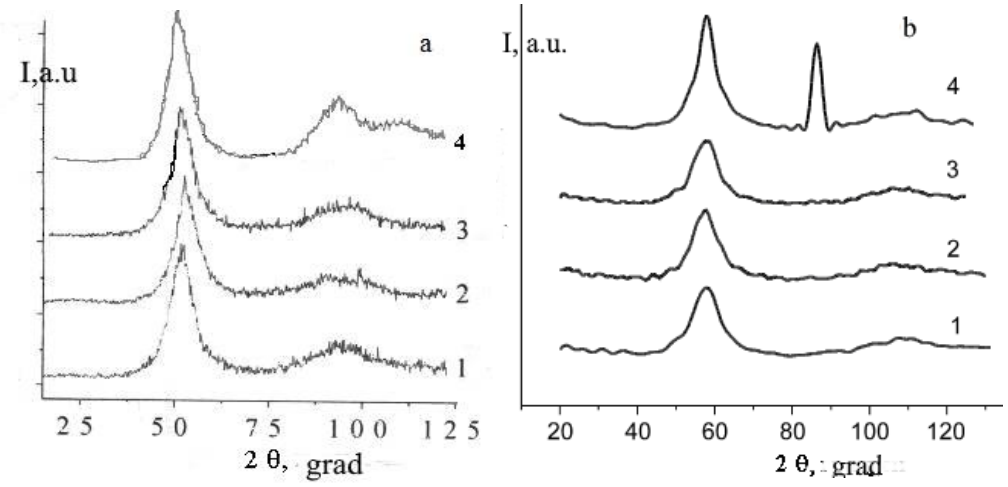

Figure 4.1 Diffractograms of the original (*a*) samples of amorphous metal alloys: *1* – $Fe_{80.0}Si_{6.0}B_{14.0}$; *2* – $Fe_{78.5}Ni_{1.0}Mo_{0.5}Si_{6.0}B_{14.0}$; $Fe_{73.1}Cu_{1.0}Nb_{3.0}Si_{15.5}B_{7.4}$; *4* – $Fe_{51.7}Ni_{21.7}Cr_{6.2}Mo_{0.6}V_{1.5}Si_{5.2}B_{13.1}$ and AMA $Fe_{78.5}Ni_{1.0}Mo_{0.5}Si_{6.0}B_{14.0}$ (*b*) of the original (*1*) and at processing temperatures 473 (*2*), 673 (*3*), and 773 K (*4*).

Table 4.1 Structural characteristics of AMA $Fe_{78.5}Ni_{1.0}Mo_{0.5}Si_{6.0}B_{14.0}$ subjected to heat treatment

T, K	s_1, nm^{-1}	r_1, nm	$a(s_1)$
293	30.6	0.253	3.14
373	30.5	0.256	3.29
473	31.0	0.254	2.98
573	30.8	0.255	3.15
673	30.6	0.257	3.16

When the temperature rises in Fe-based amorphous alloys, crystallization occurs in two phases. However, the kinetics of the process significantly depends on the heating pace and the temperature interval. In addition to crystallization, at higher temperatures the Fe_3B phase decomposes into Fe_2B and the α-Fe phases [1, 4].

If an amorphous Fe-based alloy is subjected to high-temperature heating, the diffractograms show a tendency to partial crystallization at the heating temperature increase. This is evidenced by the appearance of a diffractometric curve peak corresponding to the α-Fe nanocrystalline phase.

Within the temperature range (293–473) K, microregions with topological short-range order of α-Fe type develop in ribbon amorphous alloys $Fe_{78.5}Ni_{1.0}Mo_{0.5}Si_{6.0}B_{14.0}$ and $Fe_{73.1}Cu_{1.0}Nb_{3.0}Si_{15.5}B_{7.4}$ (Table 4.1). Such structural changes will predetermine corrosion resistance of alloys in 0.5 M NaCl aqueous solution [8–11]. The effect of temperature modification on the physicochemical properties of AMA samples $Fe_{78.5}Ni_{1.0}Mo_{0.5}Si_{6.0}B_{14.0}$ and $Fe_{73.1}Cu_{1.0}Nb_{3.0}Si_{15.5}B_{7.4}$ that have a wide range of applications in extreme conditions is important [9, 10].

The effect of preliminary one-hour heat treatment at 373 K and 473 K on the electrochemical corrosion parameters of Fe-based amorphous alloys in 0.5 M NaCl aqueous solution is ambiguous (Table 4.2). As a result of changing preliminary treatment temperature of AMA $Fe_{73.1}Cu_{1.0}Nb_{3.0}Si_{15.5}B_{7.4}$ to 473 K, the values of the potential become more positive. This indicates that resistance to dissolution of the surface of the alloy ribbon increases. We observe the opposite effect for the $Fe_{78.5}Ni_{1.0}Mo_{0.5}Si_{6.0}B_{14.0}$ alloy, i.e. reduction of resistance to dissolution of this alloy. This is accounted for by availability of defects in the protective oxide coating. This is facilitated by the volatility of Mo oxides.

Cu and Nb additives in the alloy cause accelerated stabilization of surface redox processes after heat treatment at 473 K. This is caused by active nanocrystallization and high ability of copper to oxidize, which ensures development of dense protective layers. Therefore, AMA $Fe_{73.1}Cu_{1.0}Nb_{3.0}Si_{15.5}B_{7.4}$ corrodes more slowly in 0.5 M NaCl aqueous solution even after heat treatment.

In aggressive aqueous solutions the surface of AMA is easily covered with oxide-hydroxide layers that resist active surface dissolution. Such film is characterized both by electronic and ionic conductivity. The method of electrochemical impedance spectroscopy makes it possible to measure the resistance created by similar oxide coatings to water mole-

Table 4.2 Chronopotentiometric assessment of oxidation of AMA electrodes in 0.5 M NaCl aqueous solution after one-hour heat treatment. $E = E_s \pm 0.02$ V

AMA	T, K	Surface	$-E_0$, V	$-E_{20}$, V	$\lvert \Delta E \rvert$, V	$\upsilon_{60} \cdot 10^4$, V/s
$Fe_{78.5}Ni_{1.0}Mo_{0.5}Si_{6.0}B_{14.0}$	293	*c*	0.52	0.62	0.10	9.00
		e	0.50	0.66	0.16	8.67
	373	*c*	0.46	0.63	0.17	8.83
		e	0.52	0.72	0.20	9.50
	473	*c*	0.49	0.68	0.19	9.50
		e	0.45	0.73	0.28	9.00
$Fe_{73.1}Cu_{1.0}Nb_{3.0}Si_{15.5}B_{7.4}$	293	*c*	0.43	0.44	0.01	7.17
		e	0.33	0.42	0.09	6.83
	373	*c*	0.41	0.48	0.07	7.17
		e	0.42	0.48	0.06	7.50
	473	*c*	0.24	0.36	0.12	4.50
		e	0.21	0.35	0.14	4.00

cule, oxygen and ion transportation to the metal surface. Resistance values are calculated according to the equivalent electrode scheme. The properties of oxide films on the surfaces of ribbons of alloys with different elemental compositions differ significantly. As the temperature rises, resistance of the surface layers increases due to their compaction under the heat treatment effect.

As the result of analysis of the dependences (Fig. 4.2, Tabl 4.3), it can be stated that the nature of the oxide film on both surfaces of the ribbon is highly different. Within the frequency range from $10^1 \div 10^5$ Hz, a frequency-independent section describing the electrolyte resistance is observed on the Bode curves. Within the range of frequencies from 10^{-1} to

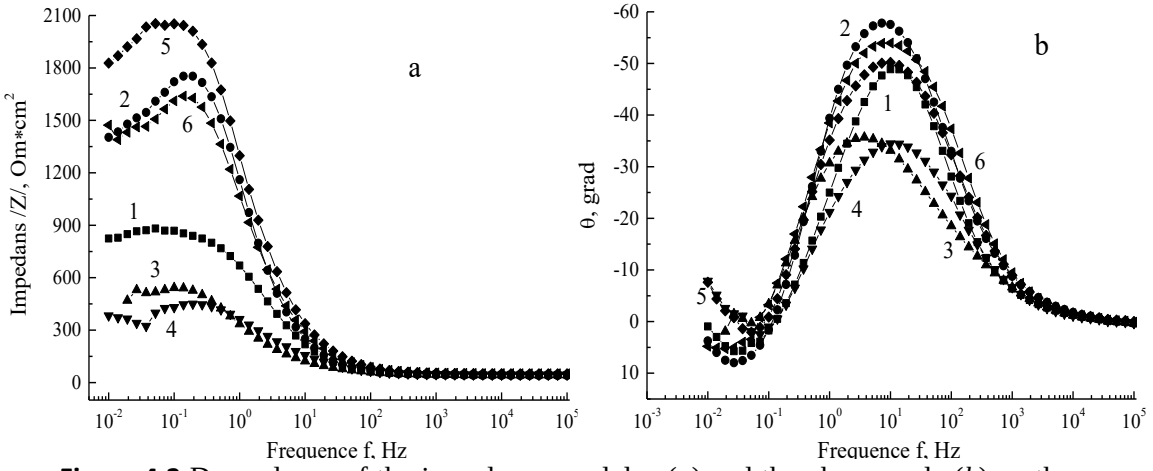

Figure 4.2 Dependence of the impedance modulus (*a*) and the phase angle (*b*) on the current frequency for the contact (*1, 3, 5*) and external (*2, 4, 6*) surfaces of $Fe_{78.5}Ni_{1.0}Mo_{0.5}Si_{6.0}B_{14.0}$ (*1, 2*) and after preliminary heat treatment at 373 K (*3, 4*) and 473 K (*5, 6*) in a 0.5 M NaCl aqueous solution.

Table 4.3 EIS parameters in 0.5 M NaCl aqueous solutions of AMA $Fe_{78.5}Ni_{1.0}Mo_{0.5}Si_{6.0}B_{14.0}$ after preliminary one-hour heat treatment

T, K	Surface	R_1, Ω	E, V	R_2, Ω	$C_{dl}\cdot10^4$, F·cm^{-2}	α	R_f
293	*c*	44.47	–0.68	834.1	1.68	0.80	0.84
	e	41.08	–0.68	1873	1.32	0.82	0.66
373	*c*	43.24	–0.68	609.7	6.74	0.64	3.37
	e	43.92	–0.66	439.8	3.83	0.69	1.92
473	*c*	50.88	–0.66	1767	1.52	0.75	0.76
	e	49.66	–0.67	2251	1.24	0.77	0.62

10^1 Hz, the impedance spectrum shows an increase in impedance – this region reflects the capacitive features of the surface layers.

Within the region of lower frequencies, if a frequency-independent section is recorded again, the sum of resistances can be observed: R_2 (film resistance) + R_1 (electrolyte resistance). Resistance (R_2) of the surface oxide film of the outer surface of AMA $Fe_{78.5}Ni_{1.0}Mo_{0.5}Si_{6.0}B_{14.0}$ is significantly higher than that of the contact side, while roughness (R_f), on the contrary, is more substantial for the contact side. Obviously, this can be accounted for by the fact that, due to the peculiarities of the AMA ribbon production technology, the contact surface, which is poured onto the copper drum, reflects its irregularities and becomes rougher. The oxide layer on such surface will also be uneven, and its protective properties may be low. As the temperature increases, resistance R_2 increases at higher temperatures, apparently due to approaching initiation of nanocrystallization centers development and probable compaction of protective layers under the heat treatment effect.

According to the results of X-ray analysis, increasing of the heating temperature to 400–600 K leads to partial crystallization of AMA (Fig. 4.1).

Samples of AMA $Fe_{80.0}Si_{6.0}B_{14.0}$ and $Fe_{78.5}Ni_{1.0}Mo_{0.5}Si_{6.0}B_{14.0}$ were structured during long-term isothermal heating (5 and 24 h) at T = 673 K (Table 4.4). It was established using energy dispersive microanalysis that in these alloys the content of the base metal (Fe) on the surface during heating decreases, and this can be accounted for by the partial release of Si onto the surface. In an alloy doped with Ni and Mo the content of Mo also drops signify-

Table 4.4 Change in the elemental composition of the AMA surface (wt. %) depending on the duration of heating at T = (673±5) K for 5 and 24 hours

τ, hour	$Fe_{80.0}Si_{6.0}B_{14.0}$			$Fe_{78.5}Ni_{1.0}Mo_{0.5}Si_{6.0}B_{14.0}$		
	Fe	Si	B	Fe	Ni	Mo
0	96.3	1.9	1.8	97.2	1.1	1.0
5	96.7	2.8	0.5	94.4	1.3	0.6
24	95.6	3.2	1.2	94.4	1.2	0.2

Table 4.5 Change in corrosion currents (μA/cm^2) of AMA in 0.5 M NaCl aqueous solution depending on the duration of heating at T = (673±5) K

τ, h	$Fe_{80,0}Si_{6,0}B_{14,0}$	$Fe_{78,5}Ni_{1,0}Mo_{0,5}Si_{6,0}B_{14,0}$
0	0.002	0.001
5	0.007	0.002
24	0.015	0.005

cantly during heat treatment, and this can be related to the volatility of molybdenum oxides, or its forced migration into the volume of the ribbon.

In the samples with no preliminary heat treatment, only single crystalline groups are found in the amorphous matrix of the alloy. After 5 hours of heating at T = (673±5) K, there appear crystals (0.2–0.5) μm in size. After heat treatment over 24 hours, crystals that are (0.5–1.0) μm in size are released. The sample doped with Ni and Mo crystallizes after 5 hours of heating with a more uniform arrangement of small particles mainly of two sizes: 0.1 and 0.4 μm. During 24 hours of heating, crystals thicken, and needle-like crystals appear next to cubic ones. Obviously, Ni and Mo addivites significantly affect amorphous alloy crystallization.

The dependence of the corrosion currents of AMA $Fe_{80.0}Si_{6.0}B_{14.0}$ and $Fe_{78.5}Ni_{1.0}Mo_{0.5}Si_{6.0}B_{14.0}$ on the duration of isothermal annealing at T=673 K was investigated (Table 4.5). Both alloys without preliminary heat treatment are quite inert in the aggressive environment of sodium chloride. However, preliminary annealing at T = 673 K for 5 and 24 hours activates dissolution of AMA electrodes. More significant changes in the corrosion current after annealing were recorded for the undoped alloy $Fe_{80.0}Si_{6.0}B_{14.0}$.

Dissolution of the $Fe_{80.0}Si_{6.0}B_{14.0}$ alloy takes place with the accumulation of a sufficient number of Fe^{2+} ions in the near-electrode layer (reaction (4.1)), since they catalyze the one-electron oxidation process of Fe^0 on the surface of the AMA electrode to Fe^+ ions (reaction (4.2)), which exist on the surface of AMA electrodes only in the adsorbed condition [13].

$$\left.\begin{aligned} Fe_{AMA} + H_2O \leftrightarrow Fe(OH)_{ads} + H^+ + \bar{e}\,; \\ Fe(OH)_{ads} \rightarrow FeOH^+_{ads} + \bar{e}\,; \\ FeOH^+_{ads} + H^+ \leftrightarrow Fe^{2+} + H_2O; \end{aligned}\right\} \quad 2\bar{e} \qquad (4.1)$$

$$Fe^{2+} + Fe^0 \leftrightarrow 2Fe^+_{ads}. \qquad (4.2)$$

A sharp increase in currents is manifested in case of interaction of Fe^{1+} and Fe^{2+} with the aqueous solution in the presence of Cl^- ions, reaction (3).

$$\left.\begin{aligned} Fe(OH)_{ads} + H_2O \leftrightarrow [Fe^{2+}(OH)_2]_{ads} + H^+ + \bar{e}\,; \\ [Fe(OH)_2]_{ads} + Cl^- \rightarrow [Fe(OH)_2Cl]_{ads} + \bar{e}\,; \\ [Fe(OH)_2]_{ads} + H_2O \leftrightarrow [Fe(OH)_3]_{ads} + H^+ + \bar{e}\,. \end{aligned}\right\} \quad 3\bar{e} \qquad (4.3)$$

As a result of surface transformations (4), which are caused by the looseness of the protective hydroxide film $[Fe(OH)_3]_{ads}$, Fe compounds with a higher degree of oxidation appear:

$$Fe_{AMA}[Fe(OH)_3]_{ads} + Cl^- + 2H_2O \leftrightarrow Fe(OH)_{3\,ads} + Fe(OH)_2Cl_{ads} + 2H^+ + 3\bar{e} \quad (4.4)$$

Hardly soluble $Fe(OH)_{3ads}$ hydroxide inhibits ion exchange at the AMA electrode – solution intersection. All these processes are characterized by a high degree of equilibrium.

Table 4.4 shows a significant difference in AMA dissolution before and after heat treatment. It is possible that the ionization of the AMA sample $Fe_{78.5}Ni_{1.0}Mo_{0.5}Si_{6.0}B_{14.0}$ occurs according to the following mechanism [13]:

$$Me(Fe)_n + H_2O = Me(OH)_{ads} + H^+ + n(Fe^*) + \bar{e}\,; \quad (4.5)$$

$$n(Fe^*) = n(Fe^{2+}) + 2n\bar{e}\,. \quad (4.6)$$

Annealing of AMA $Fe_{78.5}Ni_{1.0}Mo_{0.5}Si_{6.0}B_{14.0}$ leads to a decrease in the concentration of doping additives on the surface (Table 4.3) due to the volatility of MoO_3 oxides or diffusion of individual atoms into the volume of the sample, hence currents with an increased amplitude of oscillations are restored. Dissolution of the electrodes occurs according to Equations (4.1)–(4.4).

Different duration of heating (0–24 hours) of amorphous metal alloys $Fe_{80.0}Si_{6.0}B_{14.0}$ and $Fe_{78.5}Ni_{1.0}Mo_{0.5}Si_{6.0}B_{14.0}$ at T = (673±5) K causes an incremental increase in the crystallinity of the studied samples, this leading to a nonlinear change in corrosion currents.

Conclusions

In order to expand the use and preserve the unique physicochemical properties of Fe-based amorphous alloys, their preliminary temperature (T=373 K and 473 K) modification has been carried out for the first time and its effect on physicochemical characteristics, in particular corrosion resistance, has been investigated.

Temperature modification of amorphous alloys $Fe_{78.5}Ni_{1.0}Mo_{0.5}Si_{6.0}B_{14.0}$ and $Fe_{73.1}Cu_{1.0}Nb_{3.0}Si_{15.5}B_{7.4}$ at temperatures of 373 K and 473 K does not cause changes in the structure of the amorphous alloy, the surface of the samples oxidizes when temperature increases. High-temperature modification at T = 673 K causes nanocrystallization of the samples along with development of Fe_3B crystals that are 20–30 nm in size in the amorphous phase, and, as a result of this, the surface of the alloy is activated.

Key words

- amorphous alloy
- temperature modification
- nanocrystallization
- electrochemical parameters

References

1. *Boichyshyn L. M., Hertsyk O. M., Kovbuz M. O*. Thermal modification of amorphous metal alloys: nanostructuring and properties. Mississauga, Ontario: Nova Printing Inc. 2019. 138 p.
2. *Davies H., Gibbs M.* Amorphous Alloys. Handbook of Magnetism and Advanced Materials. London: John Wiley & Sons, 2007. 1801 p.
3. *Kulik T.* Nanocrystallization of metallic glasses // J. Non-Crystal. Sol. 2001. Vol. 287. P. 145–161. DOI: https://doi.org/10.1016/S0022-3093(01)00627-5
4. *Jakubczyk E., Krajczyk L., Siemion P., Jakubczyk M.* Crystallization kinetics of $Fe_{78}Si_9B_{13}$ metallic glass // Opt. Appl. 2007. Vol. XXXVII (4). P. 359–370.
5. *Ohnuma M., Ping D.H., Abe T. et al.* Optimization of the microstructure and properties of Co-substituted Fe–Si–B–Nb–Cu nanocrystalline soft magnetic alloys // J. Appl. Phys. 2003. Vol. 93 (11). P. 9186–9194. DOI: https://doi.org/10.1063/1.1569396
6. *Ponpandian N., Narayanasamy A., Chattopadhyay K. et al.* Low-temperature magnetic properties and the crystallization behaviorof FINEMET alloy // J. Appl. Phys. 2003. Vol. 93 (10). P. 6182–6187. DOI: https://doi.org/10.1063/1.1565829
7. *Cheng Y.Q., Ma E.* Atomic-level structure and structure-property relationship in metallic glasses // Progr. in Mater. Sci. 2011. Vol. 56. P. 379–473. DOI: https://doi.org/10.1016/j.pmatsci.2010.12.002
8. *Hennayaka H. M. M. N., Lee H. S., Yi S.* Surface oxidation of the Fe based amorphous ribbon annealed at temperatures below the glass transition temperature. J. Alloys Compd. 2015. Vol. 618. P. 269–279. DOI: https://doi.org/10.1016/j.jallcom.2014.08.160
9. *Seruga M., Hasenay D.* Electochemical and surface properties of nanocrystalline alloys // J. Appl. Electrochem. 2001. Vol. 31. P. 961–967. DOI: https://doi.org/10.1016/S1003-6326(15)64017-1
10. *Hertsyk O. M., Kovbuz M. O., Boichyshyn L. M., et al.* Corrosion Resistance of Modified Amorphous Alloys Based on Iron in Sulfuric Acid // Mat. Sci. 2021. Vol. 56. P. 755-763. DOI: https://doi.org/10.1007/s11003-021-00492-8
11. *Mariano N., Souza C., May J., Kuri S.* Influence of Nb content on the corrosion resistance and saturation magnetic density of FeCuNbSiB alloys // Mat. Sci. and Eng. 2002. Vol. 90. P. 1–6. DOI: https://doi.org/10.1016/S0921-5093(02)00032-1
12. *Hertsyk O. M., Hula T. H., Kovbuz M. O., Pandiak N. L.* Electrochemical characteristics of modified amorphous alloys in nitric acid // Metallofiz. Noveishie Tekhnol. 2021. Vol. 43 (4). P. 455–464. DOI: https://doi.org/10.15407/mfint.43.04.0455
13. *Li Liu, Ying Li, Fuhui Wahg.* Electrochemical Corrosion Behaviour of Nanostructured Materials // J. Mater. Sci. Technol. 2010. Vol. 26 (1). P. 1–14.

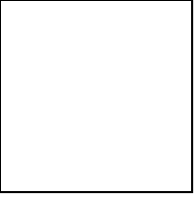

Chapter 5

EFFECT OF NANOCRYSTALLIZATION ON CORROSION RESISTANCE AND ELECTROCATALYTIC PROPERTIES IN HYDROGEN EVOLUTION REACTION OF Al-Ni-REE (REE ≡ Y, Gd) AMORPHOUS METAL ALLOYS

Kh. I. Khrushchyk, L. M. Boichyshyn, O. V. Reshetnyak

Ivan Franko National University of Lviv, 79005 Lviv, Ukraine

Corresponding author: khrushchyk.chem@gmail.com

Contents

Abstract

Amorphous metallic alloys (AMAs) are generally known to have greater corrosion resistance than their crystalline counterparts with similar elemental compositions because they do not have grain boundaries or crystal defects that can act as corrosion initiation sites. Al-based nanocrystalline alloys are often exposed to humid industrial or marine atmospheres containing chlorine ions. In such environments, the corrosion resistance of nanocrystalline ferromagnetic materials, as a rule, depends on their microstructure and phase composition. Therefore, the authors showed schemes of reactions Al-alloys occurring in environments of different protogenicity. The method of differential scanning calorimetry (DSC) showed that the process of crystallization of AMA takes place in three stages. At the first stage (under temperature T_1) AMA nanostructuring takes place. Aluminum nanocrystals in an amorphous matrix were recorded using high-resolution transmission microscopy. The corrosion resistance of AMA in 1 M KOH was investigated by cyclic voltammetry. The ratio of the oxidation rate to the reduction rate (b_{ox}/b_{red}), the width of the passivation interval (ΔE) and the density of the passivation currents (i_{pass}) of the AMC surface were determined. It is shown that nanostructuring and the combined presence of yttrium and gadolinium leads to an increase in the corrosion resistance of AMA in an alkaline environment.

5.1 Introduction

5.1.1 The Effect of Thermal Modification on the Amorphous Structure and Properties of Amorphous Alloys

The heat treatment of AMAs leads to modification of electrical, mechanical, corrosion and other properties of alloys (Fig. 5.1). For example, the authors of the article [1] found that the amorphous $Al_{84}Cu_6Co_2Y_6La_2$ alloy shows the highest hardness of 378.1 ± 15.3 HV. The hardness enhances to 394.2 ± 16.8 HV after primary crystallization at 640 K due to formation of nano-sized α-Al crystals. The hardness decreases to 340.3 ± 16.4 HV after the second crystallization stage possibly as the results of the presence of some weak intermetallic compound, growth of the α-Al and crystallization of the amorphous matrix.

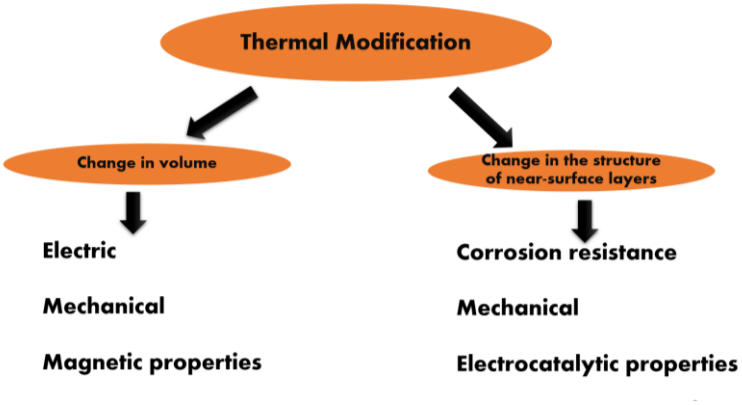

Figure 5.1 Scheme of changes in the properties of AMA as a result of thermal modification

Such differences is determined by changes of structure of AMAs, exactly by formation of nanocrystals in the initial amorphous matrix.

The authors of the article [2], based on the kinetic models of Kissinger, Ozawa and Augis-Bennett, calculated the activation energy (E_a) of the growth of nanocrystals due to heat treatment of Al-based AMAs doped by rare-earth elements (REE). Using the calculated values of E_a, it is possible to predict the mechanism of nanostructuring. $Al_{87}Y_5Ni_8$ was chosen as the base alloy. As a result of heating to temperature T_1 (Fig. 5.2), atoms diffuse in the amorphous matrix with the nucleation of nanocrystallization centers. Replacing Y with Gd leads to an increase in the energy barrier for nucleation of centers from only aluminum atoms. Because the electronic structure of Gd facilitates the facilitated interaction of atoms.

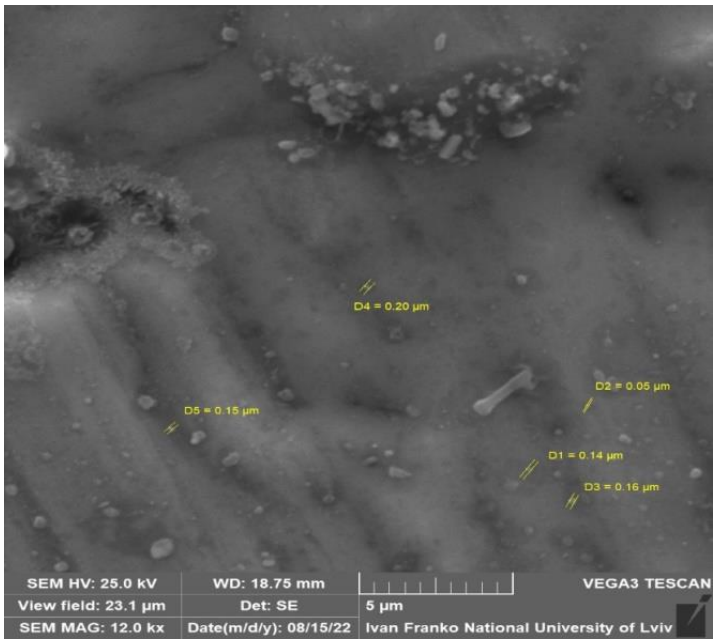

Figure 5.2 SEM morphology of $Al_{87}Gd_5Ni_8$ after annealed in air under T = 611 K for 15 min

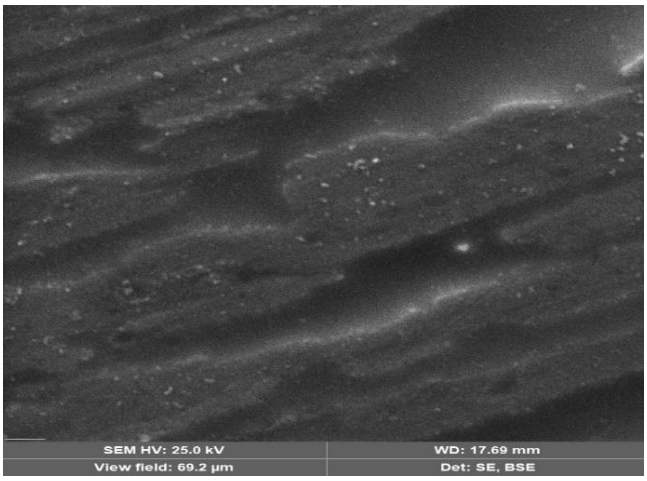

Figure 5.3 SEM image of morphologies of $Al_{87}Gd_5Ni_8$ alloy after annealed at T = 645 °C

That is, as electrons move away from the Gd nucleus, its reactivity increases. Therefore, at the stage of nucleation and growth of nanocrystals, the prevailing processes will be kinetic, that is, interaction processes that are more energy-intensive. During the third stage, a low-energy process of aggregation of nanoparticles occurs.

The authors [3] established that the $Al_{87}Y_4Gd_1Ni_4Fe_4$ and $Al_{87}Gd_5Ni_4Fe_4$ amorphous alloys crystallize in three stages. Short-term annealing leads to the formation of nanocrystals of *fcc*-Al with a size of 12–18 nm. Annealing for 45–60 min leads to the formation of nanocrystals of *fcc*-Al(REE) solid solution with a size of 32–47 nm.

The results of SEM studies indicate that in addition to the volumetric strengthening of AMA due to the formation of nanocrystals, the surface layers are transformed. They are compacted and thus strengthen the surface, that leads to the increases of the mechanical properties of $Al_{87}Gd_5Ni_4Fe_4$ and $Al_{87}Y_4Gd_1Ni_4Fe_4$ AMAs in 1.5 times after short-time annealing. In particular, the microhardness of $Al_{87}Y_4Gd_1Ni_4Fe_4$ owing to 5 minutes annealing increases from 3.1±0.04 to 5.22±0.5 GPa, but after 15–60 minutes of annealing microhardness does not change significantly.

The authors of [4] suggest that the alloy structure determines also its oxidation resistance strength, and thereby influences its surface morphology. Besides, low-temperature crystallization also can cause the composition variation of surface that also change the further oxidation behaviors of AMAs [4].

5.1.2 Formation of Oxide Films on the Surface of Aluminum Alloys

The peculiarities of the structure of amorphous metal alloys lead to many unique properties, including abnormally high corrosion resistance in aggressive environments, which is associated with the surface structure and the structure of the electric double layer at the boundary of the phase separation [5, 6]. Chemical properties, in particular corrosion resis-

tance, depend on the chemical composition of the material, i.e. on the nature of the base metal, as well as the nature of alloying applications of the amorphous alloy.

Moreover, AMAs belong to self-protected alloys, they can be self-passivated both in atmospheric conditions and in aggressive environments. The reasons for such high corrosion resistance are the chemical homogeneity of the alloy, the absence of defects such as non-metallic inclusions, vacancies, dislocations on its surface, as well as the high chemical activity of amorphous alloys, which leads to the rapid formation of a protective film.

Passivation of metals in aggressive environments occurs mainly due to the active dissolution of the metal in the initial period of time. AMA ionization precedes the formation of a passive film by deposition. The corrosion resistance of AMA is a consequence of the high rate of passive film formation. In general, the corrosion resistance of almost all metallic materials depends on the composition, stability and defect-freeness of the surface film. If a given metal is characterized by the rapid formation of a stable passivating film with a high content of useful elements, then the corrosion resistance will depend on the uniformity of this film.

In this regard, the homogeneous structure of amorphous alloys contributes to the formation of a continuous protective film and, obviously, is an important condition for their high corrosion resistance. Amorphous alloys Al–REE have high corrosion resistance. The mechanisms of improving anti-corrosion properties are related to the amorphous structure [7, 8]. Alloying additives can increase resistance to local corrosion due to the formation of a passive film with better protective characteristics, which change the kinetics of surface dissolution and also reduce the ability to form pitting [9, 10].

The amorphous structure of alloys excludes grain boundaries and particles of the secondary phase which are places of initiation of pitting, while REE can improve resistance to local corrosion by enriching the passive film, changing the kinetics of pitting dissolution, or contributing to the formation of insoluble compounds that destabilize pitting growth. For example, the corrosion current for amorphous $Al_{90}Fe_3Ce_7$ is significantly lower than for crystalline analogue [11]. The pitting potentials for amorphous alloys are more positive than for pure aluminum or crystalline samples of AMAS, which indicates on their higher resistant to pitting [12].

The growth of anodic oxide films on aluminum alloys is a very complex process and includes the localization and interaction of processes occurring over the microscopically inhomogeneous surface of the alloy. Corrosion of aluminum and its alloys is determined by composition, structure and morphology of oxide film that almost always covers them in a corrosive environment [13–14]. Cases of low corrosion resistance are often associated with the charge of the oxide film and, especially, with the degree of its hydration and porosity. High corrosion resistance, on the one hand, and chemical activity in redox processes, on the other, makes it possible to use amorphous metal alloys as catalysts in heterogeneous catalysis [13].

Alloying elements introduced to improve mechanical strength and corrosion resistance Al-based AMA or to provide the desired shade of its surface after treatment, such as anodizing, are present in the form of zones, allocations or intermetallic compounds of various shapes, sizes and compositions [10, 15]. Such uneven distribution of elements over the

entire base of the matrix does not contribute to increased corrosion resistance of AMAs. In addition, the durability of alloys in environments with different acidity is determined by the inclusion zones of intermetallic compounds of various shapes, sizes and compositions [15]. Such, a study of the ultramicroatomic section of an anodized alloy sample revealed local features associated with Al_3Ni intermetallic particles on the alloy surface [16]. During anodic oxidation, Al_3Ni particles dissolve with formation of cavities of various shapes on the surface of the alloy. The presence of cavities clearly shows that such an interface effectively acts as an oxygen generator for internal mobile oxygen ions. Due to the formation of cavities containing gaseous oxygen, the barrier layer of the porous aluminum oxide film and the intermetallic phase are locally separated. Under large anodic overvoltage the intermetallic particle dissolved with a significant rate, accompanied by the release of oxygen. Gaseous oxygen escapes from the cavity through cracks on the surface and, in turn, the electrolyte flows into the cavity, which allows it to directly contact the intermetallic particle.

In general, epy dissolution of Al_3Ni intermetallic particles is a very complex process, which occurs through the formation of a very thin, non-uniform discontinuous oxide film over the residual surface of the Al_3Ni particle, through which Ni^{2+} ions diffuse. The behavior of the Al-0.5% Ni alloy during anodization is an excellent example when the highly localized behavior of intermetallic particles plays an important role in the development of a porous anodic film on the surface of the alloy [16].

5.1.3 Corrosion Resistance of Al and Al-based Alloys

Hydrated aluminum oxide $Al_2O_3 \cdot nH_2O$ or aluminum hydroxide $Al(OH)_3$ forms a diffuse barrier layer on the surface of aluminum which prevents the penetration of oxygen and electrolyte to the metal surface. The homogeneous structure of the surface of amorphous alloys contributes to the formation of a continuous defect-free protective film and, thereby, causes their high chemical resistance [17]. Corrosion resistance is mainly determined by the chemical composition of the amorphous alloy. At the same time it should be taken into account that chemical composition on different surfaces (contact and external sides of sample) differs. In addition, it can change somewhat with time, even without external influence.

Aluminum and its alloys are prone to pitting corrosion. This process takes place when the conditions of differential aeration corrosion are realize, also if the traces of Cu^{2+} ions (even in the amount of 0.1 mg/l) or Fe^{3+} are present in the water. The electrochemical theory of corrosion explains this effect by the generation of a whole network of short-circuited galvanic elements on the surface of a metal or alloy. Presence of Cl^- ions in the solltion accelerates the corosion process. Therefore, given the prevalence of chloride-containing media, the testing of the corrosion resistance of the samples made of aluminium or its alloys in aqueous solutions of NaCl is carried out necessarily.

The first stage of the aluminium local dissolution (pitting) is the adsorption of chlorine ions on the oxide-covered surface [18–21]. The result of the hydrolysis of oxide film on aluminum in neutral solutions is acquisition of positive surface charge, that predetermine adsorption of Cl^- ions and accelerate their further transport to the aluminium surface

through oxygen vacancies or water channels [18]. This leads to the active corrosion of metal occurs with the release of various products, some of which can activate the oxidation process. Ions Cl^- penetrate into the oxide film through pores or defects more easily than other ions (for example, SO_4^{2-}). They can also disperse the oxide film and increase its permeability [12]. As a result, process of metal oxidation proceeds with the rate at which oxygen reaches the metal surface [8].

Aluminum corrodes much more intensively in acids and alkalis than in neutral medium, and the rate of corrosion in acids depends on the nature of the anion. At room temperature, the corrosion rate is minimal in the range of pH = 4...8.5. In an alkaline solutions, the corrosion rate of aluminum and its alloys increases rapidly with increasing pH, unlike iron and steel, which are corrosion resistant in such medium. In a sufficiently alkaline environment, aluminum corrodes with formation of aluminate ions AlO_2^- [22]. A large number of works are devoted to the study of corrosion processes that occur during the interaction of aluminum and its alloys with aqueous alkaline solutions [23–24]. In most of them, the corrosion mechanism of aluminum alloys in alkaline media is interpreted as electrochemical [25].

5.1.4 Hydrogen Evolution Reaction on the Metallic Electrodes

Amorphous and nanocrystalline metal alloys are promising electrode materials for hydrogen evolution reactions (HER) from alkaline aqueous solutions, because they have increased resistance to corrosion and sufficiently good electrocatalytic activity [26]. The main stages of the HER process in the case of an alkaline medium is as follows [27–33]:

1) electroreduction of water molecules with the formation of atomic hydrogen:

$$M + H_2O + e^- = MH_{ads} + OH^- \text{ (Volmer reaction)}, \quad (5.33)$$

where M is the electrode material; MHads - atomic hydrogen adsorbed on the active site of the electrode surface;

2) electroreduction of water molecules on hydrogen-adsorption sites with the release of molecular hydrogen (Heyrovsky reaction / electrochemical desorption of hydrogen):

$$MH_{ads} + H_2O + e^- = M + H_2\uparrow + OH^-; \quad (5.34)$$

3) chemical desorption of hydrogen (Tafel reaction):

$$2MH_{ads} = 2M + H_2\uparrow, \quad (5.35)$$

The same processes for an acidic medium look like this:

$$M + H^+ + e^- \leftrightarrow MH_{ads} \text{ (Volmer reaction)}; \quad (5.36)$$

$$MH_{ads} + H^+ + e^- \leftrightarrow H_2\uparrow + M \text{ (Heyrovsky reaction)}; \quad (5.37)$$

$$MH_{ads} + MH_{ads} \leftrightarrow H_2\uparrow + 2M \text{ (Tafel reaction)}. \quad (5.38)$$

Depending on the conditions of electrolysis and the nature of the electrode, two HER mechanisms can be realized, namely Volmer–Tafel (combination of reactions (5.1) and (5.2), or (5.4) and (5.5)) and Volmer–Heyrovsky (combination of reactions (5.1) and (5.3)

or (5.4) and (5.6)). Hovewer in both mechanisms of adsorbed hydrogen atom (MH_{ads}) plays a key role, because they including the stage of formation and then the breaking of the $M–H_{ads}$ bond. Therefore, the rate of the reaction of hydrogen release is determined by the energy of atomic hydrogen adsorption on the surface of the electrode/electrocatalyst. The activity of electrocatalytic materials is usually improved by the synergistic effect of the electrocatalytic components of the alloy, or by increasing the real surface area of the electrode [27–33].

The electrocatalytic properties of a wide number of AMAs ($Co_{66}Fe_4Si_{16}B_{12}Mo_2$, $Fe_{40}Ni_{40}B_{20}$, $Fe_{67}Co_{18}B_{14}Si_1$, $Fe_{40}Ni_{40}P_{14}B_6$ i $Zr_{73.22}Ti_{19.71}Cu_{1.24}Fe_{5.83}$) were studied in [34] using various methods of their preliminary treatment: polishing, acid etching, anodic polarization. The least corrosion-resistant $Fe_{67}Co_{18}B_{14}Si_1$ alloy shown the greatest activity to HER both in the polished state and after minor preliminary surface treatment. Conversely, the most corrosion-resistant alloy $Zr_{73.22}Ti_{19.71}Cu_{1.24}Fe_{5.83}$ exhibited the lowest catalytic activity in the polished state, which improved significantly after anodic oxidation of alloy samples in an alkaline solution.

The catalytic properties of AMCs can also be improved due to their structuring. The paper [35] shows the effect of heat treatment of the $Ni_{86.2}P_{13.8}$ alloy on its electrocatalytic properties as to HER. Annealing of AMA at T = 400°C for 1 h changes the surface morphology, in particular, increases the roughness parameters, which is the primary reason for the increase in electroactivity of this alloy in the hydrogen evolution reaction compared to unannealed samples.

5.2 Corrosion Resistance of AMAs Al-Ni-REE in 1 M KOH Aqueous Solution

The use of nanostructured electrodes can lead to an increase of the rate of the HER to due a decrease of the overvoltage of hydrogen release, as well as to due an increase in the effective working surface of the electrode. However their corrosion resistance under conditions of the HER realization is rather low. In particular, in alkaline solutions, in addition to the release of hydrogen, aluminates are formed, and in acidic solutions, surface hydrides are formed. Therefore, for predicting the practical use of aluminium AMAs $Al_{87}Gd_5Ni_8$ and $Al_{87}Y_4Gd_1Ni_8$ as hydrogen release electrodes from alkaline solutions their corrosion durability (both before and after annealing) was studied in the 1 M aqueous KOH.

Studied amorphous metal alloys were synthesized in the G. V. Kurdyumov Institute for Metal Physics, National Academy of Sciences of Ukraine (Kyiv). The temperatures of the beginning of the stages of origin (T_1), growth (T_2) and stable nanocrystallization with formation of α-Al nanocrystals (T_3) during annealing of samples has been determined from the results of DSC analysis (see Fig. 5.4) under the use of NETZSCH DSC 404 calorimeter.

Heat treatment of AMAs was carried out in an oxygen atmosphere. Corrosion of AMA-electrodes has been studied by cyclic voltammetry method in 1 M KOH solution under temperature of 293 K. The working electrode was performed by a sample of AMAs

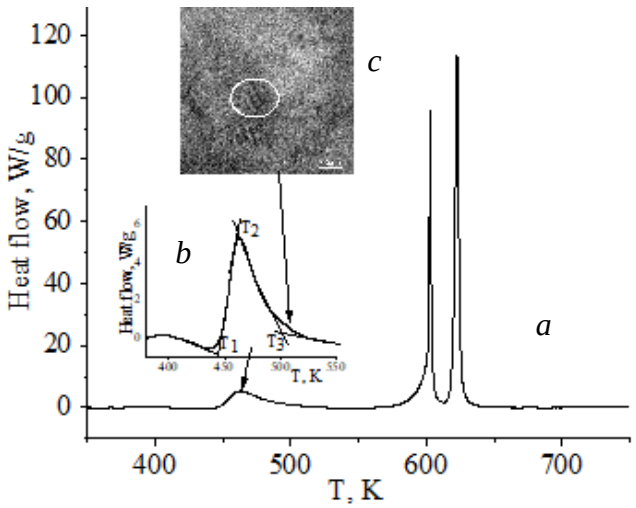

Figure 5.4 DSC curve of $Al_{87}Y_4Gd_1Ni_8$ alloy obtained at temperature scanning rate 20 K/min (*a*), scaled-up view of first DSC- maximum with denotements of characteristic temperatures (*b*) and CEM image of sample surface after 1 hour annealing at T_3 (*c*)

with an area of 0.5 cm^2, as uxiliary and reference electrodes were used platinum plate and saturated calomel electrode (SCE), respectively. The electrode potential was scanned in the (–1,2)...(+0,4) V interval with a scanning rate of 50 mV/s.

The values of E_{corr}, i_{corr}, and also coefficients of the Tafel equation (b_{ox} and b_{red}), which are directly proportional to the rate of oxidation (*ox*) and reduction (*red*) has been calculated from the recorded current-voltage curves for AMA electrodes. Results of calculations are presented (in dependence from the number of polarization cycle) on the Figures 5.5 and 5.6 and in the Table 5.1.

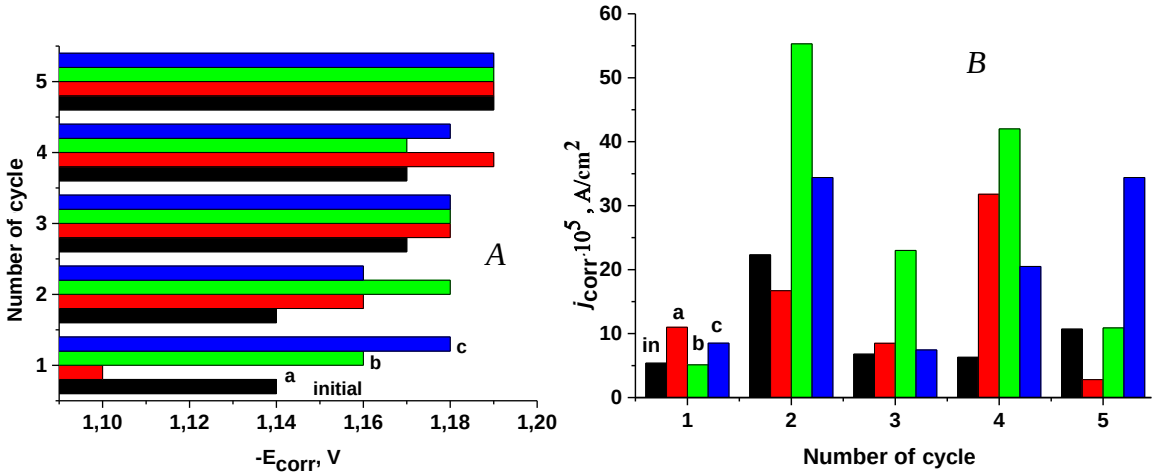

Figure 5.5 Changes of the corrosion potential (*A*) and corrosion currents (*B*) on the number of polarization cycle for $Al_{87}Gd_5Ni_8$ electrodes in 1 M KOH aqueous solution (**in**, **a**, **b**, and **c** – values for initial (unannealed) and annealed (under temperatures T_1, T_2, and T_3) samples, respectively

Table 5.1 Results of cyclic voltammetry studies of initial and annealed at different temperature (T_{ann}) AMAs in 1 M aqueous KOH solution

T_{ann}	Number of cycles	b_{ox}/b_{red}	ΔE, mV	i_{pass}, mA/cm^2	$Al_{87}Y_4Gd_1Ni_8$		
		$Al_{87}Gd_5Ni_8$			b_{ox}/b_{red}	ΔE, mV	i_{pass}, mA/cm^2
– (initial sample)	1	0.31	1040	8.51	0.13	802	7.69
	2	0.80	1010	7.40	1.30	1010	7.24
	3	1.17	990	5.90	1.13	980	6.31
	4	0.72	1080	4.85	0.63	840	5.58
	5	1.66	890	4.27	0.95	960	4.76
T_1	1	2.87	1140	1.14	1.28	1070	3.23
	2	1.05	980	8.77	1.21	960	2.54
	3	1.12	990	7.53	1.30	680	2.17
	4	1.40	960	6.21	2.21	610	1.86
	5	1.45	960	4.91	0.70	650	1.81
T_2	1	1.55	1170	7.43	1.28	710	1.38
	2	1.57	1100	9.04	1.21	720	1.36
	3	1.47	970	8.85	1.30	740	1.41
	4	1.00	910	8.11	2.21	700	1.17
	5	1.77	890	6.64	0.69	680	1.16
T_3	1	1.01	1040	9.66	1.0	980	3.94
	2	2.06	970	9.44	2.05	920	3.59
	3	2.74	960	6.52	1.74	920	3.27
	4	2.16	900	6.79	1.02	950	2.76
	5	1.81	930	5.74	1.32	990	2.78

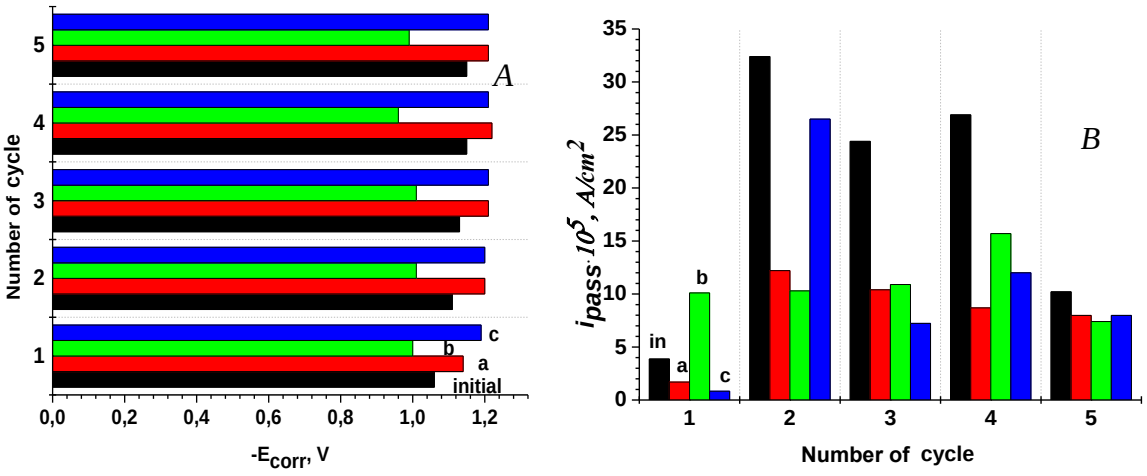

Figure 5.6 Changes of the corrosion potential (*A*) and corrosion currents (*B*) on the number of polarization cycle for $Al_{87}Y_4Gd_1Ni_8$ electrodes in 1 M KOH aqueous solution (**in**, **a**, **b**, and **c** – values for initial (unannealed) and annealed (under temperatures T_1, T_2, and T_3) samples, respectively

Based on the results of the cyclic voltammetry method, a comparison of the values of potentials and current densities of AMC corrosion was made. As it indicate results presented on Fig. 5.5 and in Table 5.1, the lowest, in absolute terms, corrosion potential values corrwspond to the $Al_{87}Gd_5Ni_8$ AMA in the initial period of electrode polarization. AMC electrodes annealed under T_1 temperature have the lowest corrosion potential at the initial stage (1st cycle of polarization) of electrochemical research. Annealing under the T_2 and T_3 temperatures leads to the intensification of electrochemical reactions, while the AMAs surface is more easily oxidized, as indicated by the values of the corrosion potentials, which shift to the cathodic side to –1.18 V. It should be noted that scanning the potential for 5 or more cycles leads to equalization values of the corrosion potentials of both the initial and the annealed AMA's samples. AMA corrosion current densities in 1 M KOH range from 50 to 550 μA/cm^2. Such fluctuations in the values of corrosion currents are due to the formation of defective surface layers on the surface of the AMAs, the metal components of which do not have time to form dense passivating layers during the anodic part of the polarization cycle of the electrodes. This is indicated by similar icorr values for the f 1st, 3rd and 5th polarization cycles. A similar trend observe for both investigated AMAs, namely $Al_{87}Gd_5Ni_8$ and $Al_{87}Gd_1Y_4Ni_8$. However, it must be noted, that the partial replacement of Gd by 4 at. % of Y has a significant effect on the corrosion resistance of AMA.

It is shown that the values of the corrosion potential of AMA $Al_{87}Gd_1Y_4Ni_8$ shift to the anodic side and fluctuate in the range of –(1.2...1.0) V, and the corrosion currents lie in the range of 25...330 μA/cm^2. It should be noted that the corrosion resistance decreases with the increasing of the duration of polarization of initial AMA. Annealing of AMA doped with 4 at.% Y leads to a 2–4 times decrease in the values of corrosion currents (Fig. 5.6, Table 5.1), which is due to the formation of denser passivation layers. The conclusions about quality of the passivation layers on the AMA surface before and after annealing can be drawn on the base of values of the ratio of the coefficients of Tafel equation. Values of $b_{ox}/b_{red} < 1$ indicate on the defectiveness of surface oxide layers on the initial samples of AMAs. Annealing of AMAs at phase transition temperatures (T_1, T_2, T_3) leads to densification of the surface layers, what indicate the $b_{ox}/b_{red} > 1$. Alloying of AMA by 4 at. % Y leads to a decrease in passivation currents i_{pass} and a narrowing of the passivation interval ΔE (see Table 5.1).

5.3 Electrocatalytic Properties of Al-based AMAs in the Hydrogen Evolution Reaction

As attested by the results of cyclic voltammetry (Fig. 5.7), intense hydrogen evolution occurs at potentials < –(0.5–0.7) V on Al-AMAs in alkaline solutions. At the same time, the fact that the output of the voltammograms on the plateau, when the density of the polarization current becomes independent of the value of the applied potential, is observed for both studied AMAs must be noted. This form of CVA was recorded mainly for 0.5–2.0 M KOH solutions. The saturation current is reached at the values of the electrode potential

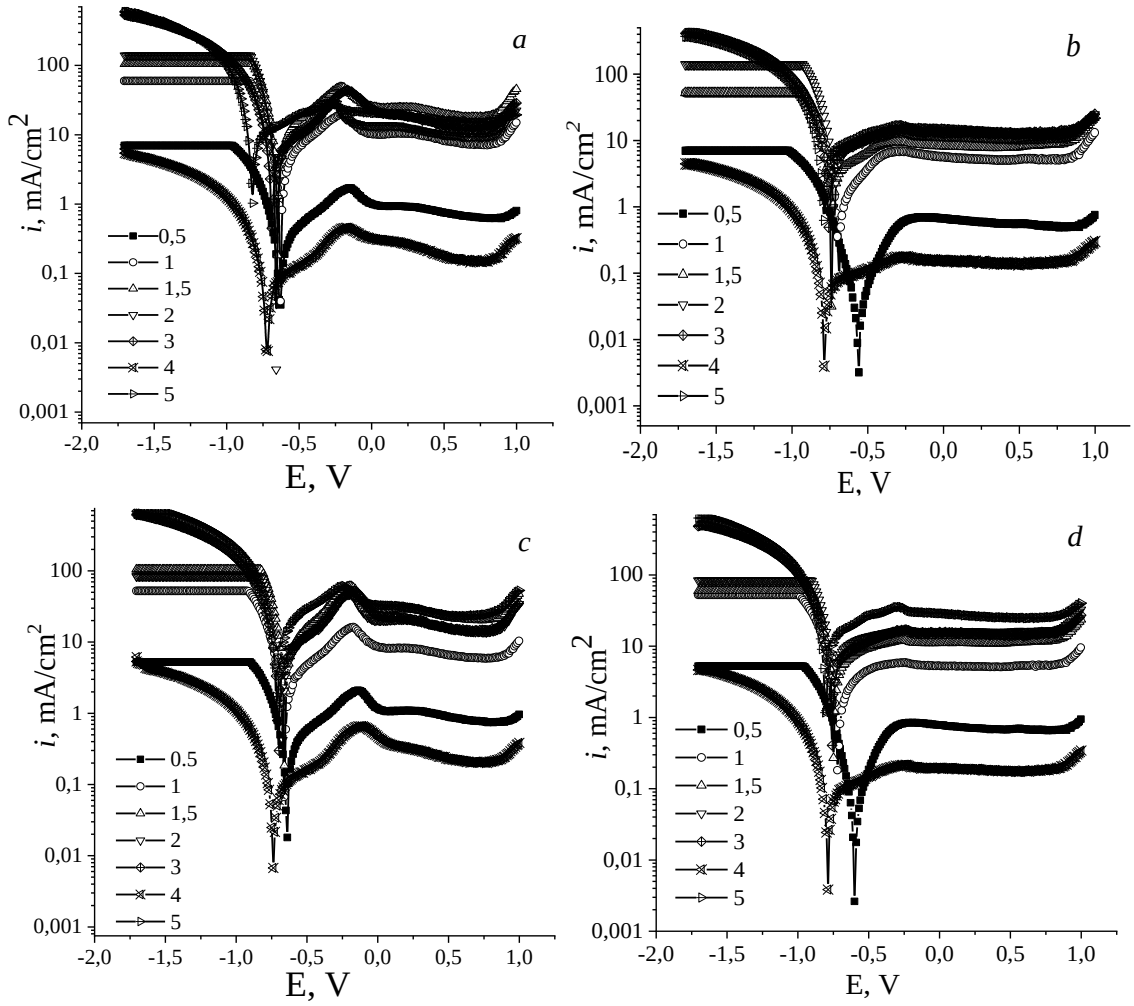

Figure 5.7 Polarization curves (first (*a*, *c*) and tenth (*b*, *d*) cycles of potential scanning, s_E = 50 mV/s) of $Al_{87}Ni_8Gd_5$ (*a*, *b*), $Al_{87}Ni_8Y_4Gd_1$ (*c*, *d*) alloys in aqueous KOH solutions with concentration, M: *1* – 0.5; *2* – 1.0; *3* – 1.5; *4* – 2.0; *5* – 3.0; *6* – 4.0; *7* – 5.0.

–(0.7–0.8) V, which indicates the transition of the HER from the kinetic to the diffusion-controlled region of the process and confirms the electrocatalytic properties of studied Al-AMAs regarding this process.

In the case of the initial (unannealed) samples of alloys (Fig. 5.7, *a*, *c*), the maximal electrochemical activity observes for the $Al_{87}Ni_8Y_4Gd_1$ alloy, for which the maximum speed of the process was recorded, namely current density ~700 mA/cm^2 in a 5 M aqueous solution of KOH (Fig. 5.7, *c*). The appearance of the cathodic parts of the CVA after 10 cycles of potential scanning practically does not change, but the densities of the polarization currents decrease slightly to the value of ~(300–400) mA/cm^2 due to the formation of a thicker layer of surface oxides (primarily hydrated oxides of REE). At the same time, the maximum current density (~500 mA/cm^2) was recorded also for the $Al_{87}Ni_8Y_4Gd_1$ alloy

(Fig. 5.7, *d*), on the surface of which, obviously, the density of the formed protective coatings is the lowest.

As shown above, Al-based AMA-electrodes with additions of Y and Gd posses an electrocatalytic activity for HER. At the same time, the activity of their nanocrystalline analogues is even higher due to the localization of catalytic centers on the surface of the samples. This conclusion is confirmed the results of the studies of influence of nanostructuring on the electrochemical characteristics of used AMA's electrodes. Annealing of AMA was carried out for 15–30 min at T = 473 K, which corresponds to the temperature of the first stage of nanocrystallization T_1 (see Fig. 5.4). Electrochemical studies of annealed samples of AMA electrodes were carried out both in the potentiodynamic (potential scan limit (–1.7)...(+1.0) V; sE=50 mV/s) and in the potentiostatic modes (E = –0,9 V) in a 1.0 KOH solution.

The results of the comparative analysis shown, that takes place significant changes regarding to in the character of observed voltage-current dependences for AMA-electrodes after their heat treatment. The main consequence is, first of all, a significant decrease in anodic currents (at E>(–0.85) V), associated with the compaction of protective films as a result of dehydration of the surface oxo-hydroxide layer. The slowing down of corrosion processes is manifested in the significant "smoothing" of the anodic branch and the absence of an oxygen release wave even when E=+1.0 V is reached.

Important feature of the original alloys is that the release of hydrogen on them practically does not affect the magnitude of the corrosion potential, while a shift of E_{corr} to anodic region is observed for the annealed samples by approximately 0.2 and 0.4 V at the duration of heat treatment of 15 and 30 min, respectively. At the same time, the appearance of the CVA for samples previously annealed for 30 min is practically identical to that of the initial (non-annealed) samples, which indicates amorphization of nanocrystalline electrodes during hydrogen evolution, primarily of the surface layer of AMA's samples, which determines their electrocatalytic properties. This conclusion is confirmed by the significant changes of the mechanical characteristics of the samples of Al-AMAs after their use as elctrodes in HER [36–37]. For example, microhardness of AMA $Al_{87}Y_4Gd_1Ni_8$ decreases by 0.88 GPa after hydrogen evolution reaction.

5.4 Conclusions

As follows, corrosion studies of AMAs $Al_{87}Gd_5Ni_8$ and $Al_{87}Y_4Gd_1Ni_8$ in alkaline aqueous solutions showed that yttrium doping and annealing at temperature which corresponds to beginning of the stage of nanocrystals origin in amorphous matrix are the most effective factors of the increasing of their corrosion resistance. The mechanism of the action of these factors is connects first of all with formation more denser protective layers (formed mainly nickel, yttrium, and gadolinium hydroxides), that is confirmed by experimental values of b_{ox}/b_{red} ratio.

Moreover, the annealing (nanocrystallization) of initial samples leads to increasing of electrocatalytic activity of Al-based AMAs in relation to the hydrogen evolution reaction in the result of concentation of active sites on the surface of nanostructured electrodes. However, it must be taken to consideration that too long use of such electrodes for hydrogen production leads to amorphization of the surface and, as a result, deterioration of their electrocatalytic properties.

Key words

- aluminium
- amorphous alloy
- temperature modification
- nanocrystallization
- corrosion
- hydrogen evolution reaction

References

1. *Salehi M., Shabestari S. G.* Nanostructure evolution, thermal stability and hardness of amorphous Al–Cu-Y (Co, La) (at. %) alloys // J. Non-Cryst. Solids. 2022. Vol. 589. P. 121663. DOI: https://doi.org/10.1016/j.jnoncrysol.2022.121663
2. *Boichyshyn L. M., Khrushchyk Kh. I., Kovbuz M. O., Hertsyk O. M., Hula T. H.* Specific Features of the Transition of Amorphous $Al_{87}REM_5Ni_8$(Fe) Alloys into the Crystalline State under the Influence of Temperature // Mat. Sci. 2019. Vol. 55, Is. 1. P. 17–26. DOI: https://doi.org/ 10.1007/s11003-019-00246-7
3. *Khrushchyk Kh., Boichyshyn L., Kordan V.* Influence of annealing on mechanical properties of alloys of Al-REM-Ni(Fe) // Mat. Today: Proceedings. 2022. Vol. 62. P. 5739–5744. DOI: https://doi.org/10.1016/j.matpr.2022.02.343
4. *Xua Zh., Xua Y., Zhang A., Wang J., Wang Z.* Oxidation of amorphous alloys // J. Mat. Sci. Tech. 2018. Vol. 34. Is. 11. P.1977–2005. DOI: https://doi.org/10.1016/j.jmst.2018.02.015
5. *Leach R.* The Measurement of Surface Texture using Stylus Instruments // Measurement good practice guide. Vol. 37. National Physical Laboratory, 2001. 84 p.
6. *Inoue A.* New aluminium base alloys / S. Banerjee and R. V. Ramanujan (Eds.) Advances in Physical Metallurgy. – Amsterdam: Gordon & Breach Publishers, 1996. – P. 127–134.
7. *Carmo M., Fritz D. L., Mergel J., Stolten D.* Comprehensive review on PEM water electrolysis // Int. J. Hydrogen Energy. 2013 Vol. 38. P. 4901–4934. DOI: https://doi.org/10.1016/j.ijhydene. 2013.01.151
8. *Mansour A.N., Melendres C.A.* A Study of the structure and the morphology of oxide films on amorphous Al – Fe – Ce alloys by XPS and SEM // J. Electrochem. Soc. 1995. Vol. 142, Is. 6. P. 1961–1967. DOI: https://doi.org/10.1149/1.2044223
9. *K. C. Neyerlin.* Study of the Exchange Current Density for the Hydrogen Oxidation and Evolution Reactions // J. Electrochem. Soc. 2007. Vol. 154, Is.7. P. B631–B635.
10. *Hertsyk O., Kovbuz M., Bednarska L. et al.* Corrosion of amorphous metal alloys based on iron in the medium of nitrate and nitrite ions // Physico-chemical mechanics of materials. 2002. Spec. Is. 3. P. 189–194.

11. *Mansour A. N., Melendres C. A.* A study of the structure and the morphology of oxide films on amorphous Al-Fe-Ce alloys by XPS and SEM // J. Electrochem. Soc. 1995. Vol. 142. P. 1961–1967.
12. *Minghao G., Weiyan Lu, Baijun Y., Suode Zh., Jianqiang W.* High corrosion and wear resistance of Al-based amorphous metallic coating synthesized by HVAF spraying // J. Alloys Compd. 2018. Vol. 735. P. 1363–1373. DOI: https://doi.org/10.1016/j.jallcom.2017.11.274
13. *Brown G. M., Shimizu K., Kobayashi K.* The growth of a porous oxide film of a unique morphology by anodic oxidation of an Al-0.5 wt% Ni alloy // Corr. Sci. 1998. Vol. 40, Is. 9. P. 1575–1586.
14. *Wang Z., Scudino S., Prashanth K., Eckert J.* Corrosion properties of high-strength nanocrystalline $Al_{84}Ni_7Gd_6Co_3$ alloy produced by hot-pressing of metallic glass // J. Alloys Compd. 2017. Vol. 707. P. 63–67. DOI: https://doi.org/10.1016/j.jallcom.2016.11.212
15. *Brett C. M. A., Gomes I. A. R., Martins J. P. S.* The electrochemical behavior and corrosion of aluminum in chloride media. The effect of inhibitor anions // Corr. Sci. 1994. Vol. 36, Is. 6. P. 915–925.
16. *Hertsyk O., Kovbuz M., Bednarska L., Kotur B. Ya., Nosenko V. K.* Corrosion properties of aluminum-based amorphous alloys // Physico-chemical mechanics of materials. 2004. Spec. Is. 4. P. 95–98.
17. *Safizadeh F., Houlachi G., Ghali E.* Electrocatalytic activity and corrosion behavior of Fe-Mo and Fe-Mo-P coatings employed as cathode material for alkaline water electrolysis // Int. J. Hydrogen Energy. 2018. Vol. 43, Is. 16. P. 7938–7945. DOI: https://doi.org/10.1016/j.ijhydene.2018.03.071
18. *Mazhar A. A., Arab S. T., Noor E. A.* The role of chloride ions and pH in the corrosion and pitting of Al–Si alloys // J. Appl. Electrochem. 2001. Vol. 31. P. 1131–1140. DOI: https://doi.org/10.1023/A:1012039804089
19. *McCafferty E.* Sequence of steps in the pitting of aluminium by chloride ions // Cor. Sci. 2003. Vol. 45. P.1421–1438. DOI: https://doi.org/10.1016/S0010-938X(02)00231-7
20. *Han Y.-M., Chen X.-G.* Electrochemical Behavior of Al-B_4C Metal Matrix Composites in NaCl Solution // Mater. (Basel). 2015. Vol. 8, Is. 9. P. 6455–6470. DOI: https://doi.org/10.3390/ma8095314
21. *Chidambaram D., Clayton C. R., Halada G. P., Kendig M. W.* Surfase pretreatments of aluminum alloy AA2024-T3 and formation of chromat conversion coatings. (1) Composition and electrochemical behavior of the oxide film // J. Electrochem. Soc. 2004. Vol. 151, Is. 11. P. B605–B612. DOI: https://doi.org/10.1149/1.1804811
22. *Mika T., Karolus M., Haneczok G., Bednarska L., Lagiewka E., Kotur B.* Influence of Gd and Fe on crystallization of $Al_{87}Y_5Ni_8$ amorphous alloy // J. Non-Cryst. Solids. 2008. Vol. 354, Is. 27. P. 3099–3106. DOI: https://doi.org/10.1016/j.jnoncrysol.2008.01.020
23. *Durst J., Siebel A., Simon C., Hasché F., Herranz J., Gasteiger H. A.* New insights into the electrochemical hydrogen oxidation and evolution reaction mechanism // Energy Environ. Sci. 2014. Vol. 7. P. 2255–2260. DOI: https://doi.org/10.1039/C4EE00440J
24. *Zhang B., Ying L., Fuhui W.* Electrochemical corrosion behavior of microcrystalline aluminium in acidic solutions // Cor. Sci. 2007. Vol. 49. P. 2071–2082. DOI: https://doi.org/10.1016/j.corsci.2006.11.006
25. *Lakshmi B. B, Dorhout P. K., Martin C. R.* Sol-gel template synthesis of semiconductor nanostructures // Chem. Mater. 1997. Vol. 9, Is. 3. P. 857–862. DOI: https://doi.org/10.1021/cm9605577
26. *Mattson E*. Electrochemical corrosion. – Moscow, Metallurgia, 1991. 400 p. (in Russian).
27. *Estejab A., Daramola D. A., Botte G. G.* Mathematical model of a parallel plate ammonia electrolyzer for combined wastewater remediation and hydrogen // Water Res. 2015. Vol. 77. P. 133–145. DOI: https://doi.org/10.1016/ j.watres.2015.03.013
28. *Safizadeh F., Ghali E., Houlachi G.* Electrocatalysis developments for hydrogen evolution reaction in alkaline solutions – A review // Int. J. Hydrogen Energ. 2015. Vol. 40, Is. 1. P. 256–274. DOI: https://doi.org/10.1016/ j.ijhydene.2014.10.109

29. *Jafarian M., Azizi O., Gobal F., Mahjani M. G.* Kinetics and electrocatalytic behavior of nanocrystalline CoNiFe alloy in hydrogen evolution reaction // Int. J. Hydrogen Energ. 2007. Vol. 32. P. 1686–1693. DOI: https://doi.org/ 10.1016/j.ijhydene.2006.09.030
30. *Jukic A., Piljac J., Metikoš-Hukovic M.* Electrocatalytic behavior of the Co33Zr67 metallic glass for hydrogen evolution // J. Mol. Catal. A-Chem. 2001. Vol. 166. P. 293–302. DOI: https://doi.org/ 10.1016/S1381-1169(00)00452-0
31. *Grubač Z., Sesar A.* Electrocatalytic activity of the Ni57.3Co42.7 alloy for the hydrogen evolution // Croat. Chem. Acta. 2017. Vol. 90, Is. 2. P. 273–280. DOI: https://doi.org/10.5562/cca3174
32. *Rosalbino F., Delsante S., Borzone G., Angelini E.* Electrocatalytic behaviour of Co–Ni–R (R = Rare earth metal) crystalline alloys as electrode materials for hydrogen evolution reaction in alkaline medium // Int. J. Hydrogen Energy. 2008. Vol. 33. P. 6696–6703. DOI: https://doi.org/10.1016/ j.ijhydene.2008.07.125
33. *Navarro-Flores E. Chong Z., Omanovic S*. Characterization of Ni, NiMo, NiW and NiFe electroactive coatings as electrocatalysts for hydrogen evolution in an acidic medium // J. Mol. Catal. A–Chem. 2005. Vol. 226. P. 179–197. DOI: https://doi.org/10.1016/j.molcata.2004.10.029
34. *Brookes H. C., Carruthers C. M., Doyle T. B.* The electrochemical and electrocatalytic behaviour of glassy metals // J. Appl. Electrochem. 2005. Vol. 35. P. 903–913. DOI: https://doi.org/10.1007/ s10800-005-4726-5
35. *Fundo A. M., Abrantes L. M.* The electrocatalytic behaviour of electroless Ni–P alloys // J. Electroanal. Chem. 2007. Vol. 600. P. 63–79. DOI: https://doi.org/10.1016/j.jelechem.2006.03.023
36. *Khrushchyk Kh., Hula T, Boichyshyn L., Lopachak M.* Microhardness on the amorphous and nanostructured alloys system $Al_{87}(Y,Gd)_5Ni_8$ as electrodes for hedrogen evolution // Proceedings of the 2nd International Scientific Conference «Chemical Technology and Engineering». June 24–28, 2019, Lviv. Lviv Polytechnic National University, 2019. P. 311–316.
37. *Boichyshyn L. M., Hertsyk O. M., Kovbuz M. O., Pereverzeva T. H., Kotur B. Ya.* Properties of amourphous alloys of Al–REM–Ni and Al–REM–Ni–Fe systems with nanocrystalline structure // Mat. Sci. 2013. Vol. 48, Is. 4. P. 555–559. DOI: https://doi.org/10.1007/s11003-013-9537-y

Chapter 6

AN INFLUENCE OF THE SURFACTANT NATURE ON THE FORMATION OF SILVER NANOPARTICLES BY ELECTROCHEMICAL METHODS

O. I. Kuntyi[1], G. I. Zozulya[1], M. V. Shepida[1], A. R. Kytsya[2], A. S. Mazur[1], and L. I. Bazylyak[2]

[1]*Lviv Polytechnic National University, 79013, Lviv Ukraine*

[2]*Department of Physical Chemistry of Fossil Fuels of the Institute of Physical-Organic Chemistry and Coal Chemistry NAS of Ukraine, 79060 Lviv, Ukraine*

Corresponding author: kunty@ukr.net

Contents

Abstract

The paper presents an influence of the surfactant nature on the main parameters of silver nanoparticles (AgNPs) synthesized by different electrochemical methods, namely electrolysis, microplasma, sonoelectrochemical, and sonogalvanic replacement ones. The following surfactants containing the O-donor atoms were studied: polyacrylate (NaPA, anionic polymer); polyvinylpyrrolidone (PVP, nonionic polymer) and rhamnolipid (RL, monomeric). It has been established that via electrochemical methods it is possible to synthesize the AgNPs with small sizes under the conditions of effective stabilization of nanoclusters and nanoparticles by surfactants. The type of surfactants determines the complexes' stability as well as the cathodic polarization which are influential factors in the controlled synthesis of AgNPs. It was shown that "blue" AgNPs solutions are characterized by the absorption maximum at λ_{max} = 490–530 nm formed during reverse electrolysis and sonoelectrochemical synthesis in polyacrylate solutions. The yellow solutions with λ_{max} = 410 nm, which transform into the "blue" solutions upon heating or long-term storage were obtained by microplasma synthesis and the method of sonogalvanic replacement. In solutions of polyvinylpyrrolidone and rhamnolipid the "yellow" stable colloidal solutions of nanosilver (λ_{max} = 410 nm) are synthesized regardless the type of electrochemical method. AgNPs obtained in NaPA, PVP, and RL solutions are spherical and do not exceed 20 nm.

6.1 Introduction

The unique biological characteristics of silver nanoparticles (AgNPs) and their relatively low cost are favorable conditions for broad practical application as antibacterial materials, anticancer therapy, dentistry, cardiology, dermatology, water disinfection, etc. [1, 2]. AgNPs are stabilized by surfactants to prevent aggregation during the preparation and long-term storage. Taking into account the field of application, AgNPs should be non-toxic, and the technologies of synthesis of nanoparticles should meet the conditions of "green" synthesis.

Synthetic and natural surfactants are used to stabilize the metal nanoparticles (MNPs) including AgNPs in the solutions regardless the synthesis methods. They can be classified by the nature of the electron donor atoms involved in the formation of the surface complexes with MNPs. Often there are the surfactants with O-, N- and S-donor atoms [3, 4]. It is preferably to use the O-donor-containing surfactants to stabilize AgNPs, which provide a "green" synthesis of nanoparticles. Molecules of these surfactants contain the functional

groups COO-, C=O, and O−H. Electron donor properties of these groups significantly depend on the structure of the molecule or ion of organic matter of the surfactant. Therefore, the strength of surface complexes affects the geometry of nanoparticles and their stability during the AgNPs formation and long-term storage. O-donor-containing surfactants can be conventionally divided into the following three groups by their effect on the stabilization of AgNPs: 1) polymeric anionic; 2) polymeric nonionic; 3) monomeric (see Table).

Table Influence of surfactants nature on the main characteristics of silver nanoparticles

Type	Surfactant	Method of synthesis	λ_{max}, nm	Size (diameter), nm	Ref.
polymeric anionic	NaPA	chemical	423–426	∅ (average) = 10	[5]
		electrolysis	350(sideband), 490–530	1.5–4.1	[6]
		microplasma	~410	2−20	[7]
		sonoelectrochemical	350(sideband), 500	4−6	[8]
		sonogalvanic	290(sideband), 410	4−20	[9]
	alginate	chemical	405–440	1–4	[10]
		electrolysis	408–411	10–30	[11]
	pectins	chemical	415−420	8.0±2.6	[12]
		microplasma	409	9.33±3.37	[13]
polymeric nonionic	PVP	chemical	350 (sideband), 404	20−40	[14]
		electrolysis	~ 400	9−14	[15]
		microplasma	394−417	8−10	[16]
		sonoelectrochemical	400−410	−	[17]
	PVA	chemical	400–480	10−48	[18]
		electrolysis	~ 400, ~ 650	15±9	[19]
		microplasma	~ 410	10±7	[20]
monomeric	rhamnolipid	chemical	~ 400	3.6±2	[21]
		electrolysis	~ 410	2−20	[22]
		sonoelectrochemical	~ 411	1−3	[23]
	cytrate	chemical	~ 400	14±5	[24]
		electrolysis	416	19.7±4.3	[25]
		microplasma (*at 3, 5, 7 min, respectively)	369, 394, 396*	17.9±8.9, 14.3±1.6, 10.6±2.3*	[26]

The formation of AgNPs colloidal solutions is a multifactorial process, so the comparison of the surfactant nature influence on the formation of nanoparticles by different synthesis methods is conditional. First of all, this is due to a significant difference in the mechanisms of Ag^+-ions reducing. During the chemical and microplasma synthesis of AgNPs the reduction of silver ions is occurred in the bulk of the solution. At the same time, during the electrolysis, sonoelectrochemical and sonogalvanic methods, the reduction of Ag^+ occurs mainly on the surface of the electrodes. There are also significant differences between the methods in the rate of mass transfer and energy impact on the nucleation processes, whereas the microplasma synthesis and synthesis in the ultrasound field have significant advantages.

Despite the variety of synthesis methods (Table), there is an individual effect of some surfactants on the following main characteristics of AgNPs, namely on the UV-Vis absorption spectra and nanoparticle sizes. During the synthesis of AgNPs in polymeric surfactants solutions (anionic PA^- [6, 8, 9] and neutral PVP [14]), a sideband at $\lambda \approx 350$ nm is observed in the ultraviolet region, which corresponds to the presence of nanoclusters ("magic" cluster) of silver (AgNCs). The latter are mainly charged ($Ag_{(m+n)}^{m+}$), [27] and adsorbed on functional groups of polymer fragments. Over time, they increase in the size and transforms (or growth) into AgNPs. Therefore, a sideband at 350 nm was not observed in the some of references, for example in [5, 7] (surfactant is PA^-) and [15–17] (surfactant is PVP).

Electrochemical synthesis (electrolysis, microplasma, sonoelectrochemical, and sonogalvanic replacement methods) of MNPs, particularly AgNPs, meet the requirements of "green" technology. There are also characterized by the control of the formation of nanoparticles by geometry and size distribution. Syntheses are carried out mainly in aqueous solutions of surfactants, in which the surfactant molecules form complexes with Ag^+ ions and stabilize the formed AgNCs and AgNPs. Therefore, the aim of this work was to compare an influence of the type of surfactants on the main parameters of colloidal solutions of silver nanoparticles synthesized by electrochemical methods. The following surfactants were selected: polyacrylate (anionic polymer); polyvinyl pyrrolidone (nonionic polymer), and rhamnolipid (monomeric).

6.2 Materials and Research Methods

AgNPs were synthesized in surfactant solutions by electrolysis, sonoelectrochemical, microplasma, and sonogalvanic replacement methods. The first three methods were performed in a standard three-electrode electrochemical cell. Electrolysis was performed with reverse current, sonoelectrochemical synthesis was performed with cyclic voltammetry and microplasma synthesis was performed with stationary current supply. At the same time, the silver plate electrodes playing the role of sacrificial anodes in the anodic period were used. In the case of microplasma synthesis, the cathodes were tungsten rods. Ag/AgCl saturated electrode was used as reference electrodes in all of three methods. A detailed description of the electrolysis, sonoelectrochemical and microplasma AgNPs synthesis methods in surfactant solutions are given in [6], [8], and [7].

The technical details of the synthesis of silver nanoparticles in a solution containing $AgNO_3$ and sodium polyacrylate by galvanic replacement on aluminum powder in ultrasound are given in [9]. The shape and size of the synthesized silver nanoparticles were studied using a transmission electron microscope (TEM) JEM-I230 (JEOL, Tokyo, Japan) with an accelerating voltage of 80 kV. Samples for TEM were prepared by drying 0.05 μl of silver sol on a carbon grid at room temperature. AgNPs sizes were determined using TEM images by comparing individual particles with the scales presented in the images and using the AxioVision V 4.8.2.0 program. Optical characteristics of AgNPs solutions were studied using a UV-3100PC UV-Vis spectrophotometer in quartz cuvettes with a 10 mm optical length and at wavelength range from 190 to 1100 nm. The comparative solution was the distilled water.

6.3 Results and Discussions

Ag^+-ions in polymeric (PA^-, PVP) and monomeric (RL) surfactant solutions forms the water-soluble complexes (see schemes on Fig. 6.1). Electrochemical reduction of Ag(I) on the cathode surface occurs with the participation of complexes in forming silver atoms which are adsorbed on O-donor atoms of surfactant molecules.

The nucleation process is very energy-consuming compared to the energy of nanoparticle growth. The activation energy (E_A) of AuNPs nucleation equals 92.7 $kJ \cdot mol^{-1}$, while E_A of their growth is 24.6 [28]. Electrochemical methods (electrolysis, sonoelectrochemical, sonogalvanic replacement, microplasma) provide high Ag(I) cathodic reduction energy and high nucleation rate correspondingly. Therefore, it is possible to synthesize AgNPs with the small sizes by electrochemical methods under the effective stabilization of the formed nanoclusters and nanoparticles by surfactants.

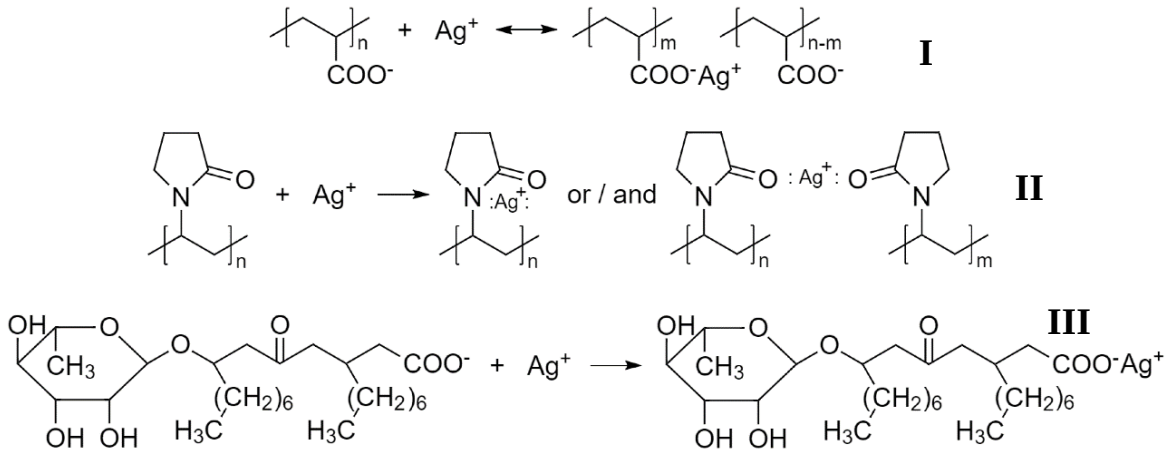

Figure 6.1 Schemes of Ag^+ complexation reactions with polyacrylate (I), polyvinylpyrrolidone (II) and rhamnolipid (III)

6.3.1 Stabilization by Polyacrylate-ions

Ag(I) reduction from the polyacrylate complex leads to the formation of the fixed Ag-adatoms (Fig. 6.2) since PA^- performs the function of a polymer matrix (polymer-templated Ag atom). After the AgNCs and AgNPs formation

$$[mAg(0)PA]^{n-} \rightarrow [Ag(0)_mPA]^{n-} \text{ (AgNCs and AgNPs).} \quad (6.1)$$

the anionic fragments of polyacrylate are adsorbed on such nanoparticles with the formation of surface complexes due to the presence of ionizable carboxylic groups and stabilize the AgNPs. Moreover, due to the polymeric nature PA^- anions undergoes reversible folding and compression depending on the environmental conditions (pH, ionic strength, temperature) [29] leading to the changing of the polymer shape, size, and volume.

It was shown that at the reverse electrolysis conditions (sonoelectrochemical synthesis) the "blue" and "violet" solutions of AgNPs with λ_{max} = 490–530 nm are formed (Fig. 6.3, *a*). And contrary, at the microplasma synthesis and sonogalvanic replacement method the formation of "yellow" AgNPs solutions with λ_{max} = 410 nm (Fig. 6.3, *b*) were observed. "Yellow" solutions are metastable and transforms into the "blue" ones during prolonged storage or at elevated temperatures (Fig. 6.4). Such a fact can be explained by the changes of the form and size of the polyacrylate anion as it was mentioned above [28].

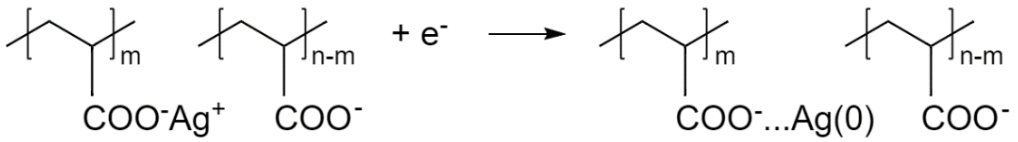

Figure 6.2 Scheme of fixed Ag-adatoms formation on fragments of polyacrylate [2]

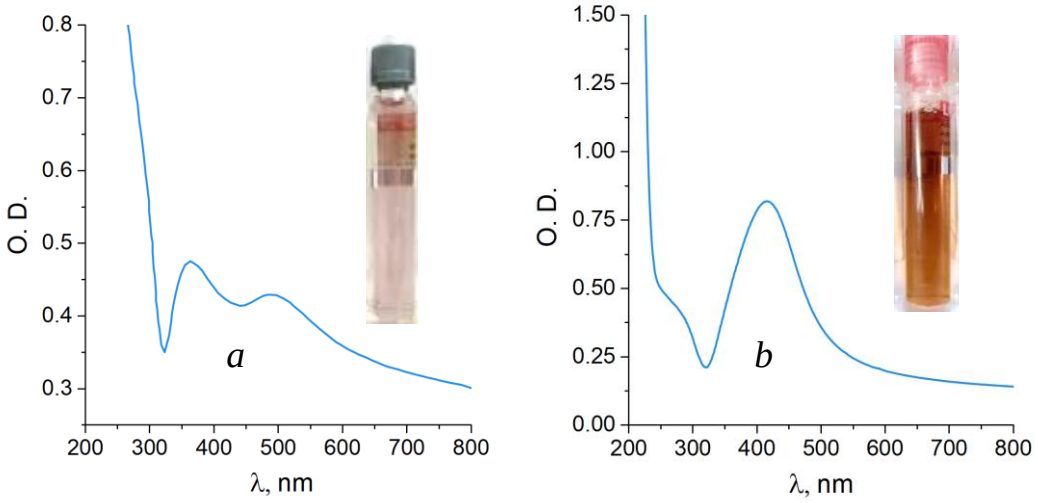

Figure 6.3 UV-Vis spectra of AgNPs solutions were obtained by sonoelectrochemical (*a*) and sonogalvanic replacement (*b*) methods

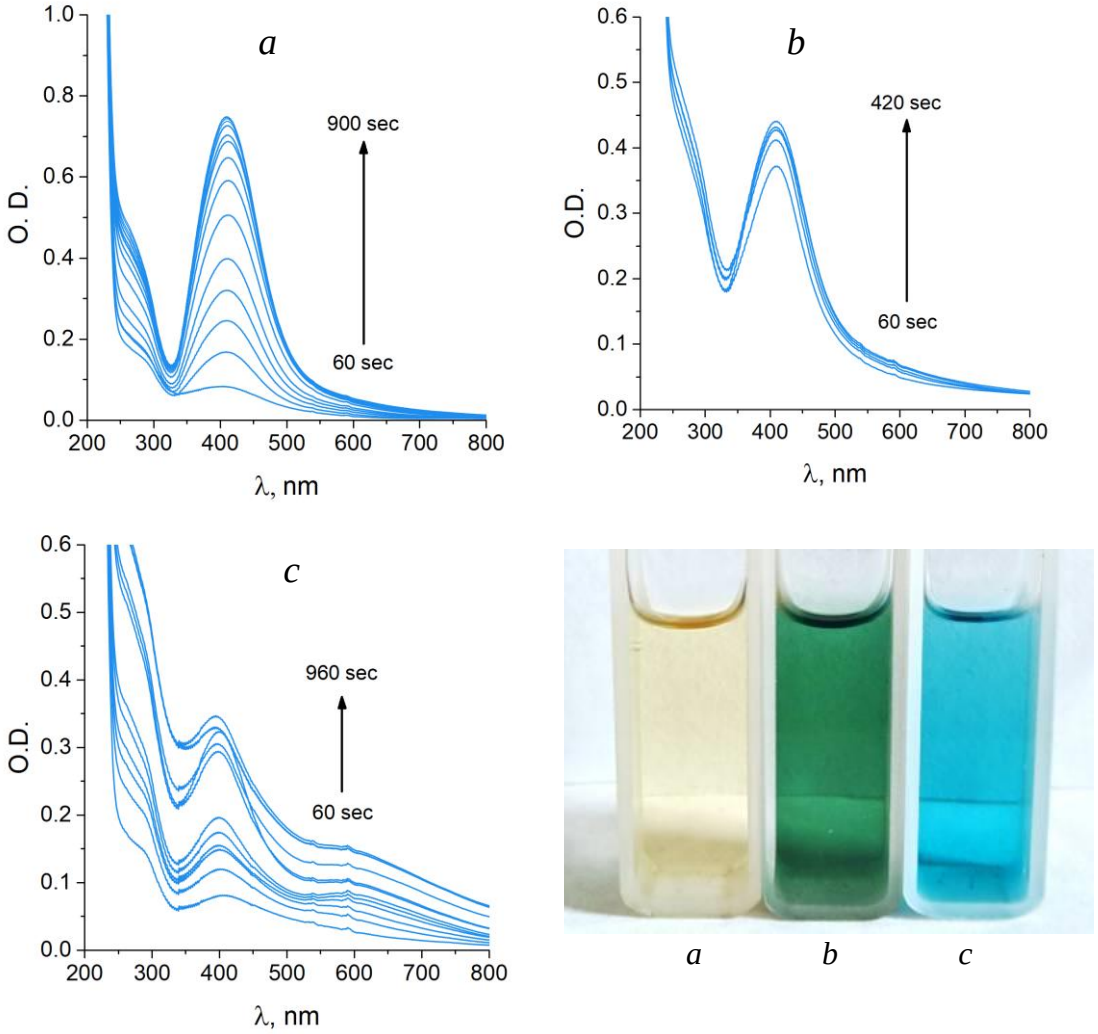

Figure 6.4 UV-Vis spectra and the photos of AgNPs synthesized in NaPA solutions by microplasma at different temperatures, °C: *a* – 20; *b* – 30; *c* – 40

AgNPs obtained in NaPA solutions are spherical regardless the synthesis method and the size of particles does not exceed of 20 nm (Fig. 6.5). Here it must be noted that the microplasma synthesis method is fundamentally differed than electrolysis or sonoelectrochemical techniques by the Ag^+ reduction mechanism and the rate of the progress. During the reversible current electrolysis [6], sonoelectrochemical and sonogalvanic replacement reduction [4] of Ag(I) takes place on the cathode surface according to the reaction

$$[mAg(I)PA]^{n-} + me^- \rightarrow [mAg(0)PA]^{n-}. \quad (6.2)$$

During the microplasma synthesis the reduction of silver ions takes place in the bulk of the solution [7] with hydrated electrons (ne^-_{aq}) which are formed in the aqueous solution in the near-cathode layer by the reaction

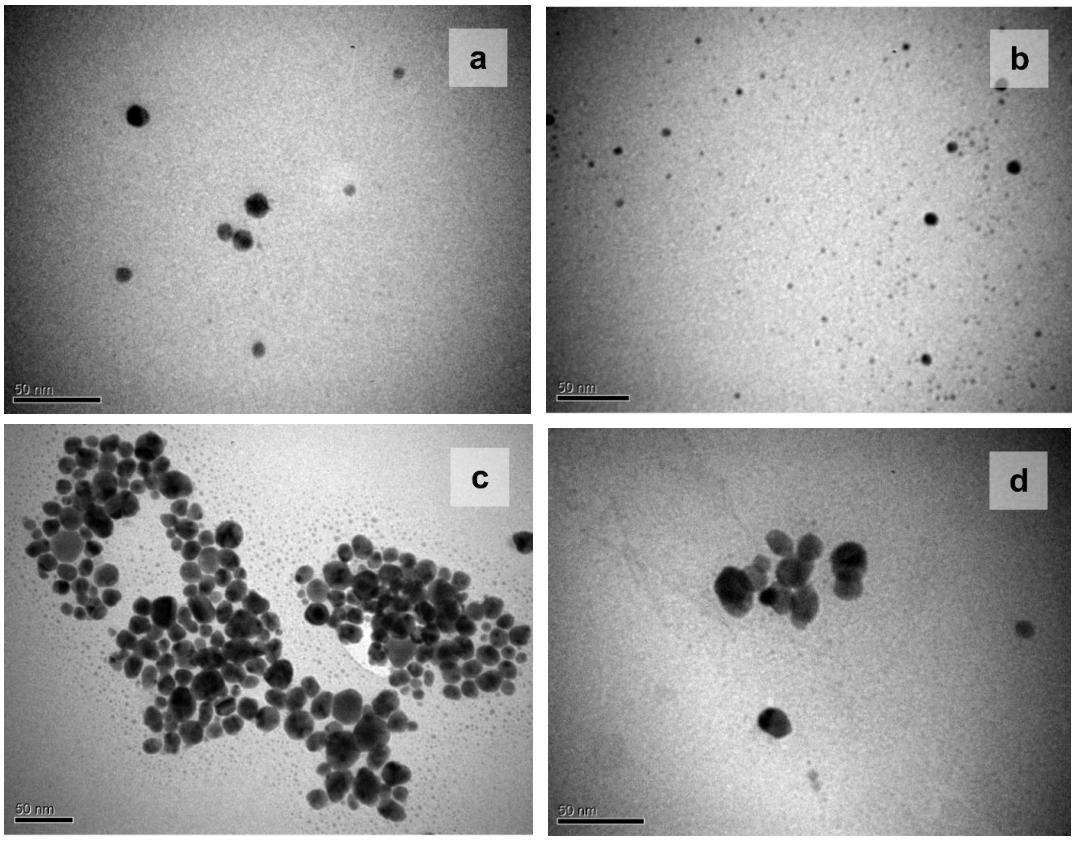

Figure 6.5 TEM image of AgNPs synthesized in NaPA solutions by electrolysis (*a*), sono-electrolysis (*b*), microplasma (*c*), and sonogalvanic replacement methods (*d*)

$$e^- + nH_2O \rightarrow e^-_{aq}. \quad (6.3)$$

Therefore, the microplasma synthesis is characterized by the highest rate of the formation of AgNPs. However, the above mentioned differences of the methods can be considered as technological since each allows the geometry-controlled synthesis of nanoparticles stabilized by polyacrylate.

6.3.2. Stabilization by Polyvinylpyrrolidone

The electrochemical synthesis of AgNPs in PVP solutions occurs due to the reduction of Ag(I) from polyvinylpyrrolidone complexes:

$$[nAg(I)PVP]^{n+} + ne^- \rightarrow [Ag(0)_nPVP]. \quad (6.4)$$

For all of four investigated methods of electrochemical production of nanoparticles, stable yellow solutions with a clearly defined λ_{max} = 410 nm are formed in a wide range of precursor concentrations and temperatures. At the same time during the synthesis, the maximum value and the peak width almost do not change (Fig. 6.6).

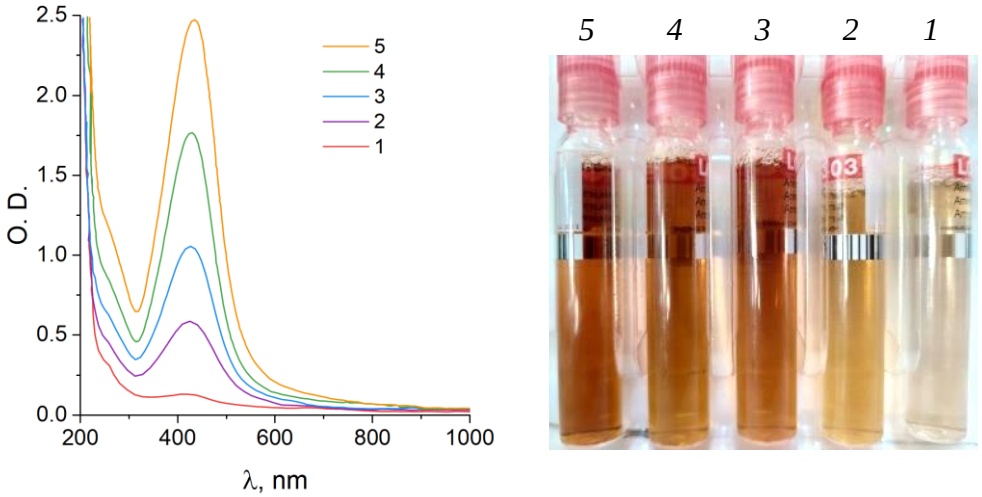

Figure 6.6 UV-Vis spectra of AgNPs synthesized in PVP solutions by sonoelectrochemical method during, min: *1* – 5; *2* – 10; *3* – 15; *4* – 20; *5* – 25.

In contrast to the synthesis of AgNPs in PA^- solutions, the shape of UV-Vis spectra of AgNPs/PVP solutions does not significantly depend on temperature. As can be seen from Fig. 6.7, the UV-vis spectra of AgNPs synthesized in PVP solutions at 20 and 40 °C are characterized by a single absorption band in contrast to AgNPs/PA^- (Fig. 6.4, *c*).

The single absorption band on the spectrum indicates a spherical shape of the formed AgNPs. However, some shift of the absorption maximum in the long-wave region with the increasing of temperature may indicate the increase of the size of obtained AgNPs [30].

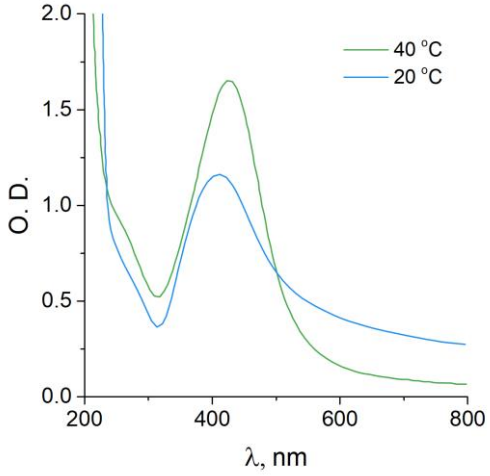

Figure 6.7 UV-Vis spectra of AgNPs synthesized in PVP solutions by sonoelectrochemical method at 20 i 60 °C

6.3.3 Stabilization by Rhamnolipid

It was found that the UV-Vis spectra of AgNPs synthesized in rhamnolipid solutions are a little differ from the spectra of AgNPs/PVP solutions. At the same time, the shape of UV-Vis spectra of "yellow" AgNPs/RL solutions obtained at different temperatures are characterized by single absorption band which may indicate a spherical shape of the formed AgNPs (Fig. 6.8).

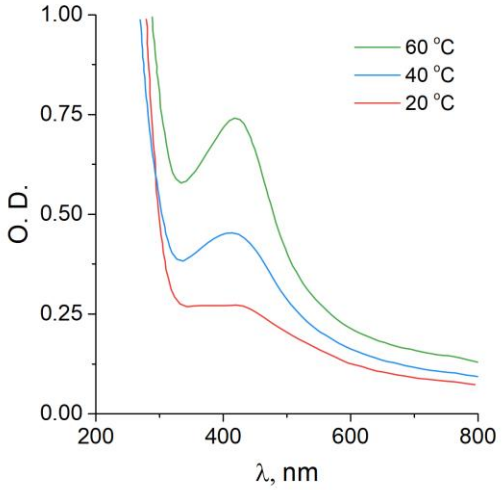

Figure 6.8 UV-Vis spectra of AgNPs synthesized in RL solutions by sonoelectrochemical method at 20, 40, and 60 °C

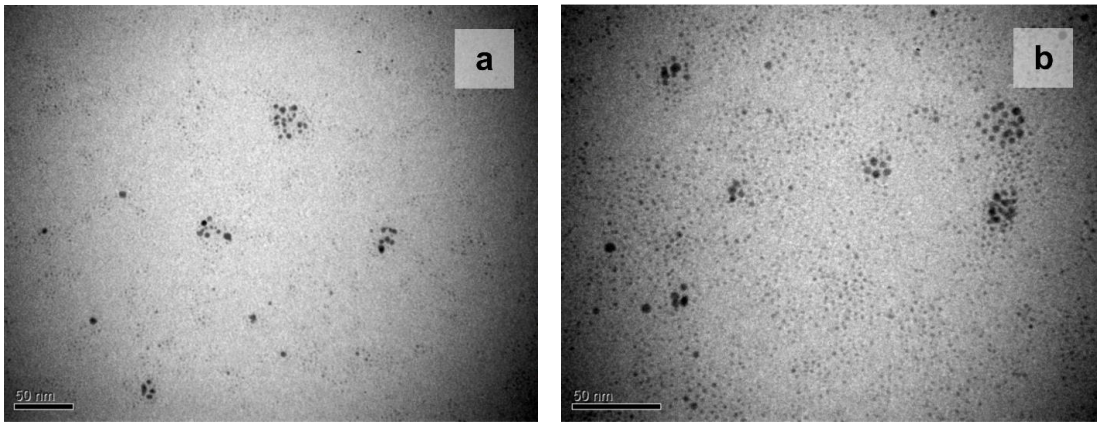

Figure 6.9 TEM images of AgNPs synthesized in RL solution at t = 40 (*a*) and 60 °C (*b*) by the sonoelectrochemical method

The effect of temperature is observed only on the increase of AgNPs size (Fig. 6.9) with the increase of the value of this factor which is indicated by the shift of the absorption band in the long-wave region (Fig. 6.8) as well as TEM-images of obtained AgNPs. It is typical observed phenomenon during the formation of nanoparticles (see Fig. 6.7 above)

since an increase of temperature causes cathodic polarization and a shift of the "adsorption ↔ desorption" equilibrium of surfactant to the right. Accordingly, the conditions for the production of nanoparticles are created.

6.4 Conclusions

1) Electrochemical methods (electrolysis, sonoelentochemical and sonogalvanic replacement, microplasma) are characterized by the Ag(I) cathodic reduction energy, which outweighs the activation energy of nucleation of silver. It allows the formation of nanoclusters and nanoparticles of small sizes. Surfactants play an important role in the fixing of such sizes and stabilizing of the particles in aqueous solutions. Therefore, surfactants are one of the main factors in the controlled synthesis of AgNPs by electrochemical methods and the provision of "green" technology.
2) For AgNPs stabilization in aqueous solutions, three main types of surfactants containing mainly O-donor atoms are used: polymeric anionic, polymeric nonionic, and monomeric. With Ag(I) ions, they form complexes that participate in the process of reduction to silver atoms. Therefore, the type of surfactants determines the stability of the complexes and the corresponding cathodic polarization.
3) A significant difference in the influence of the surfactant types is evident in the UV-Vis spectra of AgNPs colloid solutions. During electrolysis polyacrylate anions form the stable solutions with λ_{max} = 490–530 nm ("blue" solutions). Sonoelectrochemical and sonogalvanic methods at 20 °C make it possible to obtain "yellow" solutions with λ_{max} = 410 nm. However, they are metastable and, upon prolonged exposure or heating (> 40 °C), turn into "blue", solutions. Nonionic polyvinylpyrrolidone molecules and rhamnolipid monomers lead to stable colloidal solutions with λ_{max} = 410 nm regardless of the AgNPs synthesis method.

Acknowledgment

This work was carried out with the partial financial support of the National Research Foundation of Ukraine. Agreement 165/02.2020 (No 0120U105247 "Design of polyfunctional nanostructured mono- and bimetals with electrocatalytic and antimicrobial properties").

Keywords

- silver nanoparticles
- "green" synthesis
- surfactants
- electrolysis
- microplasma
- sonogalvanic replacement

References

1. *Lee S. H., Jun B.-H*. Silver Nanoparticles: Synthesis and Application for Nanomedicine // Int. J. Mol. Sci. 2019. Vol. 20. P. 865. DOI: https://doi.org/10.3390/ijms20040865
2. *Talapko J., Matijević T., Juzbašić M., Antolović-Požgain A., Škrlec I.* Antibacterial Activity of Silver and Its Application in Dentistry, Cardiology and Dermatology // Microorganisms. 2020. Vol. 8. P. 1400. DOI: https://doi.org/10.3390/microorganisms8091400
3. *Mousavi S. M., Hashemi S. A., Ghasemi Y*. Green synthesis of silver nanoparticles toward bio and medical applications: review study // Artif. Cells Nanomed. Biotechnol. 2018. Vol. 46. P. 855–872. DOI: https://doi.org/10.1080/21691401.2018.1517769
4. *Kuntyi O., Zozulya G., Kytsya A*. "Green" Synthesis of Metallic Nanoparticles by Sonoelectrochemical and Sonogalvanic Replacement Methods // Bioinorg. Chem. Appl. 2021. 9830644. DOI: https://doi.org/10.1155/2021/9830644
5. *Ni Z., Wang Z., Sun L., Li B., Zhao Y*. Synthesis of polyacrylic acid modified silver nanoparticles and their antimicrobial activities // Mater. Sci. Engineer. C. 2014. Vol. 41. P. 249–254. DOI: http://dx.doi.org/10.1016/j.msec.2014.04.059
6. *Kuntyi O. I., Kytsya A. R., Mertsalo I. P., Mazur A. S., Zozula G. I., Bazylyak L. I., Topchak R. V*. Electrochemical synthesis of silver nanoparticles by reversible current in solutions of sodium polyacrylate // Colloid Polym. Sci. 2019. Vol. 297. P. 689–695. DOI: https://doi.org/10.1007/s00396-019-04488-4
7. *Shepida M., Kuntyi O., Sukhatskiy Yu., Mazur A., Sozanskyi M*. Microplasma Synthesis of Antibacterial Active Silver Nanoparticles in Sodium Polyacrylate Solutions // Bioinorg. Chem. Appl. 2021. P. 4465363. DOI: https://doi.org/10.1155/2021/4465363
8. *Kuntyi O., Shepida M., Sozanskyi M., Sukhatskiy Yu., Mazur A., Kytsya A., Bazylyak L.* Sonoelectrochemical Synthesis of Silver Nanoparticles in Sodium Polyacrylate Solution // Biointerface Res. Appl. Chem. 2021. Vol. 11. P. 12202–12214. DOI: https://doi.org/10.33263/BRIAC114.1220212214
9. *Zozulya G., Kuntyi O., Mnykh R., A. Kytsya, Bazylyak L*. Synthesis of silver nanoparticles by sonogalvanic replacement on aluminium powder in sodium polyacrylate solutions // Ultrasonics Sonochemistry. 2022. Vol. 84. 105951. DOI: https://doi.org/10.1016/j.ultsonch.2022.105951
10. *Zahrana M. K., Ahmeda H. B., El-Rafie M. H*. Alginate mediate for synthesis controllable sized AgNPs // Carbohydr. Polym. 2014. Vol. 111. P. 10–17. DOI: https://doi.org/10.1016/j.carbpol.2014.03.029
11. *Stojkovska J., Djurdjevic Z., Jancic I., Bufan B., M. Milenkovic, R. Jankovic, Miskovic-Stankovic V., Obradovic B.* Comparative in vivo evaluation of novel formulations based on alginate and silver nanoparticles for wound treatments // J. Biomater. Appl. 2018. Vol. 32. P. 1197–1211. DOI: https://doi.org/10.1177/0885328218759564
12. *Pallavicini P., Arciola C. R., Bertoglio F., Curtosi S., Dacarro G., D'Agostino A., Ferrari F., Merli D., Milanese C., Rossi S., Taglietti A., Tenci M., Visai L*. Silver nanoparticles synthesized and coated with pectin: an ideal compromise for anti-bacterial and anti-biofilm action combined with wound-healing properties // J. Colloid Interface Sci. Vol. 2017. 498. P. 271–281. DOI: https://doi.org/10.1016/j.jcis.2017.03.062
13. *Dzimitrowicz A., Motyka A., Jamroz P., Lojkowska E., Babinska W., Terefinko D., Pohl P., Sledz W*. Application of Silver Nanostructures Synthesized by Cold Atmospheric Pressure Plasma for Inactivation of Bacterial Phytopathogens from the Genera *Dickeya* and *Pectobacterium* // Materials. 2018. Vol. 11, Is. 3. P. 331. DOI: https://doi.org/10.3390/ma11030331
14. *Maurya S. K., Ganeev R. A., Rout A., Guo C*. Infuence of PVP polymer concentration on nonlinear absorption in silver nanoparticles at resonant excitation // Appl. Phys. A. 2020. Vol. 126. P. 26. DOI: https://doi.org/10.1007/s00339-019-3208-2

15. *Fox C. M., Yu T., Breslin C. B*. Electrochemical formation of silver nanoparticles and their catalytic activity immobilised in a hydrogel matrix // Colloid Polym. Sci. 2020. Vol. 298. P. 549–558. DOI: https://doi.org/10.1007/s00396-020-04624-5
16. *Kuntyi O. I., Kytsya A. R., Bondarenko A. B., Mazur A. S., Mertsalo I. P., Bazylyak L. I*. Microplasma synthesis of silver nanoparticles in PVP solutions using sacrificial silver anode // Colloid Polym. Sci. 2021. Vol. 299. P. 855–863. DOI: https://doi.org/10.1007/s00396-021-04811-y
17. *Shepida M. V., Sozanskyi M. A., Sukhatskiy Yu. V., Mazur A. S., Kuntyi O. I*. Sonoelectrochemical synthesis of silver nanoparticles in polyvinylpyrrolidone solutions // Chem. Technol. Appl. Substanc. 2021. Vol. 4. P. 82-87. DOI: https://doi.org/ 10.23939/ctas2021.01.082
18. *Mandal P., Ghosh S*. Green synthesis of poly(vinyl alcohol)–silver nanoparticles hybrid using Palash (Butea monosperma) flower extract and investigation of antibacterial activity // Polym. Bull. 2018. Vol. 75. P. 1949–1955. DOI: https://doi.org/10.1007/s00289-017-2137-5
19. *Surudžić R., Jovanović Ž., Bibić N., Nikolić B., Mišković-Stanković V*. Electrochemical synthesis of silver nanoparticles in poly(vinyl alcohol) solution // J. Serb. Chem. Soc. 2013. Vol. 78. P. 2087–2098. DOI: https://doi.org/10.2298/JSC131017124S
20. *Vos C., Baneton J., Witzke M., Dille J., Godet S., Gordon M. J., Sankaran R. M., Reniers F*. A comparative study of the reduction of silver and gold salts in water by a cathodic microplasma electrode // J. Phys. D: Appl. Phys. 2017. P. 105206. DOI: https://doi.org/10.1088/1361-6463/AA5608
21. *Bazylyak L., Kytsya A., Karpenko O., Prokopalo A., Pokynbroda T., Mazur A., Kuntyi O*. Synthesis of silver nanoparticles using the rhamnolipid biocomplex of microbial origin // Visnyk Lviv University. Series Chem. 2020. No 61. Pt. 2. P. 404–413. DOI: http://dx.doi.org/10.30970/vch.6102.404
22. *Kuntyi O., Mazur A., Kytsya A., Karpenko O., Bazylyak L., Mertsalo I., Pokynbroda T., Prokopalo A.* Electrochemical synthesis of silver nanoparticles in solutions of rhamnolipid // Micro Nano Lett. 2020. Vol. 15. P. 802–807. DOI: https://doi.org/10.1049/mnl.2020.0195
23. *Shepida M., Kuntyi O., Sozanskyi M., Sukhatskiy Yu.* Sonoelectrochemical Synthesis of Antibacterial Active Silver Nanoparticles in Rhamnolipid Solution // Adv. Mater. Sci. Engineer. 2021. 7754523. DOI: https://doi.org/10.1155/2021/7754523
24. *Bazylyak L., Kytsya A., Karpenko I., Karpenko O.* Synthesis and antimicrobial activity of silver nanoparticles stabilized by citrate anions // Proc. Shevchenko Sci. Soc. Chem. Sci. 2020. Vol. LX. P. 127–135. DOI: https://doi.org/10.37827/ntsh.chem.2020.60.127
25. *Thuc D. T., Huy T. Q., Hoang L. H., Tien B. C., Chung P. V., Thuy N. T., Le A.-T*. Green synthesis of colloidal silver nanoparticles through electrochemical method and their antibacterial activity // Mater. Lett. 2016. Vol. 181. P. 173–177. DOI: https://doi.org/10.1016/j.matlet.2016.06.008
26. *Weerasinghe J., Li W., Zhou R., Zhou R., Gissibl A., Sonar P., Speight R., Vasilev K., Ostrikov K.* Bactericidal Silver Nanoparticles by Atmospheric Pressure Solution Plasma Processing // Nanomater. 2020. Vol. 10. P. 874. DOI: https://doi.org/10.3390/nano10050874
27. *Ershov B. G., Henglein A.* Reduction of Ag^+ on Polyacrylate Chains in Aqueous Solution // J. Phys. Chem. B. 1998. Vol. 102. P. 1066310666. DOI: https://doi.org/10.1021/jp981906i
28. *Simeonova S., Georgiev P., Exner K. S., Mihaylov L., Nihtianov D., Koynov K., Balashe K.* Kinetic study of gold nanoparticles synthesized in the presence of chitosan and citric acid // Colloids Surf. A. 2018. Vol. 557. P. 106–115. DOI: https://doi.org/10.1016/j.colsurfa.2018.02.045
29. *Kyrychenko A., Blazhynska M. M., Slavgorodska M. V., Kalugin O. N*. Stimuli-responsive adsorption of poly(acrylic acid) onto silver nanoparticles: Role of polymer chain length and degree of ionization // J. Molec. Liq. 2019. Vol. 276. P. 243–254. DOI: https://doi.org/10.1016/j.molliq.2018.11.130
30. *Kytsya A. R., Reshetnyak O. V., Bazylyak L. I., Hrynda Y. M.* UV/VIS-spectra of silver nanoparticles as characteristics of their sizes and sizes distribution. // In: Zaikov G. E., Bazylyak L. I., Haghi A. K. (Eds.) Functional polymer blends and nanocomposites: A practical engineering approach, 1st edn. Apple Academic Press, 2014, New York, pp. 231–239. DOI: https://doi.org/10.1201/b16895

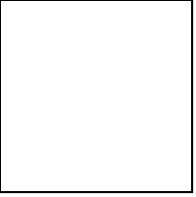

Chapter 7

KINETICS OF NANOSTRUCTURING AND PHYSICOCHEMICAL PROPERTIES OF AMORPHOUS ALLOYS OF THE Co-Si-B SYSTEM

M. M. Lopachak, L. M. Boichyshyn, and O. V. Reshetnyak

Ivan Franko National University of Lviv, 79005 Lviv, Ukraine

Corresponding author: mariia.lopachak@lnu.edu.ua

Contents

Abstract

The process of crystallization of amorphous alloys $Co_{77}Si_{11}B_{12}$, $Co_{72}Fe_5Si_{11}B_{12}$, $Co_{72}Fe_{2,5}Cr_{2,5}Si_{11}B_{12}$ at heating rates of 5, 10 and 20 K/min was investigated by the method of differential scanning calorimetry. The formation of three exothermic peaks is observed, the first of which corresponds to the process of AMA nanocrystallization. The calculated activation energies of AMA nanostructuring processes have high values in range from 266 to 481 kJ/mol. Alloying of the alloy with iron and chromium leads to an increase in thermal stability and to a change in the mechanism of AMA nanocrystallization. The growth of nanocrystals in the amorphous matrix of $Co_{77}Si_{11}B_{12}$ alloy occurs mainly by the 3D mechanism, while in $Co_{72}Fe_5Si_{11}B_{12}$ and $Co_{72}Fe_{2,5}Cr_{2,5}Si_{11}B_{12}$ the growth of nanocrystals occurs by the 2D mechanism. Identified by the X-ray diffraction method, Co_3B, Co_2Si and β-Co phases are formed in the amorphous matrix by isothermal and non-isothermal heating of the alloy. The increase in the magnetization of the AMA as a result of heating the alloy, which is explained by the formation of Co_3B crystals in the amorphous matrix, has been confirmed. The corrosion resistance of cobalt-based AMA was studied by cyclic voltammetry in an aqueous medium of 1 M KOH solution in the temperature range from 293 to 333 K.

7.1 Introduction

Amorphous metallic alloys (AMA) are of particular interest due to their unique physicochemical properties, which allow the practical application of AMA in various industries. Due to the absence of a crystalline structure, amorphous metal alloys have high strength and elasticity, excellent corrosion resistance, and wear resistance [1]. In turn, due to their extremely soft magnetic properties, cobalt-based amorphous ribbon alloys are used for the production of highly sensitive magnetic sensors, information carriers, security systems, power transformers, magnetic shielding, and magnetic heads for recording and storing information [2].

One of the important issues in the study of such alloys is the study of the features of their transformation from an amorphous state to a crystalline state, in particular to a nanocrystalline state. It is known that nanocrystallization changes the physical and chemical properties of AMA, in particular, it affects the magnetic properties [3, 4]. Therefore, it is relevant to study the kinetics of AMA nanostructuring, in particular the direction of growth of nanocrystals, on which the properties of these materials directly depend. Understanding the processes of nanocrystallization of amorphous alloys provides new opportunities to control the structure, which makes it a valuable subject of research. In addition, it is equally important to assess the impact of an aggressive environment on the change in their corrosion resistance [5].

To expand the scope of applications of cobalt-based alloys, it is necessary to find out the effect of heat treatment on the structure and properties of the amorphous alloy and to investigate the composition of the formed nanocrystalline phase in the amorphous matrix.

7.2 Phase Transformations of Amorphous Alloys under the Influence of Temperature Treatment

Under the influence of temperature treatment, amorphous alloys, which are metastable systems, change to a crystalline state. Crystal cells of compounds that can be formed during the crystallization of an alloy of the Co-Si-B system are shown on Fig. 7.1 Cobalt-based alloys are characterized by three stages of the crystallization process. The authors of [6] investigated that during the first stage of crystallization of alloys with this composition, Co-based crystals with a hexagonal close-packed structure α-Co are formed. Crystals with a face-centered cubic structure β-Co can be formed in alloys with Fe and Cr. At the second stage of crystallization of the alloy, associated with the decay of the residual amorphous phase, the formation of a metastable phase with a Co_3B type structure can be observed in the alloy $Co_{70}Fe_5Si_{10}B_{15}$ [7]. The formation of β-Co, α-Co, Co_3B, and Co_2Si structures occurs in the amorphous matrix of the $Co_{70}Fe_5Si_{10}B_{15}$ alloy during heating. The activation energy of the formation of these structures is 500, 453, 510, and 460 kJ/mol, respectively. At the final stage of crystallization, the formation of a mixture of Co, Co_2B, Co_2Si, and Co_3B structures is possible [8]. It is also possible to form a compound of the composition Co_5Si_2B [9] and CoSi [10], which is unlikely. During the crystallization process, β-Co, α-Co, Co_2B, and Co_2Si are formed in the $Co_{70.3}Fe_{4.7}Si_{10}B_{15}$ alloy matrix [11].

The growth of both forms of β-Co and α-Co crystals is observed at temperatures below 740 K. The ratio of β-Co, and α-Co structures depends on the grain size. The content of α-Co will be higher due to the small size of the grains, while in the opposite case the structure of β-Co will prevail [7].

The curves of differential scanning calorimetry (DSC) for the original amorphous Co-based alloys were obtained at the Institute of Materials Science of the University of Silesia in Katowice on a Perkin-Elmer Pyris 1 calorimeter. The received data are processed using standard application software for the device.

The activation energy E_a for the crystallization process is determined according to the Kissinger equations [12]:

$$ln\frac{T^2}{\beta} = \frac{E_a}{RT} + B, \tag{7.1}$$

where b is the sweep speed of DSC curves, E_a is the activation energy of the crystallization process, R is the universal gas constant, T is the temperature that corresponds to the maximum on the DSC curve, B is a constant.

To indicate the exact mechanisms of growth of the crystalline phase in alloys, the Matusita model was used [13]:

$$\ln\left[-\ln(1-\alpha)\right] = -nln(\beta) - 1.052\frac{mE_a}{RT} + C, \tag{7.2}$$

where α is the volume fraction of the crystalline phase, n is the Avrami index, m is the growth dimension, T is the temperature, C is the constant.

With the help of the Matusita model, the Avrami index and the dimensionality of crystal growth during AMA crystallization are determined, as well as the growth mecha-

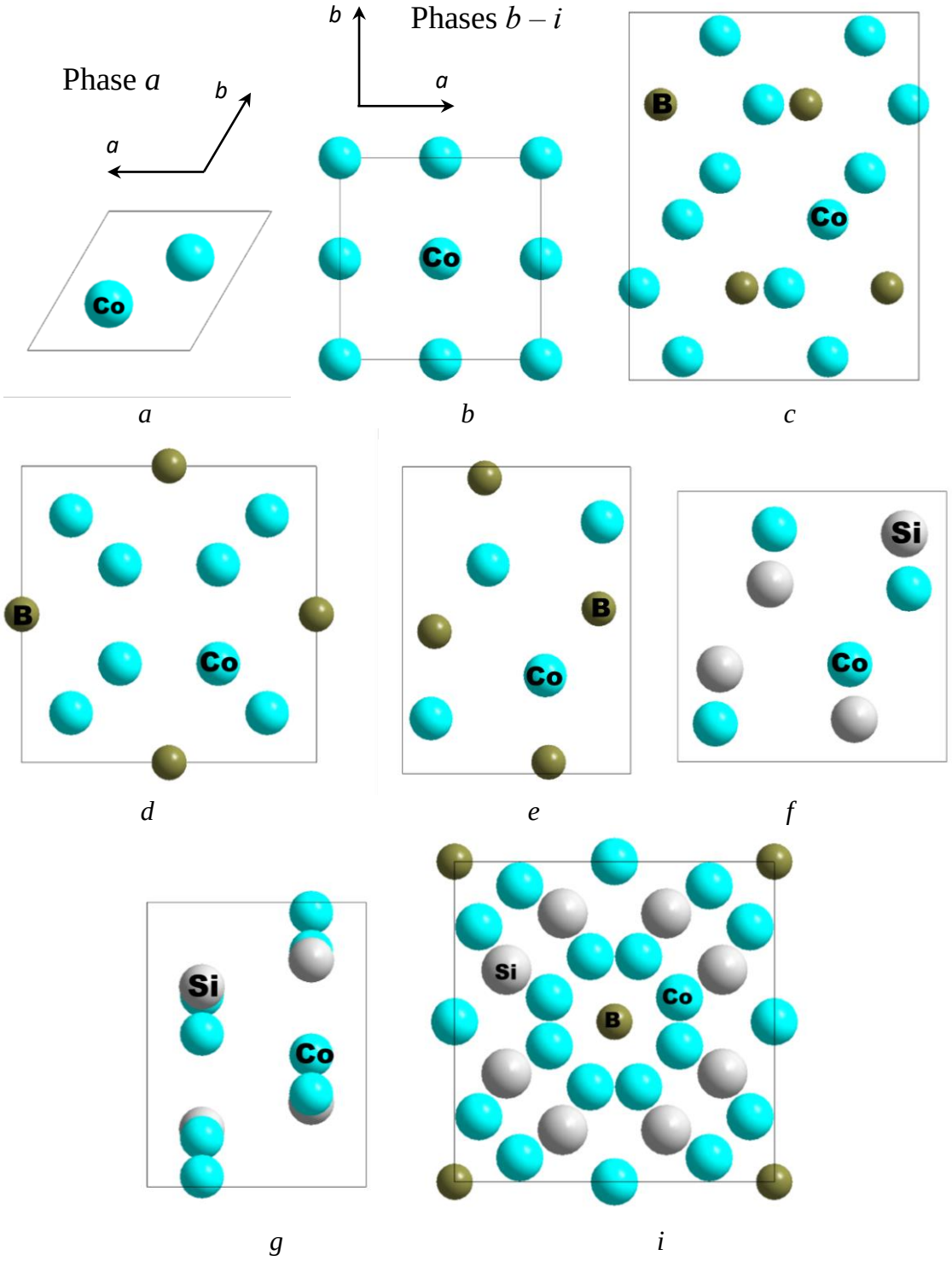

Figure 7.1 Crystal lattices of the nanocrystalline phase α-Co (*a*), β-Co (*b*), Co_3B (*c*), Co_2B (*d*), CoB (*e*), CoSi (*f*), Co_2Si (*g*), and Co_5Si_2B (*i*)

nism of crystalline phases can be estimated using this method. The Avrami index (n) can also be determined by the formula:

$$n = p + bm, \tag{7.3}$$

where b is a parameter that shows the rate of nucleation, and p is a parameter that shows the type of transformation.

The process of AMA structuring and possible phase transitions were investigated in the temperature range of 660...870 (±5) K. The study was carried out at three heating rates of 5, 10 and 20 K/min. In the case of the AMA of the Co-Si-B system, at all three heating rates, three exothermic peaks are observed, which are characteristic of crystallization processes (Fig. 7.2). When the heating rate increases, there is some shift of the exothermic maxima to higher temperatures, which indicates the dependence of the amorphous phase crystallization process on the diffusion rate of atoms. The process of nanocrystallization corresponds to the first exothermic peak, which appears in the temperature range from 761 to 822 (±5) K at different heating rates.

It was established that doping AMA with iron generally does not affect the change in the temperature of the beginning of the structuring process, which corresponds to the process of nanocrystallization, while doping with iron and chromium leads to a shift of the first exothermic peak by 30 K to the zone of higher temperatures.

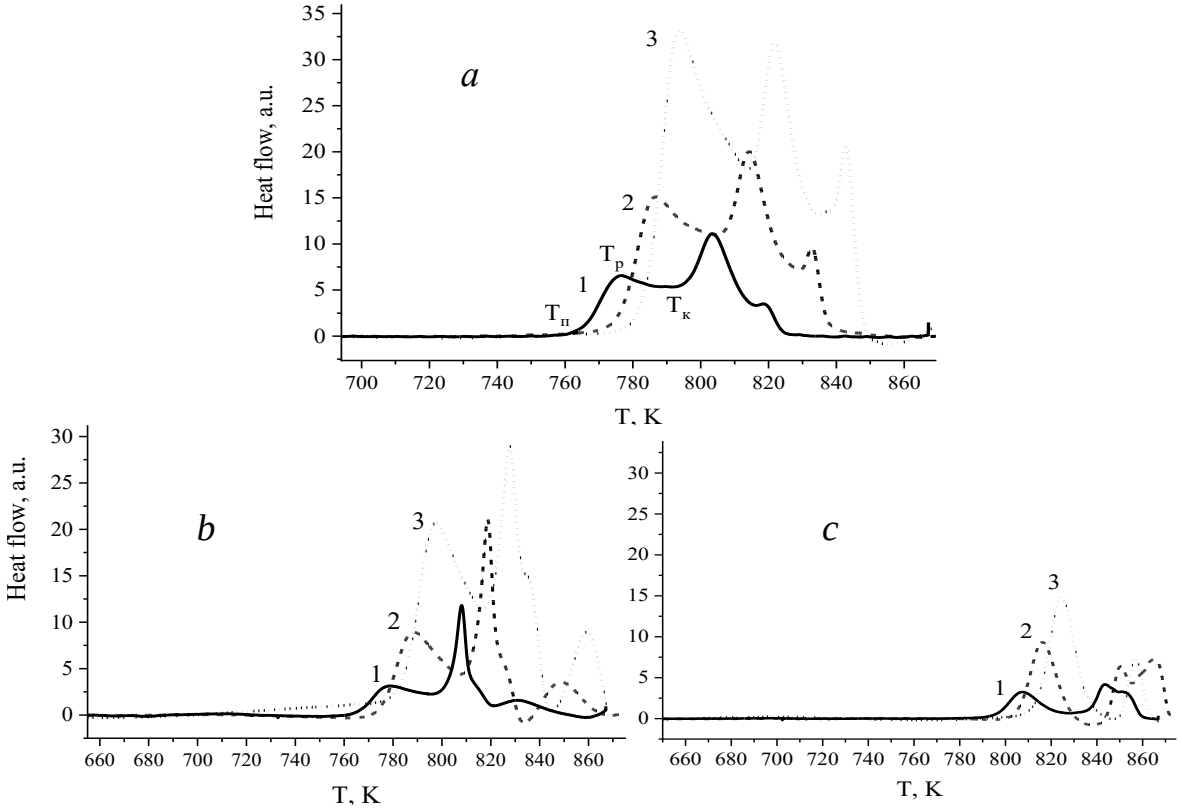

Figure 7.2 DSC curves of amorphous alloy $Co_{77}Si_{11}B_{12}$ (*a*), $Co_{72}Fe_5Si_{11}B_{12}$ (*b*), $Co_{72}Fe_{2,5}Cr_{2,5}Si_{11}B_{12}$ (*c*) under the heating rates β, K/min: *1* – 5; *2* – 10; *3* – 20

Table 7.1 Thermodynamic characteristics of the structuring of the AMA alloy of the Co-Si-B system

Peak	β, K/min	T_s, K	$E_{a(n)}$, kJ/mol	T_p, K	$E_{a(p)}$, kJ/mol	T_e, K	$E_{a(c)}$, kJ/mol
			$Co_{77}Si_{11}B_{12}$				
1	5	761	347	776	374	788	266
	10	771		787		804	
	20	780		794		814	
2	5	792	323	804	429	816	391
	10	804		814		829	
	20	814		821		834	
3	5	816	327	819	314	827	338
	10	829		833		839	
	20	839		843		850	
			$Co_{72}Fe_5Si_{11}B_{12}$				
1	5	765	474	777	344	793	294
	10	773		787		807	
	20	779		797		817	
2	5	793	294	807	350	821	319
	10	807		819		833	
	20	817		828		845	
3	5	821	319	831	283	858	567
	10	833		848		869	
	20	845		858		870	
			$Co_{72}Fe_{2,5}Cr_{2,5}Si_{11}B_{12}$				
1	5	795	481	807	437	820	290
	10	802		816		836	
	20	810		824		846	
2	5	830	482	843	576	849	423
	10	836		851		856	
	20	846		857		868	
3	5	849	584	851	269	862	320
	10	856		866		875	
	20	–		–		–	

The obtained values of activation energies of the processes of crystal phase nucleation ($E_{a(n)}$), crystal phase growth ($E_{a(p)}$), and crystal growth completion ($E_{a(c)}$) are listed in Table 7.1. Depending on the content and nature of the alloying addition, there are differrences in the values of activation energies of kinetic processes, however, high activation energy values are observed in all alloys, indicating complex diffusion processes in the amorphous matrix during heating.

The value of the activation energy of the nanocrystallization process for the unalloyed alloy $Co_{77}Si_{11}B_{12}$ is the lowest, while for the alloy alloyed with iron and chromium $Co_{72}Fe_{2,5}Cr_{2,5}Si_{11}B_{12}$ this value is the highest. This confirms the creation of diffusion barrier layers by chromium, which inhibit the growth of nanocrystals during heating. Accordingly, cobalt-based AMA can be ranked in the following order by their ability to preserve amorphousness and thermal stability:

$$Co_{72}Fe_{2,5}Cr_{2,5}Si_{11}B_{12} > Co_{72}Fe_5Si_{11}B_{12} > Co_{77}Si_{11}B_{12}.$$

From the DSC curves, the kinetic parameter α (volume fraction of the transformed structure from the amorphous state to the nanocrystalline state) was also calculated accordingly to equation $\alpha = S_i/S_S$, where S_i is the area between the beginning of the peak and any other peak point, S_S is the total area of the exothermic peak. Figure 7.3 shows dependences of the α on the temperature for the first exothermic peak, which corresponds to the nanostructuring of the system at different heating rates. The *s*-shaped form of the dependences indicates the dominance of diffusion-controlled processes.

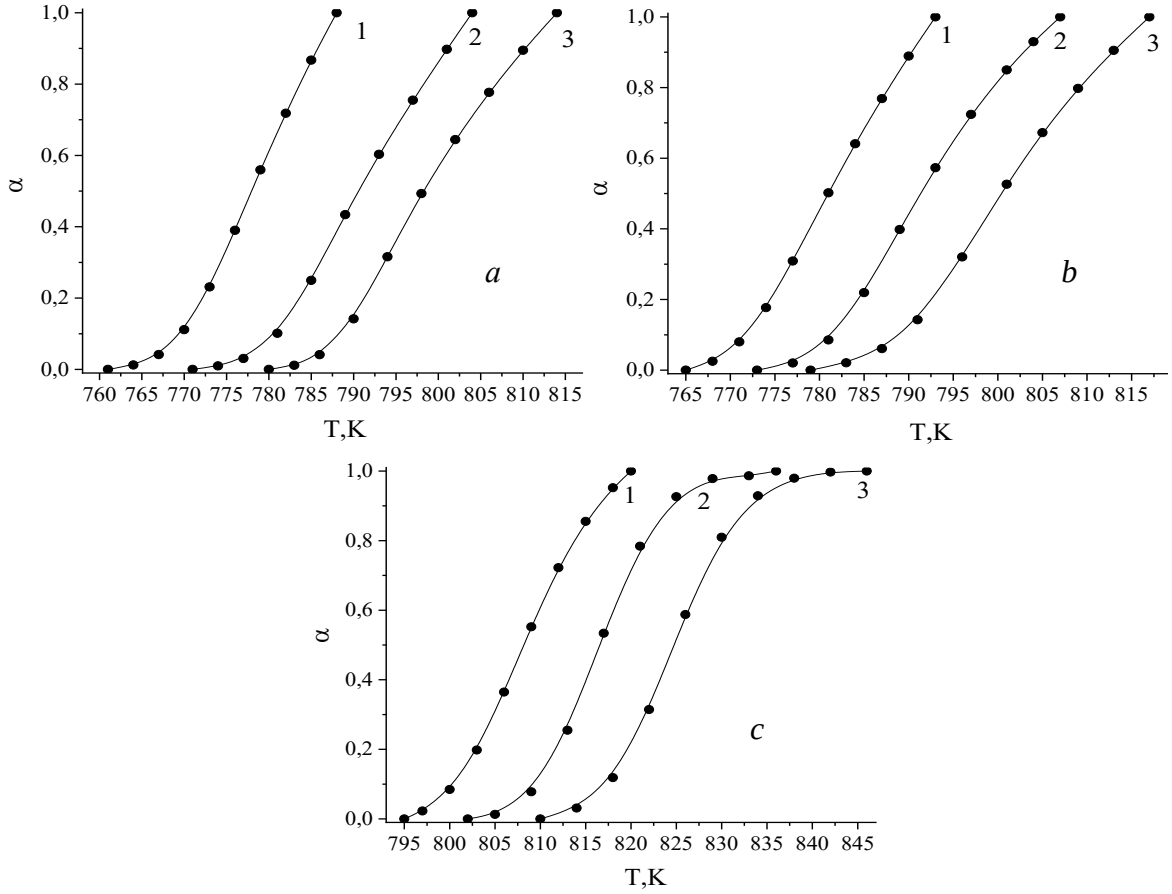

Figure 7.3 The degree of crystallization (α) of the AMA $Co_{77}Si_{11}B_{12}$ (*a*), $Co_{72}Fe_5Si_{11}B_{12}$ (*b*), $Co_{72}Fe_{2,5}Cr_{2,5}Si_{11}B_{12}$ (*c*) as a function of temperature at three different heating rates, K/min: *1* – 5; *2* – 10; *3* – 20

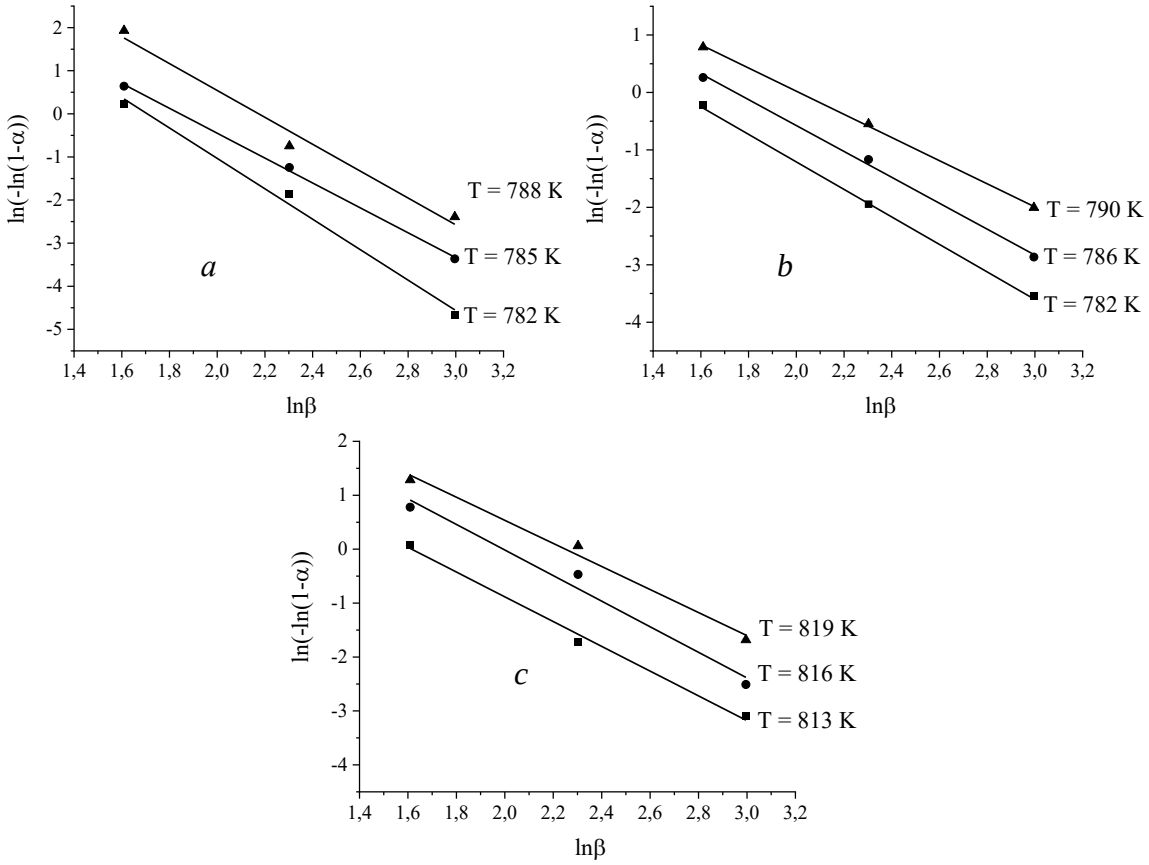

Figure 7.4 $ln(-ln(1-\alpha))$ as a function of the heating rate at a constant temperature for the alloys $Co_{77}Si_{11}B_{12}$ (*a*), $Co_{72}Fe_5Si_{11}B_{12}$ (*b*), $Co_{72}Fe_{2,5}Cr_{2,5}Si_{11}B_{12}$ (*c*).

The Avrami exponent for the first stage of crystallization of cobalt-based alloys was calculated from the dependence of $ln(-ln(1-a))$ on $ln\,\beta$ at a constant temperature (Fig. 7.4). The value of the Avrami index for $Co_{77}Si_{11}B_{12}$ is in the range of 2.9...3.5, while for $Co_{72}Fe_5Si_{11}B_{12}$, $Co_{72}Fe_{2,5}Cr_{2,5}Si_{11}B_{12}$ it is 2.0...2.4 and 2.1...2.4, respectively. This indicates that doping the alloy with iron and chromium leads to a change in the AMA crystallization mechanism. In addition, the kinetic growth parameter *m* was obtained from the dependence of *ln(-ln(1-a)* on temperature at constant heating rates (Fig. 7.5).

The obtained values of the kinetic parameters from the Matusita curves are presented in Table 7.2. The process of crystallization of AMA based on cobalt depends on the heating rate and the nature of the dopant, which is indicated by the value of the kinetic parameter *m*. It was established that the growth of nanocrystals in the amorphous matrix of the $Co_{77}Si_{11}B_{12}$ alloy at heating rates of 5 and 10 K/min occurs by a 3D mechanism, while at a higher rate, by a 2D mechanism. For an alloy with alloyed iron, the growth of nanocrystals at all speeds occurs according to a 2D mechanism. In the case of an alloy alloyed with chromium and iron, at a low heating rate, nanocrystallization occurs according to a 3D mechanism, while at higher speeds, it occurs according to a 2-dimensional mechanism.

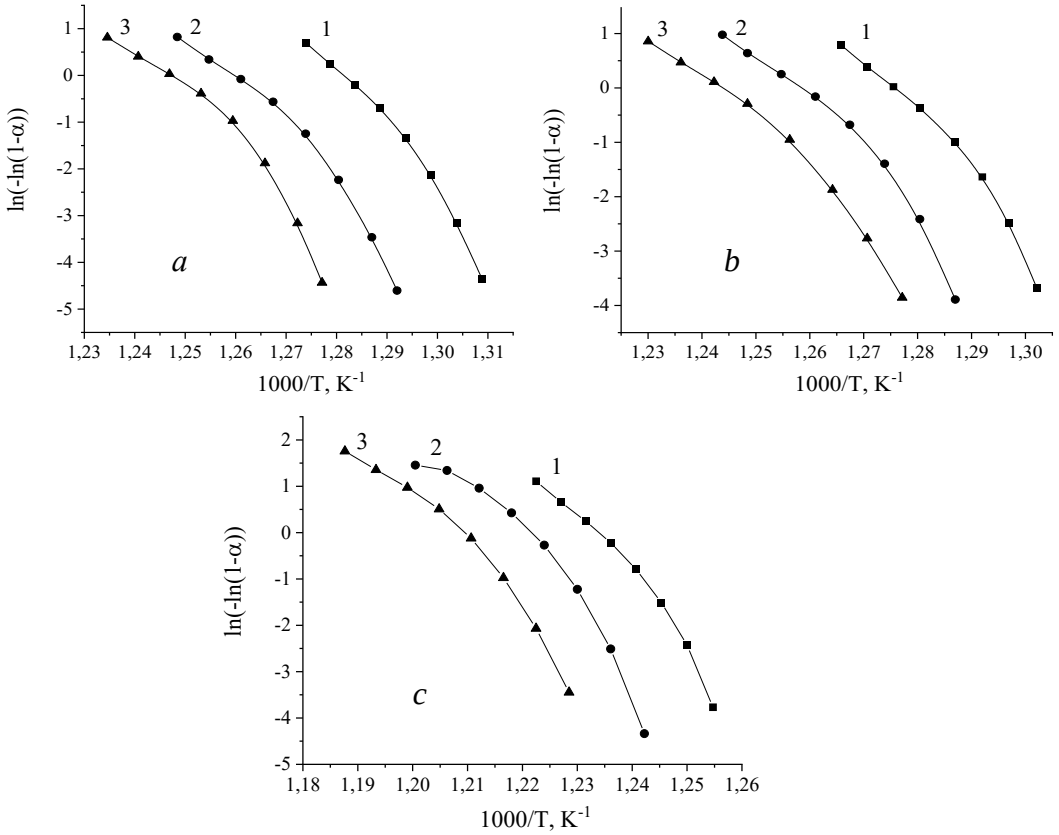

Fig. 5 *ln(-ln(1-a)* as a function of temperature at three different heating rates (1 – 5 K/min; 2 – 10 K/min; 3 – 20 K/min) for the alloy $Co_{77}Si_{11}B_{12}$ (*a*), $Co_{72}Fe_5Si_{11}B_{12}$ (*b*), $Co_{72}Fe_{2,5}Cr_{2,5}Si_{11}B_{12}$ (*c*)

Table 7.2 Kinetic parameters of the growth of nanocrystals in the structure of alloys under the influence of temperature for the first maximum on DSC curves according to the Matusita model

T, K	*n*	*b*, K/min	*m*	*p*	*b*
$Co_{77}Si_{11}B_{12}$					
782	3,5	5	2,9 ≈ 3	0,5	1,7 > 1
785	2,9	10	2,6 ≈ 3	0,5	1,7 > 1
788	3,1	20	2,4 ≈ 2	0,5	2,2 > 1
$Co_{72}Fe_5Si_{11}B_{12}$					
782	2,4	5	2,1 ≈ 2	0,5	1,2 > 1
786	2,2	10	1,9 ≈ 2	0,5	1,2 > 1
790	2,0	20	1,8 ≈ 2	0,5	1,2 > 1
$Co_{72}Cr_{2,5}Fe_{2,5}Si_{11}B_{12}$					
813	2,3	5	2,6 ≈ 3	0,5	1,0 > 1
816	2,4	10	2,4 ≈ 2	0,5	1,2 > 1
819	2,1	20	2,2 ≈ 2	0,5	1,2 > 1

The value p = 0.5 for $Co_{77}Si_{11}B_{12}$, $Co_{72}Fe_5Si_{11}B_{12}$, $Co_{72}Fe_{2,5}Cr_{2,5}Si_{11}B_{12}$ indicates diffusion-controlled nanocrystallization. Analyzing the obtained values of the kinetic parameter *b* for the process of nanocrystallization of all studied alloys, it was established that during nanocrystallization, an increase in the rate of nucleation of nanocrystals in all studied AMA based on cobalt is likely.

7.3 Study of Amorphous Alloys by X-ray Diffraction Method

X-ray structural analysis is a diffraction method of studying the structure of a substance, which is based on the phenomenon of X-ray diffraction on a 3D crystal lattice. This method allows to determine the atomic structure of a substance, which includes the spatial group of the unit cell, its dimensions and shape, as well as determine the symmetry group of the crystal.

Diffraction patterns of the original and non-isothermally annealed AMA were recordered on an X-Pert Philips PW 3040/60 X-ray diffractometer using CuKα radiation and an X'Cellerator counter. Diffraction patterns of isothermally annealed AMA samples were obtained on a DRON-2.0M X-ray diffractometer (FeKα radiation). Phase analysis was performed using the Powder Cell program. Phases were identified by comparing experimentally obtained diffraction patterns with theoretically calculated diffraction patterns of known compounds.

Cobalt-based AMA was investigated [14] by X-ray diffraction in order to establish the phase composition of the structure before and after heating. Figure 7.6 shows the diffractograms of the original and non-isothermally annealed AMA $Co_{77}Si_{11}B_{12}$ at a heating rate of 10 K/min to the temperatures of the beginning of crystallization, which correspond to three peaks from the DSC curves at 771, 804, and 829 (±5) K. It can be seen that the halo sharpens on the diffractogram, reflections of the formation of clusters and nanocrystals are observed. Phases were identified by comparing experimentally obtained diffraction patterns with theoretically calculated diffraction patterns of known compounds.

It was established that an increase in the heating temperature leads to the formation of two components of the crystalline phase: Co_3B and Co_2Si (Fig. 7.7). The appearance of peaks at $2\theta \approx 43^o$ and 61^o indicates the presence of phases that do not correspond to the currently known phases.

Annealing the sample for 1 hour at 765 K caused changes in the profile of the diffractograms (Fig. 7.8). The appearance of a pre-peak at $2\theta \approx 16.5^o$ and other three broad peaks at $2\theta \approx 43^o$, 55^o, and 82^o indicates the formation of clusters in the amorphous matrix and *β*-Co nanocrystals embedded in the amorphous matrix with a lattice parameter $a \approx 3.51$ Å.

Crystal formation processes correspond to exothermic peaks on DSC curves. Therefore, the crystallization process and the phases formed can be easily identified, and the sequence is expressed as follows:

$$\text{Amorphous alloy} \rightarrow Co_3B + Co_2Si + \beta\text{-Co}.$$

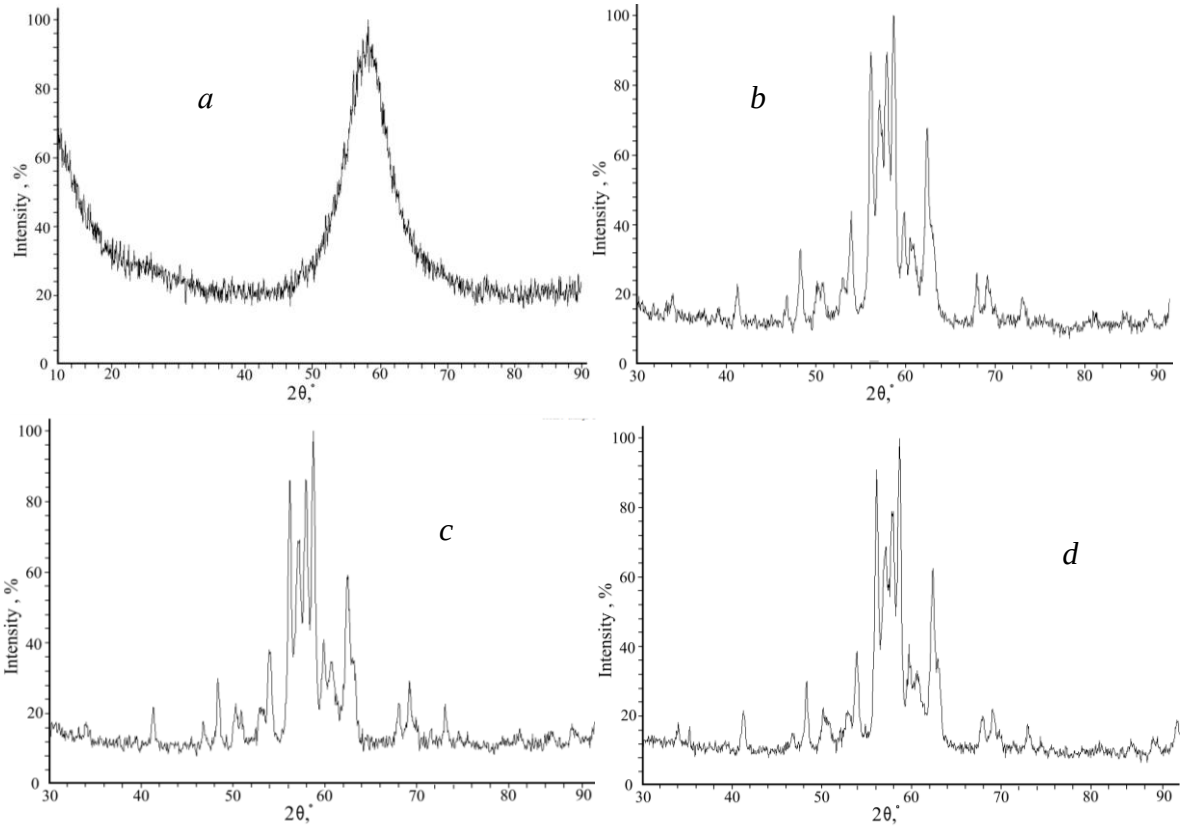

Figbre 7.6 Diffractograms of AMA $Co_{77}Si_{11}B_{12}$ initial (*a*) and annealed non-isothermally at a heating rate of 10 K/min to temperatures 771 (*b*), 804 (*c*), and 829 (*d*) (±5) K.

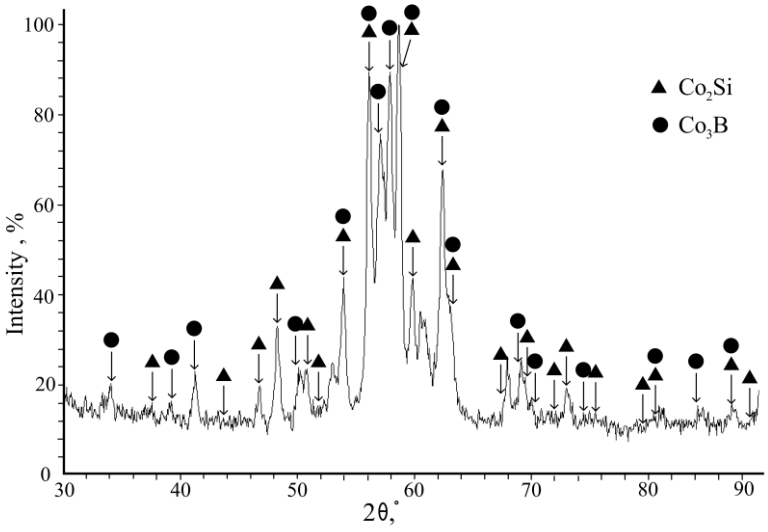

Figure 7.7 Diffractograms of AMA $Co_{77}Si_{11}B_{12}$ annealed non-isothermally at a heating rate of 10 K/min to a temperature of 771 K (±5) K

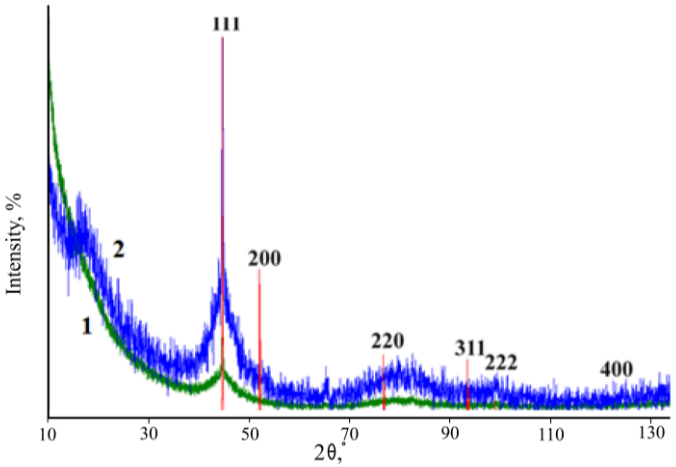

Figure 7.8 AMA diffractograms of initial (*1*) and annealed (*2*) $Co_{77}Si_{11}B_{12}$ at 765 K. Theoretical peaks and their Miller indices are given for *β*-Co with cell parameter *a* = 3.54 Å.

Comparison of SEM images of the surface of cobalt-based AMA samples before and after non-isothermal annealing indicates the absence of visible structural changes on the surface of the alloy, indicating the formation of crystals in the nanoscale system (Fig. 7.9).

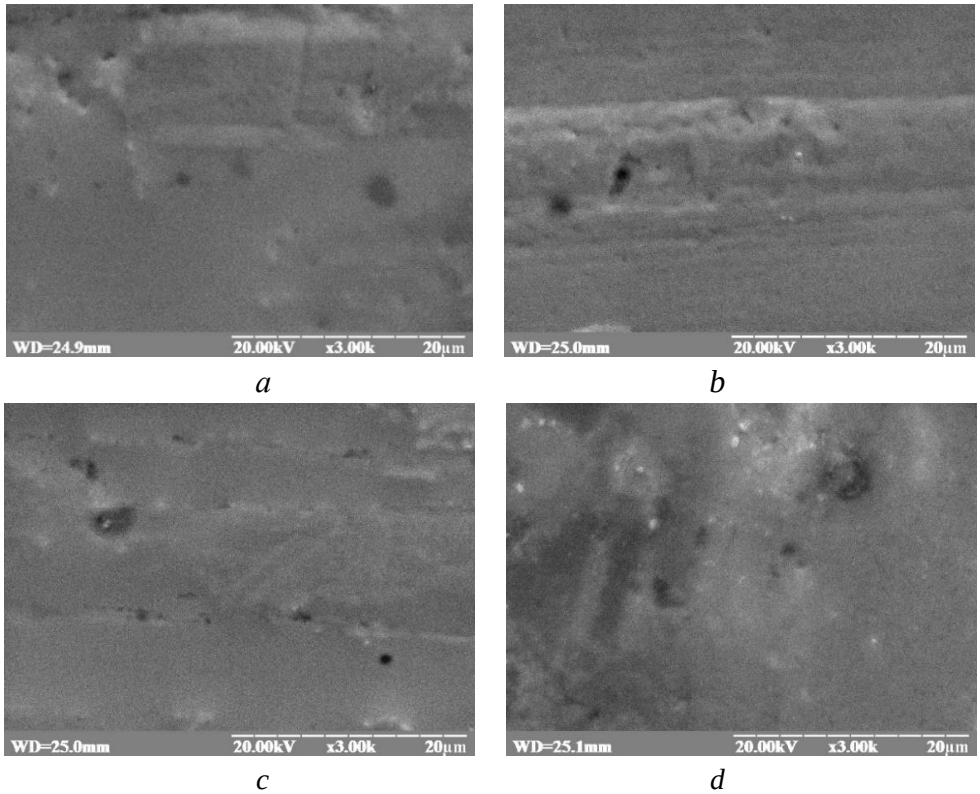

Figure 7.9 SEM image of the contact surface of the initial $Co_{77}Si_{11}B_{12}$ (*a*) and non-isothermally annealed at a heating rate of 10 K/min to temperatures of 771 (*b*), 804 (*c*), and 829 (*d*) (±5) K.

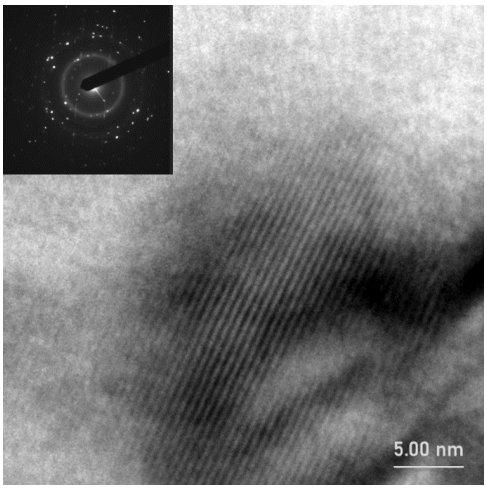

Figbre 7.10 TEM image of crystals in the amorphous structure of the alloy $Co_{72}Cr_{2,5}Fe_{2,5}Si_{11}B_{12}$.

Also, the presence of a nanocrystalline phase in the structure of the $Co_{72}Cr_{2,5}Fe_{2,5}Si_{11}B_{12}$ alloy after heating was confirmed by the method of high-resolution transmission electron spectroscopy (Fig. 7.10).

7.4. Corrosion Resistance of Amorphous Metal Alloys $Co_{77}Si_{11}B_{12}$ as Electrodes in Hydrogen Evolution Reactions in Alkaline Solution

Cobalt-based AMA have increased corrosion resistance and soft magnetic properties, which makes them a relevant object for research. They were used for cutting tools working in aggressive chemical environments, in the production of serial television and devices [15, 16]. Attention is also drawn to the possible use of ternary electrodes based on Co as electrocatalytic materials in hydrogen evolution reactions from alkaline solutions [17]. Expanding the use of AMA requires evaluating the impact of an aggressive environment on the corrosion resistance of cobalt-based alloys. Thus, the authors of [18] investigated that at a solution temperature of 310 K, the amorphous metal alloy of the $Co_{70}Fe_5Si_{15}B_{10}$ composition shows low corrosion resistance, but the chromium-doped alloy $Co_{67}Fe_3Cr_3Si_{15}B_{12}$ shows high corrosion resistance. While the addition of Cr improves the passivation of the surface layer of the amorphous $Co_{73,5}Si_{13,5}B_9Nb_3Cu_1$ alloy, thereby reducing the corrosion rate. Although increasing the Cr content to 8 at. % tends to stabilize the passive layer, the corrosion rate remains very high and the alloys are dissolved or severely damaged in 1, 2, and 5 M H_2SO_4 solution [19].

Cobalt-based AMAs were tested [20] as hydrogen release electrodes and their corrosion resistance in aqueous KOH solution was investigated by voltammetry method (VA) (Fig. 7.11). It was found that due to the increase in the temperature of the solution, the processes of oxidation of the surface of the electrodes intensify, which is manifested in the corrosion characteristics.

In particular, the corrosion potential ($E_{cor.}$) shifts to the cathodic side from –0.78±0.05 V at 293 K to –0.91±0.05 V at 333 K, which indicates a decrease of the thermodynamic

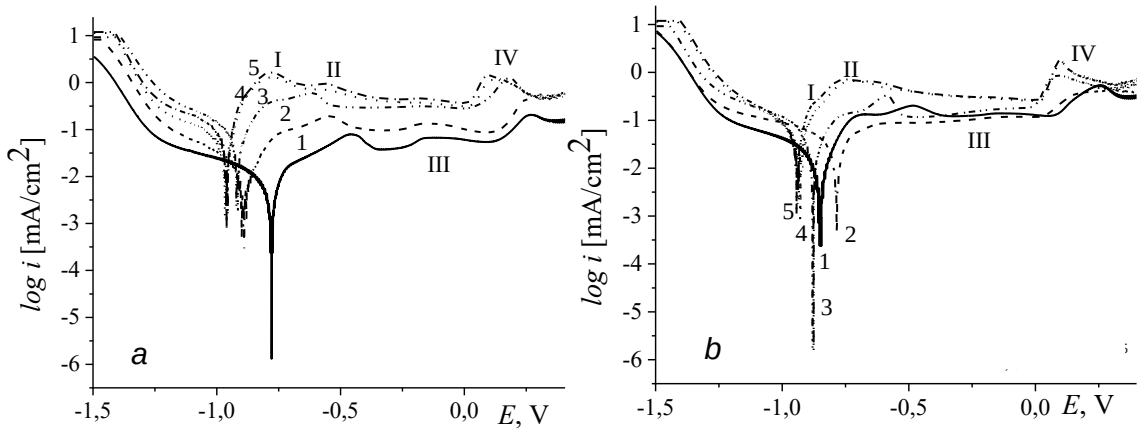

Figure 7.11 Voltammograms (VA) of the AMA $Co_{77}Si_{11}B_{12}$ in the 1 M KOH aqueous solution before (*a*) and after (*b*) hydrogen evolution under the temperature (±0,5 K), K: *1* – 293; *2* – 303; *3* – 313; *4* – 323; *5* – 333. I, II, III, IV – number of maximum.

stability of the surface and their easier oxidation (Fig. 7.12). The growth of the corrosion current density ($i_{cor.}$) is directly proportional to the concentration of ions of electrochemically active components of the alloy. The concentration of cobalt ions increases at the boundary between AMA and 1M aqueous KOH solution.

The corrosion activation energy ($E_{a,\,cor.}$) of AMA in the entire temperature range of the solution at different times of potential scanning was calculated, which is 18.7 and 17.9 kJ/mol for the first and fifth cycles of the CVA, respectively. When scanning the potential in the anode direction up to +0.5 V, four maxima are clearly visible on the anode branch of the CVA of the Co-Si-B system, which correspond to surface passivation at:

E_1 = –0.78…–0.81 V; E_2 = –0.61…–0.45 V; E_3 = –0.18…–0.16 V; E_4 = 0.11… 0.23 V.

Based on the current density of the maxima, the activation energy of the formation of oxidation compounds of the alloy surface was calculated: $E_{a,1}$ = 57.6, $E_{a,2}$ = 27.7, $E_{a,3}$ =

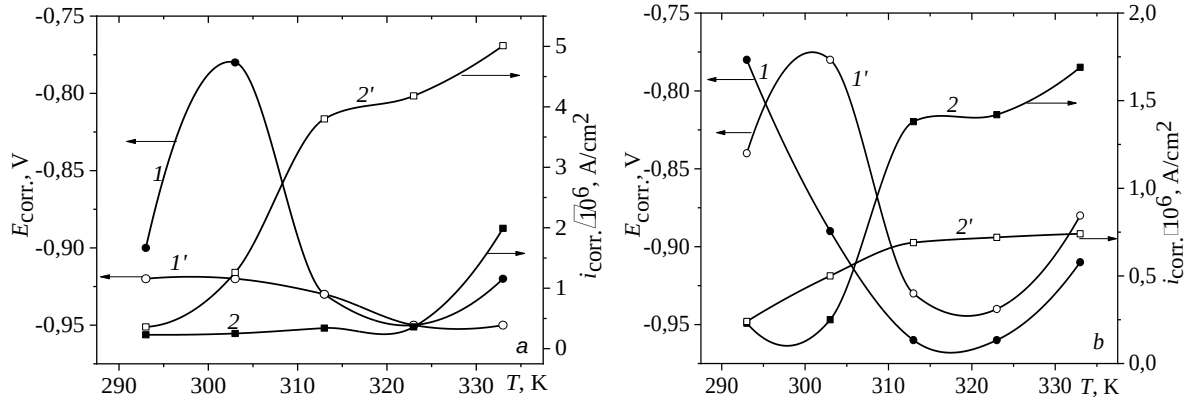

Figure 7.12 Dependence of potential (*1*, *1'*) and current density (*2*, *2'*) of AMA-electrodes $Co_{77}Si_{11}B_{12}$ in 1.0 M KOH solution (5th cycle) on the solution temperature before (*a*) and after (*b*) hydrogen evolution. 1st cycle - *1*, *2*; 5th cycle - *1'*, *2'*.

Table 7.3 Tafel equation coefficients *a* (V) and *b* (V) of AMA $Co_{77}Si_{11}B_{12}$ at different temperatures in 1 M KOH solution (5th VA cycle)

T, K	$a_{Red.}$	b_{Red}	a_{Ox}	$b_{Ox.}$	$a_{Red.}$	b_{Red}	a_{Ox}	b_{Ox}
	before hydrogen evolution				after hydrogen evolution			
293	–0.90	–0.04	–0.66	0.02	–1.02	–0.07	–0.68	0.07
303	–1.01	–0.04	–0.68	0.04	–1.00	–0.04	–0.62	0.08
313	–1.08	–0.06	–0.88	0.05	–1.03	–0.05	–0.86	0.03
323	–1.11	–0.10	–0.91	0.09	–1.09	–0.09	–0.87	0.04
333	–1.08	–0.11	–0.91	0.09	–0.97	–0.11	–0.72	0.07

22.9, $E_{a,4}$ = 22.3 kJ/mol. Therefore, corrosion occurs with a slightly lower energy barrier than the formation of protective oxide-hydroxide layers. As a result of temperature increase and potential scanning, the values of the Tafel equation coefficients *a* and *b* change. It should be noted that the coefficient *a* corresponds to the overvoltage value at a current density of 1 $A \cdot cm^{-2}$ and depends on the material of the electrode, the state of its surface, and characterizes the degree of transformation of the electrode surface.

From the results given in Table 7.3 and Figure 7.12, it can be seen that due to the increase in the temperature of the solution and the polarization of the electrode in the range of –1.5...+0.5 V, a transformation of the surface of the AMA electrode occurs, which is indicated by a change in values of the a_{Ox} coefficient and oxidation rate, the quantitative characteristic of which is the b_{Ox} coefficient.

In an alkaline solution, OH^- anions in the region of potentials of active anodic dissolution contribute to inhibition of the anodic process due to the formation of metal hydroxocomplexes firmly bound to the surface. As a result of their inhibitory effect, the interphase energy barrier increases, which prevents the transition of Co ions into the solution.

Probably, due to the interaction of the AMA electrode with oxygen, which chemisorbs on the surface and contributes to the dissociation of water according to the scheme:

$$Co–O + H_2O = [Co–O\cdots H_2O]_{ads}; \quad (7.4)$$

$$[Co–O\cdots H_2O]_{ads} = [CoOH]^+_{адс} + OH^-; \quad (7.5)$$

$$[CoOH]^+_{ads} = Co^{2+} + OH^-. \quad (7.6)$$

Appeared arreas (Figure 7.12) are associated with the formation of protective layers. On the reverse VA curves, the recorded cathodic maxima indicate the recovery of corrosion products, in particular Co^{3+}:

$$Co(OH)_3 + H^+ + 1e^- = Co(OH)_2 + H_2O; \quad (7.7)$$

$$CoOOH + H^+ + 1e^- = Co(OH)_2. \quad (7.8)$$

Further peaks are associated with cathodic depolarization, with the reduction of the Co(II) compound:

$$Co(OH)_2 + 2H^+ + 2e^- = Co + H_2O, \quad E = 0{,}095 – 0{,}059pH; \quad (7.9)$$

$$CoO + 2H^+ + 2e^- = Co + H_2O, \quad E = 0{,}134 – 0{,}059pH. \quad (7.10)$$

The potentials of the cathodic peaks on the VA curves are in the area of the reduction potentials of metallic cobalt. According to the results of VA studies of the AMA electrode in the range of –1.5...+0.5 V, hydrogen evolution potentials were established and hydrogen evolution was conducted for 30 minutes in potentiostatic mode.

Four maxima of surface oxidation are clearly visible on the anodic curve of AMA Co-Si-B after hydrogen evolution, in particular, at:

E_1 = –0.88…–0.69 V; E_2 = –0.76…–0.48 V; E_3 = –0.62…–0.52 V; E_4 = 0.08… 0.26 V.

The activation energies of the formation of AMA surface compounds were calculated, which are, respectively, 5.97; 20.25; 10.39; and 16.55 kJ/mol. The corrosion activation energy for the first cycle of the restored AMA surface is 25 kJ/mol, which indicates diffusive difficulties in the interaction of the surface with aggressive ions.

7.5 Conclusions

This chapter contains information about amorphous cobalt-based metal alloys, their properties, and uses. Using the method of differential scanning calorimetry, it was determined that at all heating rates of 5, 10, and 20 K/min, the formation of three exothermic peaks is observed, the first of which corresponds to the process of nanocrystallization of AMA in the temperature range from 761 to 822 (±5) K. The calculated activation energies of AMA nanostructuring processes have high values and are in the range of 266...481 kJ/mol.

It was also established that chromium inhibits the growth of nanocrystals during heating. AMAs based on cobalt can be arranged in the following series according to thermal stability: $Co_{72}Fe_{2,5}Cr_{2,5}Si_{11}B_{12}$ > $Co_{72}Fe_5Si_{11}B_{12}$ > $Co_{77}Si_{11}B_{12}$. Doping the alloy with iron and chromium leads to a change in the mechanism of AMA crystallization, as indicated by a change in the Avrami index from the Matusita equation from 2.9–3.5 for $Co_{77}Si_{11}B_{12}$ to 2.0–2.4 for and 2.1–2.4 for $Co_{72}Fe_5Si_{11}B_{12}$ and $Co_{72}Fe_{2,5}Cr_{2,5}Si_{11}B_{12}$, respectively. In addition, the growth of nanocrystals in the amorphous matrix of the $Co_{77}Si_{11}B_{12}$ alloy occurs mostly by a 3D mechanism, while in $Co_{72}Fe_5Si_{11}B_{12}$, $Co_{72}Fe_{2,5}Cr_{2,5}Si_{11}B_{12}$, the growth of nanocrystals occurs by a 2D mechanism. The value of p = 0.5 for all alloys indicates diffusion-controlled nanocrystallization, and the kinetic parameter b indicates an increase in the rate of nucleation of nanocrystals in all cobalt-based AMA studied.

The X-ray diffraction method identified the phases Co_3B, Co_2Si and β-Co, which are formed in an amorphous matrix during isothermal and non-isothermal heating of a cobalt-based alloy to temperatures of 771 K.

Cyclic voltammetry was used to investigate the corrosion resistance of an amorphous cobalt-based alloy before and after its use in the hydrogen evolution reaction, and the optimal temperature of a 1 M aqueous solution of KOH was determined, which is in the range of 313...323 K. In this temperature range, due to five-fold cyclic polarization of electrodes within the potentials of –1.5...+0.5 V, the corrosion potential acquires constant values of -0.90±0.05 V, the corrosion current density is $1–1.5 \cdot 10^{-6}$ A/cm^2. It is shown that the oxidation of the surface occurs in stages, with the initial formation of a chemisorbed

$[Co–O\cdots H_2O]_{ads}$ complex, the activation energy of which is 57 kJ/mol, and the corrosion processes are diffusion-controlled.

Keywords

- amorphous metal alloys
- magnetic materials
- nanocrystallization
- cobalt
- activation energy
- corrosion

References

1. *Jiang H., Shang T., Xian H., Sun B., Zhang Q. et al*. Structures and Functional Properties of Amorphous Alloys // Small Struct. 2020. P. 2000057. DOI: https://doi.org/10.1002/sstr.202000057
2. *Li J., Doubek G., McMillon-Brown L., Taylor A.* Recent Advances in Metallic Glass Nanostructures: Synthesis Strategies and Electrocatalytic Applications // Adv. Mater. 2018. P. 1802120. DOI: https://doi.org/10.1002/adma.201970050
3. *Li F., Liu T., Zhang J.Y., Shuang S., et al*. Amorphous–nanocrystalline alloys: fabrication, properties, and applications // Mater. Today Adv. 2019. Vol. 4. P. 100027. DOI: https://doi.org/10.1016/j.mtadv.2019.100027
4. *Lopachak M., Kovbuz M., Hertsyk O., Hula T., Boichyshyn L., Khrushcyk K.* Influence of Fe/Co Substitution and Nb Doping on Thermal Stability of Fe/Co-Si -B Alloys // 2020 IEEE 10th International Conference Nanomaterials: Applications & Properties. 2020. P. 01NMM06-1–01NMM06-4. DOI: https://doi.org/10.1109/NAP51477.2020.9309640
5. *Boichyshyn L.M., Hertsyk O.M., Lopachak M.M.* Electrochemical Properties of Ternary Amorphous Alloys Based on Iron and Cobalt in Alkali Solutions // Mater. Sci. 2020. V.55. P. 703–709. DOI: https://doi.org/10.1007/s11003-020-00361-w
6. *Jezeh M.R.J., Tavoosi M., Ghasemi A., Farshadnia R.* Metastable phases in $Co_{70}B_{20}Si_5Fe_4Mo_1$ alloy fabricated by non-equilibrium processes // J. Non-Cryst. Solids. 2015. Vol. 427. P. 26–33. DOI: https://doi.org/10.1016/j.jnoncrysol.2015.07.028
7. *Minić D., Maričić A., Dimitrijević R., Ristić M.* Structural changes of $Co_{70}Fe_5Si_{10}B_{15}$ amorphous alloy induced during heating // J. Alloys Compd. 2007. Vol. 430. P. 241–245. DOI: https://doi.org/10.1016/j.jallcom.2006.05.035
8. *Elmanov G., Chernavskii P., Kozlov I. , Dzhumaev P., Kostitsyna E., Tarasov V., Ignatov A., Gudoshnikov S.* Effect of heat treatment on phase transformations and magnetization of amorphous $Co_{69}Fe_4Cr_4Si_{12}B_{11}$ microwires // J. Alloys Compd. 2018. Vol. 741. P. 648–655. DOI: https://doi.org/10.1016/j.jallcom.2018.01.114
9. *Shao I., Romankiw L. T., Bonhote C.* Stress in electrodeposited CoFe alloy films // Journal of Crystal Growth. 2010. Vol. 312. Is. 8. P.12621266. DOI: https://doi.org/10.1016/j.jcrysgro.2009.11.061
10. *Chikina E., Dyakonova N., Molokanov V., Sviridova T.* Influence of initial phase composition on glass-forming ability of Co-based alloys // J. Alloys Compd. 2007. Vol. 434-435. P. 394–399. DOI: https://doi.org/10.1016/j.jallcom.2006.08.309
11. *Bednarčík J., KováčJ., Kollár P., Roth S., Sovák P., Balcerski J., Polanski K. , Švec T.* Crystallization of CoFeSiB metallic glass induced by long-time ball milling // J. Non-Cryst. Solids. 2004. Vol. 337. P. 42–47. DOI: https://doi.org/10.1016/j.jnoncrysol.2004.03.105

12. *Vyazovkin S.* Kissinger Method in Kinetics of Materials: Things to Beware and Be Aware of // Molecules. 2020. Vol. 25. Is.12. P. 2813. DOI: https://doi.org/10.3390/molecules25122813
13. *Heireche L., Belhadji M.* The methods Matusita, Kissinger and Ozawa in the study of the crystallization of glasses. The case of Ge-Sb-Te alloys // J. Mater. Sci. 2007. Vol. 4. Is. 2. P. 23–33. DOI: https://doi.org/10.3390/molecules25122813
14. *Lopachak M.M., Boichyshyn L.M., Nosenko V.K., Kotur B.Ya.* Crystallization kinetics of the $Co_{77}Si_{11}B_{12}$ amorphous alloy// Chemistry of Metals and Alloys. 2021. V. 14. Is. 1/2. P. 1-6.
15. *Bott A.W.* Electrochemistry of Semiconductors // Current Separations. 1998. Vol.17. Is. 3. P. 87–91.
16. *Zhou Z., Wei Q., Li Q., Jiang B., Chen Y., Sun Y.* Development of Co-based bulk metallic glasses as potential biomaterials // Mater. Sci. Eng. 2016. Vol. 69. P. 46–51. DOI: https://doi.org/10.1016/j.msec.2016.05.025
17. *Rosalbino F., Delsante S., Borzone G., Angelini E.* Electrocatalytic behaviour of Co–Ni–R (R=Rare earth metal) crystalline alloys as electrode materials for hydrogen evolution reaction in alkaline medium // International Journal of Hydrogen Energy. 2008. Vol. 33. Is. 22. P. 6696– 6703. DOI: https://doi.org/10.1016/j.ijhydene.2008.07.125
18. *Fal Miyar V., Cerdeira M. A., Garcia J. A., Potatov A. P., Pierna A. R., Marzo F. F., Kurlyandskaya G. V.* Giant Magnetoimpedance of Electrochemically Surface Modified Co-Based Amorphous Ribbons //IEEE Transactions on Magnetic. 2008. Vol. 44. Is. 11. P. 4476–4479. DOI: https://doi.org/10.1109/TMAG. 2008.2002245
19. *Pardo A., Merino M. C., Otero E., López M. D., M'hich A.* Influence of Cr additions on corrosion resistance of Fe- and Co-based metallic glasses and nanocrystals in H_2SO_4 // J. Non-Cryst. Solids. 2006. Vol. 352. Is. 30–31. P. 3179–3190. DOI: https://doi.org/10.1016/j.jnoncrysol.2006.05.021
20. *Lopachak M.M., Khrushchyk K.I., Dnistryan V.V. et al.* Corrosion Resistance of $Co_{77}Si_{11}B_{12}$ Amorphous Metal Alloys for the Electrodes of Hydrogen Release from Alkaline Solutions // Mater. Sci. 2021. V. 56. P. 673–677. DOI: https://doi.org/10.1007/s11003-021-00481-x

Chapter 8

MULTIFUNCTIONAL HYBRID NANOSYSTEMS BASED ON POROUS SILICON

I. B. Olenych, L. S. Monastyrskii,
O. I. Aksimentyeva, and Yu. Yu. Horbenko

Ivan Franko National University of Lviv, 79005 Lviv, Ukraine

Corresponding author: igor.olenych@lnu.edu.ua

Contents

Abstract

Inorganic nanosystems were created by depositing ZnO, reduced graphene oxide (rGO) or metal nanoclusters on the porous silicon (PSi). Nowadays hybrid nanomaterials show significant application potential in various fields of electronics. In particular, the possibility of controlling the spectrum of multicolor photoemission of the PSi–ZnO nanosystems by adjusting the excitation energy is demonstrated. Besides, the different band gaps of the silicon substrate, ZnO and PSi nanocrystals cause the broadening of the photosensitivity spectrum of sandwich-like structures. The incorporation of the rGO or metal nanoclusters into the porous layer leads to an increase in the efficiency of the photoelectric structures due to better surface passivation and the formation of additional conductive channels. The found sensitivity of the PSi-based nanosystems to γ- and β-radiation can be used in dosimetric devices. In addition, the combination of adsorption properties of various PSi-based nanosystem components increases the sensitivity and selectivity of the gas sensors. The problem of gas identification can be solved by computer analysis of the overall response of a matrix of sensor elements with an individual profile of the transfer function.

8.1 Introduction

The current stage of electronics development is closely related to functional semiconductor nanomaterials that can be the foundation of the element base of a new generation of electronic equipment. Nanofabrication and the research of new nanostructured materials are caused not only by applied tasks but also by studying fundamental regularities and discovering new physical phenomena or effects. Since silicon is the basic material of microelectronics, the research on silicon-based nanosystems is especially relevant. One of the main methods of diagnosing the formation of silicon nanostructures is the photoluminescence (PL) method. It is based on the spatial confinement of electron movement in quantum nanoobjects and, as a result, a discrete energy spectrum and a larger band gap compared to a bulk crystal [1–3]. In addition, the probability of radiative recombination of charge carriers increases in silicon nanostructures. Therefore, the identification feature of the formation of silicon nanocrystals can be the visible PL band in the 1.5–2.0 eV region, the spectral position of the maximum of which is determined by the size of the nanocrystals [4].

Consequently, low-dimensional silicon nanostructures due to quantum confinement can be used to create light emitters and receivers, optical amplifiers, and solar cells [5–8]. In particular, the presence of quantum wires makes it possible to solve the problem that arises with the traditional method of photoelectric transducer production and is associated with the processes of solar radiation absorption in the silicon bulk and dismissal of charge carriers from it: a thick photoreceiver ensures complete absorption of solar radiation whereas in thin photocell charge carriers are easier to be collected. Highly efficient conversion of solar into electric energy can be achieved through optimizing the base region and using long nanowires, which create the directional flow of photogenerated charge carriers [9].

On the other hand, a significant ratio of surface area to volume of silicon nanostructures expands the prospect of using them as sensitive elements of various sensors [10–12]. Special attention is focused on developing cheap and reliable gas sensors for scientific, industrial, and medical applications that work at room temperature. The dependence of the electrical and luminescent properties of silicon nanocrystals on the adsorption of gas molecules underlies the operation of various types of sensor elements. Catalysts or a combination of different nature nanostructures are often used to increase the sensitivity and selectivity of gas sensors [13, 14]. It should be noted that nanoparticles of catalytic metals, metal oxides, and graphene nanosheets are extremely promising from this point of view. In particular, palladium nanoclusters contribute to increasing the sensitivity of sensors to hydrogen molecules and hydrogen-containing compounds [15, 16]. The high sensitivity of zinc oxide to nitrogen oxide, ethanol and methane molecules can improve the selectivity of hybrid nanosystems to these gases [17–20]. Graphene deserves special attention. Its unique properties (such as high electric conductivity and mobility of free electrons) are caused by the gapless conical shape of the electron spectrum [21, 22]. Dependence of the Fermi level in graphene on the local electric field of adsorbed molecules allows it easy to inject carriers with a positive or negative charge into graphene and change their concentration [23–25]. In addition, the low electrical noise of graphene sheets makes it possible to register the absorption of individual molecules. In general, the advantage of silicon nanosystem-based sensor elements is the possibility of easy integration into silicon technology.

One of the common methods of obtaining arrays of silicon nanostructures is the electrochemical formation of porous silicon [26, 27]. Small cavities and nanostructures in the shape of nanowires and nanowalls are formed in silicon wafers during anodic etching. The PSi with the extensive pore system is an ideal foundation for the deposition and infiltration of nanoparticles of various natures, in particular, graphene, semiconductor, or metal nanoclusters [28–31]. The synergistic combination of useful properties of individual components can contribute to increasing the functionality of the PSi-based nanosystems. On the other hand, the PSi is a convenient model object for studying the fundamental regularities of the processes of generation, transfer, and relaxation of charge carriers in semiconductor nanosystems because it is easy to control the structural characteristics of the porous layer during its formation. The aggregation of individual silicon nanocrystals into nanosystems makes it possible to observe nanoscale effects at the macroscopic level. In addition to the interest in the fundamental properties of the nanostructured silicon materials, applied aspects related to the application of PSi-based nanosystems in sensors, photo- and optoelectronic devices, memory elements, and spintronics is also intensively researched.

Usually, PSi layers on silicon substrates are used for research. Porous layers of various morphologies are used for different tasks. The PSi microstructure depends not only on the technological conditions of formation (anode current density, duration of the etching process, electrolyte composition, irradiation silicon wafer, etc.), but also on the crystallographic orientation of the silicon substrate, type and concentration of doping impurity [10, 26]. Depending on the pore diameter d_{por}, PSi layers are classified as: nanoporous ($d_{por} < 5$ nm), mesoporous ($5 < d_{por} < 50$ nm) and macroporous ($d_{por} > 50$ nm). Nanoporous and macroporous layers that contain quantum-sized silicon structures can be used to apply the

optical and luminescent properties of the PSi in optoelectronics. The revealed features of the field effect in porous semiconductors indicate that the most significant influence of the surface charge on the electrical characteristics of the PSi is observed in the case when the d_{por} is large and the distance between the pores is less than the Debye screening length [32]. Macroporous and mesoporous silicon layers are closely associated with such structural characteristics and have a perspective in sensor electronics. The thickness of the porous layer varies from tenths to several tens of micrometers. Thus, by changing the technological regimes of electrochemical etching and selecting the appropriate initial silicon single crystals, it is possible to obtain the PSi nanostructures with the required morphology and predicted functional properties.

It should be noted that the surface state significantly affects electronic processes in the PSi nanocrystals. In particular, the passivation of silicon broken bonds with hydrogen, oxygen, or polymers reduces the non-radiative recombination of non-equilibrium charge carriers and increases the efficiency of visible PL [33]. Besides, electronic states localized on the surface can be levels of trapping of non-equilibrium carriers and participate in charge transfer processes [34, 35]. Therefore, the formation of radiation-induced defects in a natural silicon oxide thin film on the surface of silicon nanostructures and the resulting change in the electronic properties of the PSi layer can be used to create ionizing radiation sensors [36,37]. As a result, the PSi layers can be additionally processed for certain needs in order to passivate the surface, increase the thickness of the silicon oxide film, or vice versa, remove it, etc.

Finally, the PSi functionality can be improved by creating hybrid nanosystems with optimal composition and structure for a specific practical task. Therefore, establishing the conditions for the formation of hybrid nanosystems and studying the influence of external factors (such as temperature, gas adsorption, electromagnetic radiation, ionizing radiation, etc.) on the properties of the obtained nanomaterials is a topical scientific problem from both a fundamental and a practical point of view. The comprehensive research of electronic processes in the PSi-based nanosystems opens new technological possibilities and constructive approaches for creating a new generation of electronic devices.

8.2 Creation and Characterization of the PSi-based Nanosystems

The production of nanosystems based on the PSi is carried out using modern techniques, which make it possible to create or modify nanomaterials with new physical and chemical properties due to their nanosize. Two basic approaches to the production of nanostructures are distinguished in nanotechnology: “top-down nanotechnology” and “bottom-up nanotechnology”. In the “top-down” concept of obtaining nanostructured materials, the nanometer size of particles is achieved by successively reducing the size of macroscale objects. The technology of the PSi electrochemical formation can also be included in this approach. The “bottom-up” technology is based on the nanoobject assembly from elements of a lower level, in particular atoms or molecules. At the same time, atoms form an ordered

structure. This approach is implemented using self-assembly or a certain sequence of chemical reactions.

The most affordable way to obtain a system of silicon nanostructures is the technology of PSi formation. During the electrochemical etching of silicon single crystals, narrow pores directed deep into the silicon wafer are formed. Further anodizing causes not only an increase in the depth of the pores but also their expansion. Therefore, the walls between the pores can be partially etched and adjacent pores can be merged. As a result, a disordered network of remnants of walls between the pores is formed in the form of quantum wires and dispersed nanocrystals oriented mainly in the direction of the crystallographic axes. The dimensions of the PSi nanostructures can range from units to several tens of nanometers. The formation of the PSi layers on silicon wafers of different crystallographic orientations is illustrated in Figure 8.1.

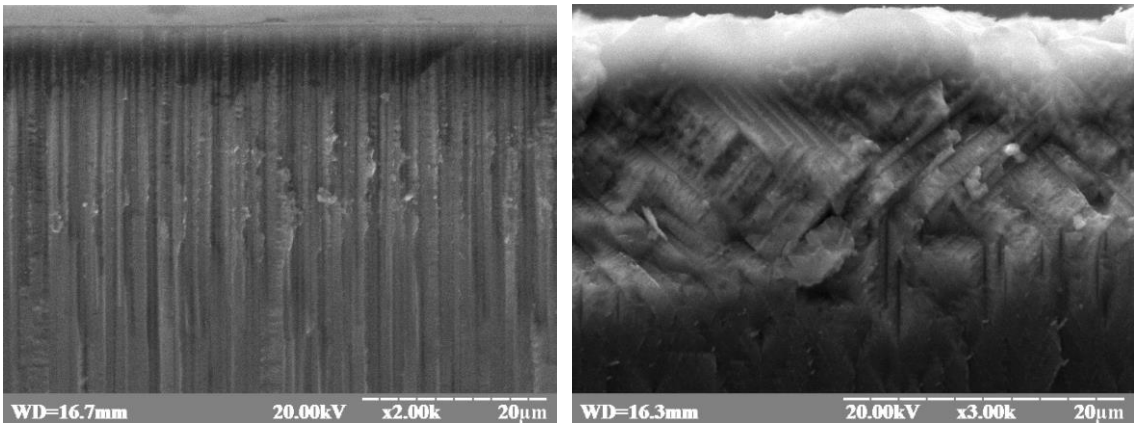

a *b*

Figure 8.1 SEM image of cross-sections of the PSi layers obtained on silicon wafers with crystallographic orientation [100] (*a*) and [111] (*b*)

The mechanism of the porous layer formation is closely related to the features of multistage and competing chemical reactions occurring on the surface of the silicon wafer [38]. The process of the PSi electrochemical etching is determined mainly by two factors: the delivery of fluorine ions to the chemical reaction zone and the presence of free positive charge carriers necessary for chemical reactions [10]. The first factor is related to the electrolyte and the electrical parameters of the etching process. In particular, the anode current density is the main one. The second factor of the electrochemical formation of the porous layer is related to the electrical characteristics of the silicon substrate, namely, the type and level of its doping. Because of that, the processes of electrochemical etching of silicon crystals of *p*-type and *n*-type conductivity have some differences. Unlike the anodizing of *p*-type silicon, the formation of a porous layer on silicon substrates doped with a donor impurity requires the additional generation of positive charge carriers. For this purpose, irradiation of the silicon wafer surface with visible or UV radiation is usually used during electrochemical etching.

In order to create hybrid nanosystems, layers of nanostructured PSi were formed on polished silicon wafers with a thickness of 400 μm and crystallographic orientation [100] and [111]. Silicon wafers of electronic and hole conductivity types with a specific resistance of 4.5 and 10 Ohm·cm were used. The homogeneity of the PSi layer was achieved by thermal deposition on the back (non-working) surface of the silicon wafer of metal (Au, Ag, or Al) film with a thickness of about 0.5 μm. After annealing at a temperature of 450°C for 20 min, the metal film also served as an electrical contact for further measurements. An ethanol or water-ethanol solution of hydrofluoric acid with a volume ratio of $C_2H_5OH : HF = 1 : 1$ or $C_2H_5OH : HF : H_2O = 1 : 1 : 1$ was used as an electrolyte. The anodic current density was 20–35 mA/cm^2 at the etching time of 5–20 min for various experimental samples. The working surface of the silicon wafer was irradiated by the 500 W tungsten filament lamp during the electrochemical etching process to generate holes in the *n*-Si near-surface layer. After the anodizing process, the obtained PSi layers were washed with distilled water and air-dried at room temperature. As a result, the PSi layers with the thickness, pore sizes, and porosity degree necessary for further research were obtained.

The modification of the PSi layers by introducing various impurities into them is of considerable scientific and practical interest. Doping the porous layer with metal nanoparticles can also cause the appearance of new properties not inherent to the initial PSi nanostructures. In particular, the nanosystems of the PSi with metal nanoclusters can be used to create efficient optoelectronic devices, energy storage devices, and gas sensors, the high sensitivity of which is due to the catalytic properties of metals and the mode of their introduction into porous layers. Considering that the photoelectric properties of the PSi-based sandwich structures depend on the height of the Schottky barrier, metals with different work functions were used to doping the porous layer: Ag (4.26–4.74 eV), Co (5.0 eV) and Pd (5.22–5.6 eV).

The simplest method of doping PSi layers with metals is their processing in solutions containing doping metal ions. When an electric current is passed through the electrolyte, metal ions are transferred to the cathode and deposited not only on the surface but also in the pores of the PSi. Metal ions with a more positive electrochemical potential compared to silicon are neutralized by the extraction of electrons from the surface silicon atoms and become the seeds of the growth of metal nanocrystals [39]. Doping of the PSi layer with metals was carried out by the electrochemical method with the passage of the 2–20 mA direct current for 5–10 min from solutions of their salts in water or an organic solvent. Silver nitrate ($AgNO_3$), cobalt acetate ($Co(CH_3COO)_2$) and palladium acetate ($Pd(CH_3COO)_2$) were used.

The incorporation of metals into the porous layer was controlled by SEM in the elastic electron scattering mode and by energy dispersive X-ray microanalysis (EDXMA). The SEM image sections with greater brightness are identified as formed metal clusters. As can be seen in Figure 8.2, a significant amount of electrodeposited silver and cobalt is located on the surface and in the near-surface layer of the PSi. In the depth of the porous layer, cobalt is found on the walls between the pores in the form of nanoparticles with a size of several tens of nanometers. Since the formation of submicron particles is not observed in the cross-sectional SEM images of the PSi structures modified with nickel and palladium, it

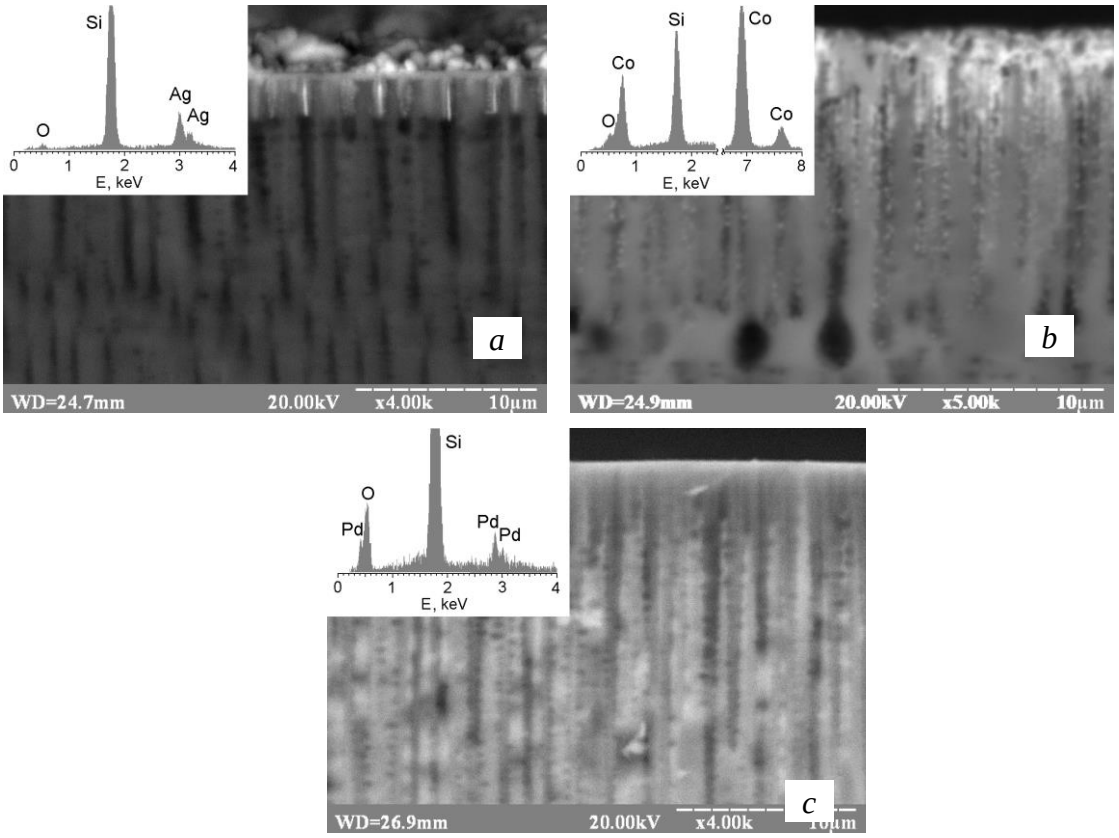

Figure 8.2 SEM image and EDXMA diagram of a cross-section of the PSi modified with silver (a), cobalt (b) and palladium (c)

can be assumed that nickel and palladium are deposited in the pores in atomic form or in the form of small nanoclusters.

The EDXMA spectra confirm the incorporation of metals into the PSi layer. In addition to the intense maximum with an energy of 1.74 keV associated with silicon atoms, peaks corresponding to metal atoms are observed. It should be noted that the intensity of the EDXMA bands associated with the incorporated metal atoms decreased with increasing distance from the PSi surface to the analyzed area. This fact indicates the predominant deposition of metals in the near-surface PSi layer.

The semiconductor PSi–ZnO nanosystems were obtained by electrochemical deposition of zinc oxide on the surface of the porous layer. The morphology of ZnO nanostructures can be effectively controlled during growth due to the peculiarities of their crystal structure. In particular, nanorods, nanowires, nanosheets, nanocombs, and nanoribbons of ZnO were synthesized by various physical and chemical methods. Chemical deposition from the gas phase [40], thermal evaporation [41], magnetron sputtering [42], pulsed laser deposition [43], hydrothermal and sol-gel methods [44, 45], electrochemical deposition [46, 47] are used to obtain ZnO nanostructures. The use of the porous layer as a substrate for ZnO deposition reduces mechanical stresses caused by the mismatch between the parame-

ters of the crystal lattice and the thermal expansion coefficients of silicon and zinc oxide. This makes it possible to grow structurally high-quality crystalline arrays of ZnO [48].

A two-electrode electrochemical cell with the 0.05 M $Zn(NO_3)_2 \cdot 6H_2O$ and 0.1 M $NaNO_3$ aqueous solution was used to obtain hybrid PSi–ZnO nanosystems. The ZnO deposition was carried out at the –1.4 V potential applied to a silicon substrate with a porous layer serving as a working electrode. The auxiliary electrode was a platinum grid. The duration τ of growing ZnO nanostructures was 10–20 min. The electrolyte was constantly mixed and heated to 65–80°C because the temperature is one of the important factors determining the ZnO morphology. The electrochemical deposition process ensures the penetration of reagents into the pores of silicon, so zinc oxide nanostructures are synthesized both directly on the PSi surface and inside the pores. Figure 8.3 shows the microstructure of the surface and cross-section of the PSi–ZnO nanosystems obtained under various technological conditions.

The morphology of the ZnO layers depends on the electrolyte temperature and electrodeposition modes. In particular, the electrolyte temperature determines the intensity of electrochemical processes, the rate of diffusion of reagents, and the rate of desorption of gaseous reaction products from the surface of grown ZnO. The formation of a disordered network of ZnO nanowires and nanosheets is observed at 65°C temperature. Increasing the electrolyte temperature to 80°C and the electrodeposition duration causes the formation of

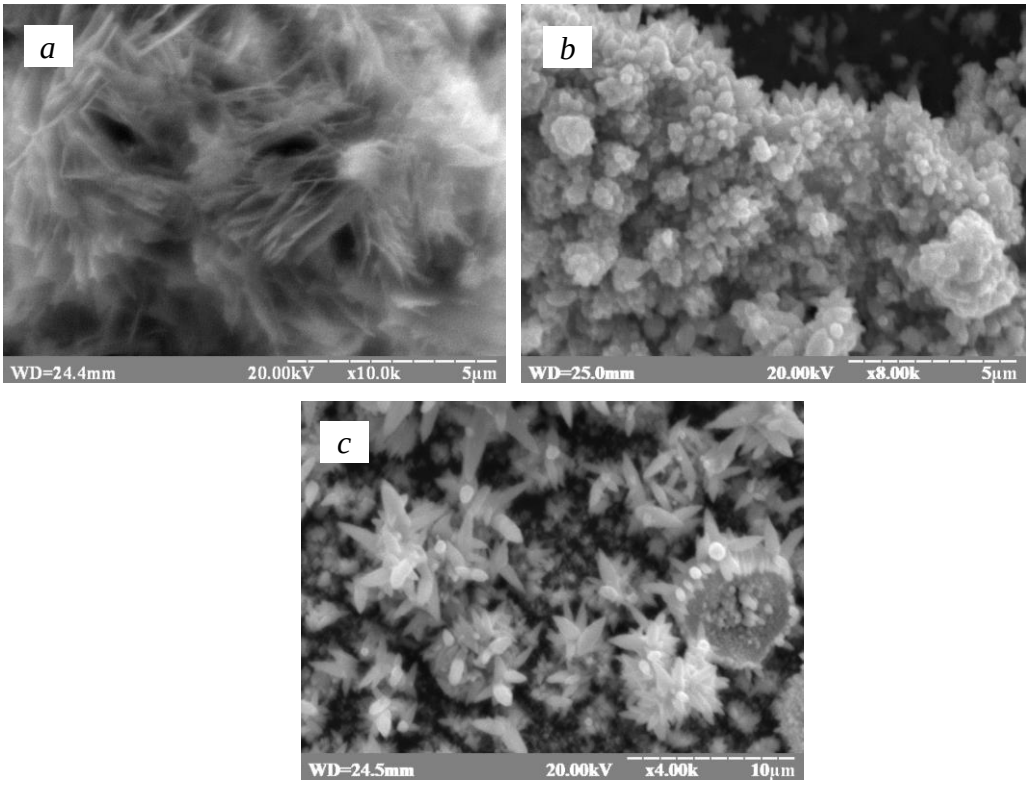

Figure 8.3 SEM images of the arrays of ZnO nanostructures grown on the PSi surface at τ = 10 min, t = 65°C (*a*); τ = 20 min, t = 75°C (*b)*; and τ = 20 min, t = 80°C (*c*)

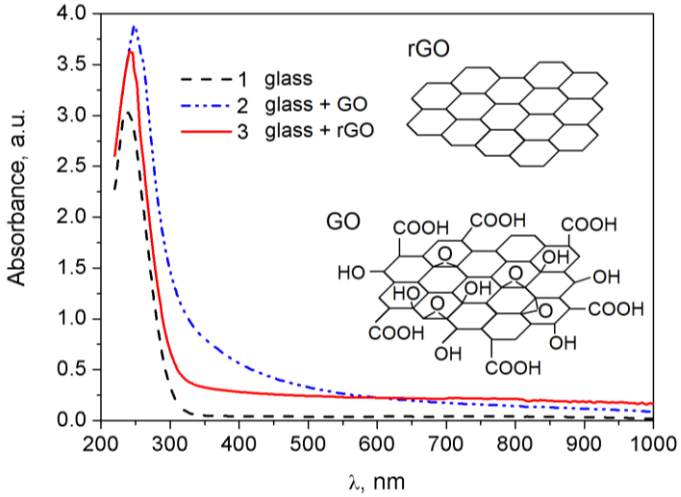

Figure 8.4 UV-vis absorbance spectra of the glass substrate (*1*), the GO (*2*) and rGO (*3*) films on the glass substrate

arrays of unoriented ZnO nanorods. The smaller ones grow on larger hexagonal crystals, the size of which reaches several micrometers. A wide range of morphological features of the ZnO structure is caused by various kinetic parameters of the growth of different crystal planes [49]. The thickness of the zinc oxide layer increases with increasing electrochemical deposition time.

The ZnO nanostructures were also deposited on a glass substrate with a SnO_2 conducting layer to study the optical properties of the growing arrays.

Graphene oxide (GO) produced by Biotool (Germany) in the aqueous suspension form was used to obtain nanosystems based on the PSi and graphene. The concentration of the GO was 2 mg/ml. The GO suspension was dispersed by ultrasonic treatment for 10–20 min and reduced by the hydrazine monohydrate. As a result, nanosheets of reduced graphene oxide were obtained. The 0.2 M aqueous solution of sodium dodecylbenzene sulfonate was used to prevent the aggregation of the rGO nanoparticles. A comparative analysis of UV-vis absorbance spectra of the GO and rGO films on a glass substrate indicates the high degree of reduction of GO nanosheets (see Fig. 8.4). In particular, a decrease in light absorption was observed in the rGO film as compared to GO in the 300–450 nm spectral range. It is usually associated with the $n \rightarrow \pi^*$ transition of the GO carbonyl groups [50, 51].

The obtained RGO dispersion was deposited to the PSi surface and dried at room temperature for 48 hours. SEM study of the PSi–rGO hybrid nanosystem cross-section was carried out in the secondary electron mode at different magnifications (Fig. 8.5, *a*). Based on the analysis of the obtained SEM images, it can be concluded that rGO nanosheets form a film on the porous layer surface, partially penetrate the pores and well passivate the PSi nanocrystal surface.

The rGO nanosheets can also be used as an electrode material for the PSi nanostructures [28, 52]. In some cases, this approach can eliminate the undesirable effect of the silicon substrate on the electronic properties of the PSi nanostructures. Therefore, PSi–rGO

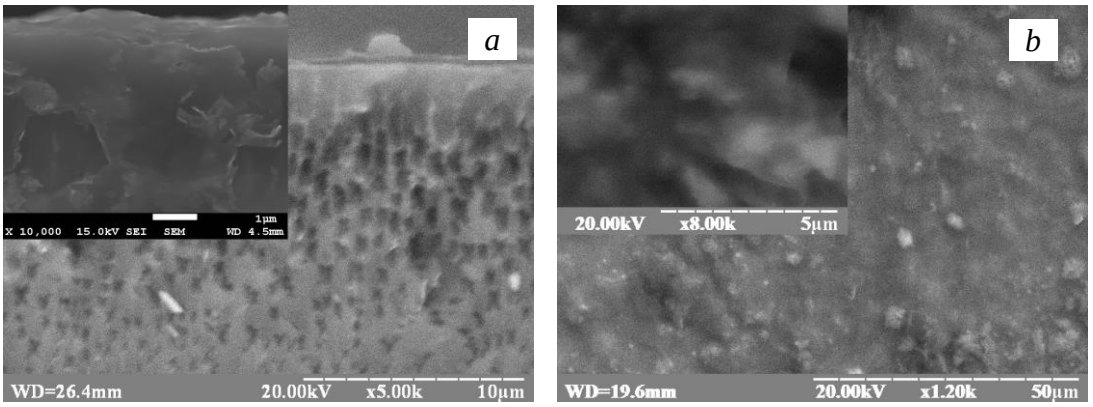

Figure 8.5 SEM images of the cross section of the PSi–rGO hybrid nanosystem (*a*) and film nanosystem based on the PSi and rGO nanoparticles (*b*)

nanosystems of a different type were created by mixing in different proportions the suspension containing rGO nanosheets with the PSi nanocrystals separated from the substrate. The resulting mixtures were deposited to prepared substrates with electrical contacts, the distance between which was 1 mm. As can be seen in Figure 8.5, *b*, the mixture of the PSi and rGO nanoparticles forms a non-monolithic and non-homogeneous film on the substrate, the thickness of which does not exceed several micrometers. The sizes of the PSi nanostructures range from several tens to hundreds of nanometers.

The individual PSi and rGO nanoparticles are combined into clusters with a size of several micrometers. In turn, the connection of these clusters forms a conductive path between the electrodes.

8.3 Research Techniques of Functional Properties of the PSi-based Nanosystems

The optical and photoluminescent properties of the PSi-based nanosystems were studied using the CM2203 (Solar) fluorometer. The optical absorption spectra of the GO and rGO films as well as ZnO arrays on a transparent substrate were studied in the 220–1000 nm spectral range. The PL excitation spectra of the PSi–ZnO hybrid nanosystems were measured in the 220–450 nm range for the maxima of the photoemission bands. The PL spectra were studied in the 350–800 range upon excitation by UV radiation from the side of ZnO nanostructures. All measurements were carried out at room temperature.

The hybrid nanosystems had a sandwich configuration to study the photovoltaic properties. The semi-transparent frontal contact was formed by the thermal deposition of a silver thin film. Other types of electrical contact were obtained using conductive paint or a spring transparent electrode (glass plate coated with SnO_2). The current-voltage characteristics (CVC) were measured when the current passed through the structures in the direction perpendicular to the surface. Photoelectric phenomena were studied by irradiating the structures with the 1 W white LED (FYLP–1W–UWB–A) that provided a light flux of 76 lu-

mens. LEDs with 390, 570, and 940 nm wavelengths of emission were also used. The photoresponse spectral dependencies were measured using standard optical equipment, including a diffraction monochromator and a filament lamp (2800 K). Obtained spectra were normalized with regard to the 2800 K black body radiation curve (Planck curve) and were corrected taking into account the equipment spectral sensitivity. The spectral dependence of photoresponse of an industrial silicon photodiode was also measured for comparison. Kinetics of the photoinduced signal of the PSi-based hybrid structures to rectangular light pulses was studied using Hantek 1008B oscilloscope.

Adsorption-desorption processes in the PSi-based nanosystems under the influence of molecules of various gases were studied in a hermetic chamber with a controlled gas environment. In particular, environmentally important gases methane, ammonia, and ethanol, as well as water vapor, were used for research. The water vapor concentration in the chamber was determined with the HIH-4000-004 (Honeywell) humidity sensor. Measurements of electrical resistance and capacitance of PSi-based sensor elements were carried out in AC mode using the RLC meter.

8.4 Multicolor Photoemission in the PSi–ZnO Nanosystem

The intense visible PL of the PSi nanostructures expands the functionality of silicon technology and the prospects of creating a new generation of optoelectronic devices based on silicon nanocrystals. In addition, surface modification of silicon nanostructures or their combination with other materials can additionally control the electronic and optical properties within wide limits. In particular, the PL spectra of organic-inorganic nanosystems based on the PSi can be controlled using the electrochromic effect in polymers [53]. Another approach relies on changing the energy of PL excitation quanta. The combination of the PL bands of individual components of PSi-based hybrid nanosystems (for example, PSi and ZnO nanocrystals) can be the ground for the creation of white light sources that are easily integrated into modern silicon technology. In particular, the PL spectrum of the PSi–ZnO nanosystems covers almost the entire visible spectral range [54]. The high transparency of nanostructured ZnO layers in the visible spectral range is also important for optoelectronic applications (see Fig. 8.6). In addition, the electrodeposited ZnO arrays are transparent enough to excite PL in the PSi nanostructures. Therefore, the ZnO layers can be effectively used as a “window” for both exciting and PSi-generated radiation.

Figure 8.7 shows the PL spectra of the PSi–ZnO nanosystems at various energies of the excitation quanta. Three visible bands of photoemission are observed in the PL spectra, the intensity of which depends on the excitation wavelength. The visible PL band of the PSi with a maximum at 660 nm is formed as a result of the radiative recombination of electron-hole pairs excited in the silicon nanocrystals of various sizes, the electronic spectrum of which is modified due to the quantum-dimensional effect [4]. Therefore, the PL band is wide and radiation maximum can be found at different wavelengths of the visible spectrum depending on the technological conditions of the PSi formation and the external environment of silicon nanocrystals.

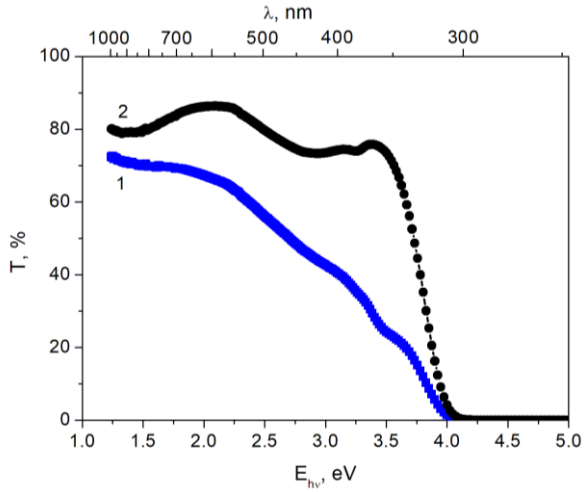

Figure 8.6 Optical transmission spectra of the ZnO layers on a glass substrate with a SnO_2 film (*1*) and the initial substrate (*2*)

In addition to a broad PL band associated with the PSi nanostructures green and yellow emission bands with maxima at 545 and 585 nm were registered. The last bands are associated with structural defects in the ZnO nanocrystals. In particular, visible photoemission in the ZnO structures is due to the radiative recombination of delocalized electrons with holes captured at deep traps of zinc and oxygen vacancies (V_{Zn-}, V_{O+}) as well as oxygen centers (O_i) [44,55].

A change in the energy of PL excitation quanta causes a redistribution of the intensity of the emission bands of the PSi–ZnO nanosystems in different spectral ranges. An increase in the intensity of PL bands in the short-wavelength spectrum region associated with radiative recombination in the ZnO nanostructures is observed when the energy of the excitation quanta increases.

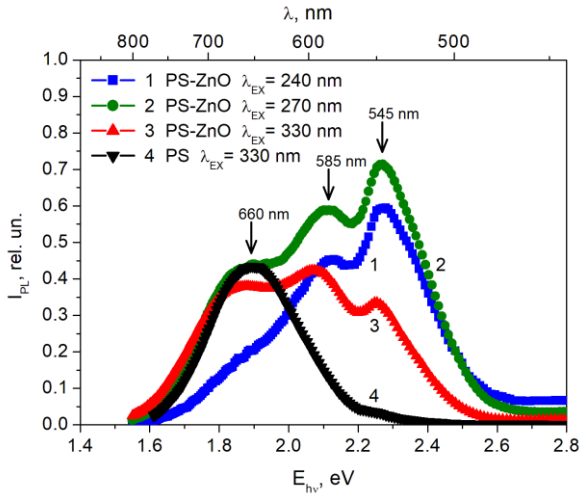

Figure 8.7 The PL spectra of the PSi–ZnO nanosystems (*1–3*) and initial PSi (*4*) upon excitation by UV light with λ_{exc} = 240 nm (*1*), λ_{exc} = 270 nm (*2*), λ_{exc} = 330 nm (*3*, *4*)

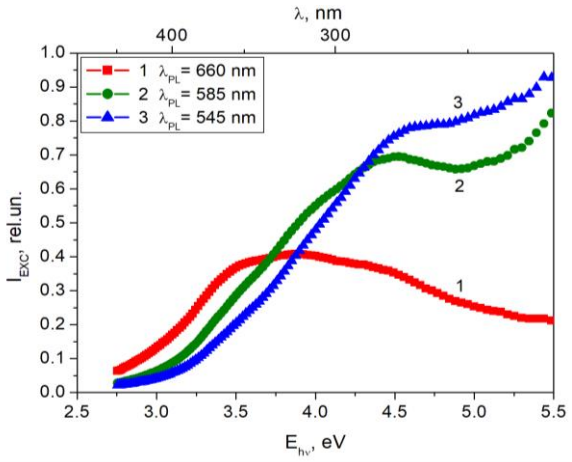

Figure 8.8 The PL excitation spectra of the PSi–ZnO nanosystem for λ_{PL}, nm: 660 (*1*), 585 (*2*), and 545 (*3*)

The PL excitation spectra of the PSi–ZnO hybrid nanosystem measured for the detected maxima of the emission bands are shown in Figure 8.8. The excitation spectrum for λ_{PL} = 660 nm is characterized by a broad band with a gentle maximum in the UV range and responds to the PL excitation spectrum of the PSi nanocrystals. The low-energy edge of the PL excitation spectrum of the PSi is in the 400–450 nm range. Similar excitation spectra with a maximum in the region of higher energies are observed for the wavelengths λ_{PL} = 545 nm and λ_{PL} = 585 nm. This fact indicates the similar nature of the corresponding emission bands associated with ZnO in the PL spectra of the PSi–ZnO hybrid nanosystems.

Based on the analysis of the PL excitation spectra of the PSi–ZnO hybrid structure, it can be concluded that the integrated intensity of photoemission will be maximal in the case of excitation by UV light in the 250–280 nm range. Besides, it is possible to control the PL spectra of the PSi–ZnO nanosystems by changing the energy of the excitation quanta.

8.5 Photoelectric Properties of Sandwich-like PSi-based Hybrid Structures

Considering that photovoltaic characteristics of sandwich-like structures "metal-PSi" are mainly determined by the Schottky barrier, the modification of the porous layer by metals with high values of work function can enhance the efficiency of photosensitive structures obtained on electron-type silicon. Photogenerated charge carriers are separated by the Schottky barrier electric field, the depth of which penetrates the semiconductor depends on the doping impurity concentration and contact potential. Therefore, by changing the contact potential, it is possible to control the photovoltaic parameters of structures with the Schottky barrier.

The CVC of sandwich-like structures based on the PSi with front Ag and back Au contacts are shown in Figure 8.9. The nonlinear behavior of the obtained dependences is caused by electrical barriers at the contact of metals with a semiconductor. Moreover, the

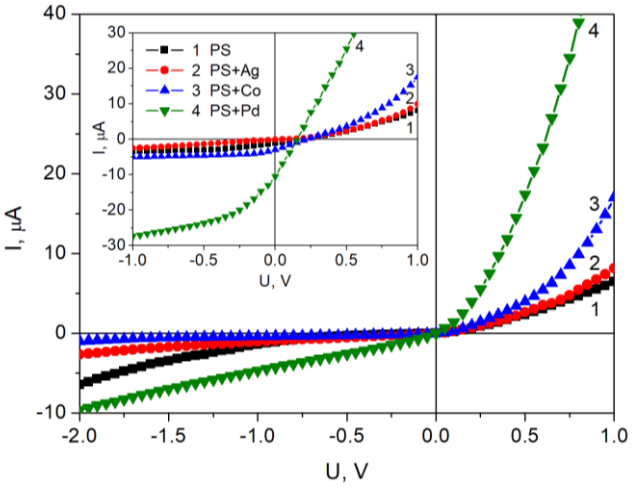

Figure 8.9 Dark current CVC of the initial PSi-based sandwich-like structure (*1*) and structures modified with nanoclusters of silver (*2*), cobalt (*3*) and palladium (4). The inset shows the CVC under the influence of irradiation by FYLP–1W–UWB–A light emitting diode

domination of one of the Schottky barriers determines the rectifying nature of the CVC. Under the irradiation influence of the porous layer by white light from the LED, the CVC of the PSi-based structures changes similarly to the photodiode (see inset Fig. 8.9). Photogeneration of free charge carriers causes the appearance of a photovoltage and an increase in the reverse current of the CVC.

It should be noted that the rectification coefficient of the CVC, photovoltage and photocurrent values increase due to the incorporation of metals into the porous layer. The deposited metals also caused a change in the surface passivation of the PSi nanocrystals. The detected increase in electrical conductivity of sandwich structures based on the PSi doped with metals can be associated with a larger metal-semiconductor contact area and the formation of additional current channels through the porous layer. Besides, the dendrite-like metal formations provide efficient collection and extraction of photogenerated charge carriers from the porous layer.

Spectral dependences of photovoltage of the PSi-based barrier structures are shown in Figure 8.10. The photovoltage spectra in no-load mode are similar to the photoresponse spectrum of a silicon diode and the PSi–silicon heterojunctions [56] and are characterized by a wide photosensitivity band in the 930–970 nm range. However, there is a dependence of the spectral position of the photosensitivity maximum of the PSi-based sandwich-like structures on the incorporated metal nature. It may be due to the shunting of silicon nanocrystals by deposited metal and various degrees of passivation of the porous layer surface.

The temporal parameters of the photoresponse were studied using pulsed IR radiation to obtain additional information about photoelectric processes in hybrid structures based on the PSi. LED with the $\lambda = 940$ nm wavelength was used, which corresponds to the photosensitivity maximum of the studied structures. The measurement results of the photoresponse kinetics to rectangular light pulses with the 0.5 ms duration and the 1 kHz frequency are shown in the inset of Figure 8.10.

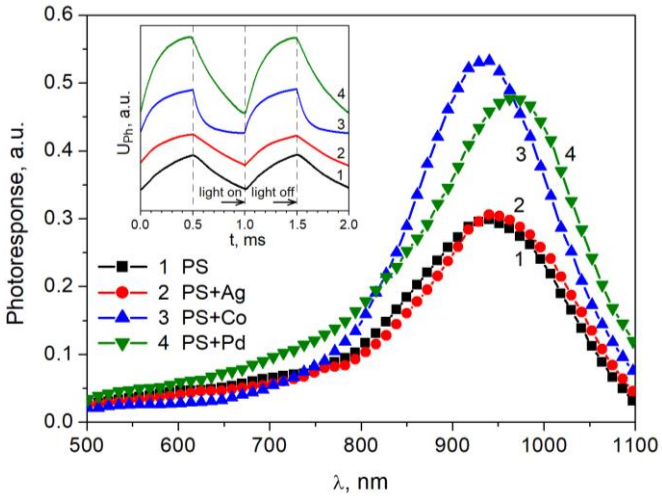

Figure 8.10 Spectral dependence of photoresponse of the initial PSi-based sandwich-like structure (*1*) and structures modified with nanoclusters of silver (*2*), cobalt (*3*) and palladium (*4*). The inset shows the kinetics of the photoresponse to rectangular 940 nm light pulses

The analysis of the obtained dependencies revealed that the sandwich-like structures based on the metal-modified PSi layer are characterized by a slightly shorter rise time of the photovoltaic signal compared to the initial structure. A decrease in the photoresponse time due to the porous layer doping with metals is probably caused by a change in the passivation of the PSi nanocrystals. Eventually, improving the passivation of the porous layer surface decreases the coefficient of surface recombination of charge carriers and increases the efficiency of the photodetectors based on the PSi [57].

Infiltration into the pores of graphene nanosheets can ensure effective passivation of the PSi nanocrystal surface. In addition, the rGO film can be the front electrode in the PSi-based photosensitive structures due to its high transparency. As can be seen in Figure 8.11,

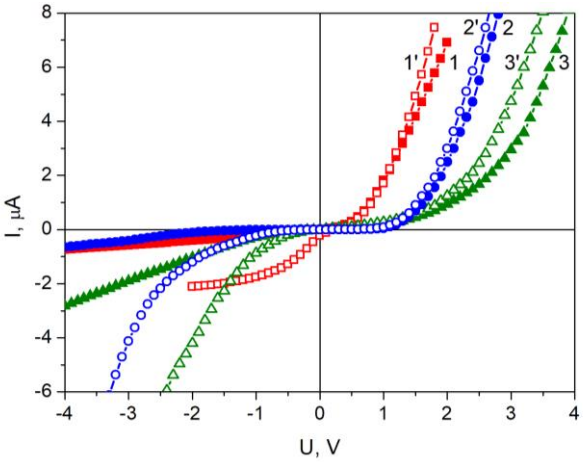

Figure 8.11 Dark current CVC (curves *1*–*3*) and CVC under the influence of irradiation by FYLP–1W–UWB–A light emitting diode (curves *1*'–*3*') of the PSi–rGO (curves *1*, *1*') and PSi–ZnO sandwich-like nanosystems on *p*-Si (curves *2*, *2*') and *n*-Si (curves *3*, *3*') substrates

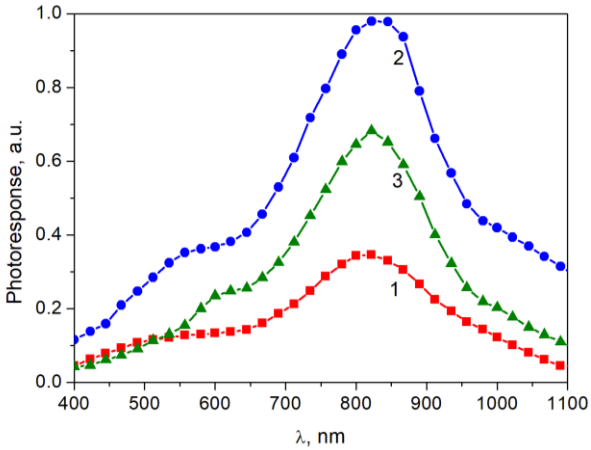

Figure 8.12 Photoresponse spectra for the rGO–PSi (*1*) and PSi–ZnO sandwich-like nanosystems on *p*-Si (*2*) and *n*-Si (*3*) substrates

the PSi structures with deposited nanoparticles of the rGO have a rectifying CVC due to photosensitive electrical barriers [58]. Photogenerated electron-hole pairs are separated at the potential barrier and form a photovoltaic signal. A change in the passivation of the PSi nanocrystals probably leads to the expansion of spectral photosensitivity in the short-wavelength range (see Fig. 8.12). In addition to the broad maximum of photosensitivity in the 750–950 nm spectral range, an increase in the sensitivity of the PSi–rGO hybrid nanosystems in the 500–600 nm range is observed.

Another approach to expanding the photodetector spectral sensitivity is based on the strategy of cascade solar cells: multilayer structures with a different band gap [59]. In particular, sandwich-like PSi–ZnO hybrid nanosystems can be attributed to multijunction photosensitive structures. Because undoped ZnO crystals have an electronic type of conductivity, one can expect a significant influence of the conductivity type of the PSi layer and silicon substrate on the electrical properties of the PSi–ZnO structures. Hybrid semiconductor structures with heterojunctions are formed on the *n*-Si substrate, while nanosystems on the *p*-Si substrate are characterized by the *p*-*n* junction.

The PSi–ZnO sandwich-like nanosystems obtained on silicon substrates of both electronic and hole conductivity types have nonlinear CVC characterized by higher current values in the case of a negative potential on the ZnO layer (see Fig. 8.11). Besides, the CVC rectification factor was greater for structures with a *p*-Si substrate. Nonlinear CVCs are caused by contact phenomena, electrical barriers in the porous layer, and at the boundaries of ZnO/PSi and PSi/silicon substrate [60]. Considering that structures with thick (over 10 μm) PSi layers are usually characterized by varistor-like CVC [16], it can be assumed that the rectifying CVC is caused by the dominance of the electrical barrier at the ZnO/PSi interface. An increase in the reverse current of the CVC indicates the generation of photocarriers in hybrid semiconductor nanosystems.

The photoresponse spectra of the PSi–ZnO hybrid nanosystems are characterized by two broad bands of photosensitivity in the 750–950 nm and 500–600 nm ranges (see Fig. 8.12). The band with a maximum near 830 nm is associated with light absorption in the

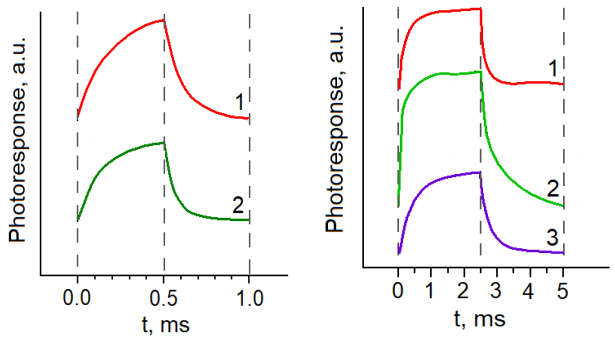

a *b*

Figure 8.13 Kinetics of the photoresponse to rectangular 940 (*1*), 570 (*2*), and 390 nm (*3*) light pulses for the PSi–rGO (*a*) and PSi–ZnO (*b*) hybrid structures

silicon substrate and non-quantum-sized PSi nanocrystals. The increase in photosensitivity of the PSi–ZnO hybrid nanosystems in the 500–650 nm range can be related to the light absorption in the ZnO layer and the PSi nanocrystals with a modified electronic structure due to quantum confinement.

The analysis of the photoresponse kinetics of the PSi–rGO and PSi–ZnO hybrid nanosystems revealed some differences in the generation-recombination and relaxation processes that occur under the influence of exciting light with different wavelengths (Fig. 8.13). In particular, a shorter time of the photoresponse (about 1 ms) is observed in the case of irradiation with IR pulses (λ=940 nm). The response time of the PSi–ZnO hybrid structures to pulses of green light (λ=570 nm) and UV radiation (λ=390 nm) is about 1.5–2.5 ms. The PSi–rGO structures are also characterized by a different photoresponse time to pulses of IR radiation (λ=940 nm) and green light (λ=570 nm).

The kinetics of the photoresponse to light pulses with different wavelengths can be an additional argument in favor of the assumption that various layers of the PSi-based hybrid structures are responsible for the absorption of light quanta with different energies.

8.6 Ionizing Radiation Detector based on PSi Nanostructures

The significant influence of both the microstructure and the state of the silicon nanocrystal surface on electronic processes in the PSi gives reason to expect a dependence of the electrical properties of the PSi nanosystems on radiation exposure. The isotope of radium ^{226}Ra with 0.1 mCi activity was used as a radiation source to study the influence of ionizing radiation on the electrical properties of the PSi structures. The decay of ^{226}Ra isotope results in the γ-rays radiation with an energy of about 0.19 MeV. The average energy of β-radiation is 0.17 MeV. The distance from the experimental PSi structures to the radiation source was about 0.6 m. Therefore, there was no need to account for α-particles with 4.78 MeV energy typically scattering already after traveling several centimeters in the air. The dosage of absorbed radiation depended on the exposure duration.

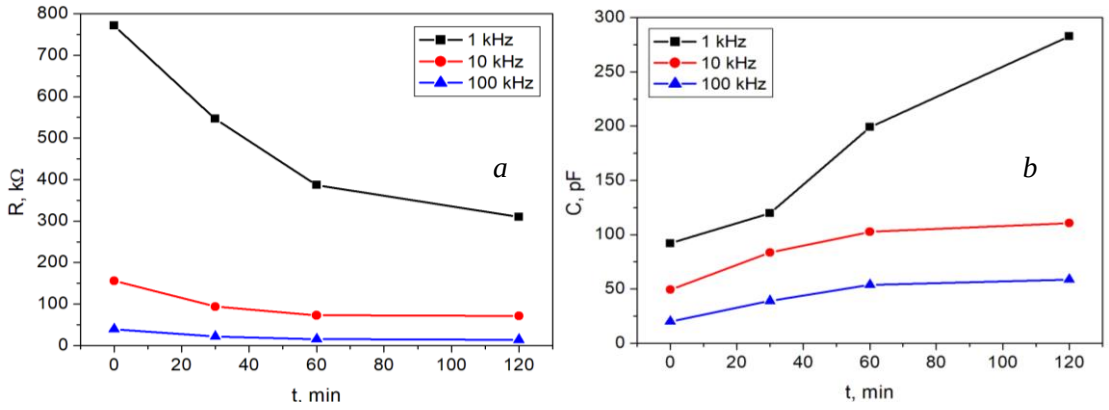

Figure 8.14 Dependence of the electrical resistance (a) and capacity (b) of the PSi structure on the time of irradiation with the ^{226}Ra isotope

A nonlinear decrease in resistance and an increase in the capacity of the PSi nanostructures with an increase in the duration of the simultaneous action of β- and γ-radiation were revealed (Fig 8.14). With an increase in the frequency of the measuring signal, there is a decrease in the effect of ionizing radiation on the electrical characteristics of the PSi.

Peculiarities of the obtained dependences can be due to the formation of radiation defects in a natural oxide thin film on the PSi nanocrystal surface [10, 36], which causes the accumulation of charge on the surface of silicon nanocrystals and an increase in their electrical capacity. Energy levels formed in the band gap of the PSi nanostructures can also be involved in charge transfer and relaxation processes.

It should be noted that disordered systems (in particular PSi structures) are characterized by a quasi-continuous energy distribution of levels of trapping of non-equilibrium charge carriers [34]. The thermally stimulated depolarization (TSD) current was measured to determine the activation energy of electrically active defects in the PSi structures. The analysis of TSD spectra makes it possible to detect the formation of radiation defects in the PSi-based nanosystems. The measured temperature dependences of the TSD current of the PSi structure before and after irradiation are shown in Figure 8.15.

The PSi structures are characterized by the emission of charges in the case of thermal stimulation from liquid nitrogen temperature with a maximum near 120 K and the current growth wide band in the 260–275 K temperature range. As a result of the ionizing radiation action, a decrease in the TSD current in the specified bands and the appearance of a new current peak at 180–190 K were observed. The additional maximum of the TSD current is likely associated with the formation of radiation defects.

The analysis of the obtained dependencies based on the phenomenological theory of TSD currents for disordered dielectrics makes it possible to determine the energy distribution of the filling density of localized states. The calculated energy distributions are shown in the inset of Figure 16. Groups of trapping levels with activation energies in the 0.20–0.25 and 0.50–0.65 eV ranges were found in the band gap of the unirradiated PSi. These charge carrier traps are typically related to the activation of hydrogen ions and defects at the Si–SiO_2 interface, respectively [34]. As a result of the action of β- and γ-radiation, a change in

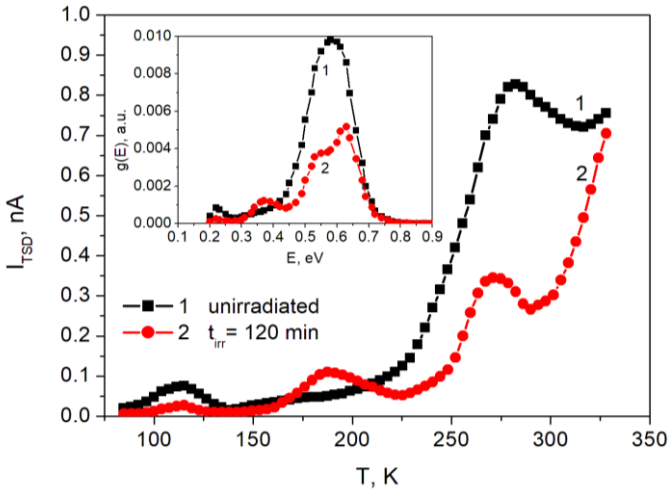

Figure 8.15 Temperature dependences of the TSD current and energy distribution of the filling density of states (on the inset) of the unirradiated PSi structure (*1*) and irradiated from ^{226}Ra isotope for 120 min (*2*)

the filling density of states in various energy ranges and the formation of radiation defects in the PSi with the 0.35–0.40 eV activation energy were observed. Found irreversible radiation-induced changes in the electrical characteristics of the PSi-based nanosystems can be used to create inexpensive dosimetric devices.

8.7 PSi-based Hybrid Nanosystems for Gas Sensing Application

The study of the electrical properties of the PSi-based structures in DC and AC modes revealed a significant dependence of conductivity and capacitance on environmental conditions. In particular, an increase in the relative humidity causes a decrease in the resistance and an increase in the capacity of hybrid composites based on the PSi nanostructures [60, 61]. Figure 8.16 shows the dependence of the electrical resistance and capacitance of the PSi–rGO and PSi–ZnO nanosystems on relative humidity. Analysis of the obtained dependencies indicates different sensitivity of the studied structures to the action of water molecules. In particular, the largest relative change in resistance and capacity at the same change in relative humidity is observed for the PSi–rGO nanosystem. Conversely, the PSi–ZnO hybrid structure exhibits the lowest electrical response.

The features of measured dependencies are caused by the interaction of polar water molecules with the surface of semiconductor nanocrystals. The electronic structure of both PSi and ZnO nanocrystals and the redistribution of free charge carriers change due to the adsorption-induced effects [32]. As a result, the concentration and mobility of charge carriers and the height of potential barriers between semiconductor nanocrystals can change. Besides, charge transfer through a network of hydrogen-bonded water molecules is possible in the case of high relative humidity (85–100%) when PSi pores contain condensed water [62]. The local electric field of adsorbed molecules also changes the conductivity of the

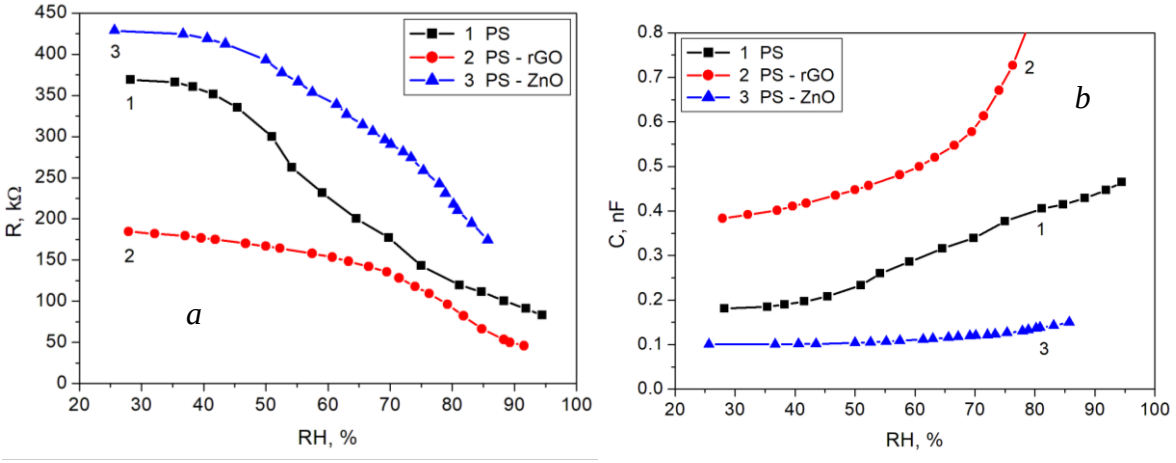

Figure 8.16 Dependences of resistance (*a*) and capacitance (*b*) of the initial PSi (*1*), the PSi–rGO (*2*) and PSi–ZnO (*3*) hybrid structures on relative humidity

rGO nanosheets forming a cumulative response of sensor elements based on hybrid nanosystems [63]. In addition, the adsorption of moisture causes an increase in the effective dielectric constant of the porous layer due to the higher value of the dielectric constant of water compared to silicon (ε = 81). Therefore the capacity of nanosystems based on the PSi increases.

A sensor material important characteristic related to the adsorption-desorption interaction with the gas medium is the sensing ability [64]. Therefore, to evaluate the sensor properties of the PSi-based nanosystems, the sensing ability of resistive γ_R and capacitive γ_C sensor elements was calculated according to the relations

$$\gamma_R = \frac{\Delta R/R}{\Delta p/p_0} \quad \text{and} \quad \gamma_C = \frac{\Delta C/C}{\Delta p/p_0}, \tag{8.1}$$

where $\Delta p/p_0$ is the change in relative air humidity, $\Delta R/R$ and $\Delta C/C$ are the relative change in resistance and capacity, respectively. The calculated dependences of the sensing ability of the PSi-based structures on relative air humidity are shown in Figure 8.17. The PSi–rGO structure shows the greatest sensitivity to water vapor in the 75–95 % range, while the PSi sensitivity is maximal in the 45–55 % relative humidity range. The PSi–ZnO nanosystem is the least sensitive to the adsorption of water molecules.

The branched system of pores determines the high sensitivity of the electrical characteristics of the PSi-based nanosystems not only to water vapor but also to the adsorption of molecules of various nature. In particular, hybrid films based on the PSi and rGO nanoparticles demonstrate excellent prospects for use in ammonia and ethanol sensors. Sensor films based on the PSi–rGO nanosystem are characterized by higher porosity than conjugated polymers-based nanocomposite films. Failure to use conjugated polymer as a host medium of the composite causes an increase in the working surface of sensitive elements. Besides, the rGO nanosheets covering PSi nanoparticles can not only increase the gas sensor sensitivity but also reduce the resistance of sensor elements due to percolation processes.

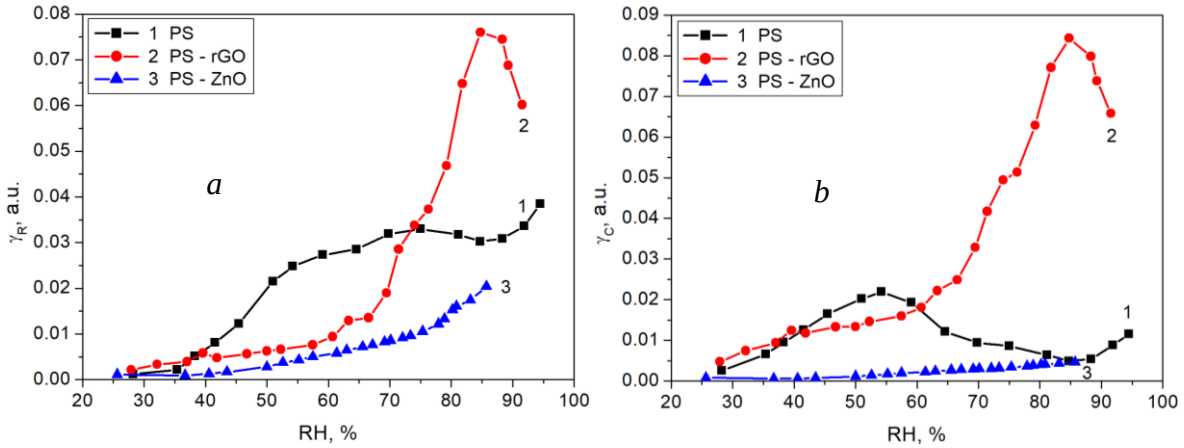

Figure 8.17 Sensing ability of resistive (*a*) and capacitive (*b*) sensors based on the PSi (*1*) and PSi–rGO (*2*) and PSi–ZnO (*3*) hybrid structures as functions of the relative air humidity

It was found that the electrical characteristics of the PSi–rGO nanosystems depend significantly on both the composition of the material and the surrounding atmosphere [65]. In particular, nanosystems with a higher content of the rGO nanosheets were characterized by lower resistance and higher capacity, which may be related to a larger contact area with the PSi nanostructures and the formation of percolation clusters in the rGO network. The conductivity of silicon and carbon nanostructures and the efficiency of the electrical contact between them determine the resistive component of the impedance in the AC mode. The charge transfer across the boundaries between nanoparticles forms the mechanism of the capacitive component of the impedance of the PSi–rGO sensor films.

Filling the working chamber with ammonia or ethanol vapors caused a decrease in the electrical resistance and an increase in the capacity of the sensor elements based on the PSi–rGO nanosystem (Fig. 8.18).

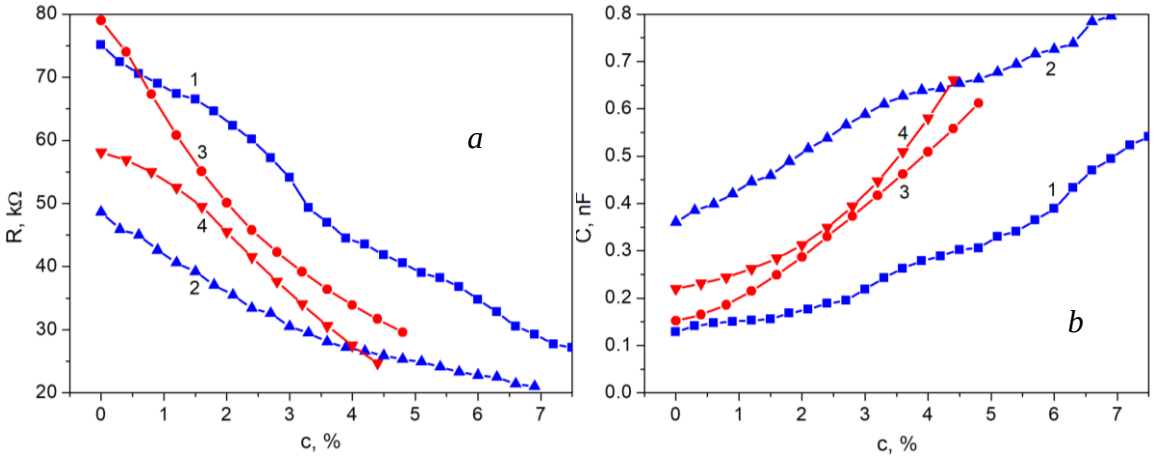

Figure 8.18 Dependences of resistance (*a*) and capacitance (*b*) of the PSi–rGO hybrid films with components ratio Psi : rGO = 3 : 1 (*1*, *3*) and Psi : rGO = 2 : 1 (*2*, *4*) on the concentration of ammonia (*1*, *2*) and ethanol (*3*, *4*) molecules

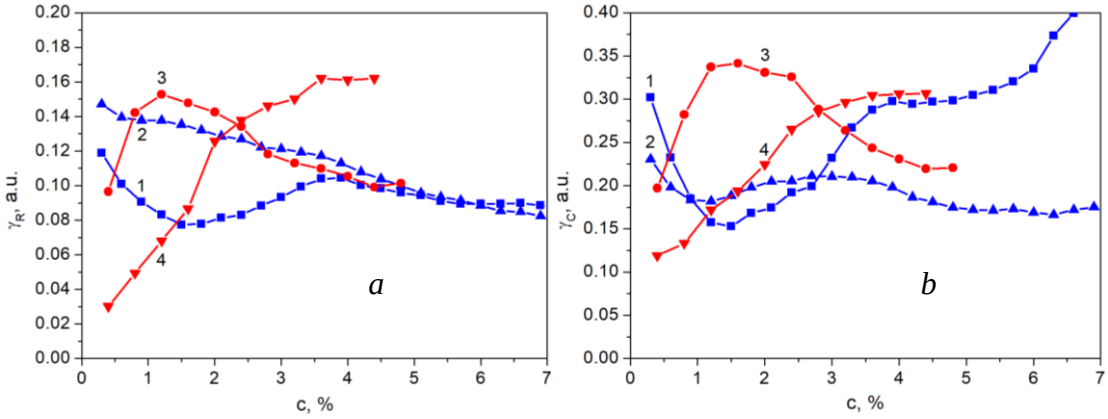

Figure 8.19 Dependences of sensing ability of resistive (*a*) and capacitive (*b*) sensor elements based on the PSi–rGO hybrid films with components ratio PSi : rGO = 3 : 1 (*1*, *3*) and PSi : rGO = 2 : 1 (*2*, *4*) on the concentration of ammonia (*1*, *2*) and ethanol (*3*, *4*) molecules

The resulting dependencies are caused by a change in the electronic structure of both silicon and graphene nanoparticles due to the interaction of adsorbed molecules with the hybrid film surface. The measurements revealed a greater sensitivity of capacitive ammonia and ethanol sensors based on the PSi–rGO film than resistive-type sensor elements (see Fig. 8.19). Sensory properties of the PSi–rGO films were analyzed based on the concentration dependence of sensing ability calculated using the relations

$$\gamma_R = \frac{1}{R}\frac{\Delta R}{\Delta c} \quad \text{and} \quad \gamma_C = \frac{1}{C}\frac{\Delta C}{\Delta c}, \tag{8.2}$$

for resistive and capacitive sensors, respectively. Here Δc is the change in the concentration of the analyzed gas in the air.

It should be noted that the PSi–rGO nanosystems with various ratios of components have the maximum sensitivity in different concentration ranges of the analyzed gases. In particular, both resistive and capacitive ethanol sensors based on a nanosystem with a higher content of silicon nanoparticles (PSi : rGO = 3 : 1) are characterized by a maximum sensing ability in the 1.0–2.5 % range. On the other hand, the hybrid film with the ratio of components PSi : rGO = 2 : 1 is more sensitive to the action of ethanol in the 3.5–4.5 % concentration range. Moreover, in the range of low gas concentrations (0.5–2.0 %), the PSi : rGO = 2 : 1 resistive sensor element has greater sensitivity to ammonia molecules, and the PSi : rGO = 3 : 1 sensor film has greater sensitivity to ethanol. Therefore, it is possible to adjust the maximum sensitivity and hence the sensor selectivity to a fixed gas type by changing the ratio of the PSi–rGO nanosystem components.

The elimination of the silicon substrate shunting effect and the use of the rGO nanoparticles sensitive to adsorbed molecules for the electrical connection of the PSi nanostructures provide an increase in the sensitivity of film sensor elements compared to sensors based on the PSi sandwich structures [66].

One of the important characteristics of sensor materials is the response time of the sensor element to changes in the tested gas concentration. The time dependencies of resis-

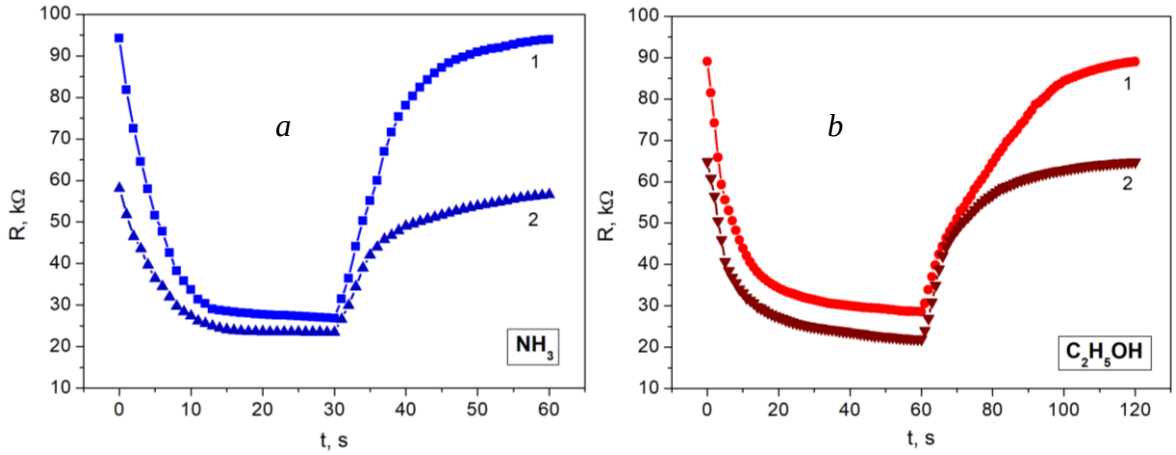

Figure 8.20 Response of resistance of the PSi–rGO hybrid films with components ratio PSi : rGO = 3 : 1 (*1*) and PSi : rGO = 2 : 1 (*2*) to changing the concentration of ammonia (*a*) and ethanol (*b*) molecules

tance for the ammonia and ethanol sensors based on the PSi–rGO nanosystems are shown in Figure 8.20. The interaction of ammonia and ethanol molecules with the sensor film surface has the character of physical adsorption because the initial film resistance is restored even at room temperature after the removal of the analyzed gases. The reaction and recovery time of the ammonia and ethanol sensors does not exceed one minute and is independent of the ratio of the PSi–rGO nanosystem components.

Since PSi-based nanosystems have a high sensitivity of electrical characteristics to the adsorption of various gases, in particular water vapor in the air, ensuring the necessary selectivity to the analyzed gas requires additional gas recognition mechanisms. One such mechanism can be a computer analysis of the cross-sensitivity of the matrix of sensory elements with an individual profile of the transfer function. Analysis of the overall response of the multi-element sensory system makes it possible to identify the gas and determine its concentration with correction for the relative air humidity.

The effectiveness of this approach is demonstrated by a line of PSi-based sensor elements [67]. The use of the PSi nanostructures on the silicon substrate simplifies the matrix of sensor elements manufacturing technology and its integration into an intelligent system. Sensitive elements based on the PSi and PSi–Pd and PSi–ZnO nanosystems were used to form the sensor matrix (Fig. 8.21). The incorporation of palladium nanoclusters into the PSi

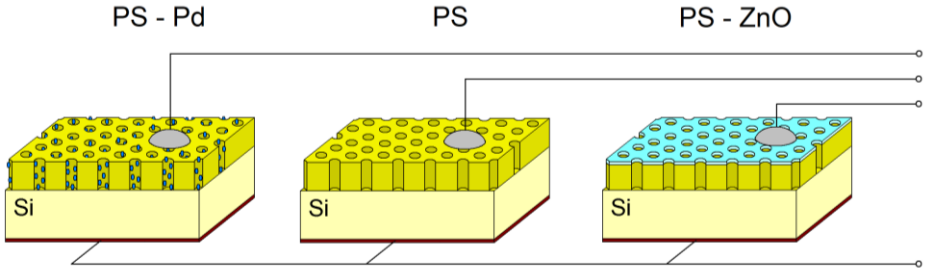

Figure 8.21 Schematic representation of the sensor matrix based on the PSi nanostructures

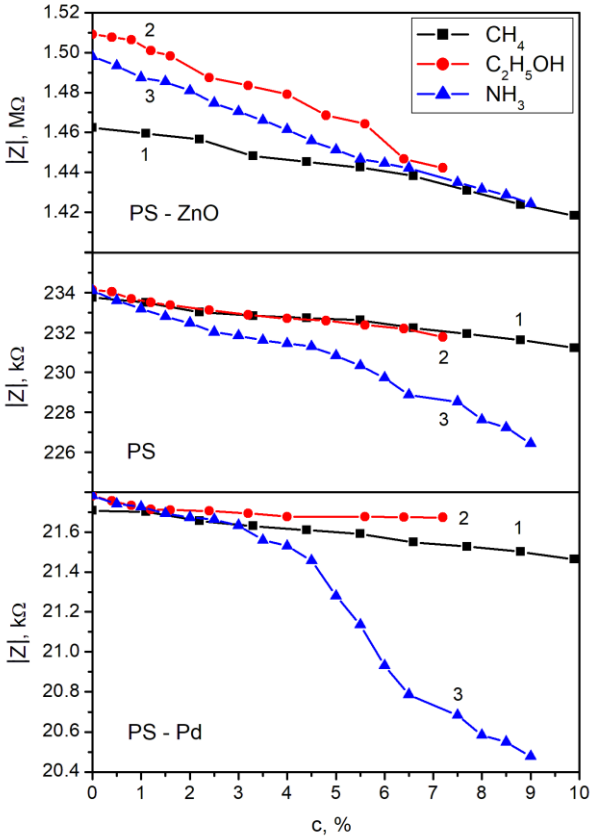

Figure 8.22 Dependence of the impedance modulus of the PSi-based sensor elements on the concentration of methane (*1*), ethanol (*2*) and ammonia (*3*) molecules

increases the sensitivity of sensors to hydrogen molecules and hydrogen-based compounds [68]. On the other hand, ZnO nanostructures are highly sensitive to the adsorption of NO_2, C_2H_5OH, and CH_4 molecules [19, 69, 70].

The response of the sensor system to the appearance of methane, ammonia, and ethanol in a gaseous state in the experimental chamber was registered. The measured values of relative air humidity in the experimental chamber were 53, 42, and 45% when studying the adsorption of methane, ethanol, and ammonia, respectively. The impedance of each sensor element was measured at a frequency of 1 kHz. As can be seen in Figure 8.22, the impedance module of sensor elements depends not only on the presence of catalytic material (Pd or ZnO) on the PSi surface but also on the nature and concentration of adsorbed molecules.

In general, for all PSi-based sensor elements, a decrease in the impedance modulus is observed in response to the introduction of methane, ammonia, or ethanol vapor into the experimental chamber. However, each of the sensor elements is characterized by individual sensitivity to these gases. In particular, the PSi–ZnO nanosystem was the most sensitive to CH_4 molecules. The greatest sensitivity to the adsorption of NH_3 molecules was registered for the PSi–Pd nanosystem. However, the sensitivity of the PSi–Pd nanosystem is not the

same in different ammonia concentration ranges. Close to linear concentration dependences of the impedance modulus of the sensor elements are observed in the case of adsorption of the C_2H_5OH and CH_4 molecules.

The problem of gas identification can be solved due to the individual profile of the transfer function of each sensor element. Analysis of the measured overall response of the line of parallel working sensor elements makes it possible to identify an individual gas and determine its concentration in the air. For example, an unknown gas that causes the 21.65 kΩ, 233 kΩ, and 1.45 MΩ impedance modulus responses of the corresponding PSi-based sensor elements can be identified as methane at the 3 % concentration. It is necessary to use a larger number of sensor elements and apply machine learning methods for computer analysis of the multi-element sensor system response to increase the accuracy of identification and analysis of a larger number of gases.

8.8 Summary and Outlook

In this chapter, we have considered the main approaches to creating optoelectronic and sensor devices based on PSi nanosystems. The discovery of the visible luminescence of the PSi at room temperature led to an increased interest of researchers in silicon nanostructures. Various applications based on the quantum confinement effect and the PSi significant surface area have been proposed. We focused on new technical solutions that improve the functional properties of the PSi-based structures. In particular, the creation of hybrid nanosystems makes it possible to combine the useful properties of individual components. The branched pore system of the PSi facilitates the combination of nanoparticles of different nature and the formation of hybrid nanomaterials.

In particular, the combination of photoluminescent properties of the PSi and ZnO nanostructures makes it possible to observe multicolor photoemission that covers almost the entire visible spectral range. Such nanosystems can be used to create white light emitters. Besides, the possibility to control the luminescent properties of the hybrid PSi–ZnO nanosystems by changing the excitation energy is demonstrated based on complex studies of the PL excitation and emission spectra.

ZnO crystal arrays can be used not only as a transparent window for visible PL of the PSi–ZnO hybrid nanosystems but also as the top layer of multijunction photosensitive PSi-based structures. The ZnO layer absorbs photons with higher energy and simultaneously transmits low-energy photons to the following layers with a smaller band gap: the PSi layer and the silicon substrate. The efficiency of photoelectric conversion in multijunction photoreceivers is higher due to absorbing a much larger part of the solar spectrum. In addition to expanding the spectrum of photosensitivity, other methods of improving operational characteristics of the photoelectric devices can be improved passivation of the surface of the PSi nanostructures, an increase in the junction area, and the formation of additional channels for the current passage through the porous layer. We have demonstrated that the incorporation of metal nanoclusters and rGO nanosheets into the porous layer ensures effective passivation of the PSi surface and collection of charge carriers.

The influence of the surface states and electrically active defects on the electrical characteristics of the PSi-based nanosystems makes it possible to use the process of formation of radiation-induced defects to create γ- and β-radiation detectors. The PSi-based nanosystems can also be sensitive elements of dosimetric devices due to the irreversibility of radiation-induced changes in their electrical characteristics. Such sensitive elements are easily integrated into silicon technology and can be used both for radiation monitoring the environment and in inexpensive individual dosimeters.

Particular attention was paid to the gas-sensing properties of the PSi-based hybrid nanosystems. It was established that due to the significant specific surface area of silicon nanocrystals, the nanosystems based on the PSi are extremely sensitive to the adsorption of various gases, in particular, water and ethanol vapor, molecules of ammonia and methane. The use of the ZnO and graphene nanostructures and palladium as catalysts makes it possible to increase the sensitivity of the PSi-based sensor to the selected type of gas. The response time of such sensory elements to changing the concentration of the analyzed molecules is sufficient for microelectronic gas sensors. Relatively low operating temperatures of the sensors are also important. Sensors based on the PSi nanosystems work effectively at room temperature.

Finally, the possibility not only to identify an individual gas but also to determine its concentration in the atmosphere using the analysis of the overall response of the multisensor system impedance is demonstrated. The use of artificial intelligence methods will significantly expand the functional flexibility of sensors compared to current capabilities. In particular, the use of new approaches and data analysis algorithms will increase the efficiency of using intelligent sensor systems for environmental monitoring.

Keywords

- porous silicon
- nanosystems
- photoluminescence
- photoresponse
- ionizing radiation detector
- gas sensor
- sensing ability

References

1. *Lifshitz E., Siebbeles L. D. A.* Fundamental processes in semiconductor nanocrystals // Phys. Chem. Chem. Phys. 2014. Vol. 16. P. 25677–25678. DOI: https://doi.org/10.1039/C4CP90174F
2. *Ogut S., Chelikowsky J. R., Louie S. G.* Quantum confinement and optical gaps in Si nanocrystals // Phys. Rev. Lett. 1997. Vol. 79. P. 1770–1773. DOI: https://doi.org/10.1103/PhysRevLett.79.1770
3. *Lu Z. H., Lockwood D. J., Baribeau J. M.* Quantum confinement and light emission in SiO_2/Si superlattices // Nature. 1995. Vol. 378. P. 258–260. DOI: https://doi.org/10.1038/378258a0

4. *Cullis A. G., Canham L. T.* Visible light emission due to quantum size effects in highly porous crystalline silicon // Nature. 1991. Vol. 353. P. 335–338. DOI: https://doi.org/10.1038/353335a0
5. *Ray S. K., Maikap S., Banerjee W., Das S.* Nanocrystals for silicon-based light-emitting and memory devices // J. Phys. D Appl. Phys. 2013. Vol. 46. P. 153001. DOI: http://dx.doi.org/10.1088/0022-3727/46/15/153001
6. *Daldosso N., Pavesi L.* Nanosilicon photonics // Laser Photonics Rev. 2009. Vol. 3 (6). P. 508–534. DOI: https://doi.org/10.1002/lpor.200810045
7. *Ahmed N. M., Al-Douri Y., Alwan A. M., Jabbar A. A., Arif G. E.* Characteristics of nanostructure silicon photodiode using laser assisted etching // Procedia Eng. 2013. Vol. 53. P. 393–399. DOI: https://doi.org/10.1016/j.proeng.2013.02.051
8. *Yamaguchi M., Ohshita Y., Arafune K., Sai H., Tachibana M.* Present status and future of crystalline silicon solar cells in Japan // Sol. Energy. 2006. Vol. 80. P. 104–110. DOI: https://doi.org/10.1016/j.solener.2005.02.013
9. *Peng K. Q., Lee S. T.* Silicon nanowires for photovoltaic solar energy conversion // Adv. Mater. 2001. Vol. 23. P. 198–215. DOI: https://doi.org/10.1002/adma.201002410
10. *Bisi O., Ossicini S., Pavesi L.* Porous silicon: a quantum sponge structure for silicon based optoelectronics // Surf. Sci. Rep. 2000. Vol. 38. P. 1–126. DOI: https://doi.org/10.1016/S0167-5729(99)00012-6
11. *Unal B., Parbukov A. N., Bayliss S. C.* Photovoltaic properties of a novel stain etched porous silicon and its application in photosensitive devices // Opt. Mater. 2001. Vol. 17. P. 79–82. DOI: https://doi.org/10.1016/S0925-3467(01)00023-4
12. *Cao A., Sudhölter E. J. R., de Smet L. C. P. M.* Silicon nanowire-based devices for gas-phase sensing // Sensors. 2014. Vol. 14, P. 245–271. DOI: https://doi.org/10.3390/s140100245
13. *Eom N. S. A., Cho H. B., Song Y., Lee W., Sekino T., Choa Y. H.* Room-temperature H_2 gas sensing characterization of graphene-doped porous silicon via a facile solution dropping method // Sensors. 2017. Vol. 17. DOI: https://doi.org/10.3390/s17122750
14. *Qin Y., Liu D., Zhang T., Cui Z.* Ultrasensitive silicon nanowire sensor developed by a special Ag modification process for rapid NH_3 detection // ACS Appl. Mater. Interfaces. 2017. Vol. 9 (34). P. 28766–28773. DOI: https://doi.org/10.1021/acsami.7b10584
15. *Rahimi F., Iraji Zad A.* Effective factors on Pd growth on porous silicon by electroless-plating: Response to hydrogen // Sens. Actuators B Chem. 2006. Vol. 115, P. 164–169. DOI: https://doi.org/10.1016/j.snb.2005.08.035
16. *Olenych I. B., Monastyrskii L. S., Aksimentyeva O. I., Sokolovskii B. S.* Humidity sensitive structures on the basis of porous silicon // Ukr. J. Phys. 2011. Vol. 56 (11), P. 1198–1202. DOI: https://doi.org/10.15407/ujpe56.11.1198
17. *Yan D., Li S., Liu S., Tan M., Li D., Zhu Y.* Electrochemical synthesis of ZnO nanorods / porous silicon composites and their gas-sensing properties at room temperature // J. Solid State Electrochem. 2016. Vol. 20. P. 459–468. DOI: https://doi.org/10.1007/s10008-015-3058-6
18. *Galstyan V., Comini E., Baratto C., Faglia G., Sberveglieri G.* Nanostructured ZnO chemical gas sensors // Ceram. Int. 2015. Vol. 41. P. 14239–14244. DOI: https://doi.org/10.1016/j.ceramint.2015.07.052
19. *Delaunay J. J., Kakoiyama N., Yamada I.* Fabrication of three-dimensional network of ZnO tetratpods and its response to ethanol // Mater. Chem. Phys. 2007. Vol. 104. P. 141–145. DOI: https://doi.org/10.1016/j.matchemphys.2007.02.099
20. *Zhu Y., Murali S., Cai W., Li X., Suk J. W., Potts J. R., Ruoff R. S.* Graphene and graphene oxide: synthesis, properties, and applications // Adv. Mater. 2010. Vol. 22. P. 3906–3924. DOI: https://doi.org/10.1002/adma.201001068
21. *Kim S.-Y., Kim Y. J., Jung U., Lee B. H.* Chemically induced Fermi level pinning eņects of high-k dielectrics on graphene // Sci. Rep. 2018. Vol. 8. DOI: https://doi.org/10.1038/s41598-018-21055-z

22. *Novoselov K. S., Geim A. K., Morozov S. V., Jiang D., Katsnelson M. I., Grigorieva I. V., Dubonos S. V., Firsov A. A.* Two-dimensional gas of massless Dirac fermions in graphene // Nature. 2005. Vol. 438. P. 197–200. DOI: https://doi.org/10.1038/nature04233
23. *Hähnlein B., Händel B., Pezoldt J., Töpfer H., Granzner R., Schwierz F.* Side-gate graphene field-effect transistors with high transconductance // Appl. Phys. Lett. 2012. Vol. 101. DOI: https://doi.org/10.1063/1.4748112
24. *Karaduman I., Er E., Çelikkan H., Acar S.* A new generation gas sensing material based on high-quality graphene // Sensor. Actuat. B Chem. 2015. Vol. 221. P. 1188–1194. DOI: https://doi.org/10.1016/j.snb.2015.07.063
25. *Yoon H. J., Jun D. H., Yang J. H., Zhou Z., Yang S. S., Cheng M. M. C.* Carbon dioxide gas sensor using a graphene sheet // Sensor. Actuat. B Chem. 2011. Vol. 157. P. 310–315. DOI: https://doi.org/10.1016/j.snb.2011.03.035
26. *Cullis A. G., Canham L. T., Calcott P. D. J.* The structural and luminescence properties of porous silicon // J. Appl. Phys. 1997. Vol. 82. P. 909–965. DOI: https://doi.org/10.1063/1.366536
27. *Föll H., Christophersen M., Carstensen J., Hasse, G.* Formation and application of porous silicon // Mater. Sci. Eng. R Rep. 2002. Vol. 39. P. 93–141. DOI: https://doi.org/10.1016/S0927-796X(02)00090-6
28. *Kim J., Joo S. S., Lee K. W., Kim J. H., Shin D. H., Kim S., Choi S-H.* Near-ultraviolet-sensitive graphene/porous silicon photodetectors // ACS Appl. Mater. Interfaces. 2014. Vol. 6. P. 20880–20886. DOI: https://doi.org/10.1021/am5053812
29. *Jiao L-S., Liu J-Y., Li H-Y., Wu T-S., Li F., Wang H-Y., Niu L.* Facile synthesis of reduced graphene oxide-porous silicon composite as superior anode material for lithium-ion battery anodes // J. Power Sources. 2016. Vol. 315. P. 9–15. DOI: https://doi.org/10.1016/j.jpowsour.2016.03.025
30. *Martinez L., Ocampo O., Kumar Y., Agarwal V.* ZnO-porous silicon nanocomposite for possible memristive device fabrication // Nanoscale Res. Lett. 2014. Vol. 9. DOI: https://doi.org/10.1186/1556-276X-9-437
31. *Amran T. S., Hashim M. R., Al-Obaidi N. K., Yazid H., Adnan R.* Optical absorption and photoluminescence studies of gold nanoparticles deposited on porous silicon // Nanoscale Res. Lett. 2013. Vol. 8. P. 35–41. DOI: https://doi.org/10.1186/1556-276X-8-35
32. *Monastyrskii L. S., Olenych I. B., Sokolovski B. S.* Simulation of field effect in porous silicon nanostructures // Appl. Nanosci. 2020. Vol. 10. P. 4645–4650. DOI: https://doi.org/10.1007/s13204-020-01321-1
33. *Olenych I. B.* Stabilization of surface and photoluminescent properties of porous silicon // Ukr. J. Phys. Opt. 2011. Vol. 12 (2). P. 54–61. DOI: http://dx.doi.org/10.3116/16091833/12/2/54/2011
34. *Olenych I., Tsizh B., Monastyrskii L., Aksimentyeva O., Sokolovskii B.* Preparation and properties of nanocomposites of silicon oxide in porous silicon // Solid State Phenom. 2015. Vol. 230. P. 127–132. DOI: https://doi.org/10.4028/www.scientific.net/SSP.230.127
35. Pan L. K., Huang H. T., Sun C. Q. Dielectric relaxation and transition of porous silicon // J. Appl. Phys. 2003. Vol. 94 (4). P. 2695–2700. DOI: https://doi.org/10.1063/1.1594821
36. Olenych I. B., Monastyrskii L. S., Dzendzeliuk O. S. Effect of ionizing radiation on the properties of porous silicon nanostructures // J. Nano- Electron. Phys. 2015. Vol. 7 (4) (in Ukrainian).
37. *Olenych I. B., Aksimentyeva O. I., Monastyrskii L. S., Dzendzeliuk O. S.* Effect of radiation on the electrical and luminescent properties of conjugated polymer - porous silicon composite // Mol. Cryst. Liq. Cryst. 2016. Vol. 640. P. 165–172. DOI: https://doi.org/10.1080/15421406.2016.1257328
38. *Smith R. L., Collins S. D.* Porous silicon formation mechanisms // J. Appl. Phys. 1992. Vol. 71 (8). P. R1–R12. DOI: https://doi.org/10.1063/1.350839
39. *Primachenko V. E., Kononets J. F., Bulakh B. M., Venger E. F., Kaganovich É. B., Kizyak I. M., Kirillova S. I., Manoilov É. G., Tsyrkunov Yu. A.* The electronic and emissive properties of Au-doped

porous silicon // Semiconductors. 2005. Vol. 39. P. 565–571. DOI: https://doi.org/10.1134/1.1923566

40. *Wu J. J., Liu S. C.* Low-temperature growth of well-aligned ZnO nanorods by chemical vapor deposition // Adv. Mater. 2002. Vol. 14. P. 215–218. DOI: https://doi.org/10.1002/1521-4095(20020205)14:3<215::AID-ADMA215>3.0.CO;2-J
41. *Abdulgafour H. I., Yam F. K., Hassan Z., Al-Heuseen K., Jawad M. J.* ZnO nanocoral reef grown on porous silicon substrates without catalyst // J. Alloys Compd. 2011. Vol. 509. P. 5627–5630. DOI: https://doi.org/10.1016/j.jallcom.2011.02.100
42. *Sundaram K. B., Khan A.* Characterization and optimization of zinc oxide films by r.f. magnetron sputtering // Thin Solid Films. 1997. Vol. 295 (1). P. 87–91. DOI: https://doi.org/10.1016/S0040-6090(96)09274-7
43. *Gafiychuk V. V., Ostafiychuk B. K., Popovych D. I., Popovych I. D., Serednytski A. S.* ZnO nanoparticles produced by reactive laser ablation // Appl. Surf. Sci. 2011. Vol. 257 (20). P. 8396–8401. DOI: https://doi.org/10.1016/j.apsusc.2011.04.084
44. *Yang J. H., Zheng J. H., Zhai H. J., Yang L. L.* Low temperature hydrothermal growth and optical properties of ZnO nanorods // Cryst. Res.Technol. 2009. Vol.44. P. 87–91. DOI: https://doi.org/10.1002/crat.200800294
45. *Bechelany M., Amin A., Brioude A., Cornu D., Miele P.* ZnO nanotubes by template-assisted sol-gel route // J. Nanopart. Res. 2012. Vol.v14. DOI: https://doi.org/10.1007/s11051-012-0980-8
46. *Kapustianyk V., Turko B., Luzinov I., Rudyk V., Tsybulskyi V., Malynych S., Rudyk Yu., Savchak M.* LEDs based on p-type ZnO nanowires synthesized by electrochemical deposition method // Physica Status Solidi C. 2014. Vol. 11 (9-10). P. 1501–1504. DOI: https://doi.org/10.1002/pssc.201300671
47. *Antohe V. A., Gence L., Srivastava S. K., Piraux L.* Template-free electrodeposition of highly oriented and aspect-ratio controlled ZnO hexagonal columnar arrays // Nanotechnology. 2012. Vol. 23 (25). DOI: http://dx.doi.org/10.1088/0957-4484/23/25/255602
48. *Hsu H. C., Cheng C. S., Chang C. C., Yang S., Chang C. S., Hsieh W. F.* Orientation-enhanced growth and optical properties of ZnO nanowires grown on porous silicon substrates // Nanotechnology. 2005. Vol. 16 (2). P. 297–301. DOI: http://dx.doi.org/10.1088/0957-4484/16/2/021
49. *Wang Z. L.* Zinc oxide nanostructures: growth, properties and applications // J. Phys. Condens. Matter. 2004. Vol. 16 (25). P. R829–R858. DOI: https://doi.org/10.1039/C2JM15548F
50. *Kazi S. N., Badarudin A., Zubir M. N. M., Ming H. N., Misran M., Sadeghinezhad E., Mehrali M., Syuhada N.* I. Investigation on the use of graphene oxide as novel surfactant to stabilize weakly charged graphene nanoplatelets // Nanoscale Res. Lett. 2015. Vol. 10. DOI: https://doi.org/10.1186/s11671-015-0882-7
51. *Dovbeshko G. I, Romanyuk V. R., Pidgirnyi D. V., Cherepanov V. V., Andreev E. O., Levin V. M., Kuzhir P. P., Kaplas T., Svirko Y. P.* Optical properties of pyrolytic carbon films versus graphite and graphene // Nanoscale Res. Lett. 2015. Vol. 10. DOI: https://doi.org/10.1186/s11671-015-0946-8
52. *Oakes L., Westover A., Mares J. W., Chatterjee S., Erwin W. R., Bardhan R., Weiss S. M., Pint C. L.* Surface engineered porous silicon for stable, high performance electrochemical supercapacitors // Sci Reports. 2013. Vol. 3. DOI: https://doi.org/10.1038/srep03020
53. *Olenych I. B., Aksimentyeva O. I., Monastyrskii L. S., Pavlyk M. R.* Electrochromic effect in photoluminescent porous silicon–polyaniline hybrid structures // J. Appl. Spectrosc. 2012. Vol. 79 (3). P. 495–498. DOI: https://doi.org/10.1007/s10812-012-9629-8
54. *Olenych I. B., Monastyrskii L. S., Luchechko A. P.* Photoluminescence of porous silicon–zinc oxide hybrid structures // J. Appl. Spectrosc. 2017. Vol. 84 (1). P. 66–70. DOI: https://doi.org/10.1007/s10812-017-0428-0
55. *Wu X. L., Siu G. G., Fu C. L., Ong H. C.* Photoluminescence and cathodoluminescence studies of stoichiometric and oxygen-deficient ZnO films // Appl. Phys. Lett. 2001. Vol. 78 (16). P. 2285–2287. DOI: http://dx.doi.org/10.1063/1.1361288

56. *Olenych I. B., Monastyrskii L. S., Aksimentyeva O. I.* Photovoltaic structures based on porous silicon // In: Sattler K. (eds) Silicon Nanomaterials Sourcebook: Hybrid Materials, Arrays, Networks, and Devices. CRC Press. Taylor & Francis Croup: New York, 2017. Vol. 2. P.499–522. DOI: http://dx.doi.org/10.4324/9781315153551-25
57. *Monastyrskii L. S., Aksimentyeva O. I., Olenych I. B., Sokolovskii B. S.* Photosensitive structures of conjugated polymer - porous silicon // Mol. Cryst. Liq. Cryst. 2014. Vol. 589. P. 124-131. DOI: https://doi.org/10.1080/15421406.2013.872400
58. Olenych I. B., Aksimentyeva O. I., Monastyrskii L. S., Horbenko Yu. Yu., Partyka M. V. Electrical and photoelectrical properties of reduced graphene oxide – porous silicon nanostructures // Nanoscale Res. Lett. 2017. Vol. 12. DOI: https://doi.org/10.1186/s11671-017-2043-7
59. *Bailey S. G., Flood D. J.* Space photovoltaics // Prog. Photovolt. 1998. Vol. 6. P. 1–14.
60. *Olenych I. B., Monastyrskii L. S.* Electrical and sensory properties of zinc oxide – porous silicon nanosystems // Mol. Cryst. Liq. Cryst. 2018. Vol. 671. P. 9–103. DOI: https://doi.org/10.1080/15421406.2018.1542092
61. *Olenych I. B., Monastyrskii L. S., Aksimentyeva O. I., Orovcík L., Salamakha M. Y.* Charge transport in porous silicon/graphene-based nanostructures // Mol. Cryst. Liq. Cryst. 2018. Vol. 673. P. 32–38. DOI: https://doi.org/10.1080/15421406.2019.1578491
62. *Gregg S. J., Sing K. S. W.* Adsorption, Surface Area and Porosity. London: Academic Press, 1982. 313 p.
63. *Lv C., Hu C., Luo J., Liu S., Qiao Y., Zhang Z., Song J., Shi Y., Cai J., Watanabe A.* Recent advances in graphene-based humidity sensors // Nanomaterials. 2019. Vol. 9. DOI: https://doi.org/10.3390/nano9030422.
64. *Vashpanov Y. A., Smyntyna V. A.* Adsorption Sensitivity of Semiconductors. Astroprint: Odesa, 2005. 216 p. (in Russian).
65. *Olenych I. B., Aksimentyeva O. I., Horbenko Y. Y., Tsizh B. R.* Electrical and sensory properties of silicon – graphene nanosystems // Appl. Nanosci. 2022. Vol. 12. P. 579–584. DOI: https://doi.org/10.1007/s13204-021-01698-7
66. *Kim S. J., Jeon B. H., Choi K. S., Min N. K.* Capacitive porous silicon sensors for measurement of low alcohol gas concentration at room temperature // J. Solid State Electrochem. 2000. Vol. 4. P. 363–366. DOI: https://doi.org/10.1007/s100089900090
67. *Monastyrskii L. S., Olenych I. B., Petryshyn O. I., Lozynskyi V. M.* Gas analysis system based on the porous silicon structures // Sensor Electronics and Microsystems Technologies. 2018. Vol. 15 (2). P. 88–96 (in Ukrainian).
68. *Rahimi F., Iraji Zad A.* Effective factors on Pd growth on porous silicon by electroless-plating: Response to hydrogen // Sens. Actuators B Chem. 2006. Vol. 115. P. 164–169. DOI: https://doi.org/10.1016/j.snb.2005.08.035
69. *Yan D., Li S., Liu S., Tan M., Li D., Zhu Y.* Electrochemical synthesis of ZnO nanorods / porous silicon composites and their gas-sensing properties at room temperature // J. Solid State Electrochem. 2016. Vol. 20. P. 459–468. DOI: https://doi.org/10.1007/s10008-015-3058-6
70. *Galstyan V., Comini E., Baratto C., Faglia G., Sberveglieri G.* Nanostructured ZnO chemical gas sensors // Ceram. Internat. 2015. Vol. 41. P. 14239–14244. DOI: https://doi.org/10.1016/j.ceramint.2015.07.052

Chapter 9

STRUCTURAL AND MORPHOLOGICAL FEATURES OF NANOCELLULOSE FROM SOYBEAN STRAW

T. V. Tkachenko, D. S. Kamenskyh,
Y. V. Sheludko, and V. O. Yevdokymenko

V. P. Kukhar Institute of Bioorganic Chemistry and Petrochemistry,
National Academy of Sciences of Ukraine, Kyiv-94 02094, Ukraine

Corresponding author: ttv13ttv@gmail.com

Contents

Abstract

From the microcrystalline cellulose obtained from air-dry soybean straw by the method of organ-solvent cooking obtained nanocellulose (NC). Using the methods of XRD, XRF, FTIR-ATR, AFM, TGA and DSC, the structure and morphology of nanocellulose were studied. Due to the destruction of amorphous binders in the original MCC, regardless of the conditions of its production, we observe further ordering of the structure of the obtainned NC. Which is expressed in narrower and more intense peaks in the range 2θ = 22–23° and IC values, as well as in reducing the degree of polymerization more than twice compared to the original microcrystalline cellulose (MCC). As can be seen from the FTIR-ATR spectra, the NC has all the characteristic peaks for the MCC. The increase in the crystallinity of the NC parts after MCC treatment is confirmed by thermogravimetric analysis and differential thermogravimetric analysis of samples. According to AFM the NC forms an anisotropic relief which consists of many parallel bands (ridges) and striped reliefs with almost parallel-oriented linear stripes.

9.1 Introduction

Nanocellulose (NC) is a natural nanomaterial which can be extracted from plant cell wall [1, 2]. Cellulose molecules with at least one dimension in nanoscale (1–100 nm) are referred to as nanocellulose [3]. The unique characters of nanocellulose, such as superior mechanical properties, low density, high specific surface area, and low thermal expansion coefficient, make them an ideal building block for flexible functional compounds [2, 4]. The characteristic properties of nanocellulose like crystallinities, surface area, and mechanical properties vary with the extraction methods and processing techniques [2, 3]. Thus, the aim of this paper is to compare structural and morphological features of nanocellulose obtained from soybean straws microcrystalline cellulose (MCC) at differern ratio pulp over liquor.

9.2 Materials and Methods

Air-dry microcrystalline cellulose obtained by the method of organ-solvent cooking described in [5] from air-dry soybean straw was used. Two samples of MCC obtained at different ratios 1 : 10 (MCC10) or 1 : 15 (MCC15) of pulp over liquor were used for research (Table 9.1). The chemical composition of MCC ash (inorganic components) determined by using XRF are shown in Table 2.

NC was obtained from MCC by a known method [6]. The cellulose yield (*Y*) was calculated using equation:

$$Y = \frac{Absolute\ weight\ of\ \ cellulose\ \ after\ treatment}{Absolute\ weight\ of\ \ cellulose\ \ before\ treatment} 100\%. \quad (9.1)$$

Table 9.1 The main characteristics of MCC from soybean straw

MCC	Ash, mass. %	Cellulose, mass. %	Klason lignin, mas. %	CI, %	DP
10	0.8	96.6	3.4	0.70	275
15	0.5	97.8	2.2	0.67	384

Table 9.2 Composition of MCC ash from soybean straw

MCC	Formula, mass. %							
	SiO_2	K_2O	CaO	TiO_2	Fe_2O_3	SO_2	Cl	P_2O_5
10	57.613	5.627	26.798	0.889	2.689	2.765	2.003	2.506
15	85.185	3.401	2.570	0.514	1.128	0.865	0	0

The contents of cellulose, hemicellulose, lignin and other chemical components in cellulosic products were determined by standard chemical analysis, described earlier [7]. All chemical analysis was carried out twice allowing to calculate the mean values and standard deviations, which do not exceed 5%. The inorganic components were determined using Expert 3L XRF (INAM, Ukraine). The degree of polymerization (DP) of cellulose samples was determined by viscosity measurements in a cadmium ethylenediamine solution using an Ostwald viscometer.

The phase identification of the products was examined under X-ray diffraction (XRD) using the MiniFlex 300/600 diffractometer (Rigaku, Japan). The diffraction patterns were recorded using Cu-Kα radiation (λ = 0.15418 nm), the operating voltage of 40 kV and current of 15 mA. XRD pattern of samples was obtained in the 2θ range between 10^o and 60^o with a step of 0.02^o. The crystallinity index (CI) [8] was calculated according to equation

$$CI = \frac{I_{22}}{I_{22} + I_{18}} 100\%, \tag{9.2}$$

where, I_{22} and I_{18} are the crystalline and amorphous intensities at 2θ scale close to 22° and 18°, respectively. FTIR analysis of the obtained cellulose was performed using IRAffinity-1S FTIR spectrometer (Shimadzu, Japan) equipped with a Quest ATR Diamond GS-10800X (Specac, UK) within the wavenumber range of 4000 to 400 cm^{-1}. The surface morphology was investigated with atomic force microscope (AFM) NT-206 (Company with double liability "Microtestmachines", Belarus) equipped with standard sonde CSC37 and rigidity of console 0.3–0.6 N/m. The scan was run in a contact static mode at 10 mcm/s with a step of 0.3 nm.

Samples of cellulose (4 mg) were stirred in ethyl alcohol (5 ml) for 15 min. The resulting suspension (0.25 ml) was applied to quartz glass and dried at 50 °C to constant weight. Then the scan was performed on AFM. Thermogravimetric analysis (TGA) and differential scanning calorimetric analysis (DSC) were performed with a PT1600 TG-DTA/DSC (STA Simultaneous Thermal Analysis, LINSEIS Messgeräte GmbH, Germany). The samples (13.0 ± 0.1 mg) were collected in a standard corundum pan. The scan was run at 5 °C/min

under a flow of air. The mass change was measured from 20 to 1000 °C. The sample was analysed three times.

9.3 Results and Discussion

A white, tasteless and odorless NC was obtained under the earlier described method from MCC 10 and MCC 15. The NC percentage yield was calculated by Eq. (9.1) (Table 9.3). The results of the chemical composition of obtained NC were determined using the above-described methods and the data were summarised in Table 9.3. The increase in lignin and ash content is due to the peculiarities of the obtaining NC. The process of its production involves the destruction of amorphous parts of the MCC under the action of acid (Fig. 9.1) [9], which is not associated with 100% yields. Under such conditions, there is no extraction of acid-insoluble lignin and ash, which is also acid-resistant because it consists mainly of silicon dioxide (see Table 9.2).

Table 9.3 The main characteristics of obtaining NC

Raw materials	Cellulose yield (Y), mass. %	Klason lignin, mass. %	Ash, mass. %	CI, %	DP
MCC 10	90.0	3.8	9.4	0.78	124
MCC 15	89.5	2.6	7.5	0.71	190

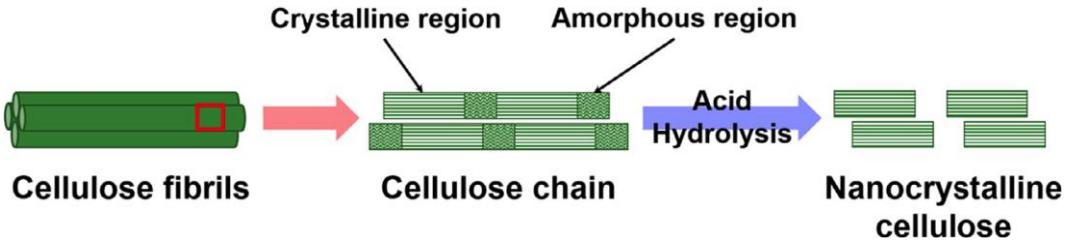

Figure 9.1 Nanocellulose production scheme [9]

The XRD patterns of the NC from the MCC 10 and MCC 15 are presented in Fig. 9.2. At the same time, as noted above, due to the destruction of amorphous binders in the original MCC, regardless of the conditions of its production, we observe further ordering of the structure of the obtained NC (Fig. 9.2, Table 9.3). Which is expressed in narrower and more intense peaks in the range $2\theta = 22–23°$ (Fig. 9.2) and IC values (Table 9.3), as well as in reducing the degree of polymerization more than twice.

As can be seen from the FTIR-ATR spectra (Fig. 9.3), the NC has all the characteristic peaks for the MCC. There are characteristic absorption bands in the regions 3000–3600, 2700–3000, 1300–1500, 1000–1200 cm^{-1}, which correspond to thesymmetric and asymmetric valent and stretching vibrations –OH and –CH, $–CH_2$ groups and deformation and valent vibrations CO and C-O-C cellulose ring, respectively [5, 10]. Strong adsorption at

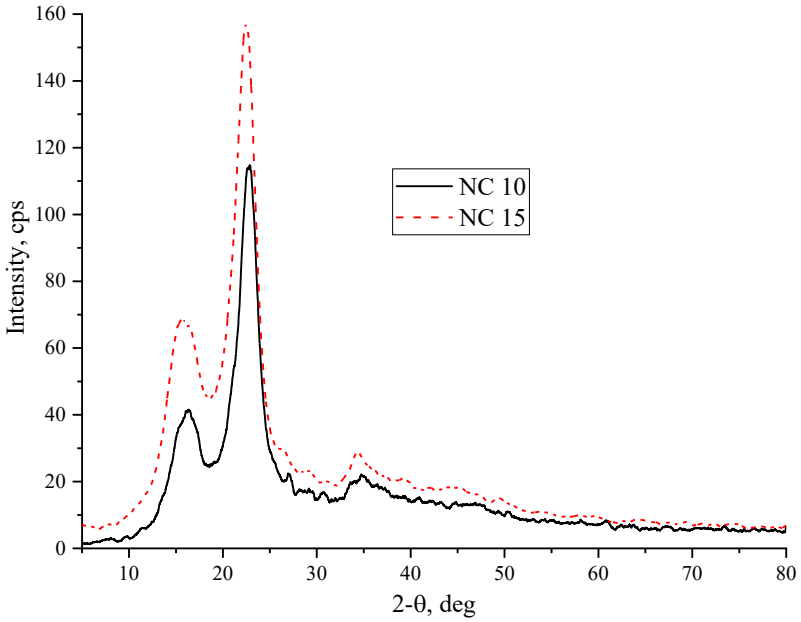

Figure 9.2 XRD patterns of NC

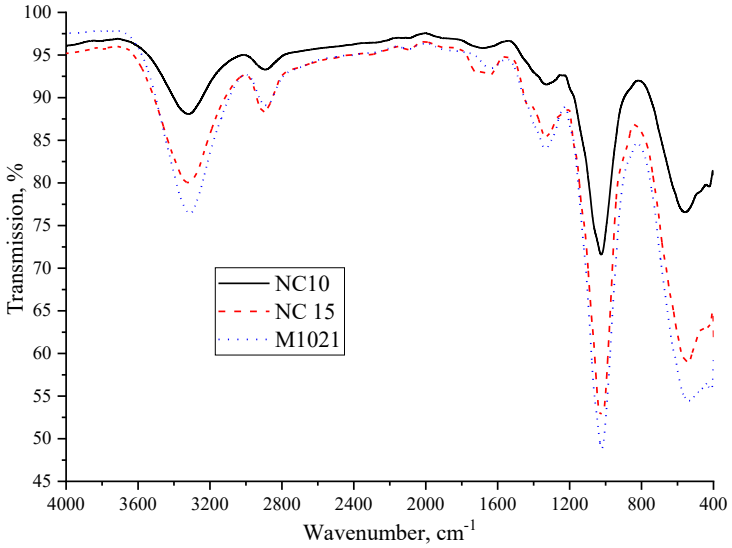

Figure 9.3 FT-IR spectra of NC compared to commercial MCC

1640–1630 cm^{-1} belonged to the surface hydroxyls [11]. The absence of the absorption band at 1511 cm^{-1}, which is characteristic of skeletal vibrations of the aromatic ring, indicates a decrease in the amount of lignin in the products. The band in the absorption region at 900 cm^{-1} characterizes the asymmetric vibrations in antiphase and the vibrations of the C1 atom and the four surrounding atoms of β-glycosidic structures. This band is called the amorphous band [12]. In the obtained samples IR spectra (Fig. 9.3), there are no characteristic absorption bands of phenylpropane units of lignin (1605–1593, 1515–1495, 1470–

1460 cm^{-1}). This indicates the occurrence of deep oxidative transformations of phenolic structures and efficient diffusion of delignification products into solution under experimental conditions [13]. However, the peak at 1740–1720 cm^{-1} in flax fibres corresponds to acetyl and uronic ether groups of hemicelluloses or ether bond of the carboxylic group of ferulic and *p*-cumeric acids of lignin and/or hemicelluloses [14], which agrees well with the data in Table. 9.3. The band which corresponds to symmetric CH_2 bendings at 1429–1428 cm^{-1} increased for NC in comparison to comercial MCC [15]. This band is known as the crystallinity band, where the increase in the intensity demonstrates a higher degree of crystallinity [15].

The increase in the crystallinity of the NC parts after MCC treatment is confirmed by thermogravimetric (TG) and differential thermogravimetric (DTG) analysis of samples (Fig. 9.4). In Fig. 9.4 shows the change in thermal stability of the NC samples. As can be seen from the thermogravimetric curves (Fig. 9.4), the weight loss of all NC samples begins at a temperature of about 60 °C, which is due to the evaporation of residual moisture from the fibre and possibly not washed acid. The main weight loss begins at temperatures of 207–220 °C and lasts up to 500 °C in contrast to the MCC has not two but 3–4 peaks (Fig. 9.4). This may be because the amount of crystalline part of cellulose increases, and it is strengthened by hydrogen bonds between cellulose macromolecules by the fact that during chemical treatment and ultrasonic homogenization a dense structure is formed between pulp molecules [6]. The TG/DTG (Fig. 9.4) and DSC (Fig. 9.5) curves show that cellulose samples should not be heated above 200 °C.

Figure 9.6, *a*, *b* shows respectively 2D and 3D images of the relief of the surface of the NC synthesized at GM 10. It should be noted that the NC forms an anisotropic relief, which consists of several parallel bands (wedges). The surface roughness is R_a = 12.6 nm. The difference between depressions and heights is from –53.6 to + 63.6 nm (Fig. 9.6, *c*).

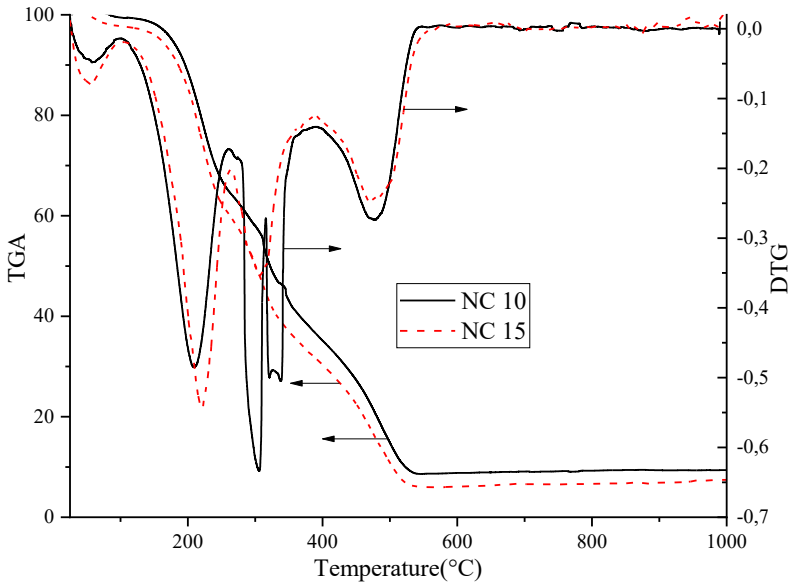

Figure 9.4 TG i DTG curves for NC

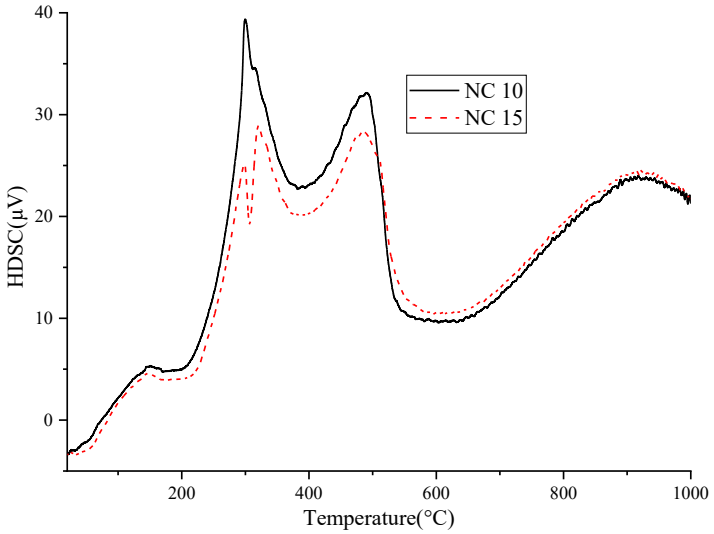

Figure 9.5 DSC curves for NC

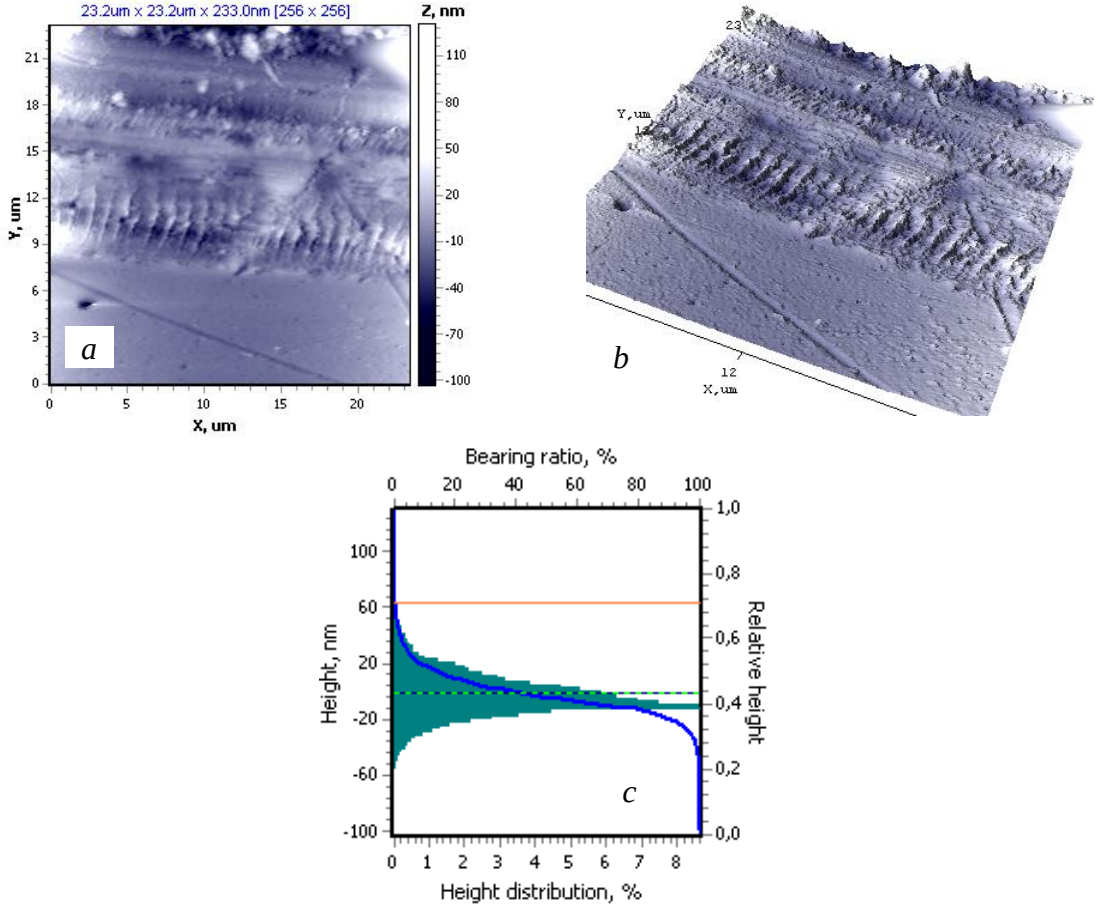

Figure 9.6 2D (*a*) and 3D (*b*) images of NC 10 and its histogram (*c*)

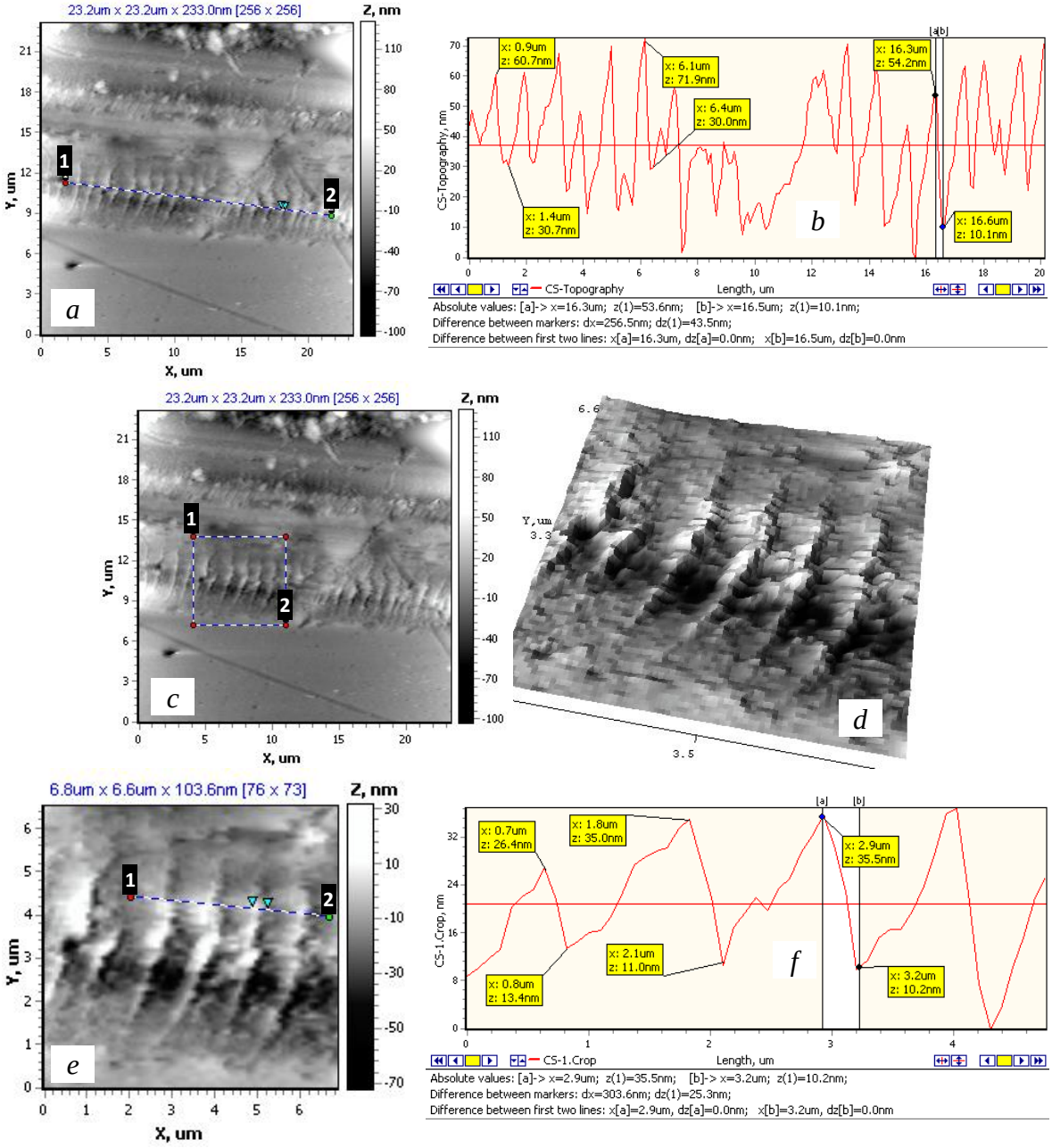

Figure 9.7 2D (*a*) image of NC 10 and its profile (*b*) and the fragment of wedges on relief (*c*) and its 3D view (*d*), as well as their section (*e*) and profile (*f*)

Figure 9.7 shows the cross-sectional line in the 2D image (*a*) and its profile (*b*). These data indicate that the heights of the wedges are within 30.0; 41.9; 44.1 nm, and the distance between the vertices of the wedges is dx = 1.1; 0.8; 0.9 μm. It should be noted the following feature of the relief. If we select a fragment of wedge on the relief (Fig. 9.7, *c*) and

change it into 3D view (Fig. 9.7, *d*), it is clear that the surface of the wedges is not continuous but consists of the tops of particles. That is, nanoparticles aggregate with each other, forming waves (d) with a surface roughness R_a = 8.8 nm. In this fragment, the height of the wedges is 13.0; 24.0; 25.3; 35.0 nm, and the distances between the vertices dx are 1.2 1.1; 1.1; and 1.2 nm (Fig. 9.7, *e*, *f* – cross-section and its profile).

The fact that the surface of the wedges (Fig. 9.8, *a*) consists of the vertices of pyramidal particles is confirmed by a section along the wedges (Fig. 9.8, *b*) and its profile (Fig. 9.8, *c*), which shows the alternation of vertices of different heights.

It should be noted another feature of the formation of nanorelief in the NC 10. In Figure 9.9, *a–d* on the 2D image of another relief area and on the selected fragment the formation of disc-shaped flat formations with a surface roughness R_a = 2.7 nm (Fig. 9.9, *b*) is clearly visible. The difference between altitudes and depressions is from –7.6 nm to + 9.4 nm (histogram Fig. 9.9, *j*). Analyzing the profiles of sections (Fig. 9.9, *f*, *g*) we conclude that the height of the disks (or thickness) is dz = 2.6; 4.2; 3.7 nm, and the width (or diameter) is 195.3; 230.9; 230.8 nm (for profile – Fig. 9.9, *f*). For profile (Fig. 9.9, *h*) these values are: dz = 1,6; 1.3 nm, dx = 590.9; 399.7 nm.

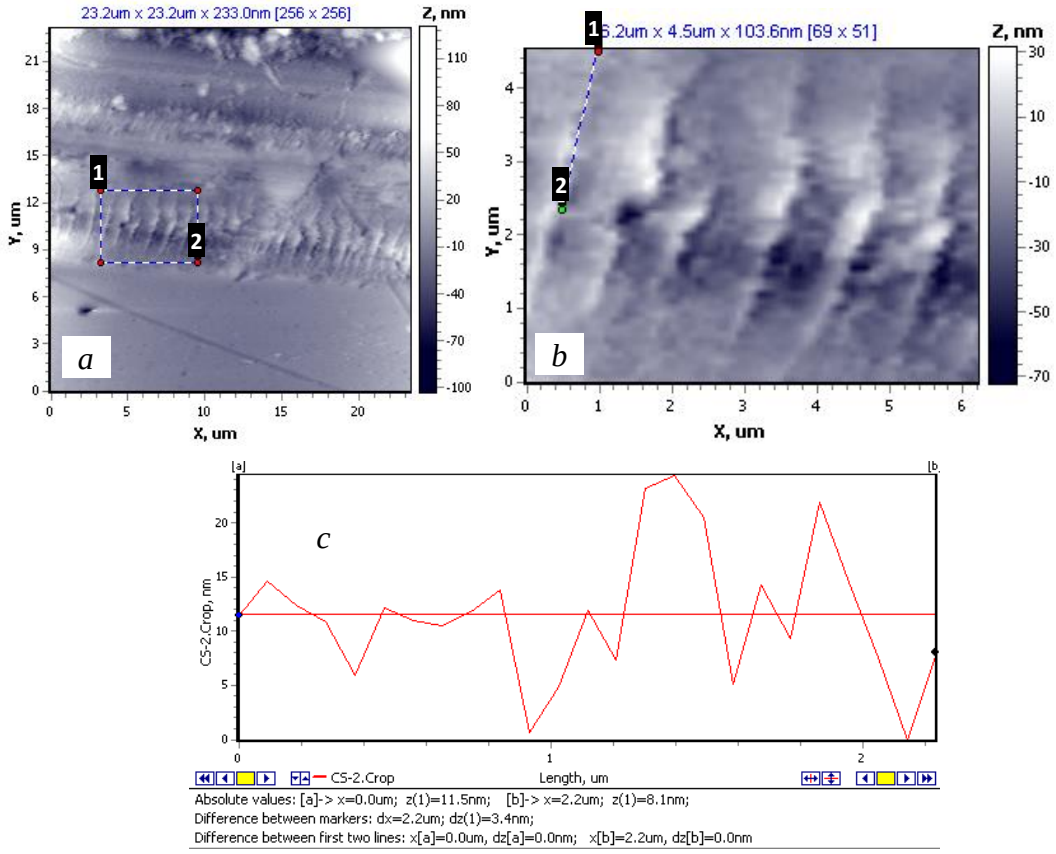

Figure 9.8 Selected fragment of wedges (*a*), fragment (*b*) with cross-sectional line and its profile (*c*)

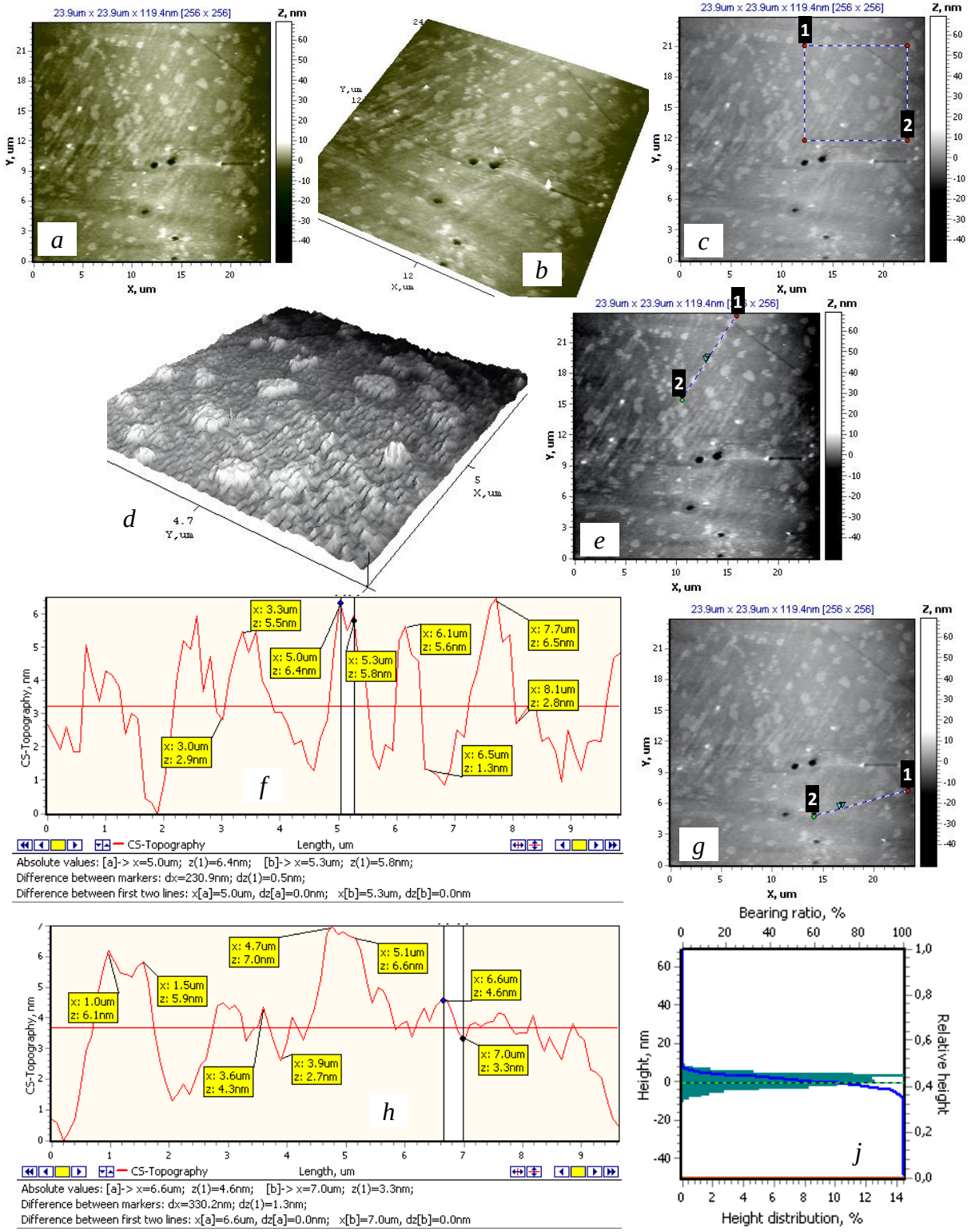

Figure 9.9 Analysis of the relief of NC 10 (see text)

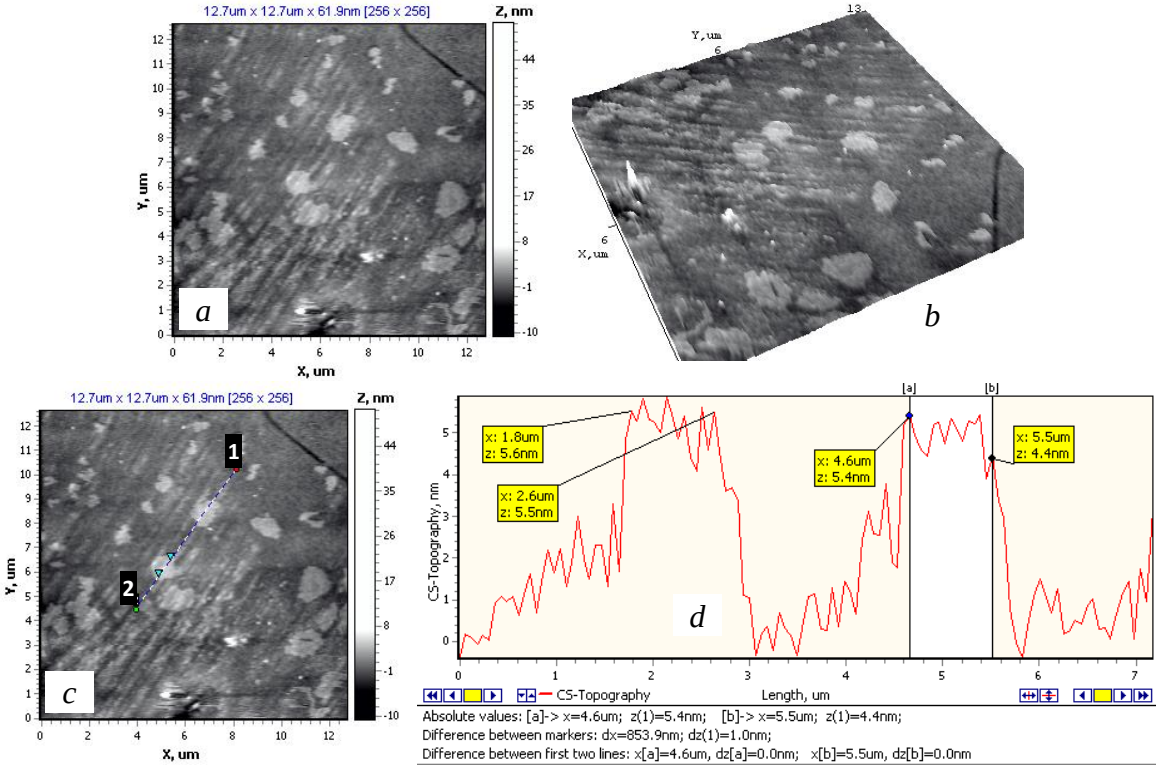

Figure 9.10 Scan 12.7×12.7 μm: 2D and 3D (*a*, *b*) image, cross-section and profile (*c*, *d*)

In Figure 9.10 shows 2D (*a*) and 3D (*b*) images of the same relief on a 12.7×12.7 μm scan. In this area, the roughness is R_a = 1.1 nm. In carrying out the section and analyzing the corresponding profile, it is possible to establish that each disk is formed by the association of separate particles (pyramids). For example, the profile (Fig. 9.10, *c*, *d*) has disks with 6 vertices at diameters dx = 856.1 nm and 853.9 nm.

To confirm the structure of flat disks by combining individual pyramidal particles Fig. 9.11 shows a 2D image (*a*) with a separate fragment (*b*) and its 3D (*c*) view. The 3D

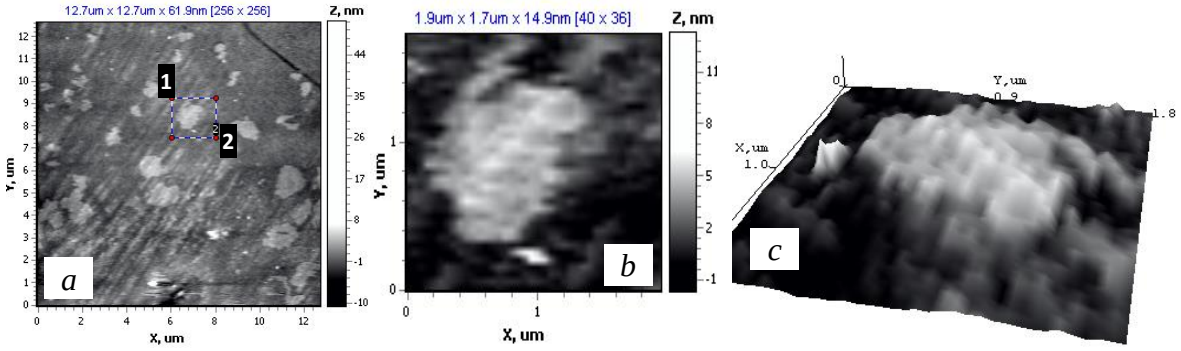

Figure 9.11 2D image of the selected flat disk fragment (*a*), the fragment itself (*b*) and its 3D image (*c*)

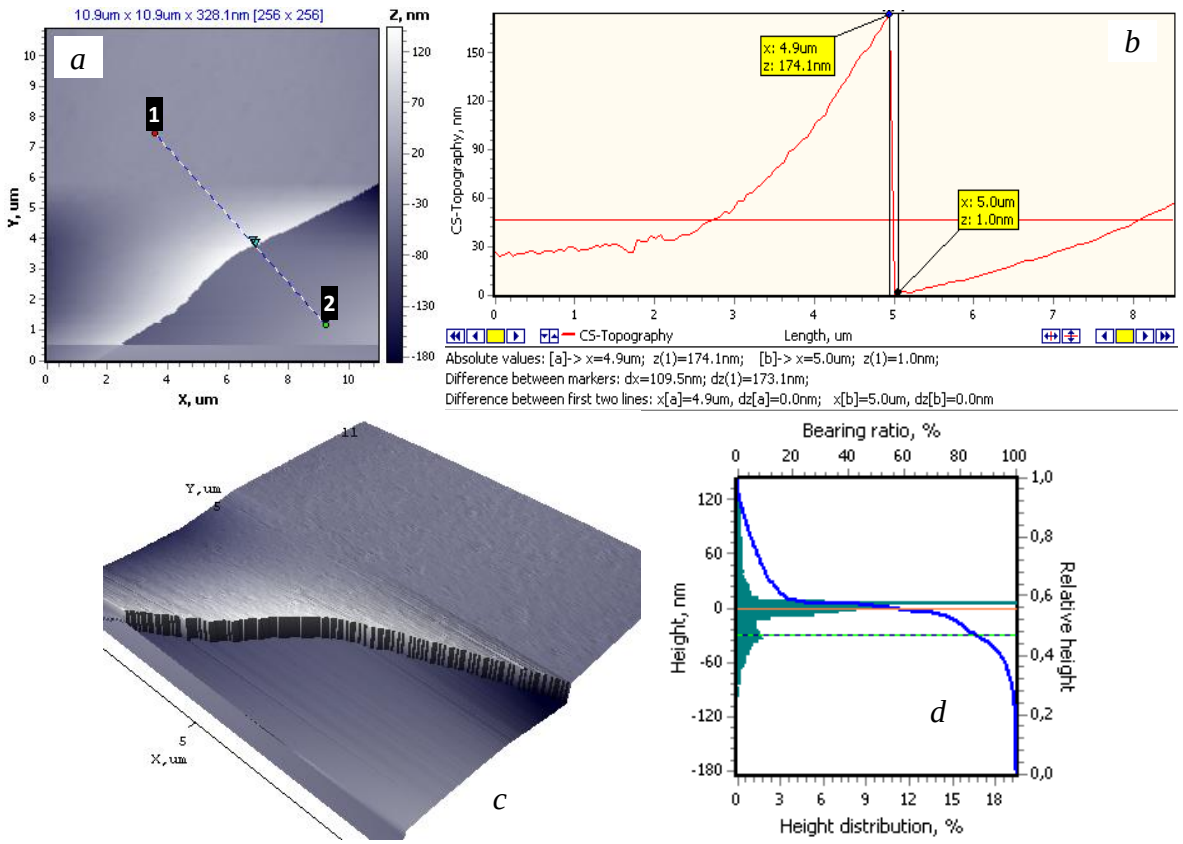

Figure 9.12 Analysis of the end of the NC 15

image (Fig. 9.11, *c*) shows that the selected fragment (Fig. 9.11, *a*, *b*) consists of individual nanoparticles that formed flat disc-shaped aggregates.

Figure 9.12 a shows the relief of the surface with a section lines 1–2. The probe unexpectedly landed on the "film-substrate" boundary. Thus, you can fix the thickness. Section profile 1–2 (Fig. 9.12, *b*). The height of the ledge-section (or layer thickness) is 173.1 nm. Characteristically, the end surface of the film (section) is formed by strictly linear vertical structures (Fig. 9.12, *c*). The scatter of heights and depressions (across the scan) judging by the histogram is from –80.4 nm to 107.9 nm (Fig. 9.12, *d*). The roughness value R_a = 22.7 nm (Fig. 9.12, *c*).

The topography of the surface with section lines 1–2 is given in Fig. 9.13, *a*. In the main section of the film, the relief is quite flat, which is confirmed by the analysis of the cross-sectional profile (Fig. 9.13, *b*). Nanometer height range for this section is: 1.3; 1.7; 1.9; 0.5; 1.3 nm.

A fragment from a 109×109 μm scan was isolated (Fig. 9.14, *a*). Scanning of the selected fragment of 3.7×3.7 μm with a line of sections 1–2 and obtaining a 2D image (Fig. 9.14, *b*). In Figure 9.14, *d* shows the section profile 1–2. In the selected area of the surface, the height of the relief is nanometer and is 0.8; 1.0; 0.3; 0.5; 0.8 nm. Therefore, the roughness is also minimal R_a = 0.8 nm, which can be seen in the 3D image (Fig. 9.14, *c*).

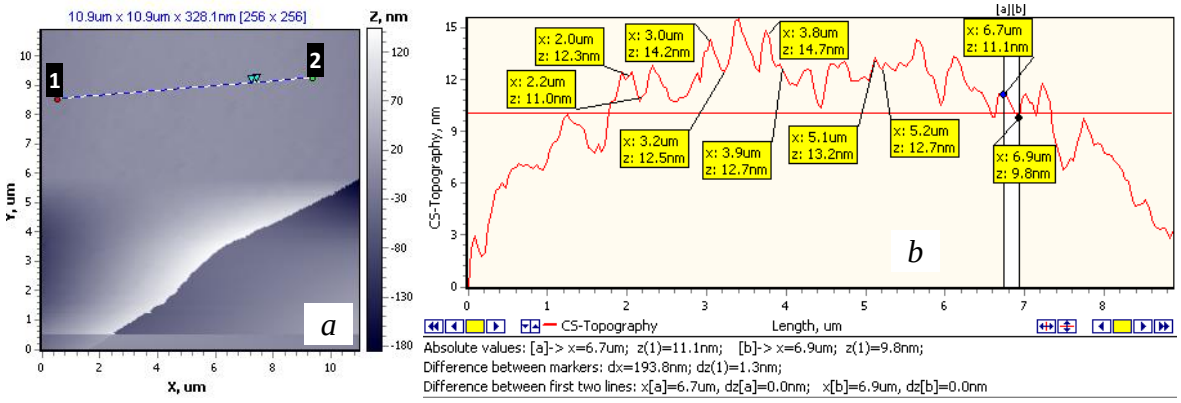

Figure 9.13 Surface topography with the line of intersection (*a*) and profile (*b*)

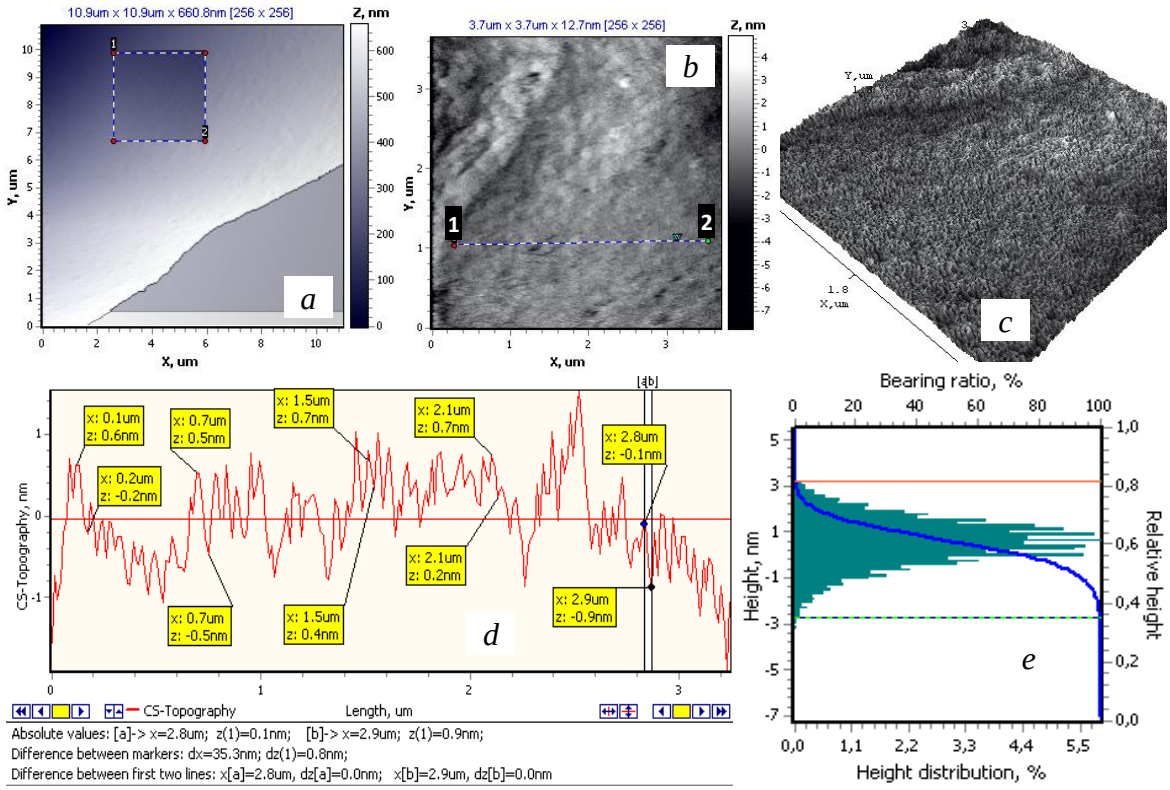

Figure 9.14 Analysis of the relief of NC 15 (see text)

The total difference in heights and depressions in this area is from –2.7 to +1.1 nm (Fig. 9.14, *e*).

A nanometer fragment of 522.5×522.5 nm (Fig. 9.15, *a*) was isolated from the previous section of 3.7×3.7 μm (Fig. 9.14, *b*). Scanning of the fragment 522.5×522.5 nm and section line 1–2 (Fig. 9.15, *b*). This area is characterized by striped relief with almost parallel oriented linear stripes. The range of heights is even smaller and is 0.4; 05; 0.8; 1.1 nm.

Therefore, the roughness in this area is even lower and is only R_a = 0.3 nm (Fig. 9.15, *c*). Judging by the histogram, the total difference of depressions and heights is from –0.9 to + 1.1 nm (Fig. 9.15, *d*).

If from the scan 522.5×522.5 nm (Fig. 9.16, *a*), select and cut an even smaller fragment of 188.5×186.5 nm (Fig. 9.16, *b*) and present it in a 3D image (Fig. 9.16, *c*), you can see the parallel nanocellulose planes 3 nm thick.

Thus, in this case, at the nanolevel, there is an oriented planar packing of nanocellulose fragments.

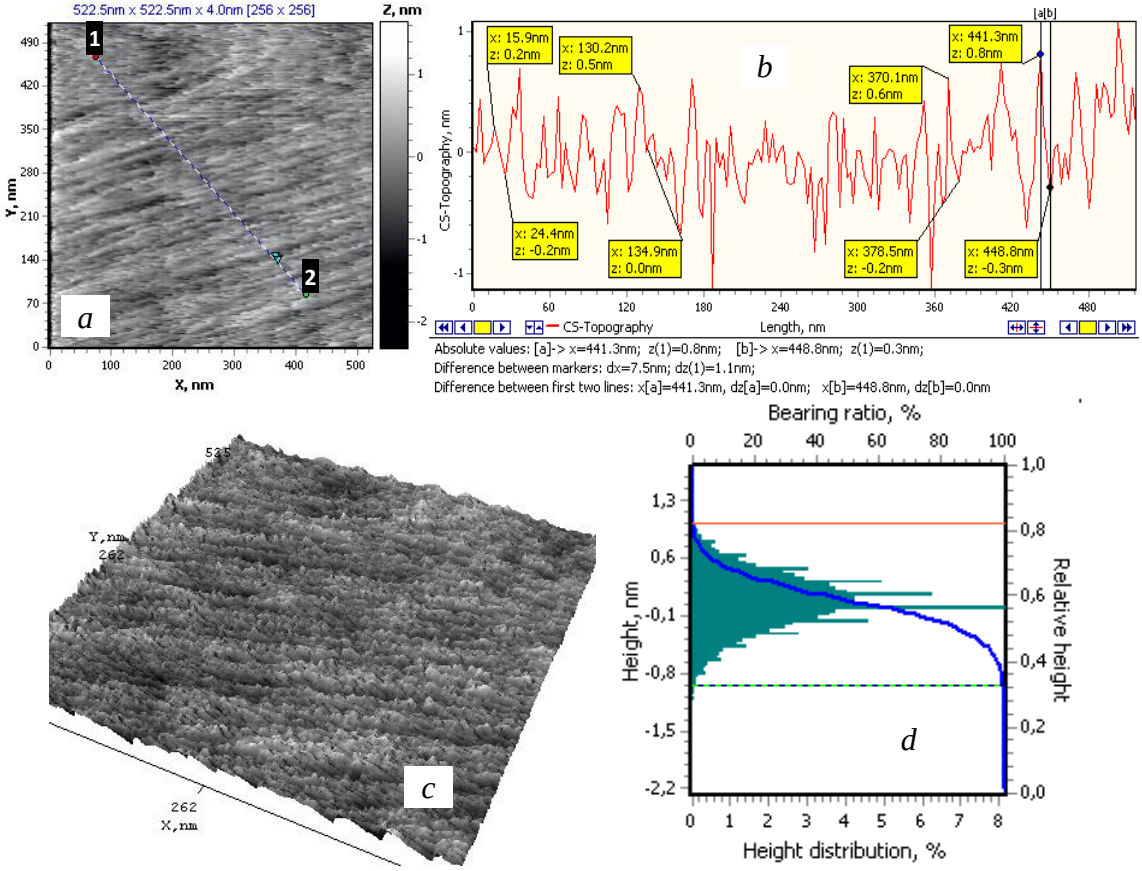

Figure 9.15 3.7×3.7 μm scan: 2D (*a*) and 3D (*c*) images, profile (*b*) and histogram (*d*) (see text)

9.4 Conclusions

Nanocellulose was obtained from MCC samples and its main physicochemical characteristics were investigated. It is shown that to obtain nanocellulose, it is necessary to take high-purity MCC since only further destruction of the amorphous components of cellulose

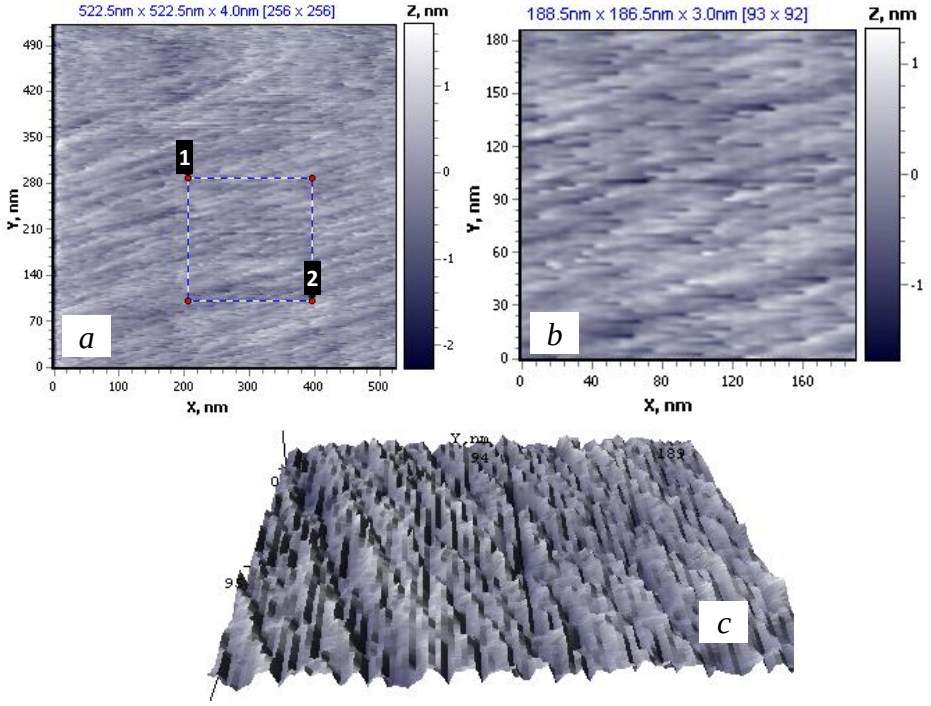

Figure 9.16 522.5 × 522.5 nm scan: 2D (*a*, *b*) and 3D (*c*) images (see text)

occurs during the preparation of NC. It should be noted that NC 10 forms an anisotropic topography consisting of several parallel bands (wedges). The surface roughness is R_a = 12.6 nm. The following feature of the relief should be noted. If you select a fragment of wedges on the relief and transform it into a 3D view, you can see that the surface of the wedges is not continuous, but consists of the tops of particles. That is, nanoparticles aggregate among themselves, forming waves. Unlike NC 10, NC 15 has a striped relief with almost parallel-oriented linear stripes. The surface roughness is R_a = 0.3 nm.

Acknowledgements

The catalytic experiments and laboratory installation assembling have been funding by Target Complex Program of Scientific Research of NAS of Ukraine “Biofuels and bioenergy” (2018–2022).

Keywords

- nanocellulose
- microcrystalline cellulose
- soybean straw
- relief of the surface
- atomic force microscopy

References

1. *Phanthong P., Reubroycharoen P., Hao X., Xu G., Abudula A., Guan G.* Nanocellulose: Extraction and application // Carbon Resour. Convers. 2018. Vol. 1 (1). P. 32–43. DOI: https://doi.org/10.1016/j.crcon.2018.05.004
2. *Heise K., Kontturi E., Allahverdiyeva Y., Tammelin T., Linder M. B., Nonappa, Ikkala O.* Nanocellulose: Recent Fundamental Advances and Emerging Biological and Biomimicking Applications // Adv. Mater. 2021. Vol. 33. P. 2004349. DOI: https://doi.org/10.1002/adma.202004349
3. *Nasir M., Hashim R., Sulaiman O., Asim V.* Chapter 11. Nanocellulose: Preparation methods and applications // Mohammad Jawaid, Sami Boufi and Abdul Khalil H.P.S. (Eds.). Cellulose-Reinforced Nanofibre Composites. 2017. P. 261–276. DOI: https://doi.org/ 10.1016/B978-0-08-100957-4.00011-5
4. *Barbash V. A., Yashchenko O. V., Vasylieva O. A.* Preparation and Properties of Nanocellulose from Miscanthus x giganteus // Journal of Nanomaterials. Vol. 2019. P. 3241968(1–8). DOI: https://doi.org/10.1155/2019/3241968
5. *Tkachenko T., Sheludko Y., Yevdokymenko V., Kamenskyh D., Khimach N., Povazhny V., Filonenko M., Aksylenko M.* Physico-chemical properties of flax microcrystalline cellulose // Appl. Nanosci. 2022. Vol. 12, Is. 4. P. 1007–1020. DOI: https://doi.org/10.1007/s13204-021-01819-2
6. *Barbash V. A., Yashchenko O. V.* Preparation and application of nanocellulose from non-wood plants to improve the quality of paper and cardboard // Appl. Nanosci. 2020. Vol. 10. P. 2705–2716. DOI: https://doi.org/10.1007/s13204-019-01242-8
7. *Tigunova O. O., Beiko N. E., Kamenskyh D. S., Tkachenko T. V., Yevdokymenko V. O., Kashkovskiy V. I., Shulga S. M.* Lignocellulosic biomass after explosive autohydrolysis as substrate for butanol // Biotechnologia acta 2016. Vol. 9, Is. 4. P. 28–34. DOI: https://doi.org/10.15407/biotech9.04.028
8. *Swantomo D., Giyatmi G., Adiguno S. H., Wongsawaeng D.* Preparation of microcrystalline cellulose from waste cotton fabrics using gamma irradiation // Eng. J. 2017 Vol. 21, Is. 2. P. 173–182. DOI: https://doi.org/10.4186/ej.2017.21.2.173
9. *Phanthong P., Reubroycharoen P., Hao X., Xu G., Abudula A., Guan G.* Nanocellulose: Extraction and application // Carbon Resour. Convers. 2018. Vol. 1, Is. 1. P. 32-43. DOI: https://doi.org/10.1016/j.crcon.2018.05.004.
10. *Bazarnova N. G., Karpova Ye. V., Katrakov I. B., Markin V. I., Mikushina I. V., Ol'khov Yu. A., Khudenko S. V.* Metody issledovaniya drevesiny i yeye proizvodnykh. [Methods for studying of wood and its derivatives]. Barnaul, 2002. 160 p. (in Russian).
11. *Kuznetsova B. N., Sudakova I. G., Garyntseva N. V., Ivanchenko N. M.* Abies Wood Delignification by Hydrogen Peroxide at Mild Conditions in the Presence of Sulfuric Acid Catalyst // Journal of Siberian Federal University. Chemistry. 2013. Vol. 6, Is. 4. P. 361–371. (in Russian).
12. *Levdanskiy V. A., Levdanskiy A. V., Kuznetsov B. N.* Ecology safe method of obtaining from firwood the cellulosic product with high content of alfa-cellulose // Himija rastitel'nogo syr'ja (Chemistry of plant raw material). 2014. Is. 2. P. 35–40. (in Russian).
13. *Kushnir E. J., Autlov S. A., Bazarnova N. G.* Preparation of microcrystalline cellulose directly from wood under microwave irradiation // Himija rastitel'nogo syr'ja (Chemistry of plant raw material). 2014. Is. 2. P. 41–50. (in Russian).
14. *Duan L., Yu W., Li Z.* Analysis of structural changes in jute fibers after peracetic acid treatmen // J. Eng. Fiber Fabr. 2017. Vol. 12, Is. 1. P. 33–42. DOI: https://doi.org/10.1177/ 155892501701200104
15. *Hazwan H. M., Husin N. A., Bello I., Othman N., Bakar M. A., Mohamad Haafiz M. K.* Isolation of microcrystalline cellulose (MCC) from oil palm frond as potential natural filler for PVALiClO$_4$ polymer electrolyte // Int. J. Electrochem. Sci. 2018. Vol. 13. P. 3356–3371. DOI: https://doi.org/10.20964/2018.04.06

WELLCOME
on 3rd International Research And Practice Conference "Nanoobjects & Nanostructuring" (N&N–2024)
September 2024
Lviv, Ukraine